Optical Studies of Gasoline Sprays and In-cylinder Mixture Formation using a High Pressure Multi-hole Injector

A thesis submitted for the degree of

Doctor of Philosophy

by

Meghnaa Paresh Dhanji

Department of Mechanical and Aerospace Engineering

College of Engineering, Design and Physical Sciences

Brunel University London

October 2020

Abstract

An on-going challenge with Gasoline engines is achieving rapid activation of the three-way catalyst during cold starts, in order to minimise pollutant emissions. Retarded combustion can help achieve rapid light-up of the three-way catalyst and can be facilitated by stratified charge using late injection. Injecting late in the compression stroke however, provides the fuel insufficient time for fuel entrainment, resulting in locally fuel rich diffusion combustion. Employing a split injection strategy can help tackle these issues. The effects of a split injection strategy on the spray characteristics and in-cylinder charge formation are investigated in the current study.

Varying pulse width (PW) combinations, split ratios and dwell times are investigated, with pressures of up to 35MPa, using a state-of-the-art solenoid actuated high pressure gasoline injector. The experiments were performed in a constant volume spray chamber. The droplet velocities and sizes were measured using Phase Doppler Anemometry. Short and large PWs, in the range of 0.3ms to 1.5ms, were investigated. The results revealed that the highest injected quantity of fuel was measured with the shortest dwell time of 2ms, owing to increased interactions between the injection events, which led to larger drop sizes measured. The drop sizes from the short PW of 0.4ms were generally larger than 0.8ms PW, due to closely spaced opening and closing events of the solenoid valve. The high injection pressure had also resisted the timely closing of the Solenoid valve when short PWs operating in the ballistic zones were used. This led to larger overall duration of injection.

The studies on the charge motion using split injections are performed inside an optical Gasoline engine using high-speed particle image velocimetry in the tumble and Omega-tumble planes, at a repetition rate of 10KHz. The engine's conditions were representative of low-load operations. The results revealed that a small split ratio of 25%-75%, with both injections in the intake stroke, was effective at generating a flow field with high turbulence levels close to the spark plug, when compared to 75%-25% split ratio. The injection coupled with inlet valve opening formed strong tumble charge motion, which was preserved throughout the compression stroke. This provides favourable conditions for fast flame propagation. The fuel injection timings which maximised interactions with the piston surface were detrimental for mixture formation due to heavy surface impingement. The findings from the study helped determine the optimum split injection properties.

Acknowledgements

List of Publications

1. Dhanji, M. and Zhao, H., "Investigations of Split Injection Properties on the Spray Characteristics Using a Solenoid High-pressure Injector," IJER 20-02-011.

2. Dhanji, M. and Zhao, H., "Effect of a Split-injections Strategy on the Atomisation Rate for Charge Stratification using a High-pressure Gasoline Multi-hole Injector," SAE Technical Paper 2020-01-0322, 2020.

3. Dhanji, M. and Zhao, H., "Spray Characterisation of a Split-injection Strategy using a High-pressure Gasoline DI Injector," SAE Technical Paper 2019-01-2248, 2019.

4. Dhanji, M. and Zhao, H., 'Studies of a Split Injection Strategy in a GDI Engine via Cycle-resolved PIV Measurements,' under preparation for submission to the International Journal for Engines Research.

Nomenclature

ASOI: after start of injection

ASOI1: after start of first injection

ASOI2: after start of second injection

AT: acquisition time

aTDC: after top dead centre

BDC: bottom dead centre

BMEP: brake mean effective pressure

bTDC: before top dead centre

CAD: crank angle degrees

CFD: computational fluid dynamics

CMOS: complementary metal oxide semiconductor

CO: carbon monoxide

COV: coefficient of variation

CR: compression ratio

DAQ: Data acquisition

DEHS: Di-Ethyl-Hexyl-Sebacic-Acid-Ester

DI: direct injection

EGR: exhaust gas recirculation

EOI1: end of first injection

EOI2: end of second injection

ETU: engine timing unit

FOV: field of view

FSN: filter smoke number

GDI: Gasoline direct injection

HRR: heat release rate

IA: interrogation area

IIS: injection-injection-spark

IMEP: indicated mean effective pressure

IMF: imaging model fit

ISFC: indicated specific fuel consumption

ISI: injection-spark-injection

IVC: inlet valve closing

K-H: Kelvin-Helmholtz

LES: Laser elastic scattering

LIF: Laser induced fluorescence

MBT: maximum brake torque

MFB: mass fraction burned

MPRR: maximum pressure rise rate

NMEP: net mean effective pressure

NOx: Oxides of Nitrogen

PDF: probability density function

PFI: port fuel injection

PIV: particle image velocimetry

PL: penetration length

PN: Particulate number

PW: pulse width

Q_{stat}: static mass flow rate

ROI: region of interest

SA: spray angle

S_D: standard deviation

SI: spark ignition

SNR: signal-to-noise ratio

SMD or D32: Sauter mean diameter

TDC: top dead centre

THC: the (unburnt) Hydrocarbons

TKE: turbulent kinetic energy

Table of Content

List of Figures

List of Tables

Chapter 1.   Introduction and Overview

The Gasoline direct-injection (GDI) engines have become the dominant powertrain for passenger cars, because of their high power density and improved fuel economy. In particular, the high injection pressure and the flexibility of the DI injectors' control play major roles in improving the engine's performance and efficiency. This has been realised through significant developments in the efforts to improve the efficiencies of the GDI engine's range of operating conditions over the last few decades.

One of these areas of development has been the injection systems, with the fuel spray's characteristics being a key focus of improvement. The earlier generation of injection systems had typically consisted of swirl-type atomisers. In this case, the fuel was guided to the spark plug by the wall or piston. Its spray structure was highly sensitive to the variations in the in-cylinder pressure, which would inevitably lead to the complete collapse of the main spray structure during the compression stroke. The result was the formation of high wall wetting and pool fires, subsequently resulting in deteriorated fuel economy and high levels of the (unburnt) Hydrocarbons (THC) and particulate matter (PM), owing to diffusion combustion [1], [2].

The more recently developed injectors are the multi-hole injectors. The number of holes, their patterns and orientations, and the internal flow cavity were designed to control the individual spray plumes and the overall spray pattern. As such, the droplets' dispersion in the cylinder was significantly improved and fuel impingement on the cylinder walls reduced [3]. The small drill angles of the holes also increased the likelihood of the interactions of the neighbouring plumes, which would enhance the spray break-up and improve the atomisation rate [4].

The key features of multi-hole injectors are thus [5], [6], [7], [8], [9], [10]:

- Lower sensitivity of the spray's structure to the variations in the fuel temperature and in-cylinder pressure, temperature, and flow-field.

- Production of repeatable and stable spray structures with well-atomised droplets.

- High exit velocities of the injected droplets.

These features have enhanced the fuel-air mixture formation for varied operating conditions and have proven to improve the fuel consumption and reduce the levels of emissions in general [11], [12].

One of the operating conditions where optimum fuel distribution is key, is the stratified charge operation related to part-load and cold-start conditions. The benefits of the GDI spark-ignition engines operating under stratified charge condition, when compared to the conventional spark ignition (SI) engines, are the capability of operating at high compression ratios due to the extra charge cooling effects stemming from injecting the fuel directly into the cylinder; the ability of operating with lean mixtures; the control over the injection and ignition processes; and multiple fuel injections capabilities [13]. These features have proven to contribute towards improved engine efficiency and reduced emissions in GDI spark-ignition engines. The higher specific heat ratio, reduced pumping losses due to the capability of operating with high manifold pressure, and improved thermal efficiency as a result of reduced wall wetting, also play key roles in improving the cycle efficiencies, when compared to wall-guided or air-guided GDI engines [14], [15].

At wide open throttle (WOT), the engine can be operated at super-lean stratified combustion at light-load, thereby reducing the pumping losses and improving the fuel economy even further [16]. The dilution with the exhaust gas recirculation (EGR) in conjunction, can help retain the stoichiometric fuelling while the charge gets diluted [15] which further improves the thermal efficiency and emissions due to its compatibility with the three-way catalyst. A recent study on fuel economy has revealed that the vehicle fuel economy has been increasing since 2005, as also represented in Figure 1.1 [17].
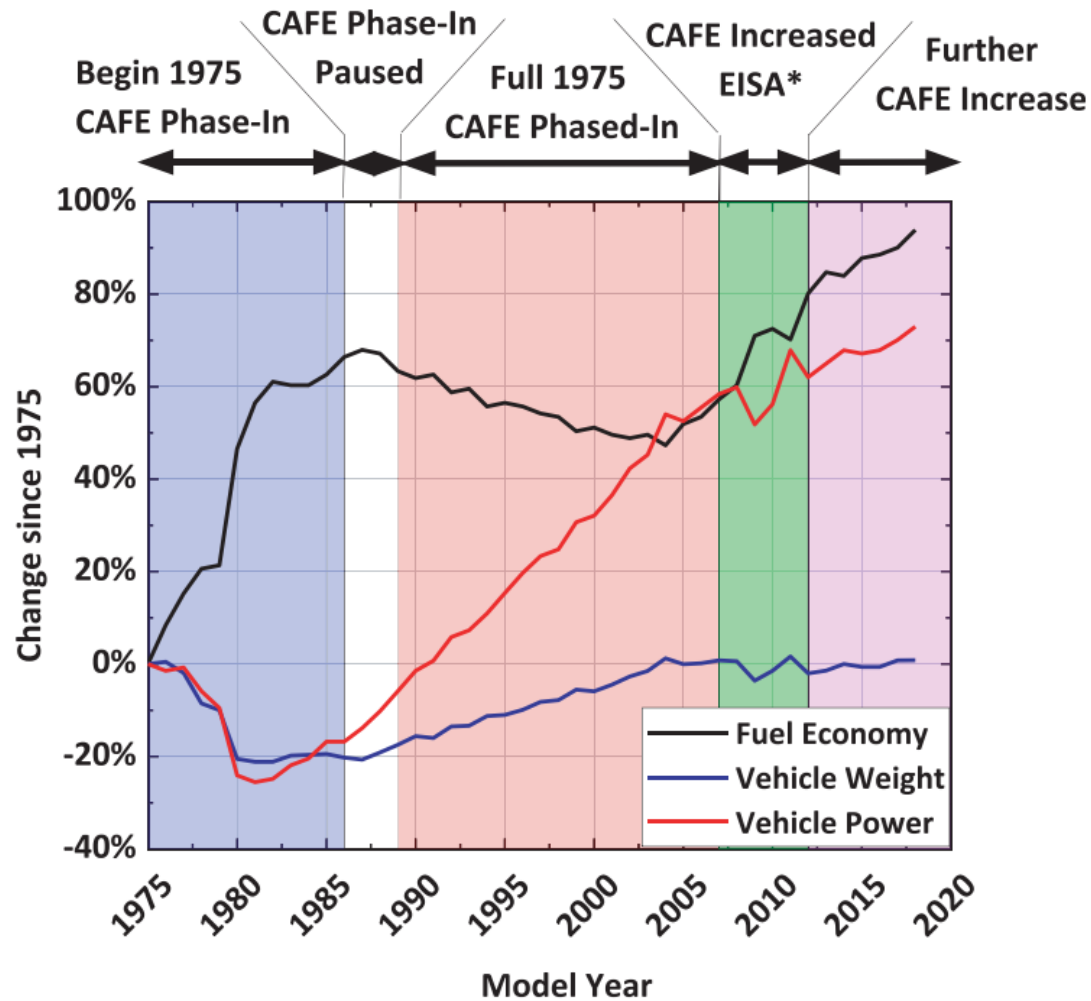
Figure 1.1: the development of the fuel economy, vehicle weight and vehicle power from 1975 to 2018 [17]. The data is from the U.S Environmental Protection Agency's Automotive trends report.

There are various features of the GDI engine which make them more attractive and practical, when compared to the port-fuel injection (PFI) engines. While the former employs direct fuel injection inside the cylinder, PFI injection systems deliver fuel in a port upstream of the intake valves, which often results in valve impingement (especially when the surfaces are cold). This difference in the fuel delivery has resulted in a variation of fuel evaporation rates. The GDI engines thus benefit from higher volumetric efficiency at wide-open throttle (WOT) conditions (and lower knocking tendencies), resulting in higher full-load torque output, when compared to PFI engines [18].

The advantages of the knock mitigation using the DI over PFI system is due to the heat of vapourisation of the fuel achieved from the charge air itself rather than metal surfaces. Additionally, combining DI fuelling with variable valve phasing, over-scavenging, or fresh air induced directly through the cylinder during gas exchange can be used to remove burnt gases without introducing unburnt air-fuel mixture into the exhaust gas stream due to the flexibility with the injection timing. These technologies help reduce the in-cylinder temperature with the DI system, thereby mitigating knock and allowing operation with high compression ratios [17].

During stratified charge operation, higher peak pressures are associated with the GDI engine when compared to PFI engines, for the same brake mean effective pressures (BMEP) [14]. The capability with the multiple fuel injections within one cycle and retarding the ignition timing during catalyst heating, to achieve rapid catalyst light-off, provides a drive cycle emissions benefit over PFI engines [19].

Despite the range of benefits obtained from GDI engines, an on-going challenge is to help tackle the deficiencies originating from stratified charge operation at cold-start or part-load operations. It is particularly difficult to obtain the optimum fuel economy when the in-cylinder charge properties such as pressure, temperature, charge velocity and atomisation rates vary so significantly. On-going studies focusing on optimising the GDI engines and reducing emissions are therefore essential to help tackle the resultant high levels of emissions.

In order to achieve a proper air-fuel mixture in the vicinity of the spark plug, the injection and ignition timings have to be precisely controlled [15], [20]. With a single injection, the fuel is typically injected late in the compression stroke to ensure that a fuel-rich charge is in the vicinity of the spark plug for late ignition in the stratified charge operation. The injector is either close to the spark plug when it is mounted centrally or further apart when it is side-mounted. As a result of the late injection, the fuel does not get enough to time to mix with the surrounding charge (which is limited anyway as a result of the throttle being only partly open) and gets inadequate evaporation time. Significant piston surface wetting and liner wetting occurs as a result of the late fuel injection impinging on these surfaces [20], [21].

Due to the low surface temperature distribution during cold-start, the fuel vapour condenses when in contact with the surfaces of the piston and combustion chamber.

The smoke levels and unburnt Hydrocarbons (THC) rise significantly, owing to diffusion combustion of the pool flame on the chamber's surfaces [19]. It has been stated in [22] that more than 60% of the THC emissions, during the Federal Test Procedure (FTP) measurements, had been produced during the first two minutes of the test. The temperature of the catalyst was too low during start-up, making it incapable of efficiently oxidising the THC levels in the exhaust system. During this period, the temperatures of the walls, intake valve surfaces and the combustion chamber surfaces were also too low to vapourise the fuel, causing the formation of pool fires.

The greater time taken for warm-up increases the frictional effects and degrades the fuel economy by about 2.5% when compared to the PFI engines [14]. The cycle-to-cycle variations in the indicated mean effective pressure (IMEP) also increase with this injection strategy, which further degrades the engine's efficiency [23].

One of the primary purposes for the stratified charge operation is to help raise the exhaust gas temperature within a short period of time for rapid activation of the exhaust catalyst during cold starts, by allowing the delayed combustion in the expansion stroke.

1.1 Thesis Structure

A detailed review of previous investigations of the stratified-charge operations in GDI engines, with the corresponding studies focused on the spray characteristics and high injection pressures, is presented in Chapter 2.

Descriptions of the range of experimental methodologies are provided in the following chapter (Chapter 3). This consists of methodologies, specifications, and descriptions of:

- injection mass measurements

- high-speed imaging

- PDA measurements along with an overview of the design of the constant volume spray chamber used for the spray characterisations

- overview of the GDI optical engine

- high-speed PIV measurements in tumble and omega tumble planes.

The subsequent chapter consists of the results' discussions of the spray characterisations (Chapter 4). This includes studies of:

- the mass measurements of the single and split injections

- spray characteristics (penetration lengths and spray angles) of varying single and split injections strategies

- droplet size distribution and velocities measured for varying split injection cases.

Discussions of results of the in-cylinder flow measurements performed inside the optical engine using high-speed PIV measurements are presented in Chapter 5. The investigations were performed on the following test cases:

- effects of the single injection timings on the in-cylinder charge formation and properties.

- effects of varying split ratios using the split injection strategy, with both injections in the intake stroke, on the mixture formation throughout the cycle.

- effects of varying second injection timings using a large split ratio on the mixture formation throughout the cycle

Conclusion and recommendations for future works are presented in Chapter 6.

Chapter 2.   Stratified Charge Operation in GDI Engines

2.1 Key Challenges with Stratified Charge Operation

A common strategy used to help raise the exhaust gas temperature in GDI spark-ignition engines, for rapid activation of the exhaust catalyst, is a combination of late injection in the compression stroke and late ignition in the expansion stroke. Although this target is achieved, the consequences are typically incomplete and unstable combustion [24]. The complex in-cylinder conditions place constraints with the injection and ignition timings as the air and fuel move and dilute at a high rate upon fuel injection, and the flame propagation of the fuel-lean mixture at the edges of the main fuel zone is slow [25].

Combustion instability is dominated by factors that prevent the flame kernel from propagating into the main stratified fuel cloud while providing sufficient time for the fuel cloud to become lean from transport and mixing. Factors for combustion instabilities identified in [26] are:

1) convective flow fluctuations that prevent the flame kernel from being transported towards the bulk of the fuel.

2) low flame speeds due to locally lean mixtures adjacent to the kernel.

3) retarded development of the ignition kernel, which allows further lean mixing to take place.

Studies of the in-cylinder flows and sprays' structures resulting from start of injection (SOI) timings of 40°CA before top dead centre (bTDC) and 43°CA bTDC, for engine speeds of 800rpm and 1500rpm engine speeds, respectively were carried out by [27]. The authors reported that the characteristics of the in-cylinder flow had dominated the cycle-to-cycle fluctuations in the spatial distribution of the liquid spray. The results from particle image velocimetry (PIV) measurements revealed that during the late injections, the flow-field in the vicinity of the developing spray structure was heavily influenced by the air entrainment along with an upward flow in between spray plumes caused by the high velocity magnitude of the flow-field, particularly for lower engine speed. A source of the cycle-to-cycle fluctuations in the

IMEP was reported to be the difference in the location of the 50% mass fraction burned, which occurred particularly when the ignition timing was retarded [28].

The major contributors of incomplete combustion and misfiring cycles when using multi-hole injectors are reported to be the low flame speeds in the lean region and the convective 'mismatch' between the flame kernel and the location of the stratified fuel cloud [26]. Investigations of the stable combustion and misfired cycles in [29] revealed that for all the misfires, the spark and flame from early rich combustion had moved upwards, past the spark plug as indicated in Figure 2.1 and Figure 2.2, instead of the flame traveling downwards towards the bulk of the fuel contained in the piston bowl.
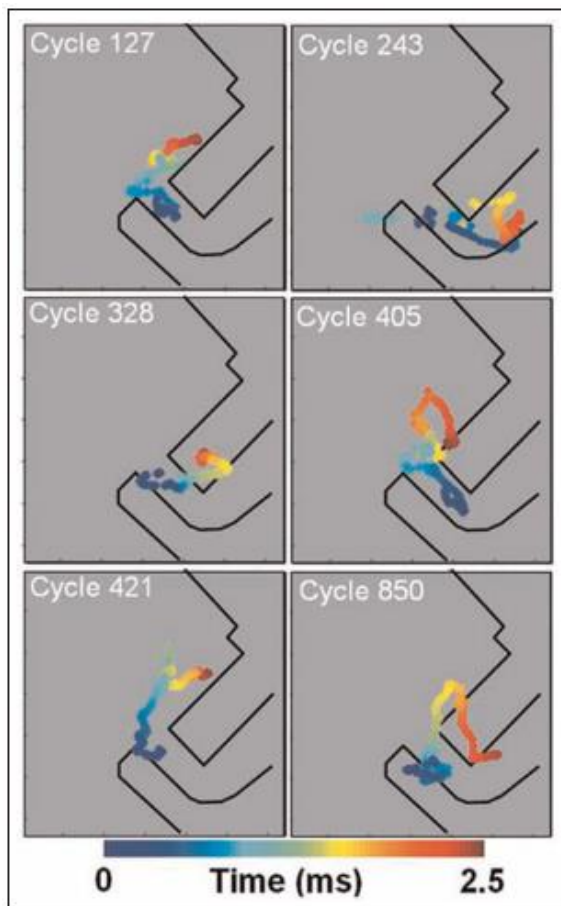
Figure 2.1: the direction of travel of the spark centroid and early rich combustion luminosity for misfired cycles. Extracted from [29].
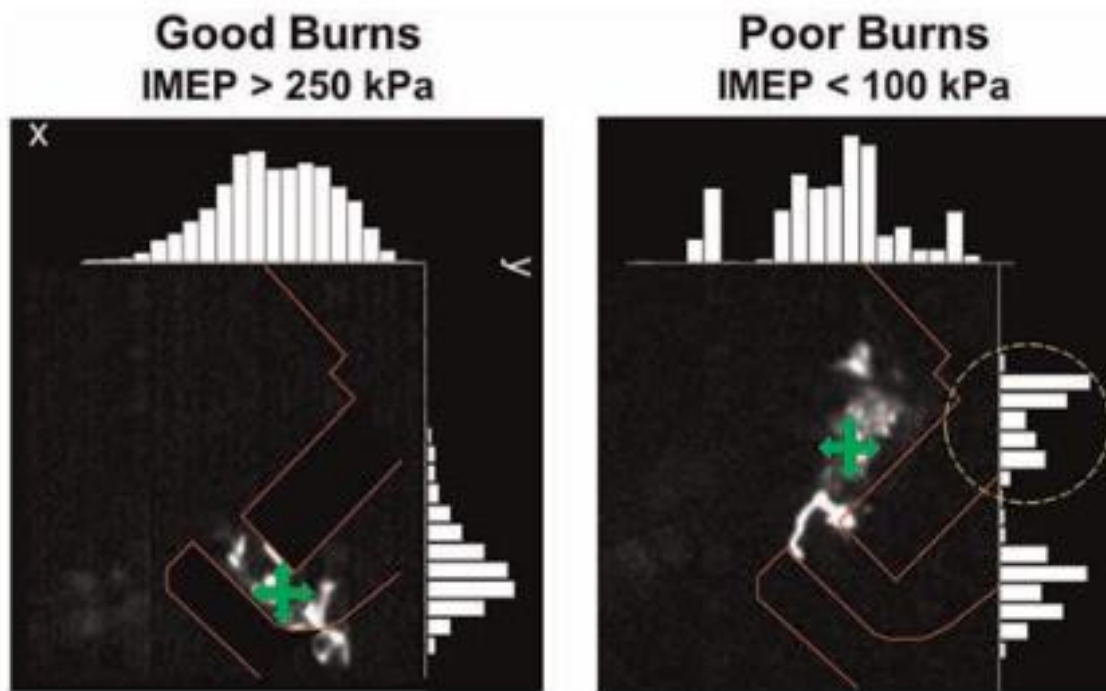
Figure 2.2: Histograms of the rich combustion image centroid from 20 °CA to 30°CA after spark initiation. Small green crosses indicate the spark centroid, dashed circle exhibits the poor-burn cycle's spark and early rich combustion zones that failed to move downwards towards the piston bowl [29].

Along with the constraints on the ignition timing, injection timings are just as crucial in achieving combustion stability for the stratified operation. With the injection too early in the intake stroke, to take advantage of the high charge motion after intake valve opening (IVO), the spray would impinge immediately onto the piston's surface. This would result in diffusion combustion of the fuel pool accumulated on the piston's surface and would subsequently form high particulate number (PN) emissions. With the fuel injected too late near top-dead centre (TDC), the fuel would settle directly on the liner and piston's surface due to the decayed air motion, which would form large PN emissions as well oil dilution. The time available for the injection, evaporation and mixing of the fuel is thus limited. The induced charge also lowers the thermal conditions, which is detrimental for the fuel evaporation rate especially during cold starts. When the fuel vapour contacts the cold engine surfaces, there is a high likelihood of the fuel condensing and settling on the liner and piston, thereby resulting in pool fires [19].

It has been further reported in [30] that the sources of the particulate emissions are twofold: (1) diffusive burning of liquid fuel in the form of pool fires of fuel films, large

fuel droplets and ligaments; and (2) gas-phase combustion of locally fuel-rich zones. The wall temperature directly influenced the wall wetting and fuel evaporation, and therefore diffusion flame combustion as exhibited in the LIF images in Figure 2.3. Reduction in the coolant temperature caused the liquid fuel film to settle and persist on the intake valve seats due to the interaction between the valves' surfaces and the injected fuel during the injection period. This was tested at an engine speed of 1200rpm and 0.45MPa IMEP, representative of cold-start conditions, along with an injection pressure of 20MPa using a Bosch injector with six holes (orifice size of 114µm) in an optical engine with a compression ratio (CR) of 10.5 and 0.4L engine displacement.

The liquid fuel film had also formed on the piston's surface as well as the injector's tip, leading to injector coking. In this case, injection phasing could control the alleviation of the fuel impingent on the chamber walls and piston's surface, while in-cylinder aerodynamics enhanced the fuel evaporation and the homogeneity of the in-cylinder mixing. A highly aerodynamic flow inhibited the formation of PN emissions globally. They also observed the PN to be highly sensitive to the engine's coolant temperature.
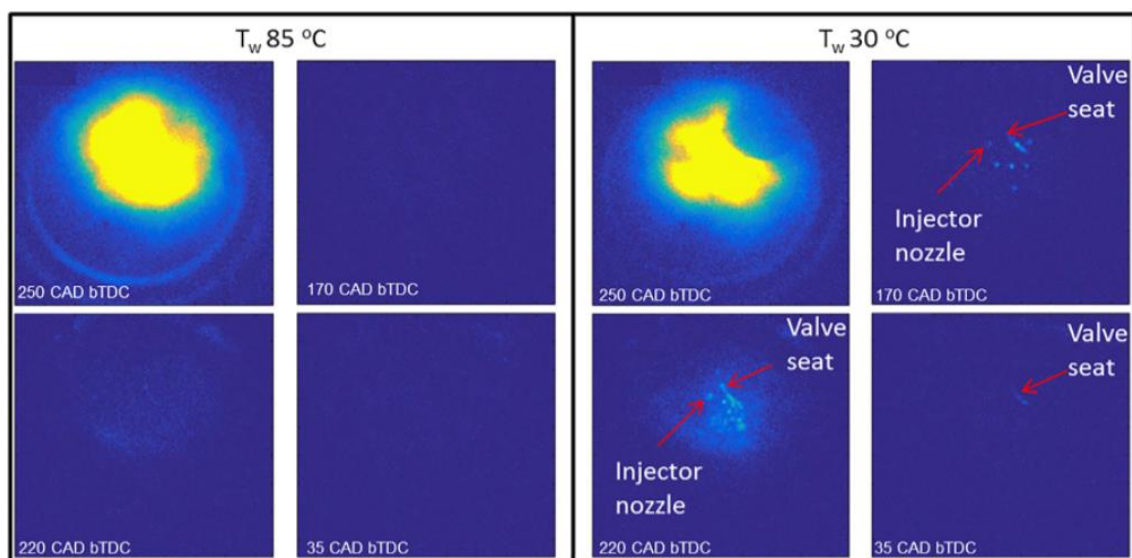
Figure 2.3: detection of the liquid film via LIF measurements for coolant temperature of 85°C (left) and 30°C (right) for SOI of 260°CA bTDC. Image extracted from [30].

Extensive studies have also focused on the effects of the injector tip wetting phenomena on the PN formations in GDI engines. Tip wetting results in progressive soot formation on the injector tip, which consequently forms high PN emissions

especially under hot engine conditions. With the fuel film accumulated on the injector tip, the late evaporating fuel forms a porous carbon deposit in this region, which is capable of absorbing liquid fuel easily [31].

Mouvanal et al., [32] further reported needle tip wetting during the injector purging process by the end of injection. In this case, the liquid was observed to leak out of the sac and nozzle after the end of injection, when employing injection pressure of 15MPa.

Medina et al., [33] have categorised the process of injector tip wetting into three key stages. The first stage is fuel deposition on the injector nozzle during injection. The second stage is fuel deposition on the nozzle tip at the end of injection caused by large droplets, ligaments and low momentum flow as the needle shuts. The third stage is fuel being deposited on the nozzle tip from the liquid and vapour inside the sac volume of the injector.

They also identified two key processes that contributed to injector tip wetting during injection. Firstly, as the fuel flows through the nozzle hole and into the pre-hole (Figure 2.4b.), the path of the fuel flow widens. The fuel flow then interacts with the pre-holes, whereby some fuel gets deposited on the surface of the wall before flowing around the corner and onto the orifice of the outlet. This was stated to be dependent on the geometry, flow dynamics, and operating conditions. Secondly, during injection, vortices formed from recirculation process between air and fuel entrain fuel and vapour within. The vortices re-entrain some of the fuel and air mixture back into the bulk flow, but some of the mixture tends to escape from the bulk flow. Fluid that escapes the vortices in the form of fuel droplets can be deposited on the injector tip due to the low-pressure zones formed near the nozzle exit. Droplets can deposit and stay on the injector tip due to the Coanda effect.
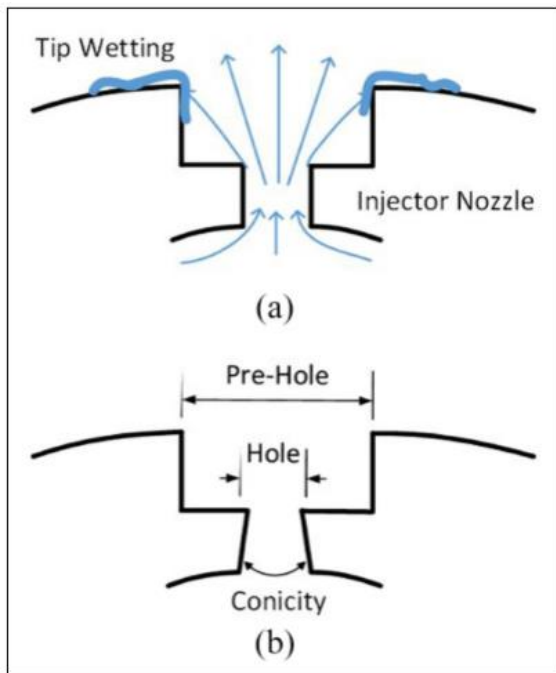
Figure 2.4: schematics showing a) the general flow of fuel which leads to injector top wetting in GDI engines and b) basic internal structure of a GSI injector's nozzle [33].

PN emissions from tip wetting were reported to be higher with the converging nozzle for both side and centrally mounted injector configurations, when compared to diverging nozzles. In addition, longer timescale and higher coolant temperature were found to decrease PN emissions, as these features allowed tip drying prior to ignition [33].

One study [34] had investigated the wave dynamics on a heated plate at varying temperatures to further understand the wall film formation phenomenon. For low plate temperature, the wave propagated slower due to the large fluid viscosity and surface tension. The wave had to overcome greater resistance forces which resulted in reduced propagation velocity. When applied to lower temperature of the chamber walls, this indicates that the residence time of the fuel impinged on the chamber's liner would be large, thereby resulting in the diffusion combustion. Higher plate temperature on the other hand, had higher fuel mass transport efficiency and so the impinged fuel film had lesser tendency of the fuel mass aggregating on the surface of the plate.

The impingement of the injected fuel on the valves' surfaces as a result of early injection was investigated in [35]. The engine test conditions were 1500rpm, 80°CA

after top-dead centre (aTDC) start of injection (SOI) with a pulse width (PW) of 0.78ms, injection pressure of 15MPa and fuel temperature of 363K. They found that by 13°CA after start of injection (ASOI), the edges of the descending intake valves caused the plumes to split. The droplets thus deflected on to the top surface of the valve head. The velocity of the droplets reduced rapidly, resulting in a liquid film settling on the top surface of the valve head. The thickness of the liquid film was found to be in the range of 100μm – 500μm, which could prove to be a source of THC and PM.

One way proposed to control the PM emissions is to thus improve fuel-air mixture preparation, as has been reported by Szybist et al., [36]. PFI engines have been reported to have lower PM emissions when compared to GDI engines. This is because of the sufficient time available for the fuel evaporation and therefore improved mixture formation. In addition, as discussed earlier, the spray in GDI engines can contact the combustion chamber surfaces, inhibiting fuel evaporation. PFI engines typically have reduced interactions with the combustion chamber surfaces. Continued development of GDI combustion systems is thus focused on reducing PM emissions, and it is stated that the improvements will most likely allow most vehicle manufacturers to meet the U.S Environmental Protection Agency's PM regulation of 3 mg/mile without a Gasoline particulate filter.

LIF measurements performed in [34] also revealed that the fuel films had formed on the intake valve seats and under the exhaust valves. In this study, the injection duration was at IVO, using a PFI system at significantly large PWs of up to 22.2ms and engine speed of 300rpm. For closed valve injection, fuel films had also formed below the intake valves and the squish region which was between the intake valves and the cylinder wall. They concluded that fuel films on the cylinder head near the intake valves were a possible source of THC, that the pool fires were the main sources of soot emissions in properly maintained GDI engines, and that the soot-laden fuel films that had accumulated on the cylinder walls were the main source of soot contamination of the oil in the crankcase.

The formation of soot was also predominant on the piston crown and the injector where some of the charge was deposited during stratified charge operation and late

injection [21], [37]. Fuel has been observed to undergo slow oxidation within crevices, which can be another major source of THCs [38].

Soot produced by pool fires was measured using Laser induced fluorescence (LIF) and Laser elastic scattering (LES) of soot in [39]. The flames from the pool fires had burned bright yellow which was characteristic of soot incandescence. For injections late in the compression stroke (SOI -90°CA), the flames had attached to the fuel film on the piston top upon ignition (Figure 2.5), and followed the piston throughout the expansion and exhaust strokes, when tested at an injection pressure of 5MPa, PW of 1.57ms and an engine speed of 1300rpm. They found the pool fires on the piston top to be a likely source of engine out particulate emissions in GDI engines. This was because the pool fires had in fact persisted throughout the exhaust stroke and even after the flame extinction. Note that for injections in the intake stroke, no pool fires were reported and observed, indicating that the fuel had sufficient time to vapourise and mix with the surrounding charge.
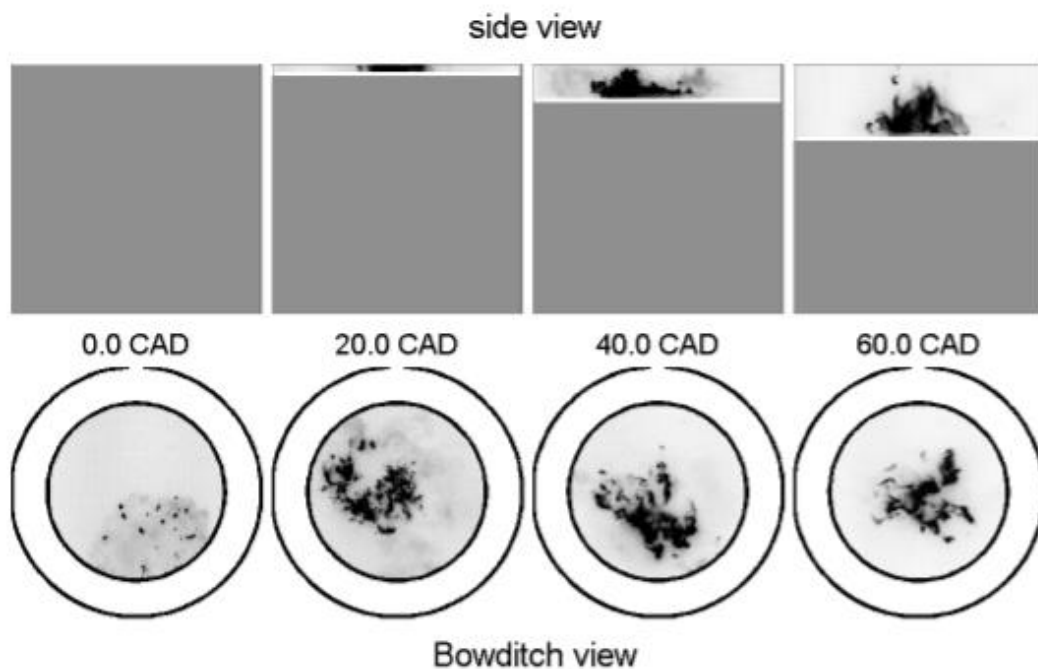
Figure 2.5: Side and Bowditch views of visible pool fire luminosity for late injection at SOI of -90°CA [39].

The effects of late ignition were investigated in [40] using a centrally mounted injector at an engine speed of 2500rpm, CR of 12.2, 0.6MPa net mean effective pressure (NMEP), stoichiometric air/fuel conditions, maximum brake torque (MBT)

spark timing and injection pressure of up to 20MPa. They observed diffusive combustion radiation, with an intense flame, in the vicinity of the coked injector for late ignition at around 30°CA aTDC, as shown in Figure 2.6. This indicated an over-rich fuel-air mixture.

They also found a direct correlation of soot, PN values and injector diffusion flame value, as shown in Figure 2.7. The trend exhibits increasing diffusion flame value and PN emissions for increasing levels of soot. The injector diffusion flame value was reportedly highly sensitive to cycle-to-cycle conditions.
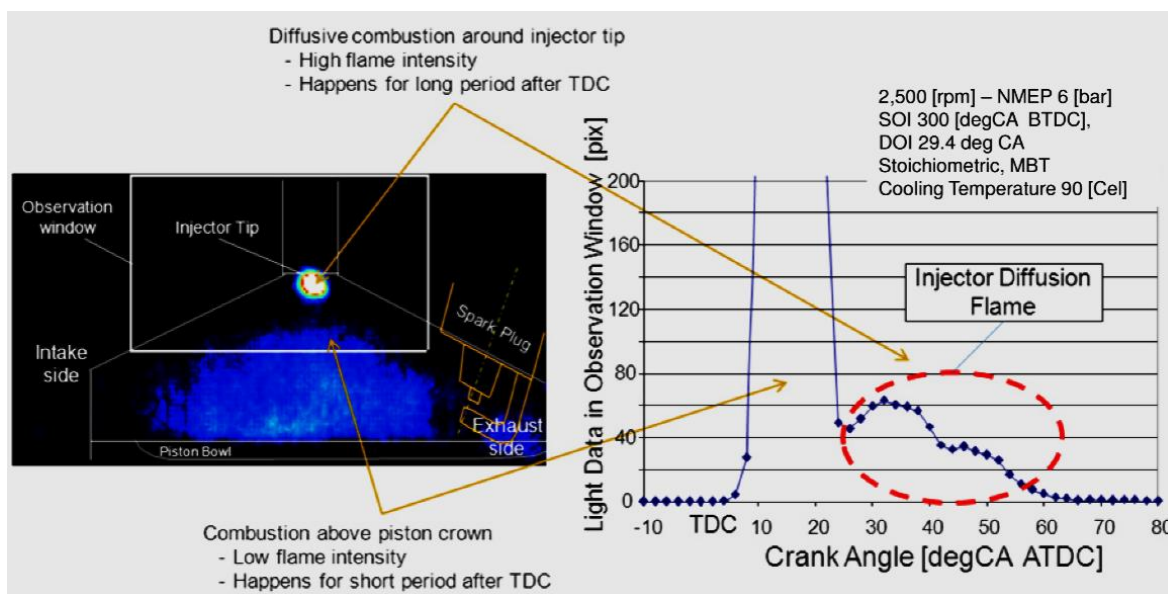
Figure 2.6: Observation of flame radiation as reported in [40] for SOI 300°CA bTDC and DOI of 29.4°CA aTDC.

Many different tests with different injector hardware
2,500 [rpm] – NMEP 6 [bar]
Stoichiometric, MBT
Cooling Temperature 90 [Cel]
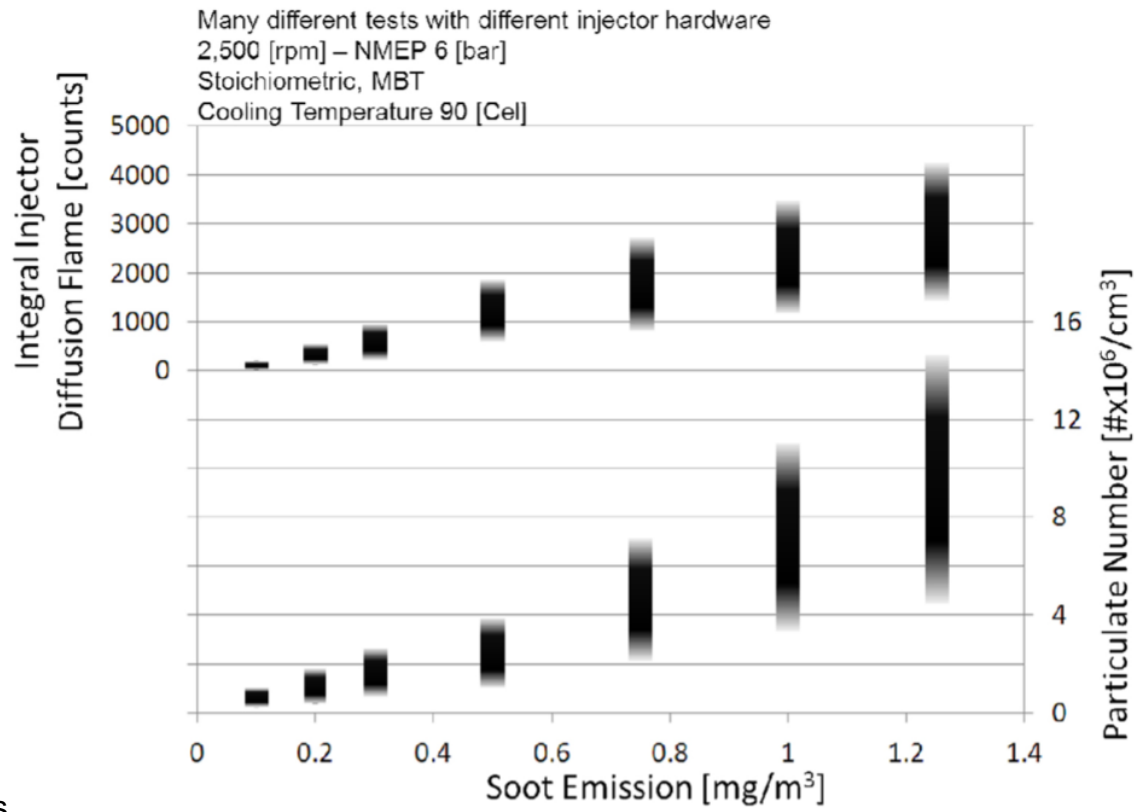
s

Figure 2.7: correlation trends between soot levels, PN levels and injector diffusion flame value, as extracted from [40].

2.2 Multiple injections for Charge Stratification

It is clear that one way to reduce the levels of particulates formed under stratified charge operation is to reduce fuel impingement on the chamber's surfaces which would lead to diffusion flame combustion. This is especially crucial when the surfaces are relatively cold for reasons discussed in the earlier sub-section. As such, accelerated warm-up of the piston, controlling the spray's trajectory, generating high rate of atomisation, reducing the penetration lengths and optimising the spray cone angle all play a crucial role in alleviating the surface impingement [41], [42].

These requirements can be achieved by employing carefully designed multiple fuel injections within one cycle (referred to as a split injection strategy in this thesis), which can generate fuel and air mixture that is well-adjusted both spatially and temporally. The split injection strategy can help improve the turbulence levels of the flow in the cylinder [43] and avoid high concentration of liquid spray piling up on the sprays' tips [44]. The strategy can also be used to retard the 50% mass fraction burned (MFB), thereby reducing the peak in-cylinder gas pressure, temperature and Oxides of Nitrogen (NOx) emissions [15].

Turbulent in-cylinder flows are essential for accelerated mixing of the in-cylinder charge while the mean velocity of the flow-field enhances the convective transport of the mixture cloud to the spark plug in order to achieve stable charge stratification. It has thus been proposed from very early on [45] that a well atomised and compact spray structure can help achieve a fast mixture preparation and charge stratification using late injections.

The split injection strategy has also been reported to reduce the overall penetration length of the injected fuel, which alleviates the cylinder liner, piston surface and intake valve wetting and helps stabilise the combustion initiation process [40]. This is particularly crucial for cold-start conditions. For warm engine condition, wall wetting is less critical as less fuel is injected to produce the same magnitude of engine torque. The fuel warm up and evaporation rates are also accelerated with the help of high thermal conditions of the injector and combustion chamber walls. Under these conditions, split injection strategy would increase the PN emissions.

It is proposed in [19] that to achieve accelerated catalyst heating, majority of the fuel injected early during the intake stroke can provide sufficient time for the fuel and air

to mix effectively and generate a homogeneous mixture. A small quantity of fuel subsequently injected during the compression stroke can help form a rich mixture near the spark plug. This would support the exothermic reaction taking place in the catalyst as well as produce stable combustion at a considerably retarded ignition time than would be possible using a homogeneous mixture. This is also supported by [38] who found that the second injection just after the inlet valve closure (IVC) and advanced spark timing can help achieve improved engine power output and reduced pollutant emissions. The advanced spark timing is especially important in stratified charge operation to enable faster flame growth and propagation, which is important in achieving a complete combustion [46], [47].

Some studies [19], [48] investigated the effects of the triple injections on the combustion performance. They found that the second and third injection pulses can be used to control the combustion stability and maximum pressure rise rate (MPRR). A combination of triple injection strategy and EGR dilution helped reduce the PM (Figure 2.8) and NOx emissions, while achieving an improvement in indicated specific fuel consumption (ISFC). With these many injections however, there are significant constraints with soot emissions. The operating ranges become more defined by the levels of soot production rather than combustion stability, especially with retarded injection timings. This has been stated to a be the major difference between triple injections and double-pulse injection strategies.
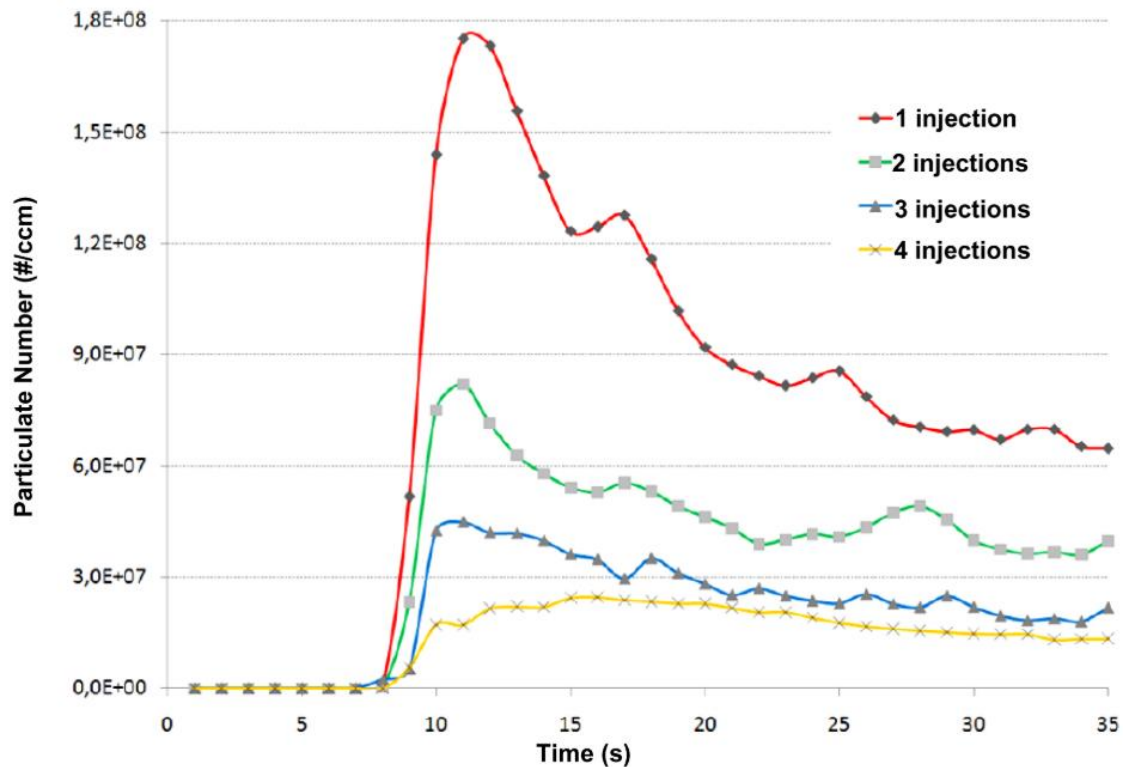
Figure 2.8: effect of the number of injection pulses per cycle on PN levels for engine cold start conditions of 22°C and extended idle [19].

The typical spark timing for this operating condition should also be controlled precisely to compliment the injection timing. It is stated that the typical injection timing should enable the placement of the middle or tail end of the spray at, or just past, the spark gap during ignition [26]. This would ensure that a fuel rich charge is in the vicinity of the spark plug. The burned gas probability density function (PDF) presented in [49] showed that a stable combustion was achieved when the flame kernel 'chased' the tail of the fuel plume.

It is also important to correlate the flame propagation with the burning cycles. [50], [51] observed that the flame development for the good burning cycle was such that the flame propagated in the clockwise direction in the tumble plane and then downwards into the piston bowl before moving upwards to the left of the spark plug. The flame development of the poor burning cycle was directed upwards towards the cylinder head and moved slowly. In essence, combustion misfires can be prevented by ensuring that the spark plug is close to the ignitable mixture and minimising the cycle-to-cycle variations of the spray structure, which can all be controlled with the split injection phasing [52].

Zhao et al., [53] have also investigated the effects of split injections on Gasoline auto-ignition processes inside a constant volume chamber using injection pressure of 15MPa and fuel temperature of 363K. They reported that the combustion using split injections was a multi stage process, whereby the ignition of each injection event was controlled by different mechanisms. For instance, auto-ignition was achieved with the first injection which accelerated ignition for the second injection as a result of to the intermediate species and increased temperature effect from the first injection.

2.3 Effects of the Split injection Strategy on GDI Engine's Performance

A range of studies have performed detailed investigations of the split injection strategies on the in-cylinder conditions, combustion performance and corresponding emissions levels. Some of their outcomes are discussed in this section.

Investigations of the effect of the split injection strategy on the piston surface impingements, with pressures ranging between 3MPa and 10MPa using a multi-hole injector and E85, at engine speeds of 1500rpm and 2000rpm, with varying engine loads (WOT and 0.3MAP) were performed in [3]. The authors observed that the split injection strategy had resulted in a reduction in the overall fuel-impingement by 50% when compared to single injections using just 5MPa pressure at 1500rpm and WOT. This can be directly correlated to the reduction in the pool fires. The overall impingement on the piston's surface had reduced by 22%. The flammability limit had extended with the help of the excess air ratio (lean mixture) and stable combustion with reduced cycle-to-cycle variability in the IMEP was observed when employing the split injection strategy, as also reported in [26], [54], [55], [56].

[57] further found that the split injection strategy helped achieve better control of the main ignition delay and the combustion duration when compared to the single injections per cycle. The tests were performed using Gasoline RON91 at 1375rpm and 1MPa BMEP (representative of cruise speeds) with an injection pressure of 145MPa and split ratio of 10:90. The MPRR had reduced from 1.46MPa/crank angle degrees (CAD) to 0.6MPa/CAD without producing high levels of emissions. The fuel efficiency was also improved as a result of less induced heat transfer losses.

Another study [58] tested the effects of the split injections on the flow-field using a solenoid-actuated injector with six holes at an injection pressure of 10MPa and a split ratio of 1:1 with 2000rpm engine speed at WOT, which was attributed to mid-load conditions. They also found a reduction in the cyclic variability in IMEP, particularly during lean-burn operation. A slightly lower in-cylinder pressure in the compression stroke was measured, which was reported to be due to a timing shift in the fuel evaporation as a result of splitting the injection into two separate events. The flame area was subsequently observed to be larger which they had linked to an increase in the flame speed. The injection strategy induced lower exhaust gas

concentration of NOx, which enhanced the control of the exhaust gas after-treatment. This would in turn work effectively to reduce the CO and THC levels.

The flame growth from the split injections has also been observed to be more spherical and local to the spark plug during ignition, while the flame from the single injection had propagated and developed more towards the exhaust valves [59]. The latter would result in reduced consumption of radicals in the regions inside the cylinder not covered by the flame. The test conditions in this case were 1500rpm engine speed and 15MPa injection pressure at both part load and WOT.

One study [60] applied 4:1 split ratio and tested varying injection timings on the in-cylinder conditions, at 12.5MPa injection pressure, 1600rpm engine speed, 1.1MPa IMEP and WOT. They observed that the second injection supplied additional turbulence levels to the flow-field. A comparison of the flame front between split injections and single injections revealed that the former yielded greater flow velocity at the tip of the flame and that the rate of propagation of the flame was more sensitive to the velocity of the flow field. The high velocity flame propagation is important because it distributes the end gas temperature across the cylinder, thereby favouring rapid warm up of the engine surfaces.

It was found in [61] that with the split injection strategy, the fuel cloud could be better controlled and maintained within the piston bowl throughout the intake and compression strokes, when compared to single injections. With the fuel cloud transported to the spark plug and the flame kernel in time for ignition in a more controlled manner, the overall burning rate and combustion stability had improved.

The effects of the split injection strategy on the turbulence intensity at the spark plug and the overall heat release rate (HRR) were investigated in [62]. They also found that the flame developed rapidly when the split injection strategy was employed, thereby yielding a twofold increase in the HRR as shown in Figure 2.9 along with high turbulent fluctuations spread over the duration of the cycle compared to the single injections. The fuel consumption and combustion stability had also improved, and the THC and soot levels reduced. The influence of increased turbulence intensity on the flame propagation speed, which increases, was also observed in [63].
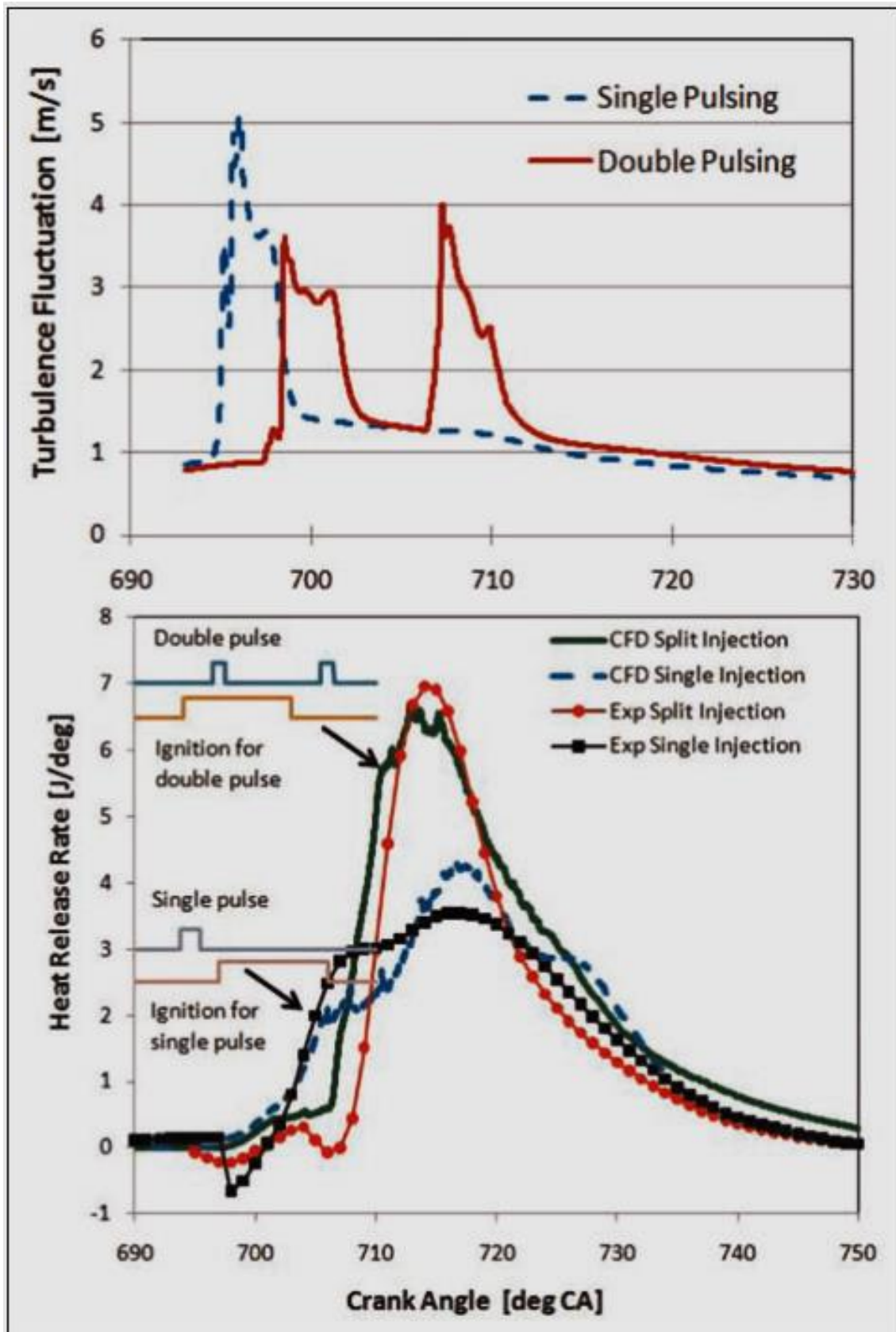
Figure 2.9: Turbulence intensity at the spark gap region (top) and measured and simulated heat release rate trends for single and double injections (bottom) [62].

A more recent study [64] tested a range of split ratios at 2000rpm and fuel injection pressure of 20MPa. They found that all the split cases tested had resulted in soot emissions lowered by almost 95% to 99% when compared to single injection cases as a result of reduced wall-wetting, pool fires and wall film combustion.

Another study [65] investigated the effect of injection-injection-spark ignition (IIS) and injection-spark ignition-injection (ISI) cycles on the engine's performance, using a Piezo-actuated outward-opening injector at 20MPa injection pressure and 1200rpm engine speed. The IIS strategy led to reduced soot levels, when compared to the ISI strategy. This was due to the homogeneous air-fuel mixture formed with the former strategy where fuel-rich pockets forming inside the cylinder were inhibited considerably. The latter strategy led to diffusion combustion, thereby generating high levels of soot.

Another study [38] tested 1:1 split ratio on the emissions, with injection in the intake stroke and compression stroke using a solenoid-actuated injector and injection pressure of 10MPa. They found that the strategy helped reduce both NOx and THC emission levels. The resultant faster HRR also enabled spark advance and late injection just prior to ignition.

Computational fluid dynamics (CFD) simulations performed in [66] revealed that the split injection strategy reduced PN levels by 60% when compared to the baseline single injection strategy at a fuel injection pressure of 15MPa, 4:6 split ratio by mass, 1000rpm and 1.1MPa BMEP. Additionally, the results indicated that the piston film mass reduced by 90% and the liner film mass had reduced by two orders of magnitude when compared to the single injections.

Even earlier studies [15], [23] found that the 1:1 injection ratio, with the first injection during the negative valve overlap and the second injection at the start of the compression stroke resulted in reduced maximum in-cylinder pressure, reduced MPRR, lowest overall emissions and significant improvements in the cyclic variability. The test conditions in this case were 1500rpm, 9.6MPa injection pressure and a solenoid-actuated swirl-type injector. Specifically, they observed 60% reduction in NOx levels and 2% improvement in indicated specific fuel consumption (ISFC) when compared to early single injections.

These previous studies provide an indication of the impact of the split injections on the overall engine's performance. They have revealed that the split ratios and injection timings play a key role in optimising the engine's performance. More specifically, they have been proven to heavily influence the resulting charge formation inside the cylinder. As such, these two features are explored in the following sections.

2.3.1 Effects of Split Ratios

A 1:1 split ratio using a piezo-actuated injector has resulted in reduced penetration length due to reduced mass of the injected fuel per pulse [67]. This strategy had led to the formation of the recirculation region near the spark plug, thereby enhancing fuel enrichment.

Split ratios of 20:80, 30:70, 40:60 and 50:50, which produced varying equivalence ratios, were tested in a GDI spark-ignition engine operating at 2000rpm and with fuel injection pressure of 20MPa in [64]. The first injection was induced in the intake stroke and second in the compression stroke. As the equivalence ratio and the pilot (first) injection quantity increased, the resultant mixture was globally homogeneous and locally fuel-rich, which was transported in time to the spark plug within the ignitable limit prior to ignition. The flame propagation speed had also improved. This led to improved combustion stability. With the 50:50 split ratio on the other hand, they achieved 11% higher in-cylinder pressure and 19.6% higher HRR when compared to 20:80 ratio. The THC levels had decreased with this strategy while the main drawback was higher NOx emissions as a result of the high in-cylinder temperature and pressure stemming from the rich mixture.

A comparison of 2:1, 1:1 and 1:2 split ratios revealed that the 2:1 split ratio formed the highest turbulent kinetic energy (TKE) levels, thereby promoting fuel oxidation while the mixture remained homogeneous. The 2:1 split ratio had also induced a flame that propagated at high velocity, which is attributed to lesser ignition delay, faster flame growth (with 50% greater flame induction angle compared to 1:2 ratio) and complete combustion [47], [63]. The faster flame induction, flame growth and propagation led to greater number of radicals being consumed.

In addition, the 2:1 ratio has been observed to produce the most consistent increase in the IMEP, with the increase being 1.2% greater than single injection. This increase

was caused by reductions in the surface impingements and improved fuel evaporation and mixture preparation, when tested in a spray-guided GDI engine tested using a stoichiometric mixture at 1500rpm and WOT [68]. As a result of the higher fuel vapourisation and heat transfer with the induced air, the 2:1 split ratio further resulted in improved volumetric efficiency [69], [68] as indicated in Figure 2.10. In addition, the split ratio also yielded higher ISFC when compared to 1:1 split ratio, as well as single injection at WOT.
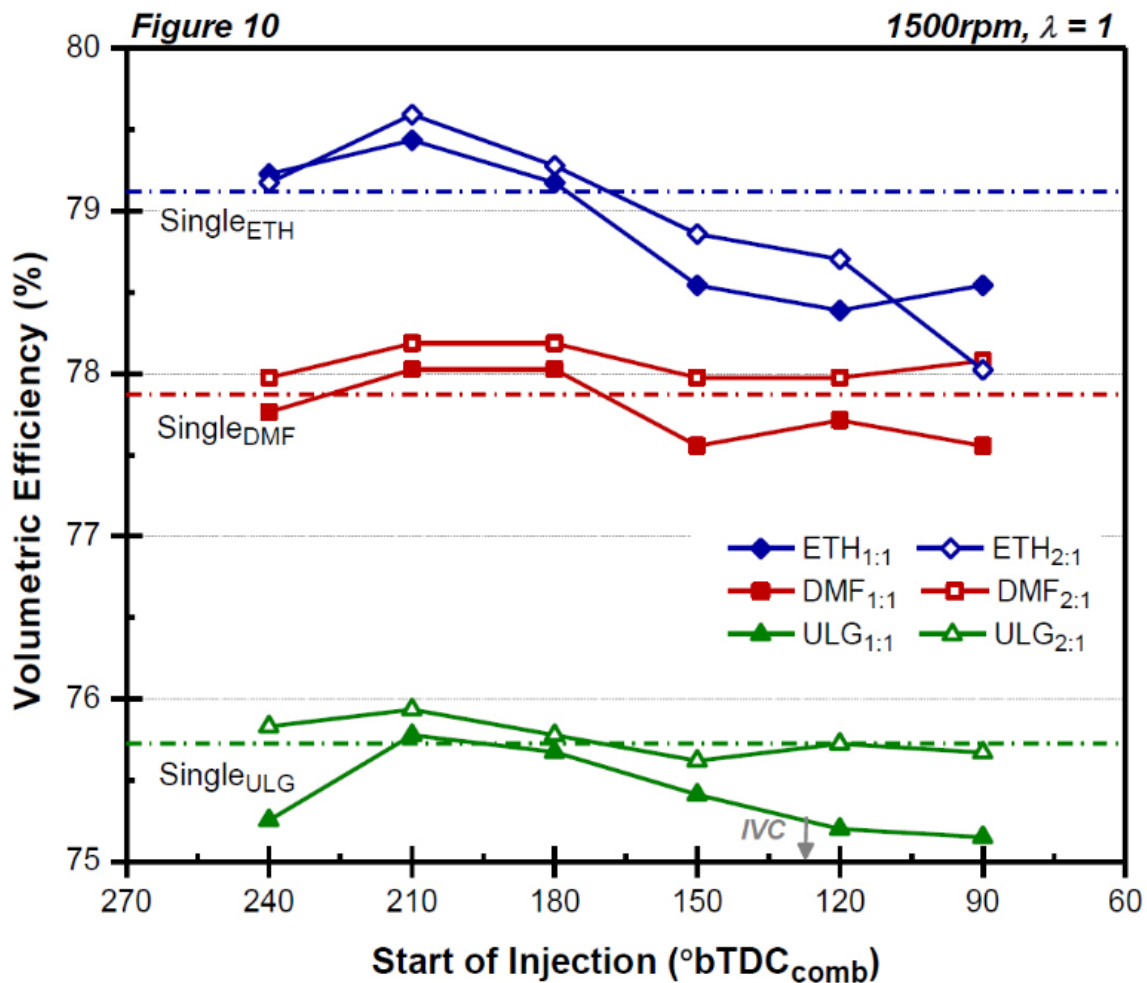
Figure 2.10: Effect of second injection timings with varying split ratios on the volumetric efficiency using ethanol, DMF and Gasoline. Trend extracted from Split injection strategies under full-load using DMF, a new biofuel candidate, compared to ethanol in a GDI engine.

Contrary to the reports on the large split ratios, it was found that a smaller split ratio (greater second injection quantity) exhibited better combustion performance and resulted in rapid catalyst light-off along with reduced soot levels, as noted in [15], [66], [70]. They argue that with the greater amount of fuel injected in the pilot

injection, the overall homogeneity increases while the rich mixture moves away from the spark plug with reduced spray momentum of the second lesser injection quantity.

This was also reported in [54], where the authors found that a large split ratio deteriorated the fuel enrichment around the spark plug along with a weakened tumble flow, when tested at an injection pressure of 20MPa using an outward-opening Piezo injector at 3000rpm and 0.4MPa IMEP. With rich mixture conditions on the other hand (lambda 1 and 1.2), the homogeneous mixture formed by early injection suppressed the smoke levels.

Further to this, with a 30:70 split ratio, the NOx emissions had decreased when tested at 1300rpm and 1.15MPa IMEP [69]. They reported that as the pilot fuel injection quantity increased, the penetration of the liquid phase in the spray decreased but with the expense of high levels of THCs formed from the homogeneous mixture.

Gainey et al., [71] further investigated the charge formation from both split injections and dual system injection (combination of DI and PFI) at engine speeds of 1200rpm to 2400rpm with 10MPa injection pressure. With the split injections using 4:1 split ratio, they observed a narrower heat release profile compared to single injection. This meant a decrease in the thermal stratification. They stated that control of induced stratification without an efficiency penalty can be achieved by employing either a dual injector system, where a fraction of the total fuel is injected into the port, or a split injection. These strategies enabled high-load low temperature combustion, at the same time avoiding excessively rich regions that contributed to combustion inefficiency.

2.3.2 Effects of Split injection Timings

The split injection timings are crucial for the purposes of controlling the mixture distribution in the cylinder. For instance, the influence of the in-cylinder flow and charge density on the spray development should be investigated when considering late ignition, where increased in-cylinder pressure and higher TKE levels are at play [27]. This section explores past studies that have investigated the injection timings and their effects on the engine's performance.

At an engine speed of 1500rpm, injection pressure of 9.6MPa, and using a Solenoid swirl-type injector and EGR dilution, it was reported in [23] that retarding the single injection resulted in increased cycle-to-cycle variability, but decreased the NOx and CO levels, with a more luminous flame. Their investigations on split injections further showed that delayed second injection delayed the start of combustion angle, decreased the MPRR and reduced NOx levels, all however at a cost of increased CO emissions.

Focusing on the spray structure formed from the late injection during the compression stroke, the high charge density reduced the spray penetration and a more compact spray was formed that could be guided towards the spark plug more easily [8]. The inherent limitations with this were insufficient time for the fuel evaporation along with low fuel temperature due to the induced fresh charge, which reduced the volumetric efficiency [72].

Part of the aim of second injection is to increase the mixture's TKE levels close to the spark ignition timing, which would in turn increase the flame propagation speed [60]. The test conditions in this study were 4:1 split ratio, 12.5MPa injection pressure, 1600rpm engine speed, 1.1MPa IMEP and WOT. A delay in the second injection has been observed to strengthen the TKE levels in the flow field. The longer the delay between the second injection and spark ignition however, the greater the likelihood of losing the turbulence intensity in the flow-field.

This suggests that too large a delay in the second injection can deteriorate the mixture formation. The effect of injection timings on in-cylinder homogeneity and TKE levels in a PFI engine at 1500rpm with varying split ratios (1:1 and 2:1) and injection pressures ranging between 10MPa and 30MPa, were studied in [63]. The first injection timing ranged between 360°CA bTDC and 80°CA bTDC, while the second injection timings ranged between 340°CA bTDC and 60°CA bTDC, with 20°CA intervals. As shown in their maps of TKE and inhomogeneity presented in Figure 2.11, the homogeneity and TKE levels increased overall with early first injection and second injection. An early first injection generated fast evaporation rate and improved the mixture homogeneity when mixed with the residual gases. The fuel also had sufficient time to vapourise, disperse and was guided in a counter clockwise direction by the tumble flow. This increase in the intensity of the tumble motion

increased the global mixture homogeneity. As a result, there is a higher demand for the second injection to generate a turbulent and homogeneous mixture in the vicinity of the spark plug.

A first injection in the intake stroke and second injection early in the compression stroke exhibited improved turbulence levels and homogeneity. Later second injection in the compression stroke increased local TKE levels, decreased the homogeneity as a result of reduced dispersion time and formed high soot levels. They concluded that with a 2:1 split ratio, early injection in the intake stroke, and a second injection in the compression stroke relatively early (140˚CA bTDC), can help achieve high turbulence intensity and a homogeneous mixture.
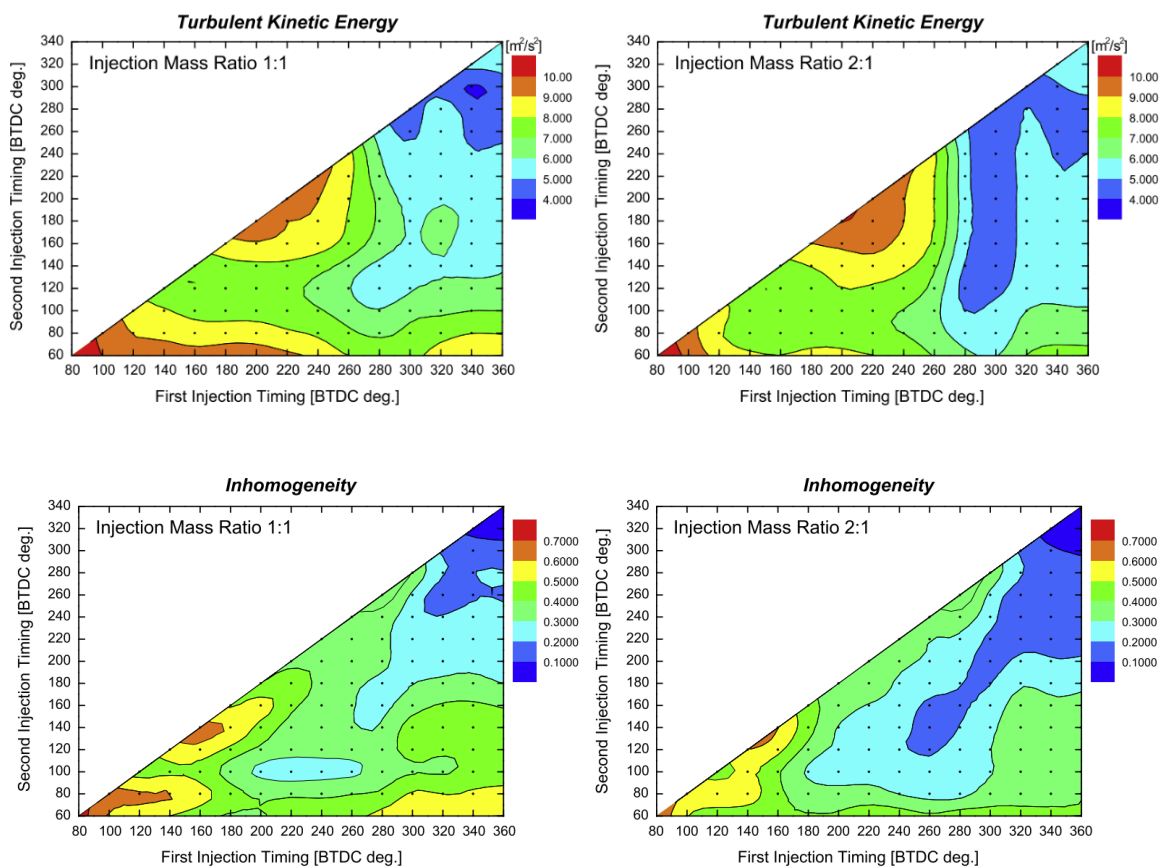
Figure 2.11: maps of TKE and inhomogeneity related to 20°CA bTDC for varying injection times [63].

The negative impact of retardation of the injection time close to TDC, on the charge formation is also observed in [38], [67]. Late second injection, close to TDC led to high mixture inhomogeneity. The growing coefficient of variation (COV) values of both IMEP and cylinder peak pressure (Pmax) were observed with delayed second

injections, thereby indicating an increase in the cyclic variability as the mixture cloud from the second injections approached TDC.

One study investigated the effect of late injection on the thermodynamic processes inside the cylinder [24]. The measurements were performed at 1200rpm engine speed and 0.09MPa BMEP, related to cold-start operation and 12MPa injection pressure, using split ratio of 6:4. The first injection was in the intake stroke at -300°CA bTDC and the second injection timing was varied. Second injection close to TDC provided insufficient time for the diffusion of the second injection, resulting in termination of the combustion and increased exhaust gas temperatures. As a result of the increased mean equivalence ratio near the spark plug, slower and more fluctuated initial flame propagation had occurred, which can be recovered if the local TKE levels are high. This had further led to increased levels of NOX and THC as a result of significant piston surface impingement. This phenomenon was also observed in [73], [15], [66], [70].

The effect of triple injections and their timings were studied in [20], where a range of in-cylinder conditions were explored extensively in a GDI spark-ignition engine tested at 1500rpm, and varied load points. They observed that closely spaced triple injections, injected near TDC, had resulted in the highest work output and peak HRR, as was also observed in [58]. The main drawback with the late triple injections however, was a large amount of soot luminescence, and therefore high levels of soot generation around the spark plug, due to a lack of mixing which formed locally fuel-rich areas. By advancing the first and second injections, thereby increasing the dwell time between the second and third injections, the work output had declined as a result of over-mixing. This had a negative impact on the combustion stability.

Increasing dwell from 0.5ms to 0.65ms on the other hand [74], had resulted in increased quasi-steady needle lift-off length and increased entrainment effects of the surrounding oxygen into the flame region. This had led to the combustion of a leaner mixture which thereby reduced soot formation.

A direct correlation between injection timing and emissions exhibited large increase in ISNOx and ISHC with retarded second injections. A slightly earlier second injection at 210 °CA bTDC showed the greatest reductions in the ISCO as a result of improved fuel vapourisation and reduced piston wetting [68].

2.4 Effects of Injection Pressure on the Engine's Performance

High pressure multi-hole injectors are widely used in GDI engines primarily because of the robust and repeatable sprays produced without resulting in spray collapse. Studies have shown that the individual plumes generate singular vapour branches as the fuel propagates far downstream of the injector, rather than forming complex cloud structures that could increase the likelihood of droplets coalescing [75]. The main advantage is that the holes' pattern, holes' orientations, internal flow cavity and the number of holes can be designed such that the individual spray plumes, and therefore the overall spray pattern, can be controlled. These features aid the droplets' dispersion inside the cylinder, reducing the likelihood of fuel impingement on the surfaces [3].

The injection pressure plays a crucial role in the atomisation rates of the injected fuel and in the mixture formation. Small Sauter mean diameter (SMD) of fuel droplets and large GDI spray angles were formed as a result of the high injection momentum, when tested in a constant volume spray chamber at an ambient pressure of 0.1MPa, using a 6-holes injector at pressures of up to 20MPa and PW of 1.5ms with n-heptane [76]. The fuel had reportedly spread radially across the cylinder, improving the mixing of the air and fuel. This helped in achieving a well-mixed homogeneous charge. Although the main tip penetration length increased with increasing fuel injection pressure, the critical spray breakup occurred closer to the injector tip.

An early study [77] found that as the injection pressure increased from 8MPa to 12MPa, the differences in the droplets' Sauter mean diameters (SMDs) between the spray tip and the spray's tail reduced, indicating that critical (primary and secondary) atomisation processes occurred closer to the injector tip at large injection pressure. In addition, the vortices formed at the outer edges of the spray had also formed closer to the injector, with their strengths intensifying with increasing pressure [78]. It has been reported in [79] however, that the injection pressure has negligible effect on the droplets' sizes in the recirculation region. It is important to note that all of these early studies were performed under ambient atmospheric conditions, and so the recirculation regions would vary.

The recirculation regions from the high injection pressure of 20MPa has been observed to accelerate the atomisation rate and the resultant slow-moving droplets

could be transported towards the spark plug with ease, as reported in [6]. The high injection pressure also formed a rich mixture inside the cylinder and thus generated stable combustion, when tested at stratified conditions and engine speed of 1200rpm in [46].

A study [80] tested the injection pressures ranging between 5MPa and 40MPa using a multi-hole injector, with injection in the intake stroke at an engine speed of 2500rpm. The average Sauter mean diameter (SMD) of droplets were measured at 9μm for the 40MPa rail pressure, whereas 5MPa rail pressure had resulted in average SMD of 50μm in the cone region. In addition to the improved atomisation quality, the high injection pressure also enhanced the intensity of the in-cylinder tumble charge motion and the mixture homogeneity. They observed the PM levels to decrease with increasing injection pressure and stated that the reasons for this were twofold: the enhanced atomisation rate and air entrainment from high injection pressure improved the mixture homogeneity; and the coking deposit accumulation and diffusion combustion had been alleviated, which was also reported in [8], [81]. With 40MPa injection pressure, they achieved reduced THC levels and a reduction in the net SFC.

[82] also found that the increase in the injection pressure had resulted in exponentially reduced filter smoke number (FSN) while the combustion efficiency had improved. The injection pressures tested ranged between 10MPa and 20MPa at 3000rpm engine speed and 0.4MPa IMEP.

Another study investigated the droplets' velocities and atomisation rates for pressures ranging between 5MPa and 60MPa, inside a constant volume chamber pressurised up to 2.5MPa [83]. The penetration length and velocity in the spray's tip had increased with increasing fuel rail pressure. This increase was progressively diminished with the highest injection pressure as the aerodynamic drag opposing the spray's motion became more intense with increasing injection pressure. The mean diameter and SMD had also reduced with the increasing pressure, with the most notable reduction observed as the pressure increased from 5MPa to 20MPa. The reduction in droplets' sizes with increasing pressure past 20MPa was attenuated, although the PDF of droplets larger than 10μm had reduced at an injection pressure greater than 50MPa. Similar observations are also noted in [8], [83].

Zhou et al., [84] observed greater variation in the spray morphology and distribution of the vapour mass when employing high injection pressures. The variation in liquid phase distribution was larger when employing 10MPa injection pressure, when compared to 5MPa. Conversely, the effect of fuel temperature (85°C and 125°C) on the variations of spray liquid morphology was relatively minor compared to the injection pressure.

The improved atomisation rates from the high injection pressures had prevented the likelihood of rich pockets of fuel in the cylinder as a result of the presence of fuel ligaments and large fuel droplets. Although the main tip penetration increased with increasing fuel injection pressure, the critical spray breakup occurred closer to the injector tip, as is also noted in [19], [76]. In spite of these benefits, increased costs, higher power consumption by the pumping system which degrades the mechanical efficiency, and higher penetration lengths accompanied with higher injection pressures (which could increase piston surface impingement) should also be considered. It has also been reported that the impingement starts earlier with higher injection pressure [3], [36].

Large injection pressure reduced the injector diffusion flame, when tested in a GDI engine at 2500rpm using a centrally mounted injector under stoichiometric air/fuel conditions, and fuel injection pressures of up to 20MPa [40]. The increased fuel pressure enhanced the atomisation rate and had led to improved combustion efficiency along with reduced PM and PN levels. With the low injection pressure on the other hand, high intensity regions were observed in the vicinity of the injector tip later in the expansion stroke (Figure 2.12) which is indicative of diffusion combustion.
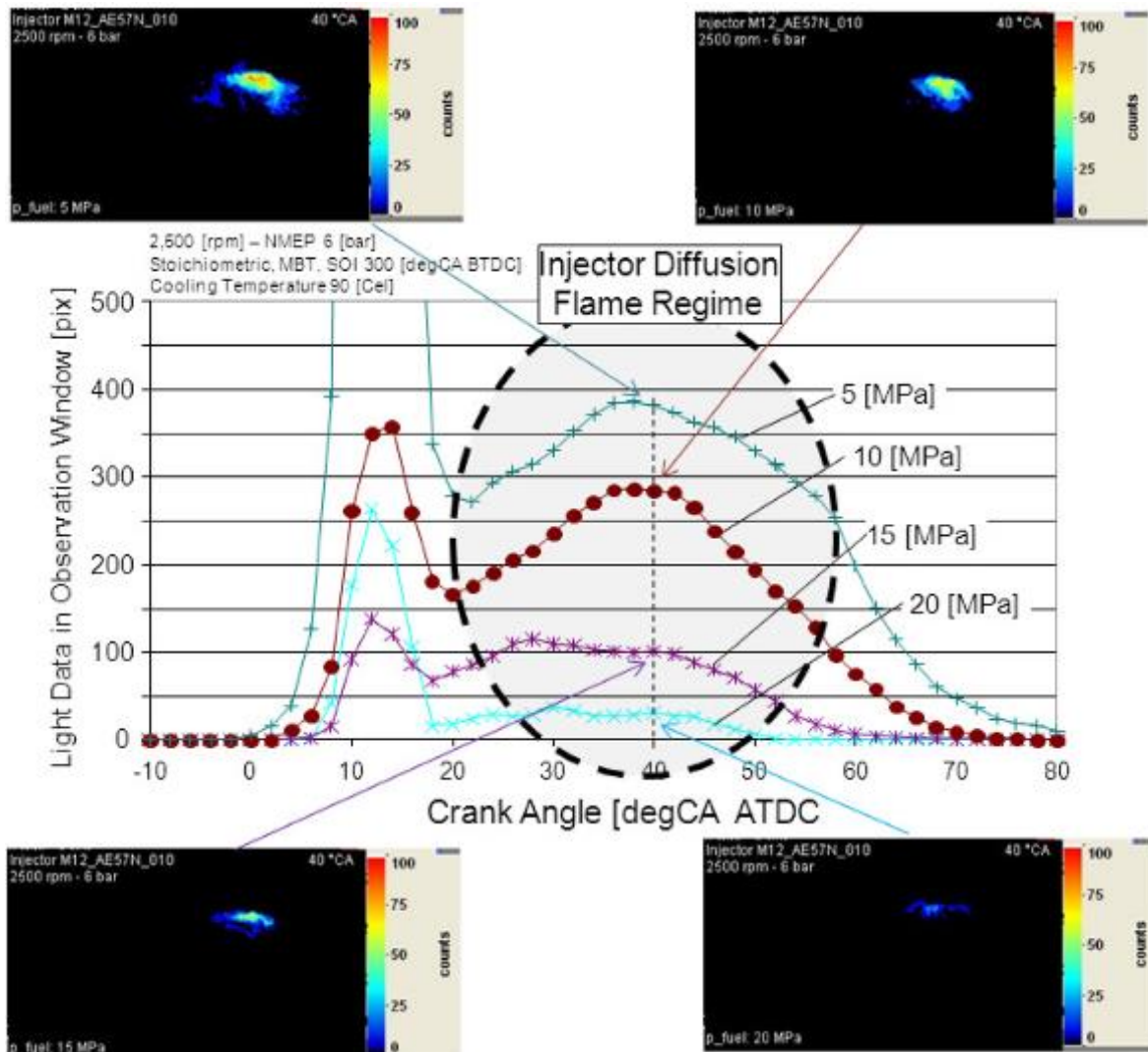
Figure 2.12: Effect of increasing fuel pressure on the flame intensity during combustion at 40°CA aTDC, extracted from [40].

Studies focusing on the injector behaviour [33], [85] revealed that a high injection pressure had the capability of accelerating the opening of the injector and shortening the delay time, due to the large inertia forces. Both smaller droplets and decreased injection duration caused by the high injection pressure had alleviated tip wetting via wide plume wetting, vortex droplet wetting, and fuel dribble wetting, which was beneficial for PN emissions.

In summary, although operations with high injection pressures are often accompanied with larger penetration lengths (if PWs are kept constant) and spray angles, which subsequently increases the surface impingement, increased costs and reduced overall mechanical efficiency due to the higher pumping systems, the benefits outweigh these drawbacks. The key benefits are optimised atomisation

rates, critical breakup which occurs closer to the injector tip and significantly improved mixture formation. Combining high injection pressures with the split injection strategies is thus proven to be highly effective for stratified charge operations.

2.5 Effects of the Split injections Spray Characteristics on the Charge Formation and Vice Versa

While extensive studies have focused on the effects of the split injection strategy on the engines' performances, it is important to understand the impact of the interactions between the sprays and the surrounding charge which ultimately determine the engine's performance. In this, studies on sprays and atomisation conducted inside spray chambers and combustion chambers provide valuable information of the complex phenomena of sprays and the effects of the injection system design. The effects of the split injection strategies on the spray characteristics and the mixture formation are investigated in this section.

The spray characteristics of the split injections were investigated using Diesel fuel at a chamber pressure of 10MPa, dwell time ranging between 5ms and 15ms and varying split ratios in [86]. The authors found that with the 1:1 split ratio, the first injection had a larger half angle compared to the second injection's spray angle. This was because both injections exhibited differences in the plumes' interactions and entrainment of the surrounding charge (which itself varied between the first and second injections), in spite of the injected mass at both events being the same. They also found the resultant spray angle to be insensitive towards the injection duration and the dwell angle.

When considering dwell times, which are typically short when using Piezo-actuated injectors, previous studies [69], [44] have observed increased likelihood of droplets' coalescence when a short dwell time of 0.2ms was employed. With a larger dwell time however, they reported a reduction in the main tip penetration length and air-fuel ratio, along with an increase in the normalised mass of vapour owing to increased evaporation of the first spray before the start of the second injection.

With a large dwell, one study reported that the split injection strategy led to the formation of smaller droplets, when compared with single pulse injection [87]. The

test conditions were (1) homogenous cold-start conditions, at atmospheric temperature and pressure conditions and (2) stratified cold-start conditions with the chamber pressurised to 0.5MPa and heated to 350K with the fuel cooled to 243K. They used a Piezo injector and tested with injection pressures of 5MPa, 12.5MPa and 20MPa. The triple injection PWs employed were 0.2ms, 0.15ms and 0.05ms, in that order, with the dwell times of 0.3ms and 0.2ms. They also observed that different fuel compositions (of gasoline and ethanol blends) had affected the spray characteristics less than expected. The liquid fuel had penetrated rapidly when injected at 12.5MPa and 20MPa cases, to depths of 30mm within 0.6ms ASOI, but it did not penetrate much further thereafter due to the formation of vortices at high injection pressures. The triple injections had resulted in shorter penetration lengths, indicating that the split injection strategy forms stronger vortices when compared to a single injection tested with a PW of 0.4ms.

Comparing the resultant SMDs between the single injections and split injections using a piezo-actuated injector [88], large droplets' SMDs (>15µm) were observed 40mm downstream of the injector (far-field region) with the single injections. The number of large droplets had reduced significantly using split injections, which was caused by finely atomised droplets formed at the early stages of the second injection. In addition, a sufficiently short dwell time resulted in improved atomisation rate, as the flow-field generated by the first injection was highly turbulent and in the vicinity of the injector.

Observing the effect of dwell times on the mixture distribution, it was found in [88] that the second injection undergoes significant entrainment effects in the wake of the first injection. If the dwell time is short, the second injection ends up with higher mean velocity, resulting in slip-streaming where the second injection inevitably penetrates into the first injection, as was also observed in [89]. This effect is alleviated with the longer dwell time whereby the resultant mean velocity of the droplets from the second injection would be reduced.

The fuel vapour distribution from the split injection strategy was found to be wider than the single injection case, when tested using a solenoid injector at 10MPa injection pressure and 1:1 split ratio, with each injection's PW of 0.9ms and dwell time of up to 1.5ms [90]. The engine conditions tested were twofold: (1) 7500rpm

WOT, 1.2MPa BMEP and air-fuel ratio of 13 and (2) 5000rpm, mid-load, 0.3MPa BMEP and air-fuel ratio of 17. The wider vapour distribution was stated to be the consequence of the momentum exchange between the fuel droplets and the surrounding charge. As a result of the wider vapour phase from the split injection, higher injection pressures in conjunction would inhibit the formation of large main tip penetrations formed from injecting the fuel in one long pulse. Their improved atomisation characteristics can be beneficial for the in-cylinder mixture formations.

A similar observation was made in [91]. The comparison in the vapour and liquid phases between single injections and split injection (Figure 2.13), shows that the vapour-phase quantity in the stable region (equivalence ratio of 0.7-0.3) for stratified charge operation, increased when the split injection strategy was employed. Contrary to the split injections, the region in the map for the vapour phase for the single injection case is much narrower. The larger mass of fuel in the liquid phase with the single injections was due to the greater liquid mass at the spray's head, which persisted for longer the end of injection and would eventually settle on the liner and the piston's surface.
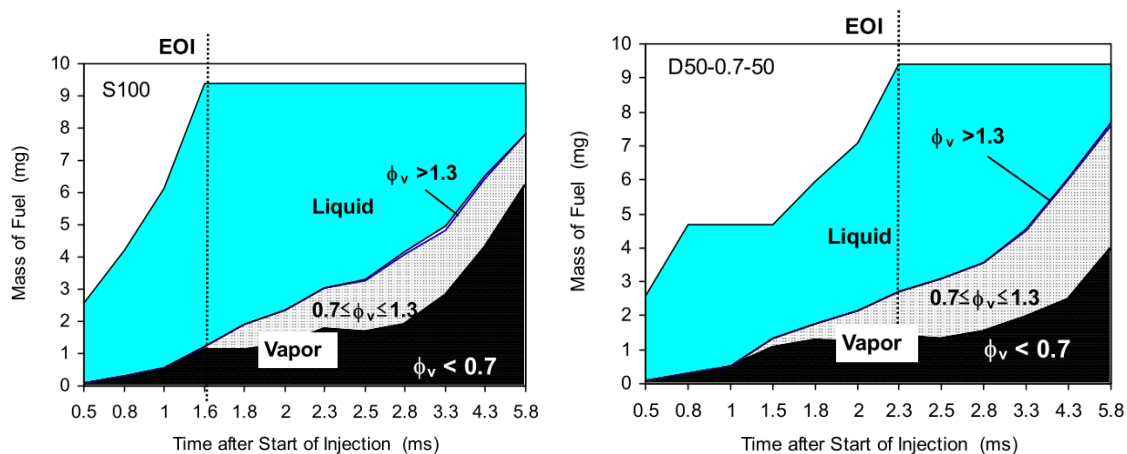
Figure 2.13: temporal variations in the liquid and vapour phase quantities of the sprays from single injections (left) and split injection with 1:1 split ration and dwell time of 0.7ms. Measurement conditions: injection pressure of 5MPa, ambient pressure and temperature of 1MPa and 500K. Images extracted from [91].

For the single injections, the liquid fuel that had piled up at the spray's leading edge had increased the penetration length. This was circumvented by split injections (Figure 2.14). The result was a reduction in the formation of over-rich mixtures and smoke levels.
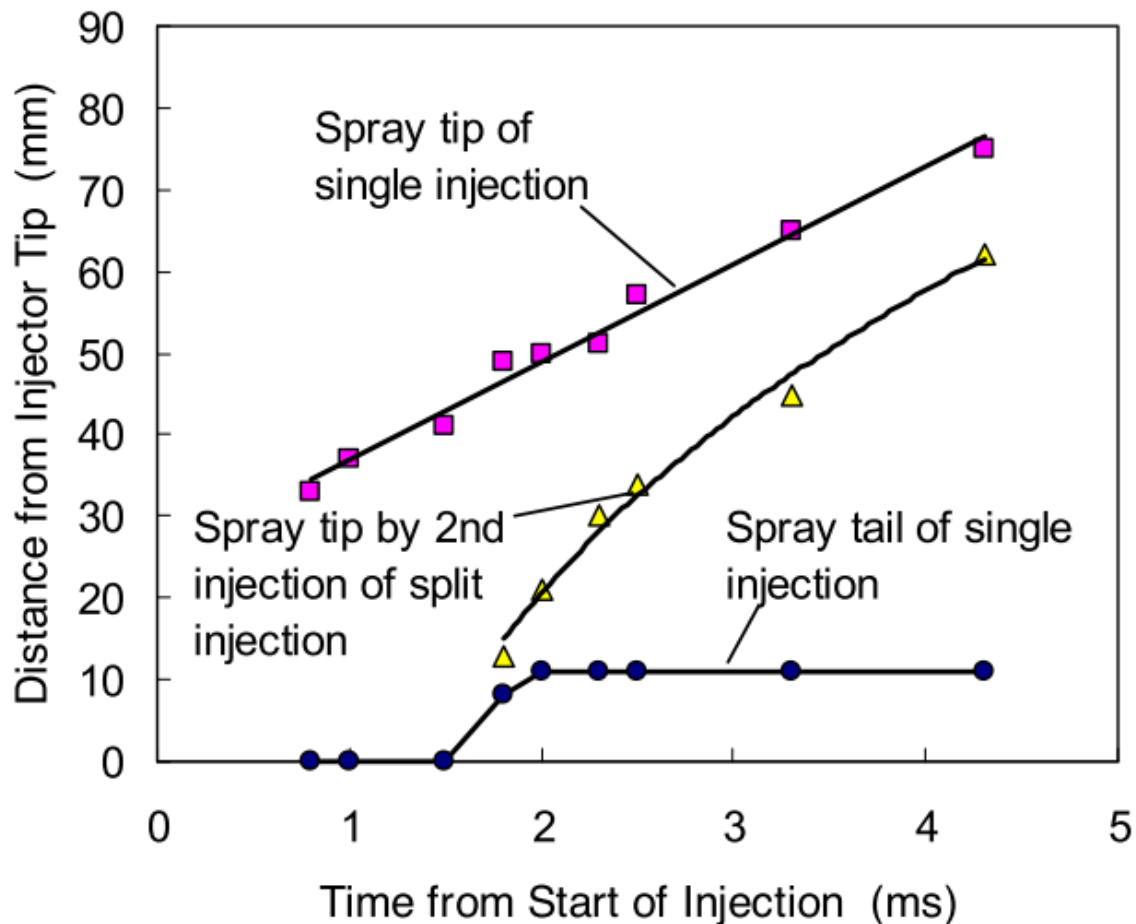
Figure 2.14: differences in the distances between the spray tail and spray tip in single and split injections at injection pressure of 4.6MPa, ambient pressure and temperature of 0.6MPa and 300K. Images extracted from [91].

Using a piezo-injector for split injections [92], the second injections had also exhibited reduced spray angles. This in turn resulted in increased instability in the spray structures, attributed to the perturbation of the still evolving charge from the first injection. This turned out to be the source of the large COV in IMEP, which is one of the drawbacks if the split injection events are timed poorly.

When considering the split injection timings, a late second injection and its sprays momentum is stated to heavily influence the charge characteristics particularly near TDC. This is because the liquid spray would have less time for the momentum dissipation. As a result, the high velocity and density of the liquid spray injected late would change the charge characteristics significantly prior to ignition. It is stated that the combustion would be dominated by the mixture formation, which in turn is influenced by the timing of the injection [93].

Another drawback of retarded injection is that the upward fluid flow forced by the compression stroke would impinge of the cylinder's head and at the injector tip (known as funnel flow). This has been identified as the leading cause of the spray deformation of the post-injections (second and third injections) in [94]. The test conditions here were 2000rpm, intake manifold pressure of 0.095MPa, and 20MPa injection pressure. Three types of triple injection schemes were investigated. The first injection consisted of 70% of the total injected mass. Its SOI was varied from 36.25°CA to 44.5°CA bTDC. Second (energising time 125µs, 23% of total injected mass) and third (energising time 80µs, 7% of total injected mass) injections were fixed at 29.5°CA bTDC SOI and 24.25°CA bTDC SOI, respectively.

The first injection resulted in high momentum transfer to the gaseous flow, which generated high shear forces between the spray and the surrounding charge. This led to the formation of the local vortices that would contribute to the local turbulence levels inside the combustion chamber. The spray tip penetration of the second injections fluctuated when compared to the stable first injections, which were caused by the highly turbulent charge formed from the first injection, as well as the temporal variations in the rail pressure. After the first injection, oscillations in the rail pressure were also observed for subsequent injections, which would intensify at short dwell times. Injection pressure would then directly influence the penetration length and the spray angle. The fluctuating spray characteristics would then also impinge on the cylinder head as the injected fuel is forced upwards if not allowed to propagate downwards into the cylinder.

The effect of the injection on the cylinder charge has been the topic of many detailed discussions. There are also significant effects of the surrounding charge on the injected spray characteristics and the distribution of the vapourised fuel inside the combustion chamber, which is of course dependant on the engine speed, injection timing and injection duration [95], [96], [93], [97], [26]. The charge properties in the intake and/or compression stroke can affect the spray penetration and liquid/droplets' distribution [97]. The cyclic variability of the spray structure, fuel distribution, mixture formation and combustion development can all be affected by the cyclic variability in the charge's flow momentum.

Advancing the injection timing (when the in-cylinder pressures are lower) has resulted in wider spread of the spray when tested at an engine speed of 200rpm at WOT and 10MPa injection pressure [21]. Same quantity was injected for all five single injections' SOIs (260°CA, 280°CA, 300°CA, 320°CA and 340°CA bTDC). By injecting late in the compression stroke, with high ambient pressure conditions, the spray front was decelerated, caused by increased aerodynamics drag as well as increased momentum exchange between the droplets at the tip of the spray and the surrounding charge in its gaseous-phase. This was the case even when the charge density was low (low-load), as observed in [89] at an injection pressure of 38MPa.

A 30% reduction in the penetration length was further observed in [23] when the in-cylinder pressure was increased by 0.5MPa, using a solenoid swirl-type injector tested at 1500rpm engine speed and fuel pressure of 9.6MPa. This effect would be less dominant however with increase in the fuel injection pressure, unless if the ambient pressures, and therefore the aerodynamic resistance, increased.

By increasing the chamber pressure from 0.1MPa and 1.6MPa (chamber temperature at 100°C, 150°C and 200°C), a widening of the spray was observed, while the penetration length reduced, as reported in [98]. The measurements were performed inside a spray chamber at injection pressures of up to 50MPa and PW of 2ms. The effect of the ambient pressure on the penetration length was significant, due to greater aerodynamic drag resisting, and thereby decelerating, the propagation of the spray front. The lower the difference between the injection pressure and ambient pressure, the lower the momentum of the initial spray momentum. This subsequently lowered the droplets' velocities close to the injector tip. As such, the penetration length remained constant due to the consistency of the large aerodynamic resistance from the surrounding charge. The injected fuel was directed radially due to the large inertia of the fuel mass. This effect intensified with increasing chamber pressure.

There is however a range of earlier literature stating that increase in the ambient pressure reduces the spray angle along with the penetration length, resulting in a compact spray structure [45], [99], [37], [100]. This was observed however, with low injection pressures of less than 10MPa whereby the fuel inertia during the injection was low.

At high ambient pressure, the total mass of the ambient air entrained was found to be greater than lower ambient pressure conditions, as reported in [101] using a swirl type injector at a fixed pressure of 5MPa, split ratios of 1:1 and 1:2, and ambient pressure tested between 0.1MPa and 0.4MPa. This could be ideal in achieving a fuel rich mixture close to the spark plug. In addition, at low ambient pressure and a short dwell time, the second injection penetrated into, and overtook, the first injection. Here sophisticated mixing took place, whereby collision and coalescence of droplets occurred which changed the internal structure of the spray. This effect had alleviated with higher ambient pressure. They also observed larger penetration length of the second injection, and found that the first spray and its entrainment with the ambient air reduced the air resistance, as a result of which the second spray's mean velocity was higher than that of the first spray.

With the increased ambient temperature on the other hand, the spray cone angle and penetration length decreased [102]. Flash boiling can in fact lead to the complete spray collapse at a high rate, as noted in [103].

Further investigations have been conducted inside heated pressure chambers to observe the effect of flash boiling of the fuel spray [104], [105], [106]. Flash boiling effect is described as fuel that is superheated above its boiling temperature, such that the fuel breaks into small droplets upon injection. It was concluded that flash boiling effects result in a high rate of fuel evaporation generating a high proportion of small droplets in the spray region, improves mixture formation, and thus improves the overall combustion performance. Due to the reduced pressure of the droplets, however, the small droplets formed as a result of the flash boiling effects are forced to move in the spray's centreline. This increases the density of the droplets in the spray's core and thus reduces the spray cone angle.

The effect of chamber temperature and pressure was also studied in [107], when tested in a chamber pressurised to 0.5MPa, 300K and at an injection pressure of 10MPa, with 1:1 split ratio and varying dwell times using an outward opening injector. The chamber temperature had significant influence on the spray evaporation rate, which was stated to be the main difference between the first and second injections' penetration lengths. The second injection's penetration length had decreased in comparison to the first injection, and this was stated to be independent

of the chamber pressure. Along with the ambient temperature, the collision between both injections caused further reductions in the second injection's penetration length. Increasing the dwell time alleviated this effect.

The high ambient temperature and injection pressure also reportedly accelerated the plume interactions as reported in [4]. The test chamber was heated up to 1000K, and pressurised up to 0.6MPa, with the fuel temperature cooled to 363K, and an injection pressure of 20MPa. The ambient gas entrainment into the individual plumes had started to occur from the early stages of the injection. This generated recirculation regions between the plumes, as well as the ambient gases being entrained from the tip and edges of the spray. This in turn increased the rate of interaction of the neighbouring plumes. When this happened, the plumes stopped travelling along the axes of the nozzles, which meant that the spray structure's collapse was imminent.

A similar observation was reported in [108], where the authors studied the spray characteristics inside a spray chamber at ambient pressures of 0.05MPa to 0.6MPa, ambient temperature of 293K. The tested injection pressure was 20MPa, fuel temperatures were 293K and 363K and PWs of 0.3ms and 0.7ms were investigated. They found recirculation zones at the leading edge of the spray formed shortly after the start of injection, which was caused by the momentum exchange between the injected fuel and the surrounding charge. Air entrainment helped form a second, counter-rotating vortex in between the plumes. The led to reduction in the penetration length and enhanced the atomisation rate. The droplets' sizes measured in the upper spray region of the leading-edge vortices were smaller and moved slowly, when compared to the droplets at the spray front. One disadvantage of the spray-induced vortices was that the liquid fuel was transported back to the nozzle after the end of injection, which can be detrimental in terms of accumulating injector deposits at the tip, thereby coking it.

Achieving a collapsed spray structure easily, has in fact proven to be increasingly difficult when using the multi-hole injectors, which produce robust spray patterns typically aligned in straight lines. They consist of individual vapour branches as discussed earlier. As such the spray collapse does not typically occur, which is why they have been proven to be so effective for stratified operation [109].

2.6 An Overview of the Spray Breakup Processes

The fundamental spray breakup processes are explored in this section, which would further aid in the understanding the spray characteristics and the interactions between the spray and the surrounding charge formation. The fuel atomisation process is typically divided into two stages: primary atomisation (near field breakup) and secondary atomisation (far-field breakup).

Kelvin-Helmholtz (K-H) instabilities is a phenomenon whereby the initial instabilities in the liquid jet are introduced by the surrounding charge. The interactions between the air stream at high velocity and liquid forms a shear layer between the co-flowing fluids due to the difference in the flow velocities, as represented in Figure 2.15. A vortex is formed on the surface of the liquid column, which causes droplets' entrainment. It moves upward and adheres to the central tube surface with increasing air velocity. This decreases the liquid intact length, also known as the penetration length.

The wave growth of the liquid jet and the resulting rate of atomisation, influenced by K-H instabilities, is thus critically dependant on the air-stream's velocity.

Primary atomisation occurs close to the injector's exit, upon interaction between the liquid jet and the co-flowing air stream of high velocity. It is dominated by the Rayleigh-Taylor (R-T) breakup mechanism, which occurs when fluids of different rheological properties interact with each other initially. In the case of air-blast atomisation, the instabilities in the liquid jet result in large liquid ligaments and droplets shearing off from the liquid intact length.
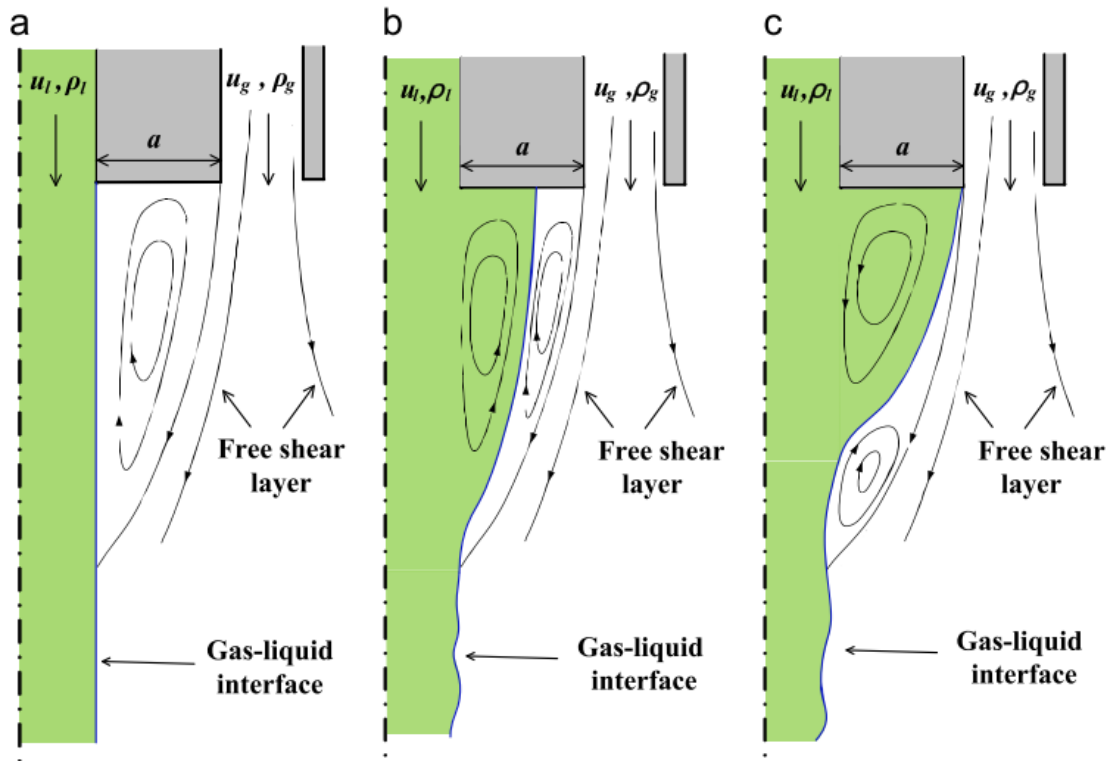
Figure 2.15: stages of liquid entrainment over time due to the air and water flow interaction close to the nozzle exit [110].

The spray penetration length is typically characterised by the non-dimensional aerodynamic Weber number (which is the ratio of aerodynamic disruptive force to the restraining surface force), and the air-liquid momentum ratio (M) defined as:

$$M = \frac{\rho_g U_g{}^2}{\rho_l U_l{}^2}$$ (Equation 2.1)

Where ρ_g, U_g, ρ_l and U_l are air density, air velocity, fuel density and fuel velocity respectively.

Large Weber number (We) and M result in large instabilities in the liquid jet. This increases the liquid shedding frequency, reducing the liquid intact length and improving the rate of primary atomisation. With low M or We, whereby the liquid injection velocity is large, the rate of wave growth is initially high. Upon achieving maximum wave amplitude, the liquid jet's growth rapidly diminishes. This is the point where the jet is damped just before breakup (Figure 2.16a.). This is an example of poor atomisation.
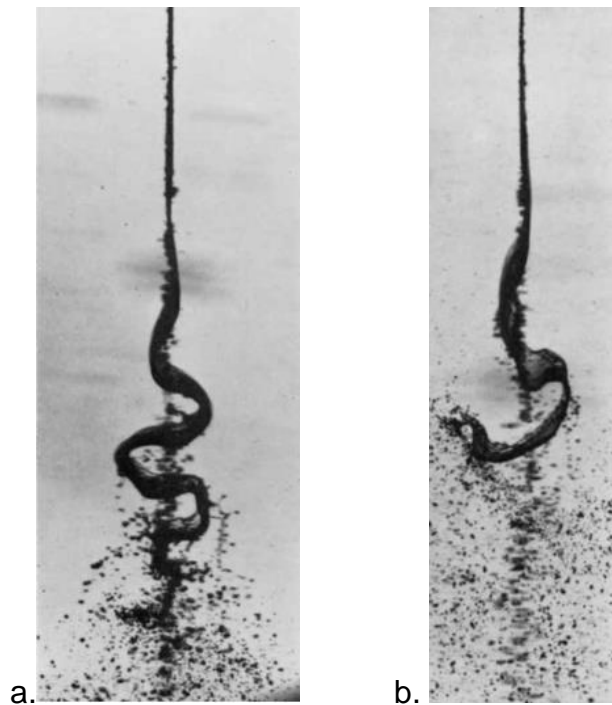
Figure 2.16: (a) high liquid velocity resulting in dampening of waves induced by Kelvin-Helmholtz instability, and (b) low liquid velocity resulting in breakup of liquid sheet after achieving maximum amplitude [111].

The surface tension forces of the liquid jet influence the liquid intact length despite the instabilities in the liquid jet. The consequence of high surface tension forces in the liquid jet is dampening of the wave, as the large surface tension forces overcome the shear forces of the surrounding air. One way to reduce the dominant surface tension forces, and encourage the spray breakup-up, is by decreasing the size of the fuel injector's nozzle and considering convergent-divergent nozzle designs, which are employed in the current generations of injectors.

With large M and We, the growth rate of the wave increases such that the maximum amplitude is reached, after which the liquid intact length breaks up into droplets (Figure 2.16b.) [112], [113].

Fluids of high viscosities, such as gasoline fuel, require large air velocities or We to overcome the large surface tension forces, in order to generate instabilities and encourage high atomisation rate [114]. With a large We number, the rate of atomisation is improved and it occurs closer to the injector's exit. This results in the formation of large spray angles and smaller SMD of droplets [115], [116]. As the SMD of droplets decreases, the axial velocities of the droplets typically increase.

SMD is defined as the mean diameter of a droplet with the same surface area/volume ratio as the spray as a whole.

$$SMD = \frac{\sum N_i D_i^3}{\sum N_i D_i^2}$$
(Equation 2.2)

N_i represents the number of droplets of the same group size and D_i represents the measured droplet diameter.

Bag breakup is a primary breakup phenomenon which occurs when pressure accumulates inside the crest of the oscillating waves. They progressively detach from the liquid jet and expand, resulting in the formation of small droplets upon disintegration [117]. The resultant droplets have large velocities, compared to the velocity of the corresponding main spray. Two reasons for this are:

a. the internal pressure is higher than the external pressure. The droplets thus gain high momentum as a result of the pressure difference inside and outside of the bag at the instance when the bag breaks.

b. drag forces caused by the air flow increases the velocity of small, light droplets.

Secondary atomisation is generally observed further downstream of the injector's tip. Large droplets and liquid ligaments formed from primary atomisation break up further into smaller droplets as a result of large shearing forces present in the flow field. This is the phase in which maximum stable droplets are achieved.

The droplets occasionally collide with each other and consequently coalesce under specific conditions. When two droplets are about to coincide, a thin film of air is formed between them which may cause the colliding droplets to rebound. If the time of the collision of the two droplets is sufficiently large to allow for the thinning of the air boundary below a specific threshold, the droplets will coalesce.

 The collision residence time is stated to be dependent on: the size of the colliding droplets, properties of dispersed and continuous media, and the intensity of turbulence in air and liquid media [118]. Droplets' coalescence is undesirable as it results in increased resultant droplets' sizes, increasing the likelihood of soot formation.

High in-cylinder pressure generates entrainment of the fuel droplets due to the presence of the high aerodynamic drag and large pressure differences across the cylinder wall. This results in the formation of fine droplets from secondary atomisation (Figure 2.17), high rate of evaporation of the fuel droplets (Figure 2.18), and smaller spray cone angles.
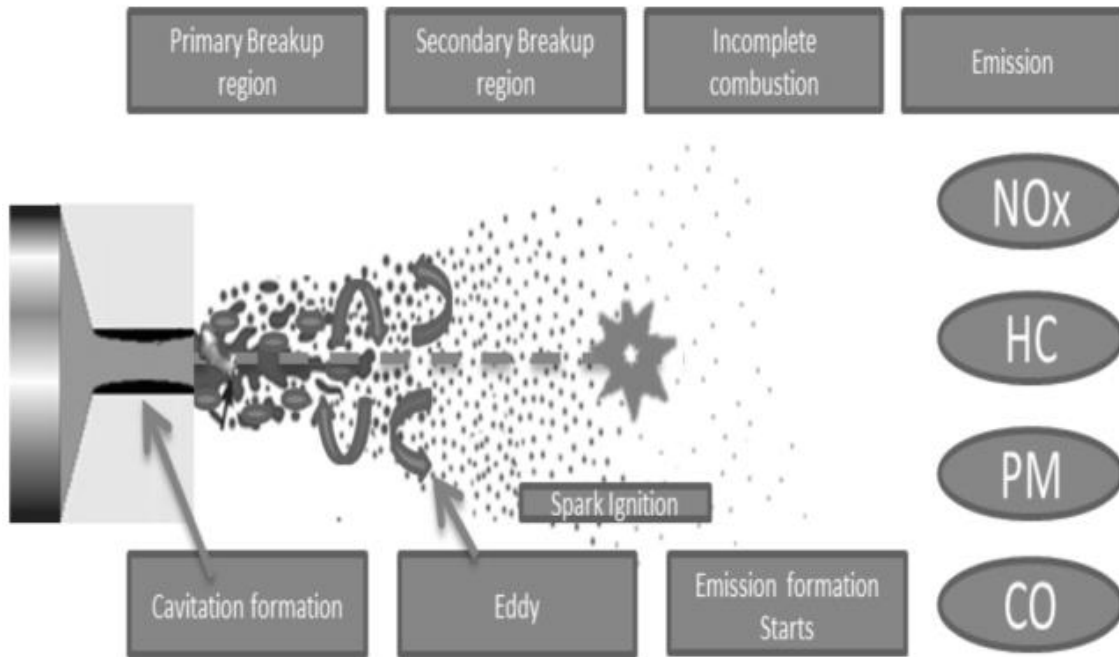
Figure 2.17: representation of primary and secondary atomisation from a GDI injector [119].
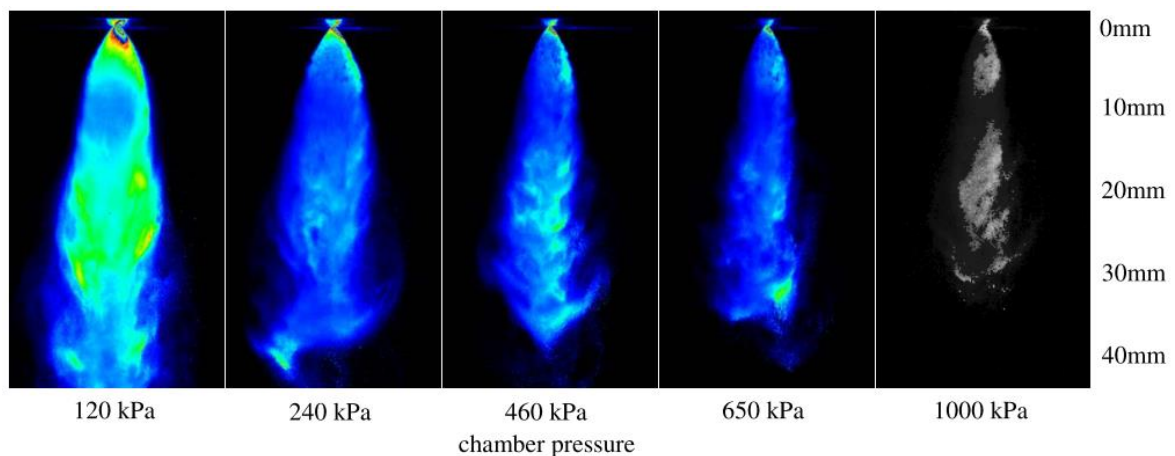
Figure 2.18: LIF images showing the effect of in-cylinder pressure on the spray tip penetration [120].

2.7 On-going improvements in GDI Spark Ignition Engines

Continued research and development works are focused on the feasibility of employing higher injection pressures of up to 100MPa, which are typically representative of Diesel injection pressures [121], [122] along with downsizing the GDI engine's boosted operation. This is to extend the upper load limit of stratified charge operation, without excessive engine-out soot productions [123], [124], using a multi-hole injector and EGR dilution which would allow the continued use of the three-way catalyst for after-treatment of the emissions [125].

Both multi-pulse injection and multi-strike ignition strategies are also being pursued to further optimise the mixture preparation and avoid pool fires in stratified charge operations [15].

2.7.1 Gaps in the Current Understanding

In summary, it has been widely realised that employing the split injection strategy is beneficial for the stratified charge operation in GDI engines. Some of the key benefits stemming from a split injection strategy, when compared to single injections, include: the production of repeatable spray structures and thus reduced cyclic variability [5] - [10]; improved turbulence levels of the flow-field if the correct split ratios and dwell times are employed suitable for the operating loads and speeds [43], [47], [63]; inhibition of the high concentration of the liquid spray piling up on the spray tips [44], [91]; reduced overall fuel impingements and therefore pool fires [3]; reduced soot formation and improved overall drive cycle emissions [19], [65].

To employ the injection strategy effectively, key consideration needs to be provided to the second injection's timing and quantity. This is to avoid late second injections which could be detrimental for the mixture formation as the fuel would not get enough time to mix with the surrounding charge [20], [21] and would result in the formation of fuel film on piston's surface, chamber walls, injector tip and cylinder head [21], [37].

Despite the clear benefits with the strategy published by a range of literature, there are a few gaps in the understanding of the effects of the strategy, which the current study aims to explore. Specifically, there is a lack of understanding of the effects and interactions of the first and second injections throughout the cycle. In addition to concerns related to the retarded injection not having sufficient time to atomise, there

are various key factors for consideration, including the effects of split ratios and dwell times on the atomisation rates, and impingement on the chamber surfaces.

While the spray has significant effects on the surrounding charge, the surrounding charge also has a large effect on the evolution of the spray during injection. The extent of this effect using high injection pressure remains to be explored. An attempt to address these gaps in the understanding have been made by performing cycle-resolved high-speed PIV inside an optical GDI engine. Not many studies have undertaken detailed optical studies of the charge formation, using a high-pressure DI injector. To the author's knowledge, the previous high pressures applied using split injections were up to 20MPa [30], [64], [65]. The current study aims to perform the stated investigations at injection pressures of up to 35MPa, with improved atomisation characteristics but inherently larger penetration lengths compared to lower pressures.

There are also a limited number of studies of the split injections' spray characterisations, atomisation rates and the effects of the flow field generated by first injection at varying dwell times and split ratios. In addition, the behaviour of the injector, in terms of needle opening, is not always consistent between subsequent injections when using a multiple injection strategy [88]. It is hoped that detailed spray characterisations performed inside a spray chamber, can provide comprehensive understanding of the injector and spray characteristics on the charge formation using a split injection strategy.

Finally, majority of the studies focusing on the stratified charge operation using the split injection strategy have typically been carried out using a Piezo-actuated injector. Its fast needle response means the ability of operating with short dwell times and PWs. The precision and repeatability of closely spaced injections however have been stated to be problematic. A limited number of studies have been performed using a Solenoid actuated multi-hole injector, especially when tackling stratified charge operation and employing split injection strategies. These injectors are attractive because of their lower costs, and the capability of operating in the ballistic region. In this case the dwell times and PWs are larger than the tests performed using a Piezo injector. The downside is the difficulty in achieving repeatable and closely spaced injections, which would be ideal for the split injection strategy for low-

speed and part-load operations [26]. As such, it is hoped that performing studies on the injection strategy by using a Solenoid-actuated injector will provide further understanding of the application of the injection strategy using less conventional and more cost-effective injectors.

2.8 Project Aim and Objectives

The current work thus aims to investigate (1) the effects of the split injection strategies on the spray characteristics; and (2) the GDI engine's in-cylinder mixture formation for stratified charge part-load operation. This is done by using a state-of-the-art multi-hole solenoid injector and advanced laser diagnostic techniques.

It should be noted that the thesis consists of the two separate major studies mentioned in the above paragraph which are not interlinked. The studies and many parameters discussed in this Thesis were influenced by the needs of the project's sponsors.

2.8.1 Spray Characteristics of Single and Split Injections

The objectives to study the spray characteristics for a variation of injection strategies are as follows:

- mass measurements of single injections at varying pressures and pulse widths (PWs). The purpose was to understand the effects of pressures and a range of short PWs (ballistics zones) and large PWs on the overall injection quantity.

- mass measurements for the split injections at varying PW combinations, split ratios and dwell times for the injection pressure of 35MPa. This was to understand the effects of varying split injection properties on the injected quantities. This would also provide some indication of the needle behaviour.

- spray characterisations of the single injections at varying pressures and PWs, using high-speed imaging technique. This was to understand the effects of increasing pressures and PWs on the single injections' spray characteristics (penetration length and spray angles).

- spray characterisations of the split injections at varying pressures, PW combinations, split ratios and dwell times via high-speed imaging. This was to understand the effects of the first injections on the extent of radial and axial spread of the global sprays of the second injections.

- atomisation characteristics and droplet velocities of the single and split injections for a variation of PWs, split ratios and dwell times, measured at an injection pressure of 35MPa. The measurements were performed using phase Doppler Anemometry (PDA) inside a constant volume spray chamber. The nearest measurement location to the injector was 11mm downstream and the focus of the study was on a single plume in the spray. This was to understand the effects of varying injection strategies on the spray characteristics. As a result, the droplet sizes, vortex generations and droplet velocities of the single plume were studied.

2.8.2 Effects of the Injection Strategies on the In-cylinder flow and Charge Formation

The next part of the study consisted of in-cylinder flow characterisation of single injections and split injection strategies in an optically accessible GDI engine using cycle-resolved high-speed particle image velocimetry (PIV) at a repetition rate of 10KHz in tumble and omega-tumble planes. This was to understand the effects of the injection strategies (varying injection times, dwell times and split ratios) on the in-cylinder charge formation (entrainment effects, charge velocities, turbulent kinetic energy levels and fuel impingements) at engine part-load conditions using the Solenoid injector at an injection pressure of 35MPa. The study was split into three key areas of interest:

- The first part included investigations of the velocity vectors, TKE contours and maps of standard deviation in velocities for early and late single injections in the intake stroke.

- This was followed by a comparison of the effects of large split ratio (75%:25%) and small split ratio (25%:75%) on the mixture formation. In this case, the two injections events for each test case took place in the intake stroke.

- The third part consisted of evaluating the effects of a first injection in the intake stroke and delayed second injections with sweeps across the compression stroke. In this case, the split ratio of 75%-25% was kept constant.

Chapter 3.   Experimental Techniques and Methodologies

3.1 Spray Characterisation

The methodologies for the spray characterisation measurements are discussed in this section. The methodologies for measurements inside the single-cylinder optical GDI engine will be discussed in the subsequent section.

3.1.1 Injector and Injection Parameters

The injector under investigation was a solenoid actuated, multi-hole DI injector with six holes, capable of injecting at fuel rail pressures of up to 35MPa. The six nozzles were positioned asymmetrically designed for effective fuel distribution inside the cylinder of a production engine, which housed a special piston design.

Single and split injection strategies were investigated. For the single injections, a combination of small and large pulse widths (PWs) were tested (Table 3.1). The small PWs were in the range of 0.3ms to 0.5ms, with 0.05ms increments. The large PWs ranged between 0.5ms and 3ms, with larger increments of 0.5ms.

Figure 3.1 shows the injection events tested with the varying PW combinations and split ratios. The PW of the corresponding single injections (compared against the split injection) was equivalent to the total PW of the two injections. The tested split injection parameters are listed in Table 3.2 The equivalent number of engine crank angles related to the dwell times, at an engine speed of 850rpm (representative of cold-start) and 1200rpm (cruise speeds), are presented in

Table 3.3. Varying injection ratios, PWs and dwell times were investigated for the split injection strategy.

The range of PWs were selected to study the operation of the injector in the ballistic region when employing short PWs and large PWs that would allow the spray to reach a transient steady state period. Additional details of the test parameters when performing the PDA measurements are discussed in 3.1.4.

Table 3.1: injection test parameters and types of fuel used.

Injection pressure range (MPa)	5 to 35 (5MPa increments)
Single injections pulse widths (ms)	0.25, 0.3, 0.35, 0.4, 0.45, 0.5, 0.7, 1, 2 and 3
Frequency (Hz)	10
No. of bursts	1000
No. of repetitions per injection event	10
Type of fuel	• Gasoline RON 95 - used for static mass flow rate measurements and high-speed imaging measurements • N-Heptane - used for PDA measurements
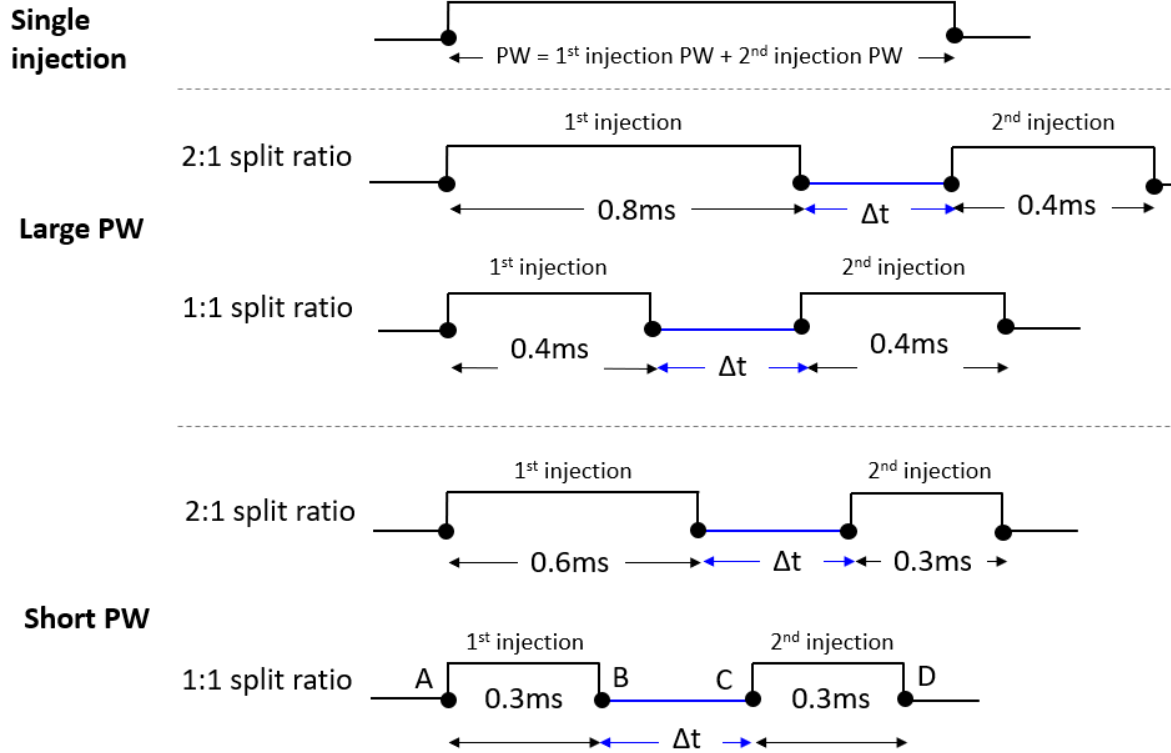
- A: start of 1st injection (SOI1) • B: end of 1st injection (EOI1) • Δt: dwell time

- C: start of 2nd injection (SOI2) • D: end of 2nd injection (EOI2)

Figure 3.1: representation of the single and split injections' parameters.

Table 3.2: main parameters of the split injection cases tested.

First Injection PW (ms)	Second Injection PW (ms)	Injection Ratio 1st:2nd	Dwell Times, Δt (ms)
0.3	0.3	1:1 (low PW)	2, 4, 6, 11, 14
0.6	0.3	2:1 (low PW)	2, 4, 6, 11, 14
0.4	0.4	1:1 (high PW)	2, 4, 6, 11, 14
0.8	0.4	2:1 (high PW)	2, 4, 6, 11, 14

Table 3.3: equivalent crank angles corresponding to the dwell times for engine speeds of 850rpm and 1200rpm attributed to cold-start and part-load conditions, respectively.

Dwell Time (ms)	No of Crank Angles (°) at 850rpm	No of Crank Angles (°) at 1200rpm
2	10.2	14.4
4	20.4	28.8
6	30.6	43.2
11	56.1	79.2
14	71.4	100.8

It is worth noting that the data was primarily used for the validation of the CFD simulations, which were performed by the collaborators. As a result, the measurements cover a wide range of parameters to provide sufficient data for CFD model development and validation.

3.1.2 Mass Measurements

The injected masses for the single and split injection strategies were measured. The injection test parameters are provided in Table 3.2. The injected mass was measured using a precision mass balancer with a resolution of 0.01g. Ten measurements per injection event were obtained and the average injected mass was determined along with the standard deviations. The fuel was injected in a beaker at ambient atmospheric temperature and pressure. The injected fuel was collected in a beaker with a height of 130mm and internal diameter of 75mm.

For validation purposes, the resultant static mass flow rate (Q_{stat}) was compared against supplier's Q_{stat}. Any significant variation in the Q_{stat} would have indicated injector coking.

A National Instruments (NI) DI driver system, NI CRIO 9066 and NI 9751 module, were used to trigger the solenoid injector (as indicated in Figure 3.2). After verification with the supplier, the injector's current-voltage profile was defined in the driver's software. An external delay generator and NI 9411 external trigger module

were used to trigger the 1000 pulses at 10Hz injection frequency. The PWs and dwell times were specified on the external delay generator.

A Hi-Pro P464 diaphragm pump was used to supply rail pressures of up to 35MPa. It operated on the principles of differential area, whereby compressed air (0.6MPa) forced the liquid through a small area. This in turn provided high output pressures. A fuel filter was installed downstream of the pump to prevent impurities from infiltrating into the injector. The fuel used for the experiments was RON95 and the fuel temperature was maintained between 19°C to 25°C, which was monitored using a thermometer installed in the fuel tank.

3.1.3 High-speed Imaging

High-speed imaging with back-light illumination was used to investigate the macroscopic spray characteristics (i.e. penetration lengths and spray angles). In this experiment, the external delay generator was used to trigger the injector and the high-speed camera simultaneously (Figure 3.2). The delay in the output pulse signal from the delay generator was 2μs and the camera's input delay was set to 100ns. The delay between the camera's trigger input and start of exposure time was 0.668μs. Photron FASTCAM Viewer (PFV) software was used to acquire and process the images.

The measurements were performed inside a glass tank under atmospheric conditions. The injector was mounted vertically on top of the glass tank in central position. The internal length, width and height of the glass tank were 380mm, 240mm and 255mm, respectively. The details of the high-speed imaging setup and parameters are provided in Table 3.4. The PWs and pressures tested for the split injections are presented in Table 3.1 and Table 3.2.
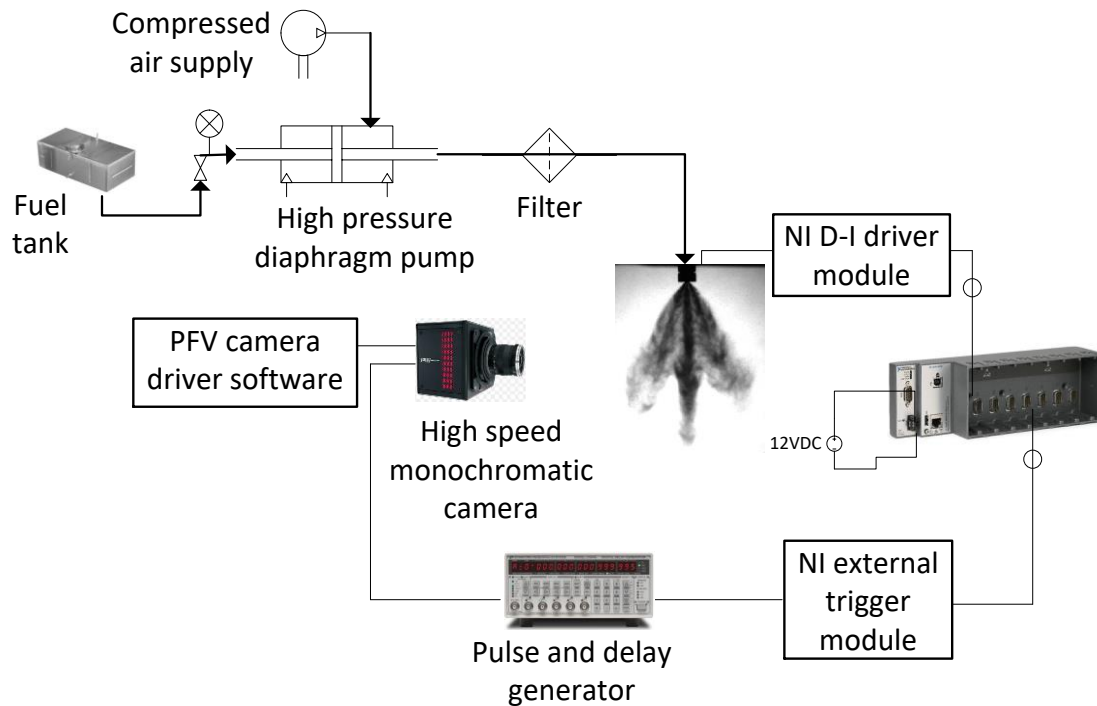
Figure 3.2: fuel supply and high-speed imaging setup.

Table 3.4: high-speed imaging test setup and parameters.

Camera body	FASTCAM Mini AX100
Lens type	NIKKOR 105mm
Backlight illumination	GSVITEC multi-LED
Aperture	f/4
Frame rate (KHz)	20
Resolution (pixel)	384 x 384
Magnification factor (pixels/mm)	4
Shutter speed (s)	1/950000

The first stage was to determine the magnification factor of the setup (convert the number of pixels in metric units). In order to obtain this, a calibration tab with markers of known distance in metric units was placed directly underneath the injector tip. The vertical orientation was confirmed using a spirit level. The back-light illumination, imaging settings and the camera's position remained fixed throughout

the experiments. The image was then imported into MATLAB to determine the magnification factor.

Ten high-speed images per injection event were acquired. These were post-processed using MATLAB image processing toolkit to obtain the average penetration lengths and average GDI spray angle for the varying injection events and fuel rail pressures. The post-processing for the measurements of the main tip penetrations and the GDI spray angles were conducted in accordance to the JSAE 2715 recommended practice [126]. A representation of this is provided in Figure 3.3.

GDi Spray angle $= \theta_R + \theta_L$
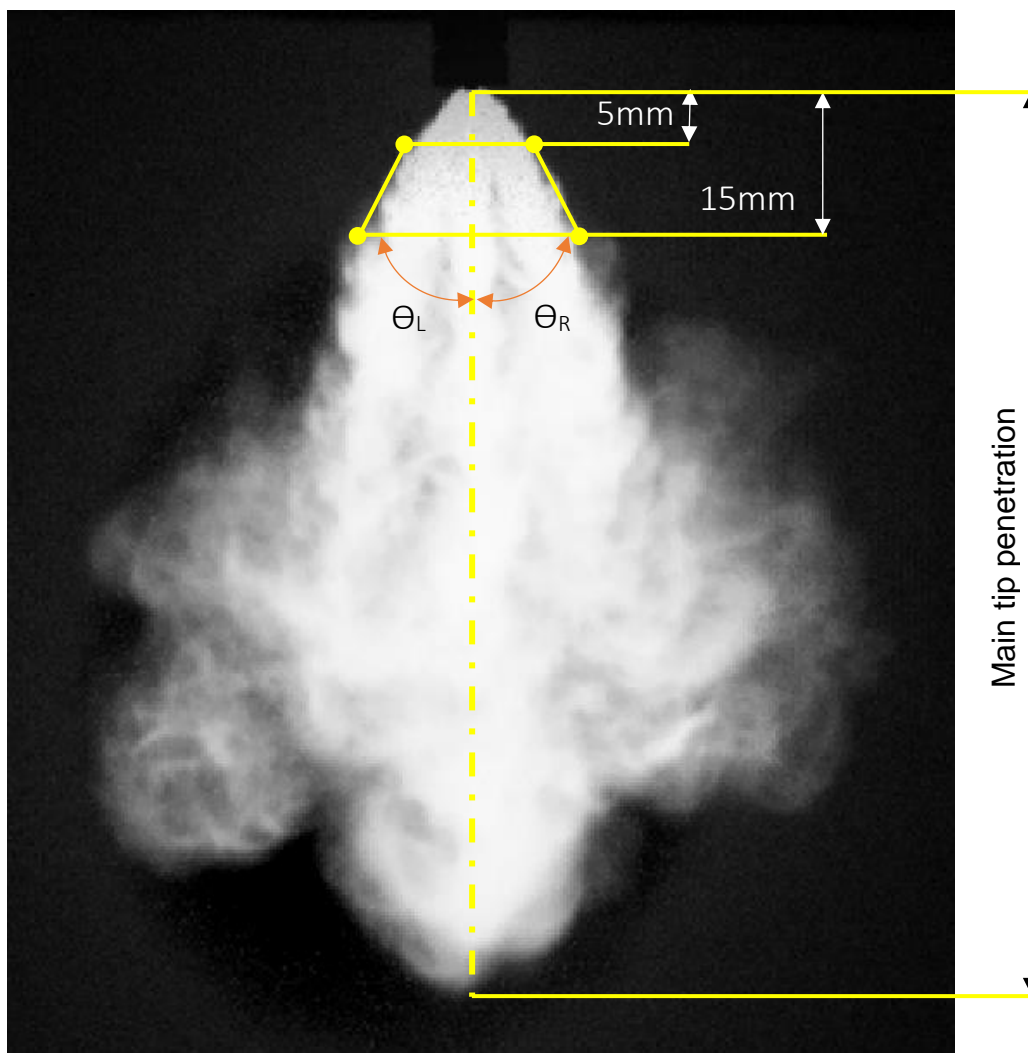
Figure 3.3: recommended standards for main tip penetration and GDI spray angle measurements [126].

The image processing steps to acquire the spray characteristics are as follows (also represented in Figure 3.4):

a) The original image was subtracted from the background image.

b) The light intensity was increased to ensure that all the details of the spray were detected. This was to enable the detection of the vapour formed mainly around the spray's edges which was less intense.

c) The image was binarised, with the small objects of set pixels sizes (which would be in the form of atomised droplets independent of the main spray, surrounding the main spray structure) removed.

d) The holes in the main spray plume were filled.

e) The maximum penetration length and GDI spray angles were measured and converted to metric units.
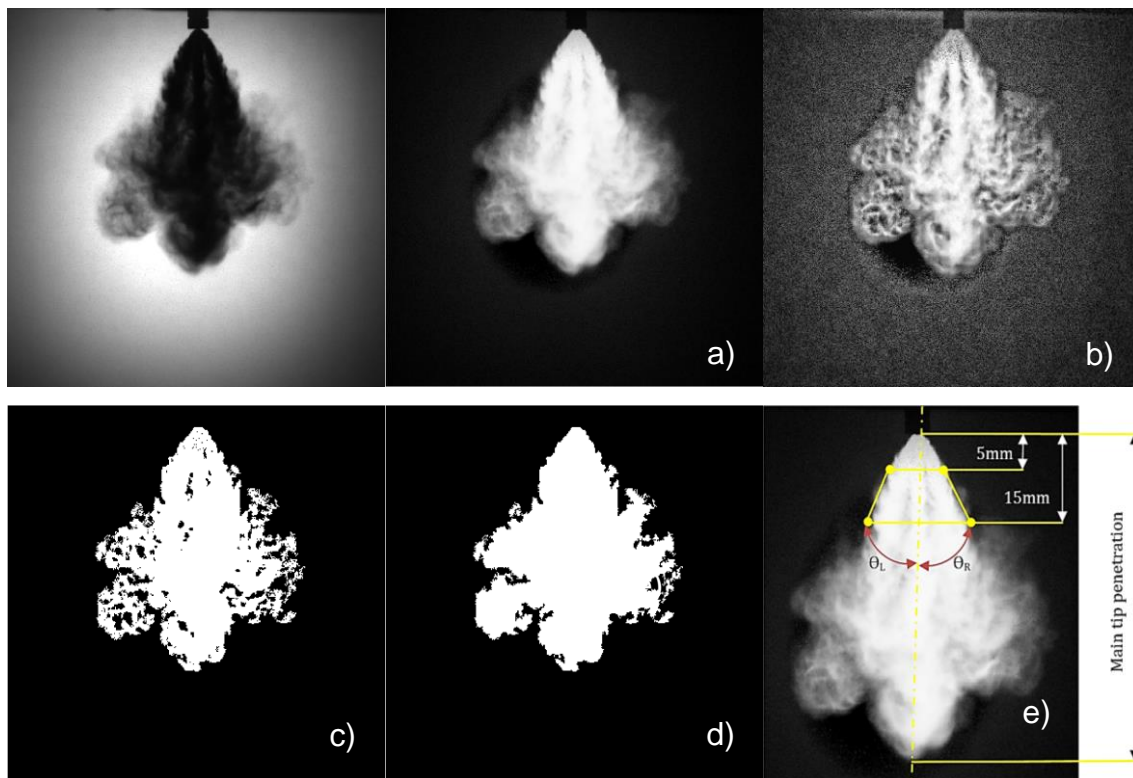
Figure 3.4: stages of image processing to obtain sprays' characteristics.

For the split injection events, to determine the penetration lengths and spray angles of the second injections, the image of the fully developed plume at the end of the second injection was subtracted from the image obtained one frame before the start

of the second injection (flow field before the SOI2). This enabled the measurement of the second plume solely, without the remnants of the first injection present in the flow field.

3.1.4 Phase Doppler Anemometry

3.1.4.1 Principles of Phase Doppler Anemometry

Phase Doppler anemometry (PDA) is a non-intrusive point-based laser diagnostic technique which is used to measure nearly spherical and spherical droplets sizes and their velocities in a constant volume chamber. Its response to the test fluid's velocity is linear as the measurement is based on the stability and linearity of the optical electromagnetic waves which are unaffected by temperature and pressure. The technique thus requires little to no calibration. Additional advantages of the system are well defined directional response, and high spatial and temporal resolutions, as the measurement volume can be very small. This, in combination with fast signal processing electronics, permits high bandwidth time resolved measurements of fluctuating velocities which provides good temporal resolution [127].

Laser Doppler anemometry (LDA) is based on the linear relationship between the Doppler shift and the particle velocity. A Doppler shift occurs when a particle of a fluid is illuminated by a laser beam of frequency f, and the particle in turn scatters the light at a frequency f_1, which is different from the frequency of the incident beam. The relationship is:

$$f_1 = f \left(1 - \frac{u.n_1}{|c|}\right)$$
<div align="right">Equation 3.1</div>
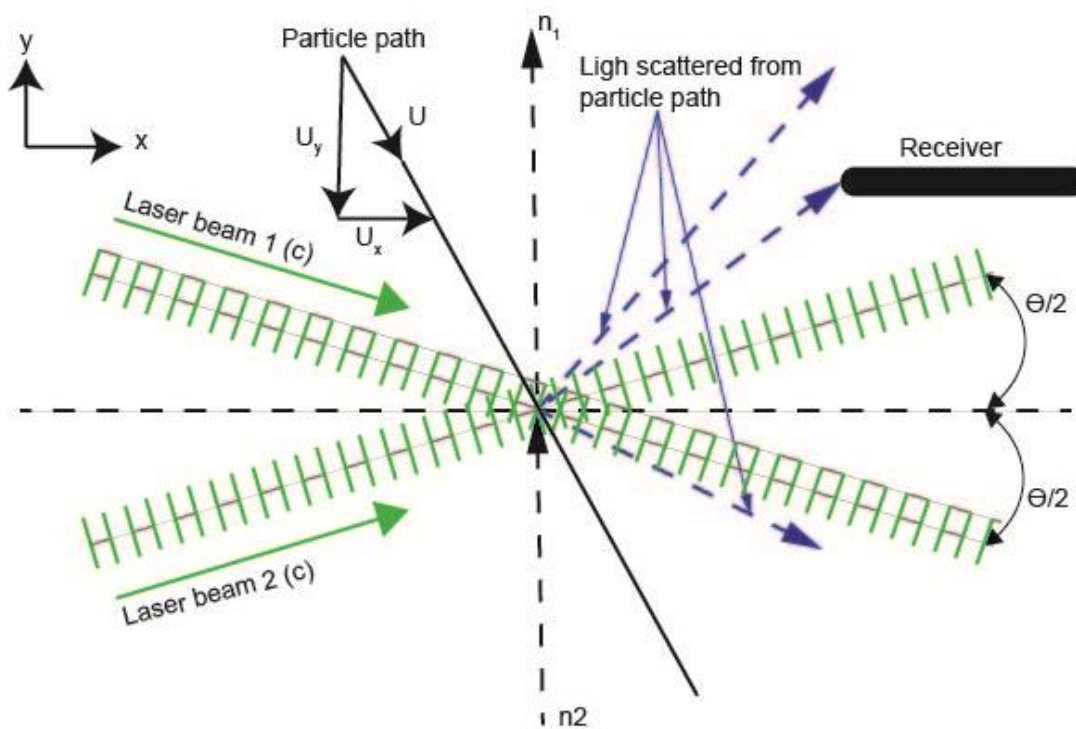
Figure 3.5: principles of PDA.

When two laser beams are focused towards a point as shown in Figure 3.5, the incident light from both the beams is scattered in all directions but is Doppler shifted by equal and opposite amounts (differential Doppler mode).

The light scattered by the second beam has a frequency of f_2:

$$f_2 = f\left(1 + \frac{u.n_1}{|c|}\right)$$
<div align="right">Equation 3.2</div>

Thus, the Doppler frequency, f_b is a function of f_1 and f_2.

$$f_b = f\left(\frac{u.(n_2 - n_1)}{|c|}\right) = f\frac{u_x}{|c|}2\sin\left(\frac{\theta}{2}\right) = 2\frac{u_x}{\lambda}\sin\left(\frac{\theta}{2}\right) = \frac{f_2 - f_1}{2}$$
<div align="right">Equation 3.3</div>

For ease of understanding the process at the intersection of the laser beams in LDA, a fringe model is typically used. A set of stationary dark fringes are produced when the beams intersect, as shown in Figure 3.6. When a particle passes the beam intersection region, also known as a probe volume, the particle is illuminated when it passes through these dark fringes. The intensity of the illumination in turn varies with a frequency that is proportional to the component of the particle velocity.

Figure 3.6: representation of the fringes in the control volume.

The distance between the interference bands or fringes, δ_1 can be obtained using equation below:

$$\delta_1 = \frac{\lambda}{2\sin\left(\frac{\theta}{2}\right)}$$ Equation 3.4

The intensity of illumination, f_i, is the same as f_b. So velocity, v_f can be calculated using the following equation:

$$v_f = \delta_1 f_i = \frac{\lambda}{2\sin\left(\frac{\theta}{2}\right)} f_i = C f_i$$ Equation 3.5

Where C is the calibration factor:

$$C = \frac{\lambda}{2\sin\left(\frac{\theta}{2}\right)}$$ Equation 3.6

Directional ambiguity exists in the measured particles' velocities as the modulated wave is independent of direction in which the particle is travelling. This is resolved by applying a suitable signal bias, which can be achieved by changing the frequency of one of the two laser beams to f_o. This results in a velocity shift:

$$\Delta v = C f_0$$ Equation 3.7

This frequency shift is introduced by a 40MHz Bragg cell in the system. The Bragg cell, which with the current equipment also acts as a beam splitter, splits one laser beam into two and generates a frequency shift in one of the laser beams.

3.1.4.2 Setup of the Constant Volume Spray Chamber

A constant volume spray chamber was designed and manufactured to perform spray characterisation, as well as droplet sizing by laser Phase Doppler Anemometry (PDA). The primary design requirements were (1) sufficient optical access to conduct the PDA measurements and (2) good structural integrity of the chamber. The refractive index of the laser transmitted through the glass and the dominant scattering mode for detection were key phenomena that dictated the design of the optical access in the spray chamber. Table 3.5 provides an overview of the target design requirements and specifications.

Table 3.5: design requirements and specifications for the spray chamber.

Design Requirements	Requirements' Analysis	Requirements' Verification
Operating pressure of 0.1MPa, design pressure of 1MPa. Operating and design temperature of 293.15K.	Design pressure of 1MPa was chosen as it simulates engine in-cylinder pressure. The design thickness of the spray chamber was required to thus withstand the design pressure without causing deflection or cracks. The design pressure and a factor of safety were included when calculating the material thickness.	Thickness calculations done in accordance to PD5500:2015 [128]. A factor of safety of 1.5 was used.
Suitable optical access for PDA measurements	The chamber's internal diameter had to be sufficiently large to avoid spray impingement, which would have affected the accuracy of the data. It was also required to be small enough for the spray and the corresponding droplets to be within the range of the focal lens. A minimum of two wide optical access points had to be installed to enable PDA measurements with side-scatter configuration. Detection of the first order refraction (scattering angles in the range of 30°-70° with respect to the laser path) was prioritised when designing the windows' configuration.	The range covered by the smallest focal lens available, which was ⌀310mm, were considered during the design calculation. Design calculations for the size of the windows and spacing between them accounted for the laser's refraction through the windows and the scattering angles for the dominant first order scattering mode.

Installation of the fused quartz windows on the spray chamber	The glass thickness was required to withstand the design pressure without forming cracks or leakage. The main body's design was to accommodate for a sealing gasket between the glass and the main body to avoid contact between the glass and the steel. This would reduce the likelihood of leakage, scratches, or damages which could have been caused by pressure differences or corrosion. The windows were to be removed with ease for regular cleaning. They were bolted to the spray chamber using stainless steel M6 bolts.	Thickness calculations had to be done in accordance to PD5500:2015. Factor of safety of 1.5 to be used. Klingerseal C-5400 (synthetic fibre and Neoprene binder) was used as a sealing gasket, placed between the glass and metal. The gasket thickness was 1.5mm, with a tolerance of +0.1mm.
High durability	The material had to be corrosion resistant to enable long-term use.	Spray chamber material: stainless steel grade 304, which is corrosion resistant and prevents carbide precipitation in the high temperature areas affected during welding.
Installation of the injector	A bespoke injector rail was designed to mount the injector and the fuel supply system on the spray chamber. The injector was centrally mounted to avoid impingement. Any potential leakage was to be prevented in the design.	
Purging system	Necessity to install a purging system to ensure that remnants of the THC from the previous tested injection was	

	removed from the spray chamber. This would prevent the droplets from the previous tested case affecting the spray of the subsequent injection event. The spray chamber was purged using compressed Nitrogen gas at 0.2MPa in order to reduce the likelihood of potential ignition of the accumulated THC within the spray chamber. The purging was introduced at the inlet at the top of the spray chamber and exited through an exhaust installed downstream of the spray chamber. The base of the spray chamber had to be bolted to its main body, to allow for ease of removal for cleaning any settled liquid fuel film.	
THC treatment	Active carbon filter was required to be installed downstream of the spray chamber so that the THC could be treated prior to the gases being exhausted into the atmosphere.	The activated carbon filter was installed with a THC concentration sensor for monitoring purposes. Care was taken not to exceed the manufacturer's stated life span of the filter during operation.
Leak free	The spray chamber was to be leak free. Leakage would have not only affected the results, but the fumes from THC could have been harmful. Measures taken included: 1) reduced number of joints in the spray chamber and 2) robust welds, using correct welding material and filler wires.	Welding was carried out by a certified welder at the appropriate standards.

3.1.4.2.1 Design Calculations of the Constant Volume Spray Chamber

The chamber's inner diameter was designed to be 288mm and the inner height 300mm. This provided sufficient in-cylinder volume to conduct sprays' characterisation at a range of injection pressures.

The thickness of the optical windows dictated the thickness of the spray chamber's main body. They were made of fused quartz glass. The diameter was initially set to 170mm, which would provide the flexibility to conduct PDA measurements at various points in the flow field, both in the radial and axial directions.

The minimum thickness of the window was calculated using equation below:

$$t = \sqrt{\frac{-6M}{\sigma_{UTS}}}$$
Equation 3.8

where t is the minimum required thickness, M is the maximum moment at the edge of the windows and σ_{UTS} is the ultimate tensile strength of the fused quartz glass, which is 48.3 MPa.

The maximum moment occurring at the edge of the windows is calculated using equation below:

$$Maximum\ moment = \frac{-\Delta P r^2}{8}$$
Equation 3.9

ΔP is the pressure difference encountered by the window and r is the radius of the window. The calculated and final dimensions are provided in Table 3.6.

Table 3.6: design dimensions of fused quartz glass.

Maximum moment (Nm)	-631.881
t (mm)	8.860
t with a factor of safety of 1.5 (mm)	13.290
Final design thickness (mm)	15

The refraction angle, θ_r, of the laser fired through the window was calculated using Snell's Law (equation below):

$$Sin(\theta_r) = \frac{Sin(\theta_i) \times n_i}{n_r}$$
Equation 3.10

$Θ_i$ is the incident angle of the laser, n_i is the refractive index of air which is 1, and n_r is the refractive index of the quartz glass which is 1.46. This was used to confirm that the laser's refraction distance did not exceed the window's design diameter of 170mm. If the PDA transmitter was to be positioned at an incident angle of 45° with respect to the glass, the refraction angle of the laser through the quartz glass is calculated to be 28.97°. If the transmitter was to be positioned perpendicular to the glass instead, the refraction angle of the laser is 43.23°. The larger the angle of incidence, the greater the resultant refraction angle. The width of the deflection of the laser through a 15mm thick quartz glass, would thus be in the range of 7.2mm to 12.2mm, for the angle of incidence ranging between 45° and 90°, which is well within the window's diameter.

For the range of the dominant scattering angle of 30°-70° planned to be detected, the minimum window diameter was calculated to be 95mm, which is much less than the designed diameter. These figures suggest that the window diameter and thickness of 170mm and 15mm respectively, and the windows spaced 120° apart, would allow sufficient flexibility to conduct the PDA measurements in the constant volume spray chamber. A representation of the setup is provided in Figure 3.7.
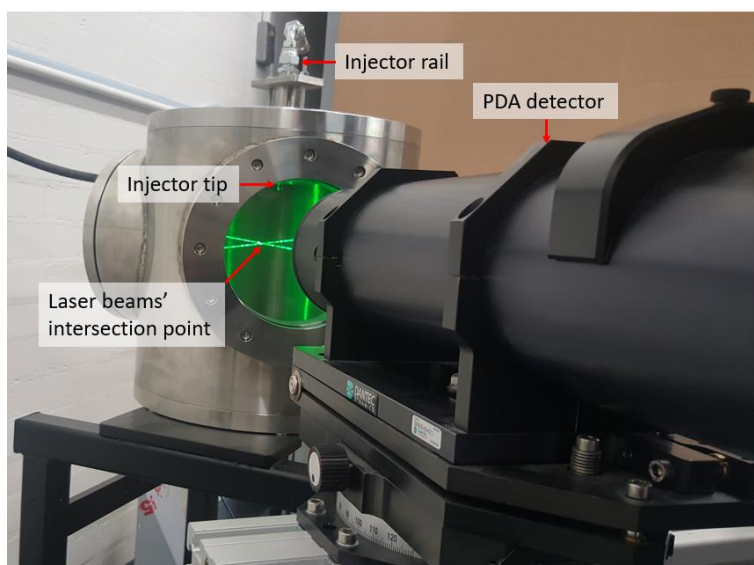
Figure 3.7: photograph of the PDA system setup on the constant volume chamber. The intersection point of the two laser beams is the control volume. The beams are introduced through the window places 120° apart from the window in view of the current picture. The injector tip is centrally mounted and is visible at the top of the window as indicated. The PDA detector is positioned 71° with respect to the path of the laser.

3.1.4.2.1.1 Spray Chamber's Main Body, Lid and Base

The dimensions of the spray chamber's main body, albeit dictated by the optical window's thickness, were also calculated using PD5500:2015 [128] for confirmation. The spray chamber was modelled as a pressure vessel. The thickness of the spray chamber's main body was therefore also dictated by the design pressure.

The minimum required thickness of the walls of the spray chamber was calculated using equation below:

$$t = \frac{Pd}{2\sigma - d}$$
Equation 3.11

where t is the minimum wall thickness, P is the design pressure, d is the outer diameter of the chamber and σ represents the design stress of 304 stainless steel at room temperature, which is 241MPa.

The design thickness of the spray chamber walls was thus calculated to be 1.19mm, which included a factor of safety of 2.

The thickness of the walls calculated above does not account for the holes accommodating for the windows, the dents on the main body to seat the sealing gasket and the load of the bolts. The thickness was thus calculated using equation below:

$$e = \sqrt{\frac{0.3G^2p}{S_{FO}} + \frac{1.909W_{m1}h_G}{GS_{FO}}}$$
Equation 3.12

Where e is the required thickness, G is the mean diameter of the gasket contact face, which is 160mm for a 10mm width by 1.5mm thick gasket wrapped around the window holes, p is the design pressure which is 1MPa in this case, S_{FO} is the design stress of 304 stainless steel at ambient temperature which is 241MPa, W_{m1} is the minimum required bolt load and h_G is the radial distance from the gasket load reaction to the bolt circle.

The minimum required bolt load (W_{m1}) and the radial distance (H_G) from the gasket load reaction to the bolt's hole were calculated using the following equations.

$$W_{m1} = H_G + H$$
Equation 3.13

$$H_G = 2b\pi Gmp$$
Equation 3.14

'b' represents the basic gasket seating width, which is half of the contact width of the gasket (5mm), and m is the gasket factor, which, according to BS PD5500:2015 is 2.5 for Klingerseal gasket. These calculations were done with reference to [128].

The design thickness of the spray chamber walls was therefore 20mm. This thickness ensured support of the optical windows of 15mm thickness.

The lid and base of the spray chamber were designed to house M6 tapped bolts in the circumference of the spray chamber, as well as an extrude to house the sealing gasket whose diameter was 3.5mm. Their thicknesses were therefore also 20mm.

3.1.4.2.1.2 Window Flange

The thickness of the flange for the windows was calculated using the same principles, using Equation 3.13 and Equation 3.14. The material of the flange was 304 stainless steel. The minimum required thickness of the flange was calculated to be 14.25 mm, taking a factor of safety of 1.5 into account. The final thickness of the flange was thus 15mm. They were welded to the chamber's main body. Four windows were installed: three on the main body placed 120° apart, and one at the base. This would provide the flexibility to conduct high-speed imaging at various planes. The window frame provided support for the windows and the sealing gaskets.

The CAD modelling, assembly and technical drawings were made to manufacturing standards using Siemens NX10. Figure 3.8 is a completed assembly of the designed spray chamber.
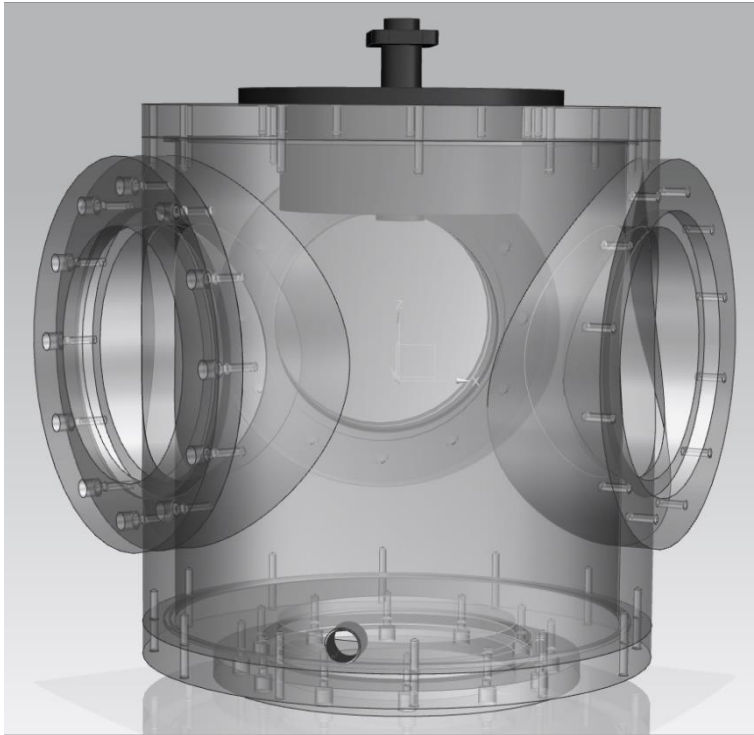
Figure 3.8: completed assembly of the constant volume spray chamber.

One of the main concerns with the system was the trapping of spent fuel (THC) upon each injection cycle. The optimum solution was to purge the chamber with compressed Nitrogen and install activated carbon filter to trap the harmful substances downstream of the chamber.

Figure 3.9 provides a schematic of the constant volume spray chamber system setup. After each injection cycle, compressed Nitrogen was used to purge the spray chamber unit. The accumulated fuel film was purged through and treated using active carbon granules before being exhausted into the atmosphere.
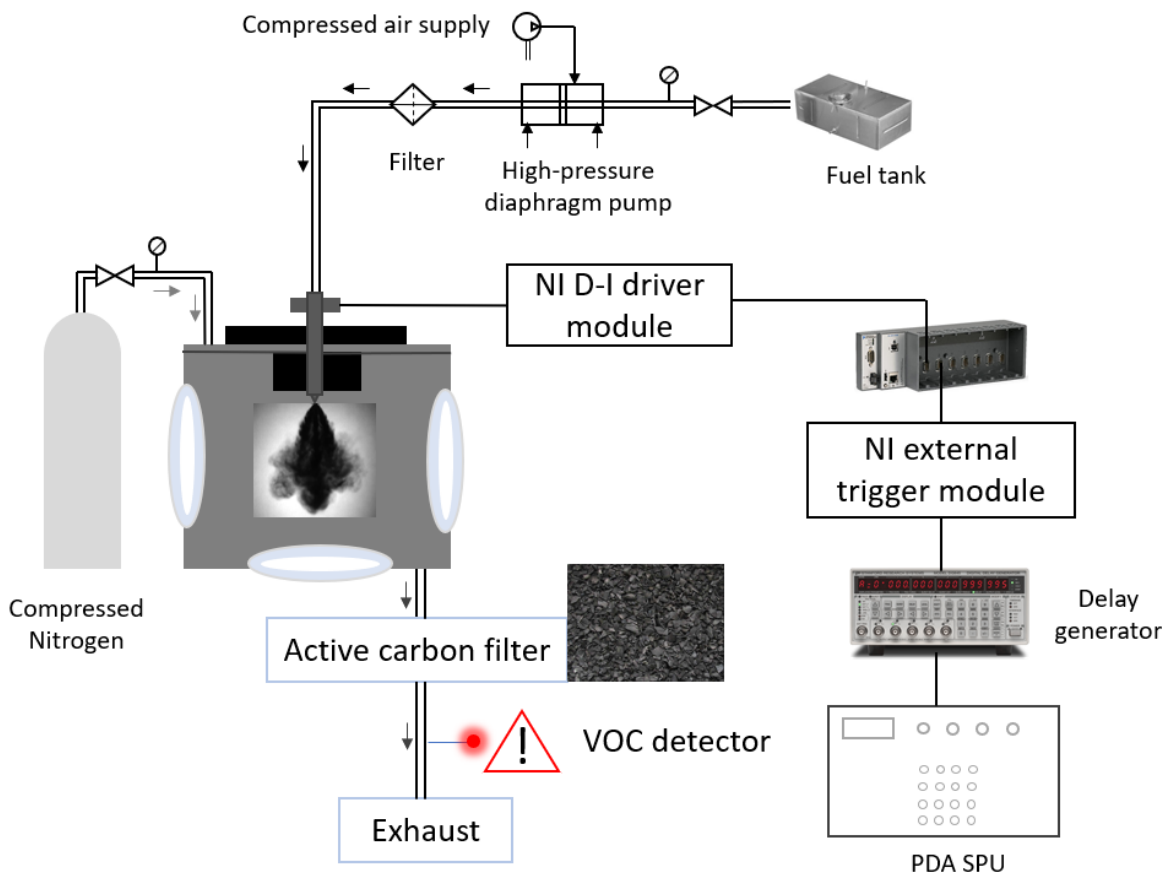
Figure 3.9: schematic of the setup used for spray characterisations. The injector is centrally mounted.

3.1.4.3 PDA System Setup

Figure 3.10 represents the setup of the PDA measurements carried out in the constant volume spray chamber under ambient pressure and temperature conditions of 1.05bar and 22°C, respectively. 112mm FiberFlow PDA system with 60mm probe diameter **(1)**, by Dantec Dynamics, was used to conduct the experiments for spray characterisation of the high-pressure injector. The Argon-ion diode-pumped solid-state (DPSS) laser emitted a 532nm wavelength, with 2.2mm beam diameter. Its maximum power output capability was 1W.
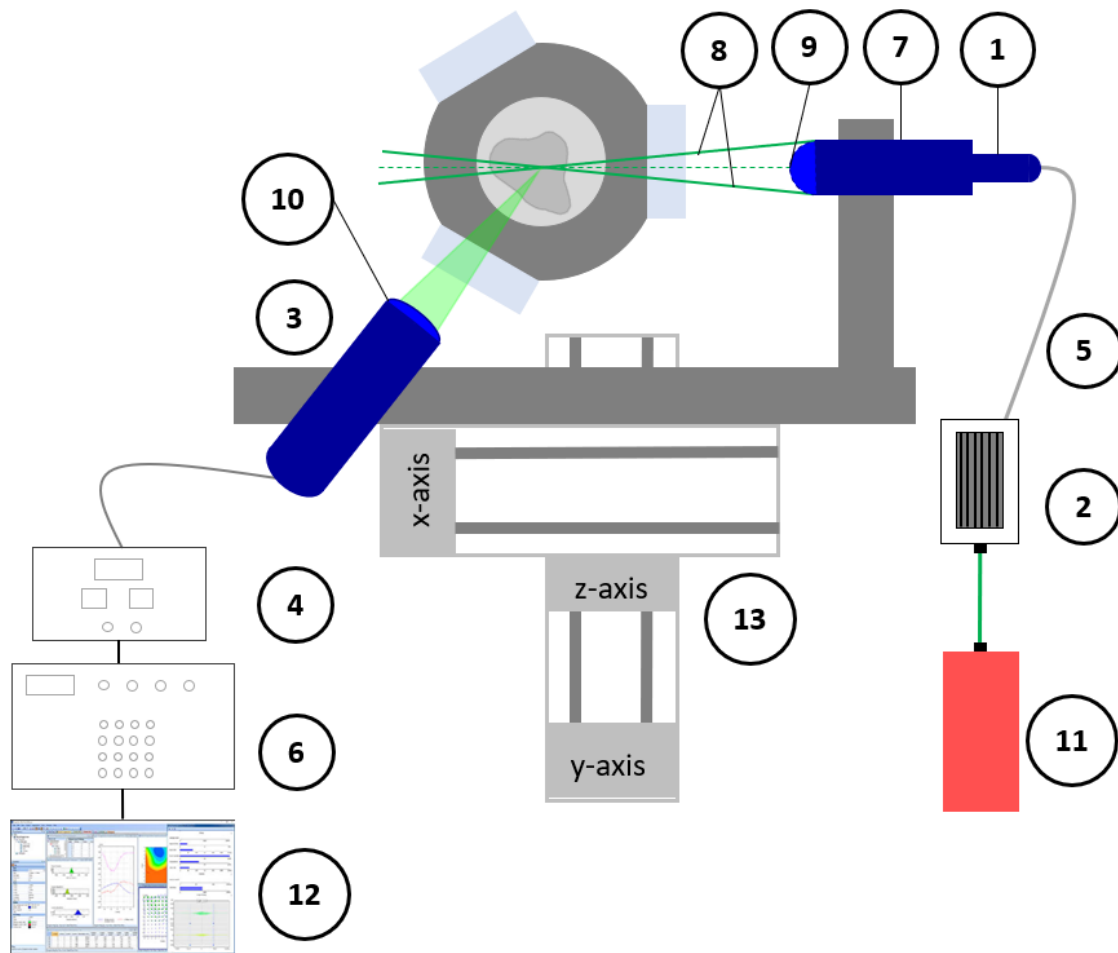
Figure 3.10: schematic of the PDA setup.

The laser beam was transmitted from the laser head to the transmitter using fibre-optic cables **(5)**. A 40MHz Bragg cell **(2)** was used to split the laser beam into two and produce a variable frequency shift. This enabled the direction of the droplets to be resolved by the detector.

Light scattered from the fuel droplets was detected by the receiver optics **(3)**. The receiving signal was transferred to the photo detector and its photo multipliers **(4)** by the fibre optic cables, which subsequently transferred the electrical signal to the signal processing unit (SPU) **(6)**. The SPU had the capability of analysing the signal and produced particle velocity and size data.

A beam expander **(7)** was used to increase the diameter of both the beams exiting the transmitter as well as to increase the spacing between both the beams, as the aperture is larger with the use of a beam expander. The result is a larger intersection angle between the two beams **(8)** and thus a smaller probe volume. The beam

expander therefore improved the signal-to-noise ratio (SNR) at the given measuring distance. The beam expander ratio was 1.98.

Due to somewhat restricted optical access close to the injector nozzle, the transmitter focal length, F, used was 500mm **(9)**. This meant that the intersection volume was 500mm away from the transmitter and the beam expander assembly. This provided the capability of having a smaller intersection angle, in comparison to the 310mm focal lens, so that the intersection volume could be positioned as close to the nozzle exit as possible. The drawback with having the intersection volume further from the transmitter was that the power output of the laser beams at the point where the two beams intersected was reduced, due to the Gaussian intensity profile, along with the number of fringes in the intersection volume.

The light intensity distribution within the probe volume was of Gaussian distribution. The probe volume was an ellipsoid which is widely assumed to be bordered by $1/e^2$ surface intensity. The dimension of the probe volume was determined using the following equations.

$$\delta x = \frac{4F\lambda}{\pi E D_L \cos\left(\frac{\theta}{2}\right)}$$
Equation 3.15

$$\delta y = \frac{4F\lambda}{\pi E D_L}$$
Equation 3.16

$$\delta z = \frac{4F\lambda}{\pi E D_L \sin\left(\frac{\theta}{2}\right)}$$
Equation 3.17

Where F is the focal lens used which was 500mm, E is the beam expansion ratio of 1.98 and D_L is the beam diameter prior to expansion and is equivalent to 2.2mm. The probe volume produced by the current setting was thus δx=8μm, δy=77.8μm and δz=1.036mm.

The fringe separation, δ_f and the number of fringes, N_f, can be determined using the following equations:

$$\delta f = \frac{\lambda}{2\sin\left(\frac{\theta}{2}\right)}$$
Equation 3.18

$$Nf = \frac{4F\lambda}{\pi E D_L \sin\left(\frac{\theta}{2}\right)}$$
Equation 3.19

The fringe spacing was thus 3.545µm and there were 21 fringes within the probe volume with the current setting. This meant that the droplets would pass through sufficient number of fringes, validating the Doppler signal received.

The receiver's focal length was 310mm so the distance between the receiver and the intersection volume was 310mm **(10)**. An aperture plate was placed behind the focal lens and was used to divide the scattered parallel light beam detected into three segments, corresponding to three photomultipliers. As a result, the maximum detected droplets size was 80µm. 0.1mm spatial filter further allowed only small droplets sizes to be detected.

The PDA system was of side scatter configuration so that the unwanted light reflected from the wall directly towards the receiver optics would be minimised. This is recommended as the SNR and spatial resolution are improved compared to back-scatter mode. The receiver was positioned 71° with respect to the laser's path in order to capture the dominant first order refraction mode from the fuel droplets according to the Brewster's scatter angle. The detected signal was transferred to the SPU.

The laser power used was 500mW, which was adjustable from the power supply unit **(11)**. BSA flow software was used for signal processing, data acquisition and post-processing **(12)**. The software fulfilled a variety of functions: the in-built oscilloscope enabled monitoring the Doppler bursts (after filtering out the Doppler pedestal) to optimise the flow detection settings (these included the photomultiplier's signal and gain, SNR settings, centre velocity setting and velocity span settings at varying injection conditions), synchronisation of the data acquisition to the injector and TTL signal generator, data acquisition, and data post-processing.

A 3-dimensional traverse system **(13)** was used to make precision movements of the intersection volume within the flow field. The traverse was also driven by the BSA Flow Processing software. The traverse could be moved in millimetre precision.

N-Heptane was used to perform the PDA experiments, which was maintained between 19°C and 25°C. This is because the liquid property (e.g. the refractive index) is consistent globally at varying ambient conditions, as opposed to gasoline. This was also advised in the JSAE 2715 standards paper [126]. It is worth noting however, that the spray characterisations, when using n-heptane and gasoline fuels,

would differ to an extent. The boiling point of n-heptane for instance is 98°C while that for gasoline RON 95 is up to 210°C. For this reason, differences in the spray characteristics when using the different fuels is expected.

For the data acquisition, either 10,000 droplet samples were acquired or maximum acquisition timeout (AT) of 100s was reached for each test position, whichever occurred first. This provided sufficient validated data samples and the requirements are also often applied by numerous PDA studies. 500 pulses per burst at an injection frequency of 5Hz were tested for each injection event. The start of data acquisition was synchronised with the start of the injection using a TTL signal generator.

The quality of the setup, laser alignments and data accuracy of the measurements were confirmed by observing the quality of the signal, phase plot and sphericity of the measured droplets in the software. The quality of the signal was observed via the in-built oscilloscope in the software. Clear display of the Doppler bursts confirmed that the droplets were passing through the probe volume and that the laser and detectors were well aligned. Another feature that confirmed proper optical alignment was the phase plot. It detected and displayed the number of droplets passing through the probe volume.

The acceptable sphericity of the droplets was 98% and above. Some sources of uncertainties were still present in the measurement. 100s of data acquisition meant that towards the end of the injection cycle, the chamber progressively became highly fuel dense, which affected the detection of the droplets. This was observed to be the case in the latter half of the measurements for all tested cases. As a result, data past 50s were rejected. In addition, the test points in the flow field that detected less than 100 droplets in the 50s of acquisition time (AT) were rejected.

The axes and points of measurements in the flow field are indicated in Figure 3.11. The focus of the study was to characterise the droplets in the core of the rear plume. The measurements were therefore performed along the axis of the rear plume, as indicated in Figure 3.11b. The elevations (z-coordinates) tested were 11mm (also referred to as near-nozzle region), 15mm and 20mm for the 0.4ms PW. The elevations measured with larger PWs also included 30mm and 40mm downstream of the injector tip.

The uncertainties in velocities presented in the results are the standard deviations of the measured droplet velocities. The uncertainty in SMDs were calculated using the ratio between the CoV of $D_i{}^3$ and $D_i{}^2$ as defined below:

$$\text{SMD uncertainties} = \frac{\left(S_D(D_i{}^3)/\ \overline{D_i^3}\right)}{\left(S_D(D_i{}^2)/\ \overline{D_i^2}\right)}$$

Equation 3.20

S_D in this case is the standard deviation and D_i is the measured droplet size. The SMD uncertainty calculation has no unit.

a.

b.
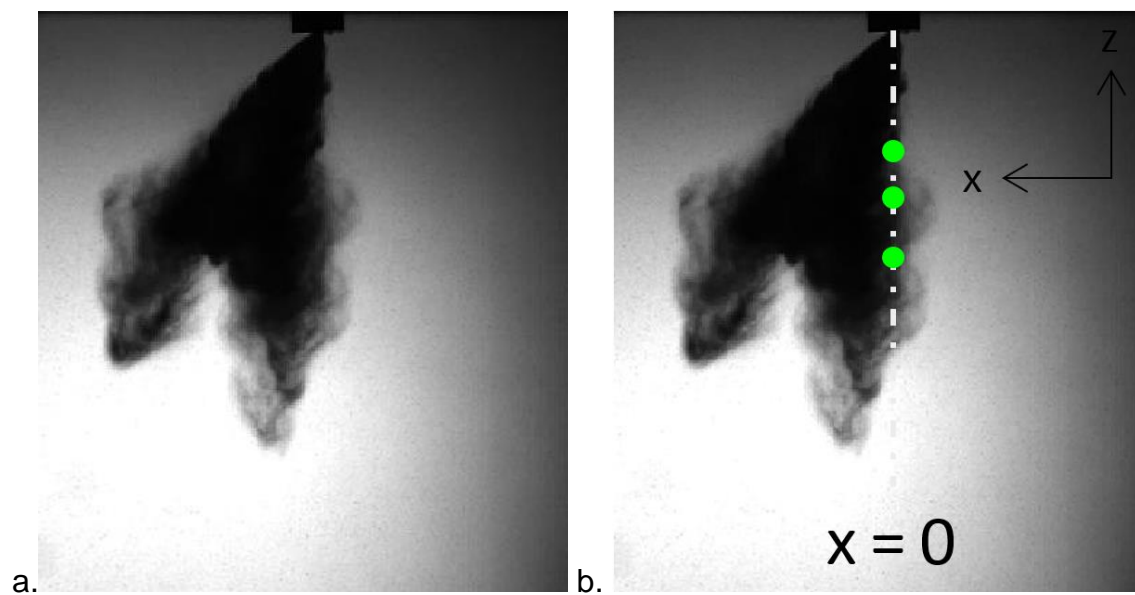
Figure 3.11: representation of the measurement points in the flow field for the 0.4ms PW. Image a. is the spray captured using back-light imaging at the end of injection for the 0.4ms PW and 35MPa injection pressure. Image b. represents the control volumes (green dots) positioned in the core of the rear plume for elevations of 11mm, 15mm and 20mm downstream of the injector.

3.2 Measurements in a Single Cylinder GDI Engine

3.2.1 Single Cylinder Optical GDI Engine

A single-cylinder GDI research engine with optical accesses was used for the in-cylinder flow investigations. The engine was a naturally aspirated, spark-ignition engine with a full stroke optical transparent liner made of quartz glass. The high-pressure multi-hole injector was side mounted at an angle inclination of 25°.

The combustion system was a four-valve pent-roof GDI engine operating on four strokes. A flat panoramic optical piston was used for the measurements.

Table 3.7: key engine specifications.

Cylinder bore (mm)	82
Stroke (mm)	86
Swept volume (ccm)	454
Maximum speed capability (rpm)	3000
Speeds tested (rpm)	1200
Compression ratio	10.5
Spark plug orientation	72°

The valves' opening and closing times are represented in Figure 3.12. The inlet valves opened at -10°CA aTDC so towards the end of the exhaust stroke. They fully opened halfway into the intake stroke. The exhaust valves on the other hand opened at -240°CA bTDC so in the power stroke.
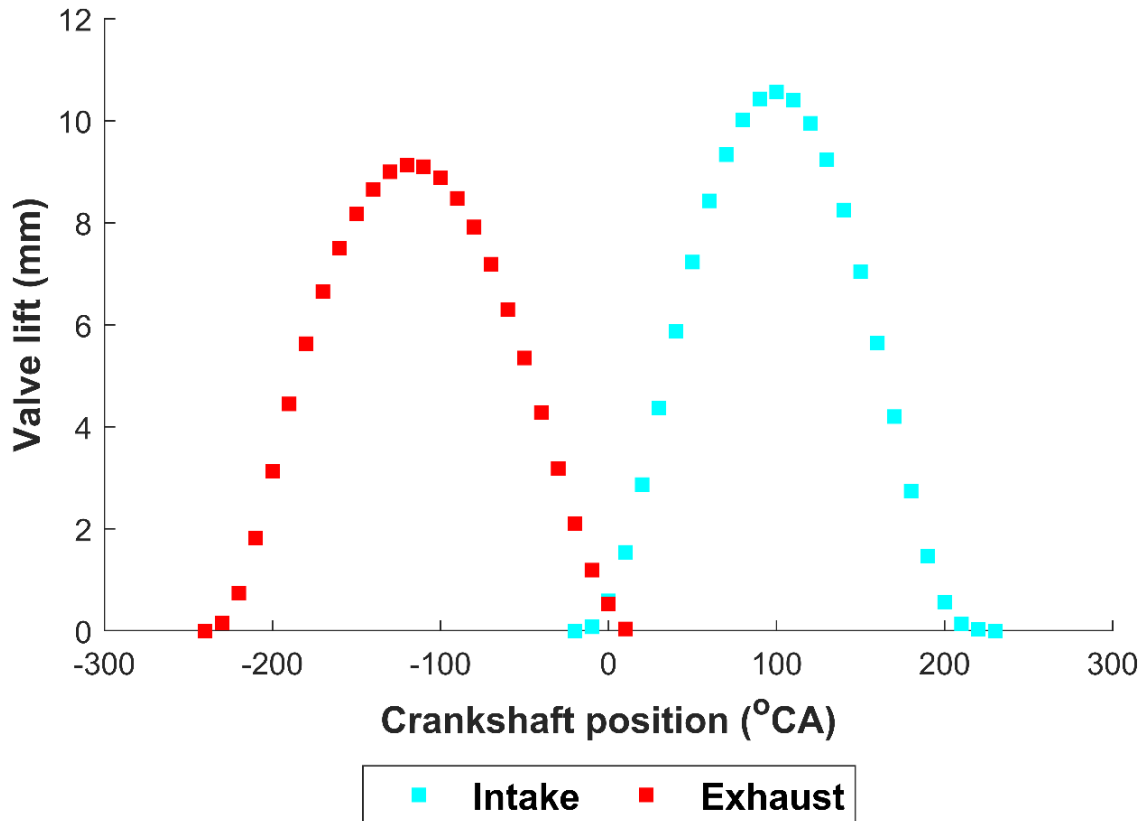
Figure 3.12: Intake and exhaust valves' lift timings based on engine's crank angle positions.

3.2.1.1 Dynamometer

A McClure DC motor was used to drive the single-cylinder engine. Its specifications are presented in Table 3.8. It was mounted on trunnion bearings supported by pedestals. An electrically driven fan provided ventilation to the dynamometer.

It was operated by a KTK thyristor converter unit so that it could act as a DC motor to drive the engine during starting and motoring operations, or as a DC generator when loading the engine. A tachogenerator was mounted on its shaft and provided speed signal to the closed-loop speed control system. This way the speed selected at the controller was maintained by automatic adjustments to motoring or loading torque of the engine.

A separate (in-house built) dynamometer controller was used to set the engine speed and monitor the torque and current. It also housed start/stop switches for the water pump, water heater, oil pump and oil heater. An emergency stop pushbutton was also installed. Its operation caused the shutdown of the engine, dynamometer, engine oil and water pumps.

Table 3.8: specifications of the dynamometer.

Type	Shunt wound DC machine with separate excitation.
Rating (kW)	30
Max speed (rpm)	6000
Max armature	400V and 65A
Field	370V
Ventilation	Electrically driven fan
Tachogenerator	R. E type AC14, 40V/1000rpm
Control	KTK type 6P4Q30 converter for motoring and regenerative loading

3.2.1.2 Cooling and Lubrication System

The engine's lubrication was a dry-sump system. SHELL Helix Ultra SW30 oil was used to lubricate the system. A pump and pressure gauge were installed upstream of the oil tank to ensure that the pressure in the main oil gallery was maintained at 4bar. A vacuum unit was installed in the crankcase to generate negative pressure of -100mbar. This prevented excess oil residues from accumulating on the optical components. The oil inlet was at the bottom of the cylinder block as shown in Figure 3.17. The path of the oil circuit covered the main bearings from the cylinder head to the cylinder block.

A closed-circuit cooling system was installed on the engine. De-mineralised water and 25% ethylene glycol were used for coolant and anti-freeze respectively. The coolant system cooled the mirror housing area, cylinder block and cylinder head.

A heating element was installed to heat the oil and coolant. The normal working temperature of the engine coolant and oil was maintained and monitored to be in the range of 49°C and 54°C.

A piston cooling mechanism, which supplied compressed air to the piston at a pressure of 0.65MPa, was installed on the side mounted mirror. This prevented the glass piston from overheating during operations.

3.2.1.3 Sensors and Data Acquisition System

3.2.1.3.1 Angle Encoder

An AVL optical angle encoder 365C was mounted at the end of the engine's crank shaft. This provided reference signals of the engine timing and position. It sent an optical signal from the crankshaft, which was based on the principles of reflections and used a reference rotating marker disc on the crankshaft. It then converted the analogue momentum angle (optical signal) into analogue voltage signals. This was connected to the data acquisition systems and supplied information of the engine speed and position.

The crank pulley consisted of 24 teeth. It was mounted on the engine block which supported the encoder from severe engine vibrations. The signal from the encoder was sent via optical transmitter electronics and fibre optic cables. The electrical transmitter was connected to a pulse converter which generated a trigger pulse of 720 pulses per revolution. This provided a reading resolution of 0.5°CA. In addition, a reference signal was generated at combustion TDC. The two signals were then connected to the engine timing unit (ETU).

3.2.1.3.2 Engine Timing Unit

The engine timing unit (ETU) was the main interface between the signals from the sensors installed on the engine to the data acquisition systems (DAQs). In this case, the AVL 427 ETU was used. The unit was controlled by a micro-processor and was used to generate both crank angle and time-based control and trigger signals.

The ETU had a counter running in steps of tenth of a degree, in time with the crankshaft. For the counter to work correctly, the crankshaft signals were obtained via the exhaust camshaft sensor, trigger pulse and 720 pulses per revolution (mentioned above) from the crank angle encoder. The ETU was connected to the PC for remote control via AVL's ETU software.

The ETU's TTL output channels were subsequently connected to the data acquisition systems (DAQs), sending out crank-angle resolved signals. This is indicated in Figure 3.13. This enabled the control of the injection timing, spark timing,

along with synchronisation between optical systems and the laser, based on the engine's position. These could be adjusted via the ETU software by defining either the trigger based on crank angle position or by time. It was also used to define the offset for TDC so the data at correct engine timings would be read by the DAQs and combustion analyser software. The software would also provide the real-time engine speed readings in addition to the data acquisition system. The signal delay from the ETU outputs was 2μs.

The ETU's TTL output channels also enabled crank-angle resolved monitoring and recording of signals connected to the DAQs. These included signals from the intake pressure sensor, in-cylinder pressure transducer, lambda sensor, intake temperature and exhaust temperature, indicated in Figure 3.13.

3.2.1.3.3 In-cylinder Pressure Transducer

An uncooled pressure transducer (AVL GU22C) was installed on the cylinder head. The Piezo-electric pressure sensor measured the in-cylinder pressure traces.

The measurement range was up to 25MPa with a sensitivity of 34pC/bar. The cyclic drift was ±0.4bar. The pressure signal from the transducer was sent to a charge amplifier (FI Piezo Amplifier 2P2E/F/G/H) in the form of an electrostatic charge, yielding quasi-static measurements. A voltage signal was then sent out to the data acquisition card to process the in-cylinder pressure measurements. The in-cylinder pressure traces were recorded using the combustion analyser software developed at Brunel by Dr Yan Zhang.

3.2.1.3.4 Intake Pressure Sensor

Omega pressure sensor was installed on the engine's intake manifold to record the manifold intake pressure (MAP) as the throttle position and engine speed varied during testing. The measurement range was 0-2bar gauge pressure and the transmitter sent a voltage reading to the high-speed DAQ. The MAP readings were recorded using the combustion analyser software.

3.2.1.3.5 Throttle

Throttle mechanism used was that of a servo tester connected to a butterfly valve with a remotely controlled dial. This sent electrical signals to the valve to give open/close command and the extent to which it needed to open. The throttle opening

was adjusted according to the MAP readings on the combustion analyser software. The mechanism was connected to a 12V mains socket.

3.2.1.3.6 Data Acquisition System

Two DAQ cards were used to acquire data and send the analogue readings to the combustion analyser software. This is presented in Figure 3.13.

A high-speed NI USB-6353 card was used to obtain the readings for in-cylinder pressure transducer, inlet pressure sensor, angle encoder (to read trigger and angle increments) and engine speed. The acquisition sample rate could be as high as 1.25 MS/s and the timing resolution was 10ns. The actual data acquisition rate was determined by the engine speed and the shaft angle encoder output, which was used as the timing clock of the data acquisition.

A low-speed NI USB-6218 card was used to provide the readings for lambda values and intake, exhaust, coolant and oil temperatures. The acquisition sample rate was 250 kS/s and the maximum timing resolution was 50ns.
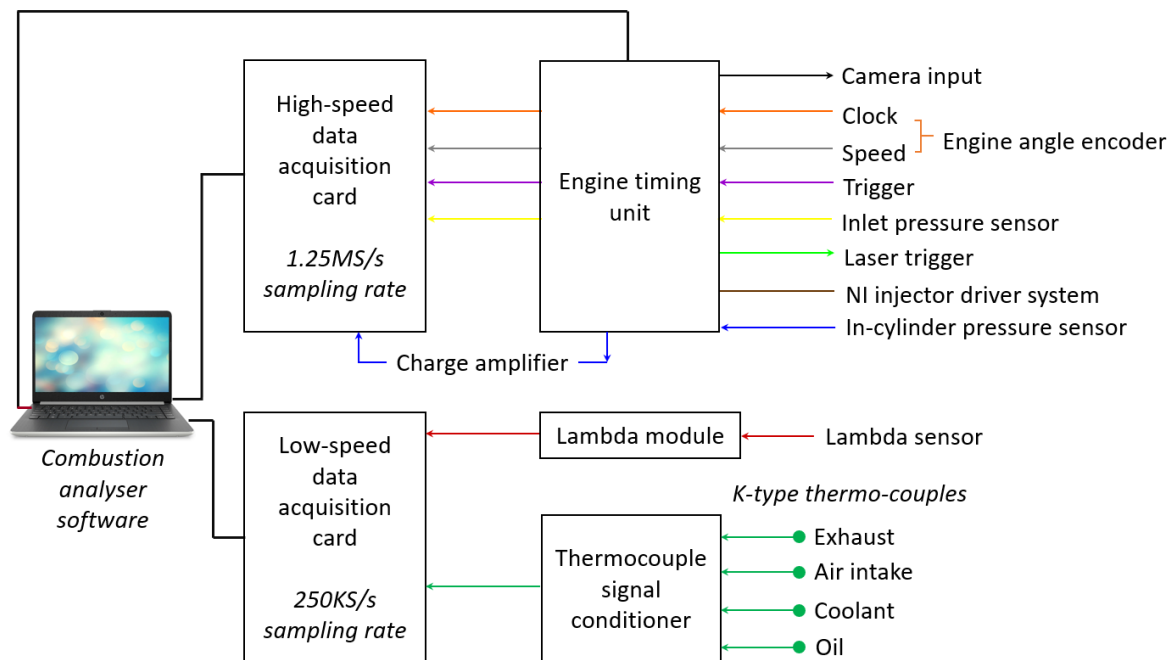
Figure 3.13: overview of the data acquisition systems setup using the two NI data acquisition cards.

An in-house built MATLAB based combustion analyser software was used to monitor and acquire data from the data acquisition cards. For all tests, data was recorded over 300 cycles.

3.2.1.4 Injection System

The test injector was side mounted, at an angle of 25°. An O-ring and clamp on the cylinder head were used to fix the injector's placement. The fuel rail and fuel supply system used was the same as that used for the measurements in the spray chamber. Refer to Figure 3.2 for representation of the fuel supply system.

3.2.1.5 Spark Plug and Ignition System

The spark plug's orientation was 72˚ with respect to swirl plane. Figure 3.14 shows the orientation of the spark plug, injector, in-cylinder pressure sensor and the valves.
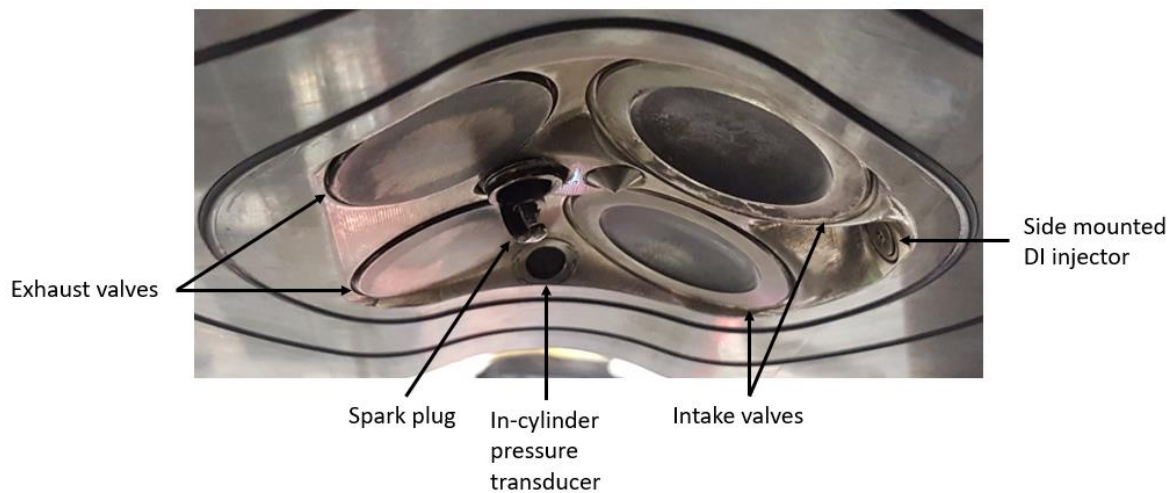
Figure 3.14: optical engine's cylinder head configuration, indicating the positions of the spark plug, injector and valves.

The ignition coil required a power supply of 24V. The coil was connected to a TTL output channel on the ETU. The ignition time and delay, along with the high and low limits were adjusted on the ETU software.

3.2.1.6 Engine Cylinder Head

The cylinder liner could be hydraulically lifted using a hydraulic oil supply unit. This raised and sealed the liner to the cylinder head at a pressure of 130PSI. The liner could be easily accessible for the purposes of regular cleaning of the liner and piston unit, as well as for easy exchange of piston unit and O-rings. The gap between the optical liner and the cylinder head when sealed was 100μm.

3.2.1.7 Intake Manifold

The intake manifold was used to draw in clean air from the atmosphere into the combustion chamber through the intake valves. A filter was attached at the tip of the manifold (Figure 3.15) to ensure that the air drawn in was clean and free of large contaminants. The throttle was installed downstream of the filter. The seeding unit for PIV measurements was installed downstream of the throttle with a T-connection. This induced both fresh air and seeded particles into the intake. This meant that in order to achieve the desired manifold pressure, both the throttle and T-connection with the atmospheric air valve had to be adjusted. The thermocouple at the air intake and the intake pressure sensor were installed upstream of the throttle, which was 300mm away from the intake valves.
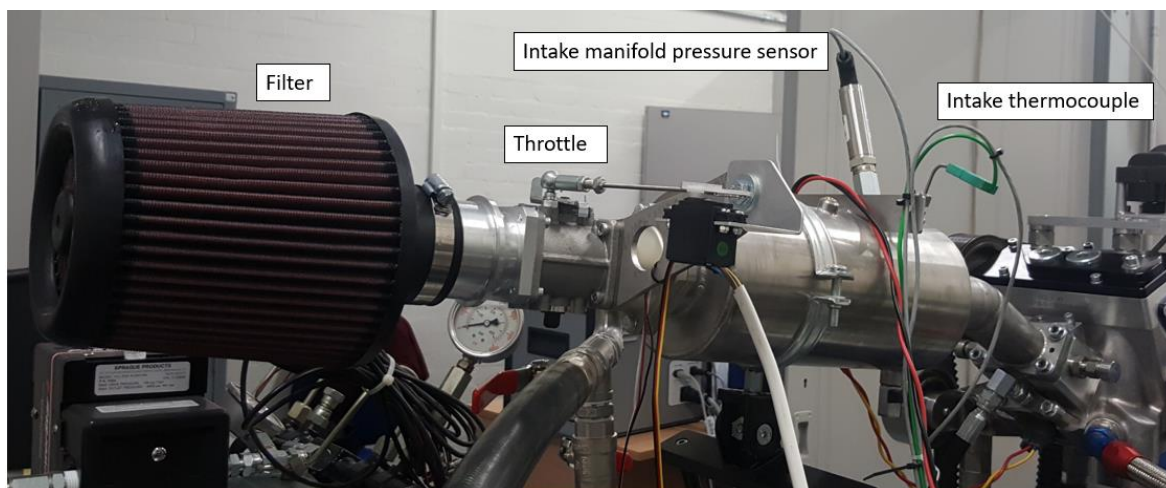
Figure 3.15: photograph of the intake manifold and the corresponding sensors' and throttle positions.

3.2.1.8 Exhaust System

The exhaust system comprised of an exhaust pipe connected downstream of the exhaust valves. A silencer was installed further downstream of the exhaust pipe. The exhaust manifold housed the lambda sensor and exhaust thermocouple which was installed 150mm from the exhaust valves.
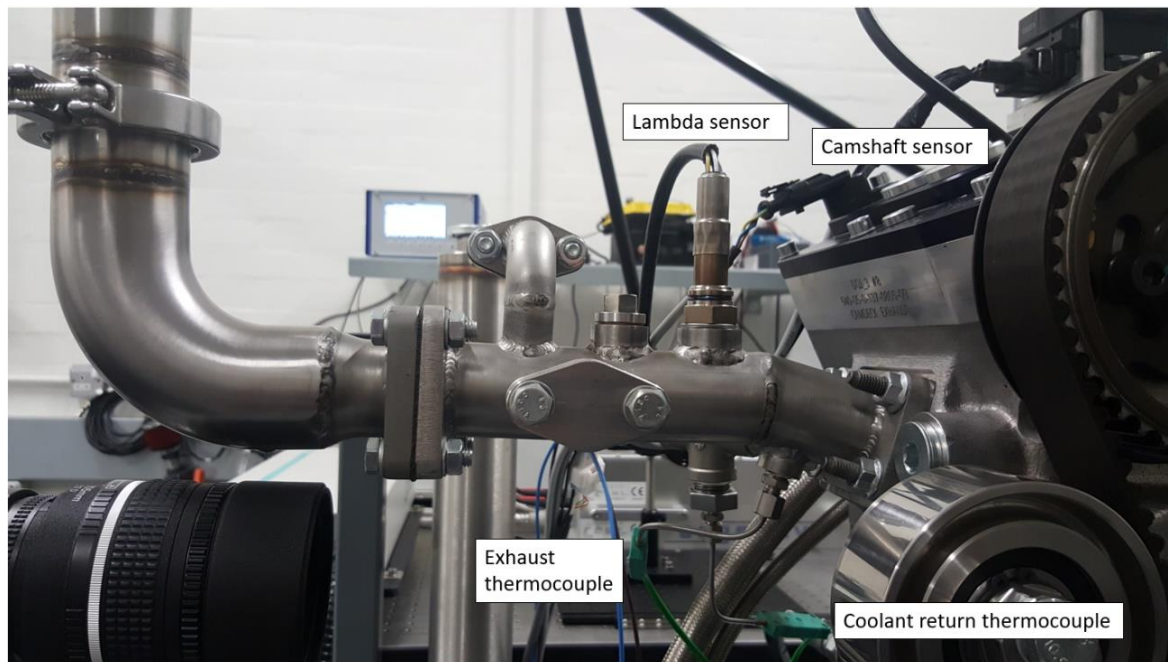
Figure 3.16: photograph of the exhaust manifold and the corresponding sensors' positions.
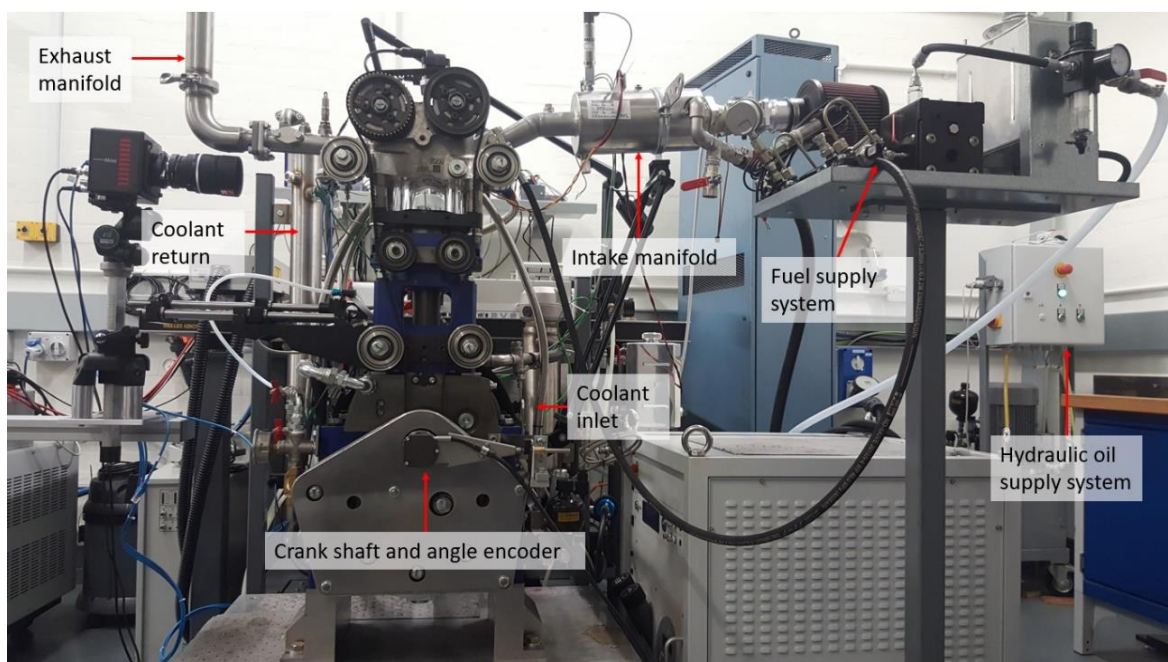
Figure 3.17: setup of the optical engine.

3.2.2 Particle Image Velocimetry

3.2.2.1 Principles of PIV

Particle Image Velocimetry (PIV) is a non-intrusive technique used to measure the velocity and sizes of tracer particles in transient flows based on the known time difference and the distance covered by the particles. The tracer particles in the flow are illuminated by a light source at least twice with short time intervals. The duration of the pulse widths of the light source must be short enough, or frequency high enough, to "freeze" the motion of the particles during the pulse exposure. This improves particle tracking and prevents blurred images of the particles.

The light scattered by the tracer particles are captured by a frame grabber, recording either a single frame or a sequence of frames. The time delays between the laser pulse and frame grabber used to capture the scattered light:

- are determined using pre-existing knowledge of the mean velocity of the flow-field being tested.

- must be long enough to determine the displacement between the images of the tracers.

- Must be short enough to avoid particles with out-of-plane velocity components leaving the light sheet between subsequent illuminations.

The time difference between an image pair is estimated using equation below.

$$\Delta t = \frac{\Delta n.(x_m; y_m)}{(U_{bulk}.x; y)}$$
Equation 3.21

Δn is the pixel shift here, $(x_m; y_m)$ is the field of view in mm, $(x; y)$ is the field of view in pixels and U_{bulk} is the bulk velocity. A maximum pixel shift of $\Delta n = 8$ pixels was chosen, with respect to the calculation method and the size of the interrogation window selected (for details, refer to section 3.2.2.2.6), for all Δt estimations.

The distance covered by the tracer particles per interrogation area (IA) is subsequently used to process the velocity and other parameters of the particles in the flow-field. The fluid velocity can be calculated using equation below.

$$u = \frac{(x_{i+1}, y_{i+1}) - (x_i, y_i)}{(t + \Delta t) - t} = \frac{\Delta s}{\Delta t}$$
Equation 3.22

IAs are small sub-areas in a digital recording frame. Statistical methods such as cross-correlation are used to determine local displacement vectors of the tracers of the two illuminations, per IA.

3.2.2.2 High-speed PIV System Setup

For the 2D planar high-speed PIV measurements, an Edgewave diode-pumped solid-state (DPSS) Nd:YAG laser was used, with a wavelength of 532nm. The laser was particularly useful for the high-speed application due to its high beam quality of over 140mW at 532nm wavelength and a repetition rate of 10KHz, in the TEM_{00} mode (uniform distribution of Gaussian intensity along the beam's cross section) during continuous operations. The high efficiency provided high average and peak power required for the high-speed PIV measurements [129]. The schematic of the setup is presented in Figure 3.18. The laser was cooled using a chiller unit **(1)** which pumped coolant around the head unit of the laser **(2)**.
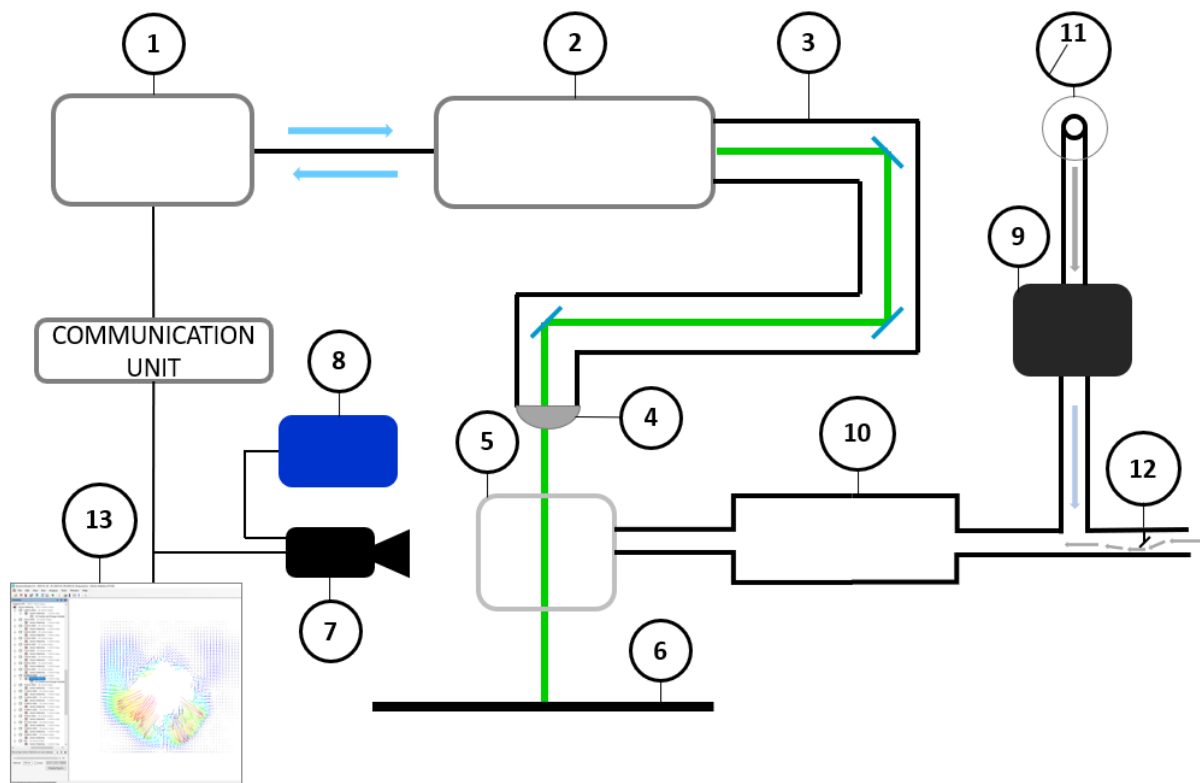
Figure 3.18: schematic of the PIV setup.

At the exit of the laser head, the beam (Ø3mm) was delivered to the combustion chamber using a flexible light-guide arm **(3)**, which housed seven 45° mirrors, reflecting the beam inside the black anodised tube. The typical loss of energy of the

beam is 5% per surface [129]. At the exit of the light-guide arm, a beam waist adjuster and parallel light-sheet optics were mounted made of three cylindrical lenses **(4)**. A diverging lens was placed first to prevent a focal point which could burn dirt particles (caused by ionisation) in its path and cause significant changes to the beam's properties. The two cylindrical lenses thereafter delivered a vertical light sheet with minimum divergence to the combustion chamber **(5)** with near-even intensity distribution.

The laser sheet's thickness at the waist, placed inside the flow field, was 0.5mm (FWHM). The expected maximum in-cylinder flow velocity was 30m/s. The suitable dwell time between each pulse and thus the trigger frequency of the laser pulse was determined using the expected maximum velocity of the flow and the maximum displacement of the particles Δn=8pixels or 1.45mm.

The trigger frequency was thus 10KHz which had a PW of 13ns at 45A current and 2.24mJ pulse energy. The images were captured in double frame double exposure mode. For the measurements in the tumble and omega tumble planes, the vertical laser sheet was positioned in the centre of the cylinder, towards the centre of the tip of the spark plug (Figure 3.19). The laser was dumped using a non-reflective black anodised beam dump **(6)** on the other side of the chamber.

a.

b.
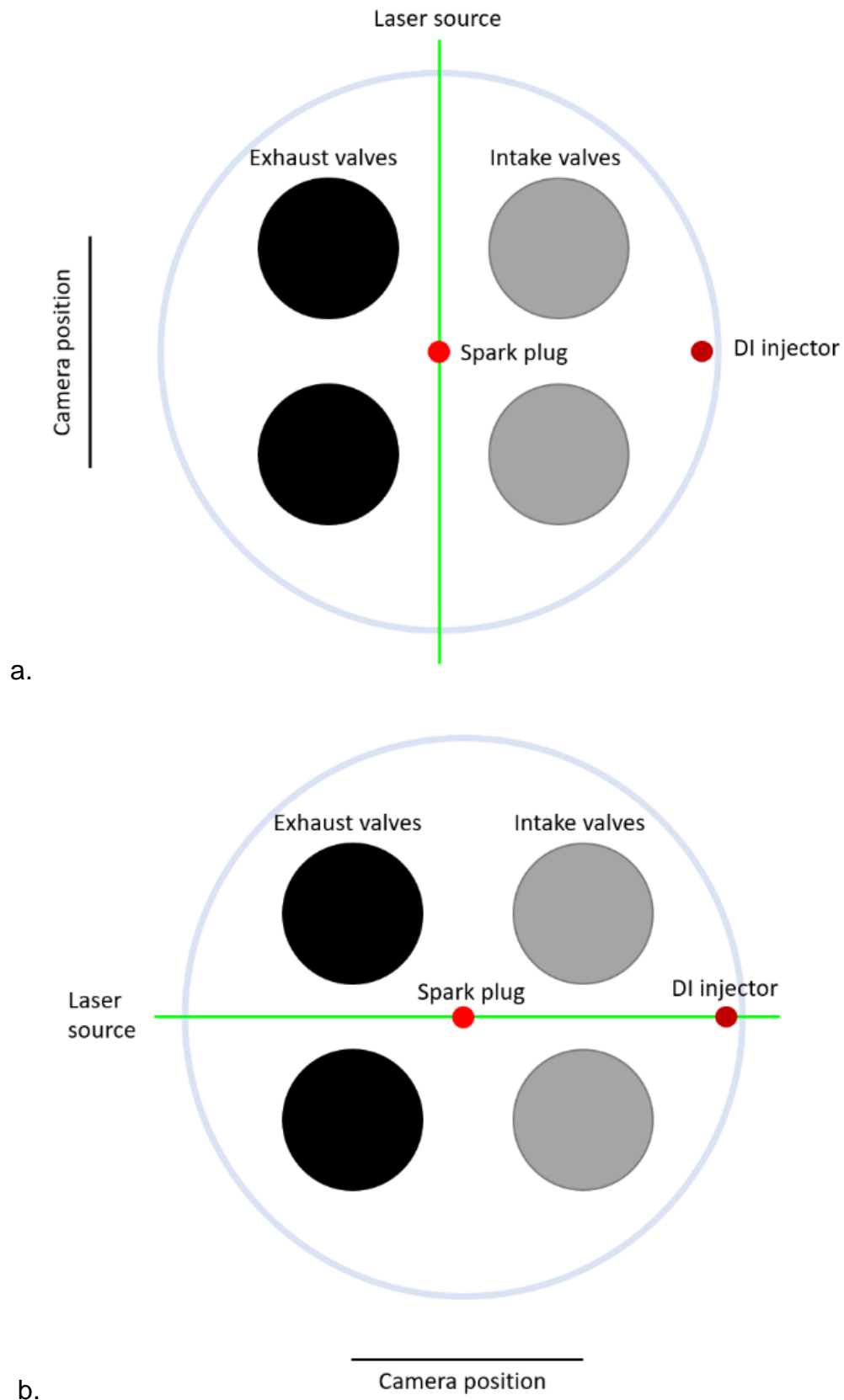
Figure 3.19: representation of a. the Omega tumble and b. tumble plane of measurements inside the combustion chamber.

3.2.2.2.1 Seeding

There were various requirements for the consideration of the seeding particles suitable for PIV measurements in the combustion chamber. They had to be large enough to scatter light with sufficient intensity for the seeded particles to be detected by the camera and lens, they could not affect the flow investigated, and that they followed the motion of the charge with minimum velocity lag.

The seeding fluid used was Di-Ethyl-Hexyl-Sebacic-Acid-Ester (DEHS), which was induced with the air via the intake valves. A large volume liquid droplet seeding generator **(9)** was used to atomise the DEHS and deliver the seeded particles to the intake manifold **(10)**. The generator required 0.6MPa of compressed air supply **(11)** in order to atomise the DEHS by applying principles of differential pressure. Detailed description of the working principles of the seeding generator is provided in [129]. The average diameter of the atomised droplets of the tracer particles was 2μm.

The seeded particles entered the intake manifold downstream of the throttle **(12)**. The seeder outlet was placed 500mm away from the intake valves. This enabled the air and droplets to mix uniformly along the path prior to entering the combustion chamber via the intake valves.

3.2.2.2.2 Imaging Unit

A high-speed monochromatic camera (Photron Fastcam Mini AX100) **(7)** was used to capture the images. It housed of a 1Megapixel complementary metal oxide semiconductor (CMOS) image sensor whose size was 20.48mm x 20.48mm and pixel sizes of 20μm x 20μm (1024 x 1024 pixel^2 resolution). A Nikon 60mm lens (Micro NIKKOR AF-D) was used with an aperture setting of f/2.8.

The camera was placed perpendicular to the plane of the vertical laser sheet. The laser and camera were triggered at 10KHz. This frequency provided a resolution of 0.7°CA/frame at the engine speed of 1200rpm. The field of view (FOV) was 512pixels x 512pixels. The lens magnification factor was (180μm /pixel)^2 and (170μm /pixel)^2 for the omega tumble plane and tumble plane respectively.

The camera was triggerd using the ETU **(8)** at the specified engine crank angle position, which was always gas exchange TDC for the current study. The laser pulses were subsequently triggered and synchronised by the camera's TTL output signal. The logic for the trigger timings is provided in Figure 3.20. The signal delay

from the ETU to the camera was 2µs. The delay between trigger input and start of camera exposure time was 0.668µs and the exposure time was 83µs. The delay between the camera's exposure and the synchronisation output signal to the laser was 0.55µs. Edgewave's software system was used to define the trigger mode and the current settings for the laser emission.
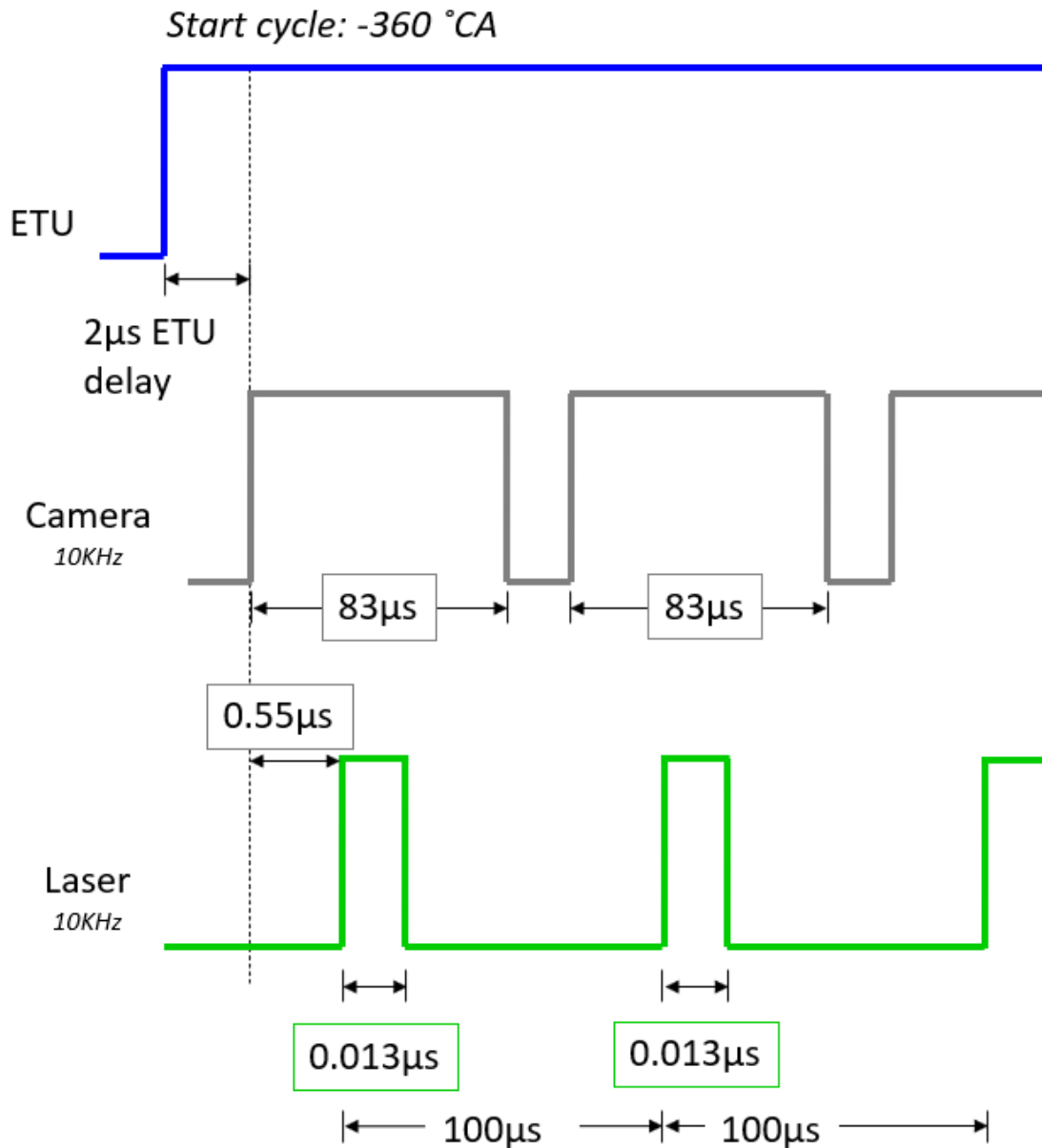
Figure 3.20: overview of PIV systems' synchronisation.

For data acquisition, data processing and data post-processing, Dantec's Dynamics Studio software version 6.11 **(13)** was used. This is also where the trigger frequencies, synchronisation details of the system and acquisition mode were registered.

3.2.2.2.3 Calibration

Once the setup was completed, prior to performing the tests, a calibration procedure was performed to define the spatial FOV in Dynamics Studio. This involved inserting a calibration tab inside the combustion chamber and perpendicular to the lens as shown in Figure 3.21. The tab had black markers 2mm in diameter and at a grid spacing of 5mm.
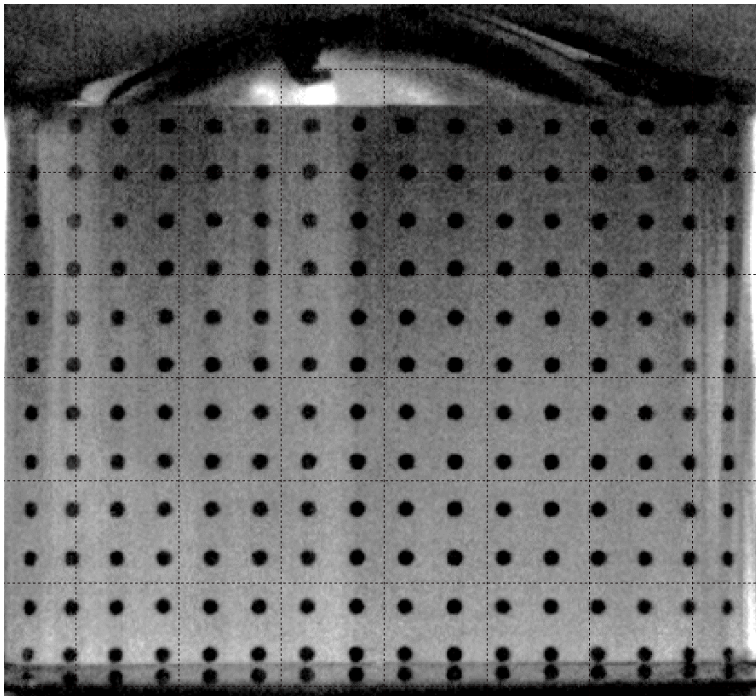
Figure 3.21: determination of spatial distances and magnification factor in the region of interest (ROI). Image obtained under room's ambient light conditions for representation purposes.

An image of the calibration tab placed inside the glass liner was captured using the aforementioned camera settings. It was important to place the calibration tab coincident to the light sheet, and view it through the glass, as these conditions represented the image plane.

A calibration algorithm was performed by the software to detect the black markers based on the input markers' sizes and grid spacing. 3rd order XY-polynomial algorithm (Equation 3.23) was applied, which then calculated the mapping between the object space and the image space. The 3rd order XY-polynomial was chosen as it is a suitable imaging model fit (IMF) that tackles non-linearities in the sample image, which in the current case were significant due to the curved liner and the refraction

caused by the 30mm thick quartz glass through which the calibration tab was being viewed.

The re-projection error based on this method, for the omega tumble plane and tumble plane were 0.6pixels and 0.18 pixels, respectively. The re-projection error is largely affected by the distance between the image plane and the object plane or the magnification factor. As the camera for measurements in the omega tumble plane was placed further away from the image plane, the re-projection error was thus larger.

$$\begin{bmatrix} x \\ y \end{bmatrix} = \begin{array}{l} \vec{A}_{000} \\ +\vec{A}_{100}X + \vec{A}_{010}Y + \vec{A}_{001}Z \\ +\vec{A}_{110}XY + \vec{A}_{101}XZ + \vec{A}_{011}YZ \\ +\vec{A}_{200}X^2 + \vec{A}_{020}Y^2 + \vec{A}_{002}Z^2 \\ +\vec{A}_{300}X^3 + \vec{A}_{210}X^2Y + \vec{A}_{201}X^2Z \\ +\vec{A}_{030}Y^3 + \vec{A}_{120}XY^2 + \vec{A}_{021}Y^2Z \\ +\vec{A}_{102}XZ^2 + \vec{A}_{012}YZ + \vec{A}_{111}XYZ \end{array} \qquad \text{Equation 3.23}$$

3.2.2.2.4 Convergence Analysis

A convergence analysis was performed to determine the optimum number of cycles for data validation purposes. The measurements were run under the engine conditions presented in Table 3.9.

Table 3.9: test conditions for convergence analyses.

Engine speed (rpm)	1200
MAP (bar)	~0.74
CR	10.5
SOI (°CA bTDC)	180
PW (ms)	2.5
No. of cycles	32

The points of local velocity vectors were obtained at 255°CA bTDC, where the fuel film had broken up, but the flow field was still turbulent and fuel dense. The processing for obtaining the velocity measurements are described in Section

3.2.2.2.6. The point of measurements was 42mm from the LHS and 33mm from the bottom of the omega-tumble plane. The point and the frame at which the convergence analyses were performed, are indicated in Figure 3.22.
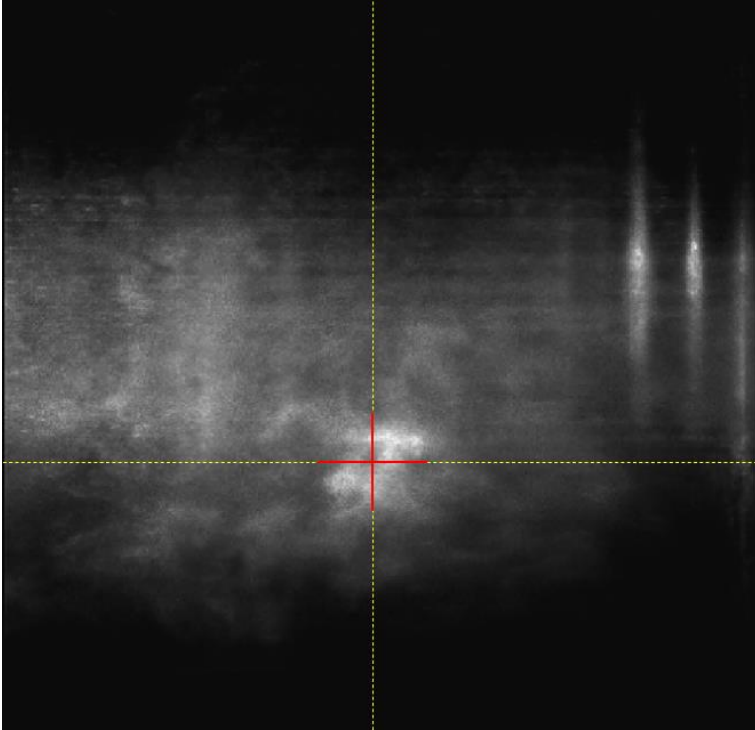
Figure 3.22: point in the flow-field, at 255°CA bTDC, where the convergence analysis was performed.

The trend for the convergence is presented in Figure 3.23. The optimum number of cycles determined from this analysis was 20 cycles of double frame, double exposure images.
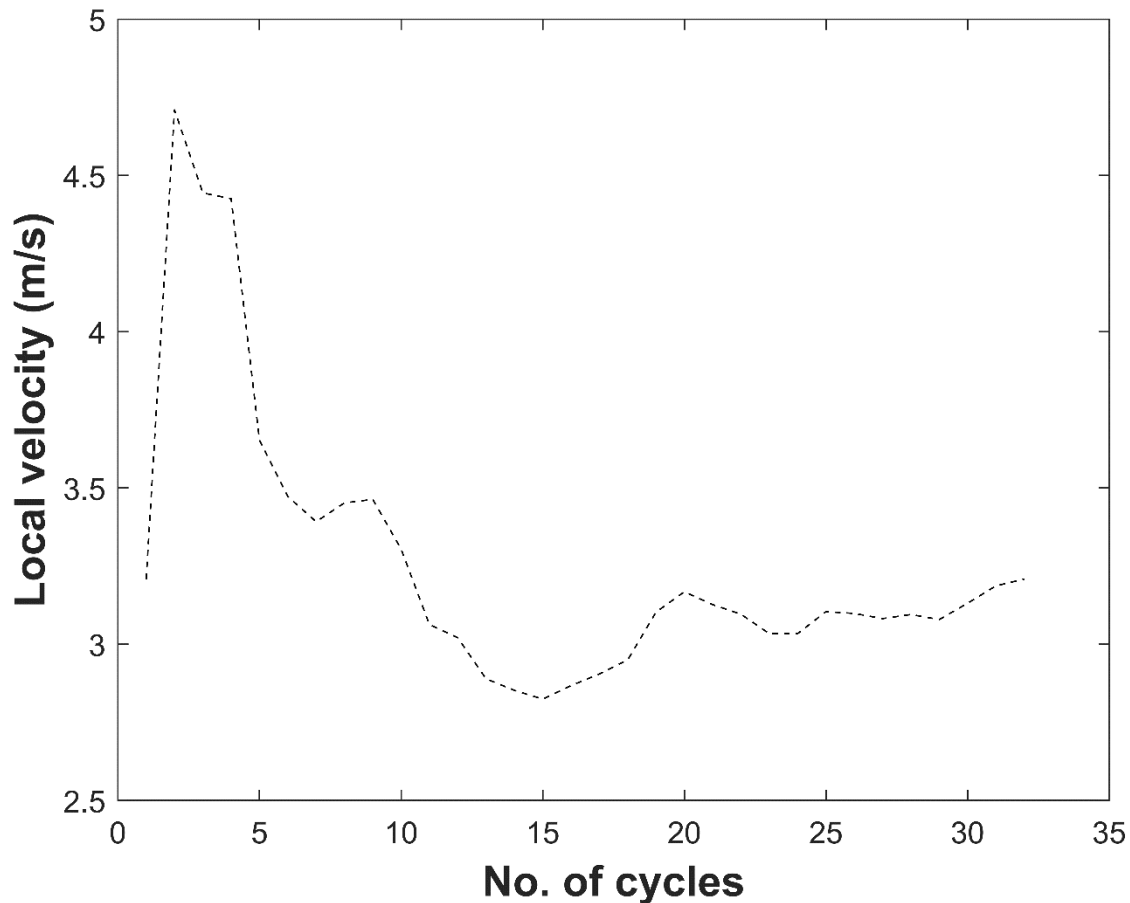
Figure 3.23: convergence trend of the local velocity over 32cycles

3.2.2.2.5 High-speed PIV Tests

Prior to performing the tests, the engine was allowed to warm up until the coolant return temperature exceeded 47°C. The average oil return temperature was 37°C throughout the tests. The room temperature was maintained between 22°C and 25°C.

The tests were performed at 1200rpm, part load conditions (MAP of about 0.74bar) and compression ratio of 10.5. The exact parameters are presented with results in Chapter 5. The injection cases were compared against a motored case, with no injection but with the remainder of the conditions kept the same (1200rpm, 0.74bar MAP and compression ratio of 10.5). It is important to note here that all measurements are performed under cold-flow conditions. As such combustion had not taken place.

For each tested condition, 25 cycles were recorded and saved in the dataset. Out of these, 20 cycles were processed, according to the convergence analysis discussed in section 3.2.2.2.4.

3.2.2.2.6 Data Processing

3.2.2.2.6.1 Pre-processing

In order to remove the perspective errors due to any off-axis camera setting, the dataset was initially de-warped using the IMF performed during the calibration process (discussed in section 3.2.2.2.3), which had registered the presence of any distortions. The process (run by the software) had consisted of adding a resampling grid in the object plane. Using the IMF, each point in the resampling grid was mapped to a corresponding point in the image plane. The pixel positioning was thus calculated by the software, and a grayscale value was derived from the original image and subsequently assigned to a pixel in the de-warped image.

The resulting pixels' co-ordinates were positioned inside an area of 2pixels x 2pixels in the original image. The grayscale values of the resulting pixels in the de-warped image was then determined using bi-linear interpolation [130].A mask was thereafter defined on the dataset, which removed the regions that were of no interest when it came to data processing. For the omega tumble plane, these areas included non-optical regions of the engine, past the boundaries where the glass would contact the metal surface and the curved edges of the wall which generated significant distortions, especially during the times of injection. FOV for the omega-tumble plane was thus masked from the original FOV of 78.9mm (bore) x 76mm (stroke) to 67.1mm x 63.8mm. The FOV for the tumble plane was masked from the original FOV of 87.9mm x 76.6mm to 83.3mm x 76.6mm.

Figure 3.24 provides details of the masked regions of the cylinder head and the intake valves. The masks for the intake valve opening were adjusted according to the engine position during data processing.
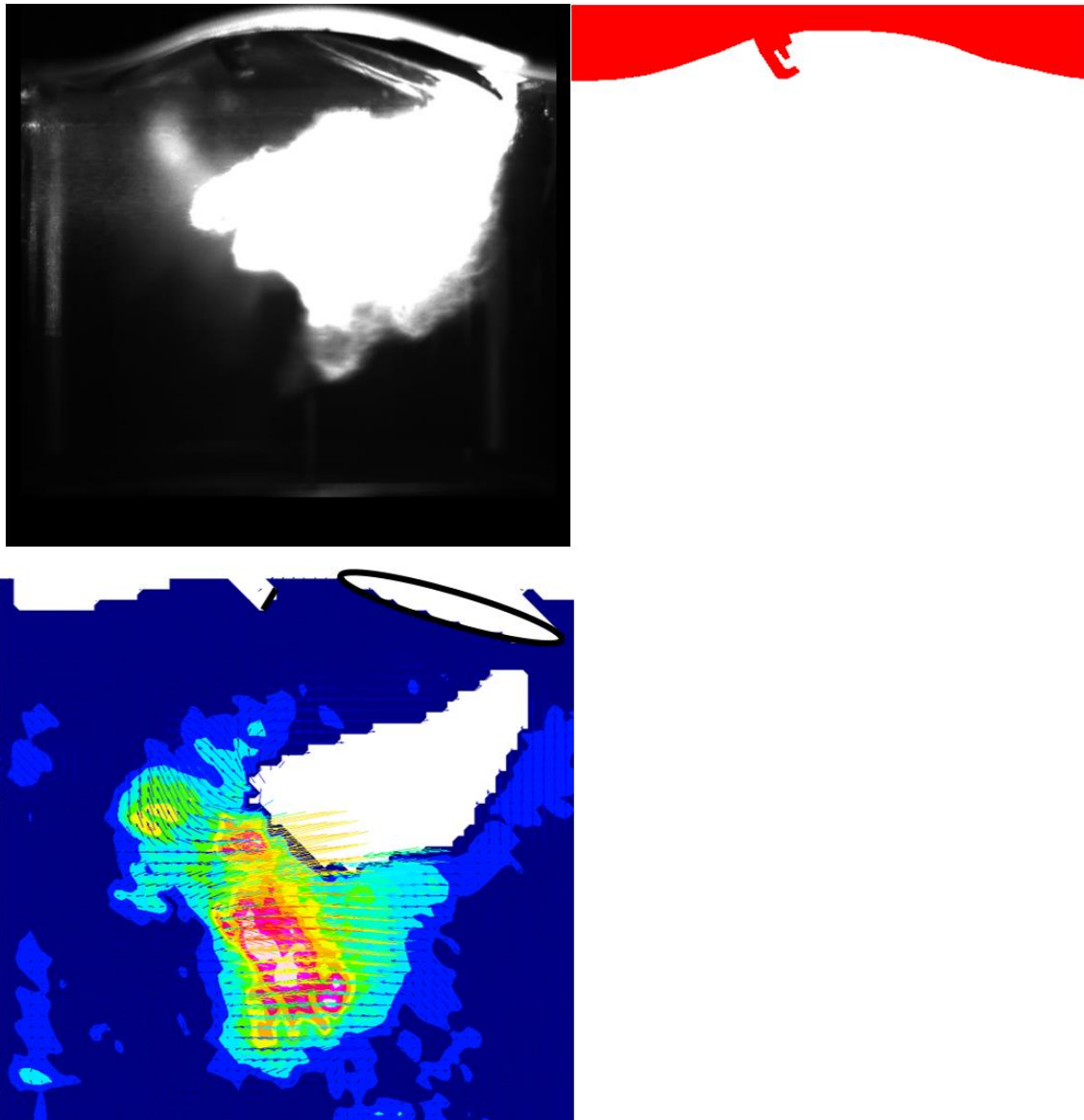
Figure 3.24: raw image for SOI 200°CA bTDC in the tumble plane (top left), definition of the cylinder head and spark plug masks (top right) and processed TKE contours of the flow field indicating pixelated masked boundary region, including opening of intake valve, where a dynamic mask was applied (bottom left).

3.2.2.2.6.2 Processing

Adaptive PIV algorithm in the software was used to measure the velocity vectors in each frame. This method is used to calculate the velocity vectors based on particle image pairs, whereby an image is evaluated repeatedly, first with large IAs in order to find the local mean displacements, then with smaller IAs and increasingly higher spatial resolution. The method iteratively optimises the size and shape of each IA in order to adapt to the local flow gradients and seeding densities [129], [130].

The maximum in-cylinder velocity was expected to be 30m/s. Based on this information, the time step between each frame and the magnification factor, the maximum IA was selected to be 128pixels x 128pixels. This size of IA could calculate maximum velocity magnitudes of 50m/s. The minimum IA was set to 16pixels x 16pixels, with a grid step size of 8pixels x 8pixels. This meant that the minimum IA would overlap by 50%.

The signal-to-noise ratio (SNR) was set to as high as 3.5 in the omega tumble plane and 2.5 in the tumble plane. The flow-field in the tumble plane appeared to be less noisy in comparison to the omega-tumble plane due to the differences in the light scattering by the fuel, based on two different planes of measurements. Such high SNRs mostly eliminated the noisy signals being processed. Majority of the noise had originated from the distortions from the curved regions of the glass liner, as shown by the saturated areas in green in Figure 3.25. In this case, the noise level in the correlation plane is evaluated initially using the Root Mean Square of the negative correlation values. If the ratio between the correlation peak height (0.15) and the noise level is above the specified value, then the calculated displacement is considered valid.
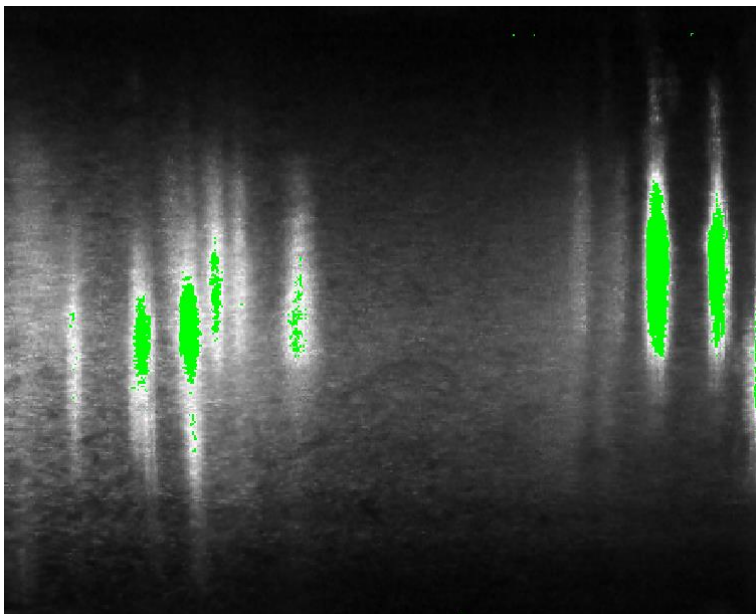
Figure 3.25: representation of the over saturated region/noise generated due to the light reflected by the curved surfaces.

The settings for adaptive PIV were determined using a cross-correlation analysis. The determination of the particle displacement is done by shifting the second image

relative to the first image and summing the product of the corresponding pixels for each shift. This sum reaches its maximum when the shift is equal to the displacement. In discrete terms, the cross-correlation is given by equation below.

$$R(i,j) = \sum_{x=-\frac{w}{2}}^{x=\frac{w}{2}} \sum_{y=-\frac{w}{2}}^{y=\frac{w}{2}} I_1(x,y) + I_2(x+i, y+j)$$

Equation 3.24

In this case, the cross-correlation function shows only a single intense peak whose position with respect to the centre gives the particles' displacement direction and distance in the IA, as shown in Figure 3.26.
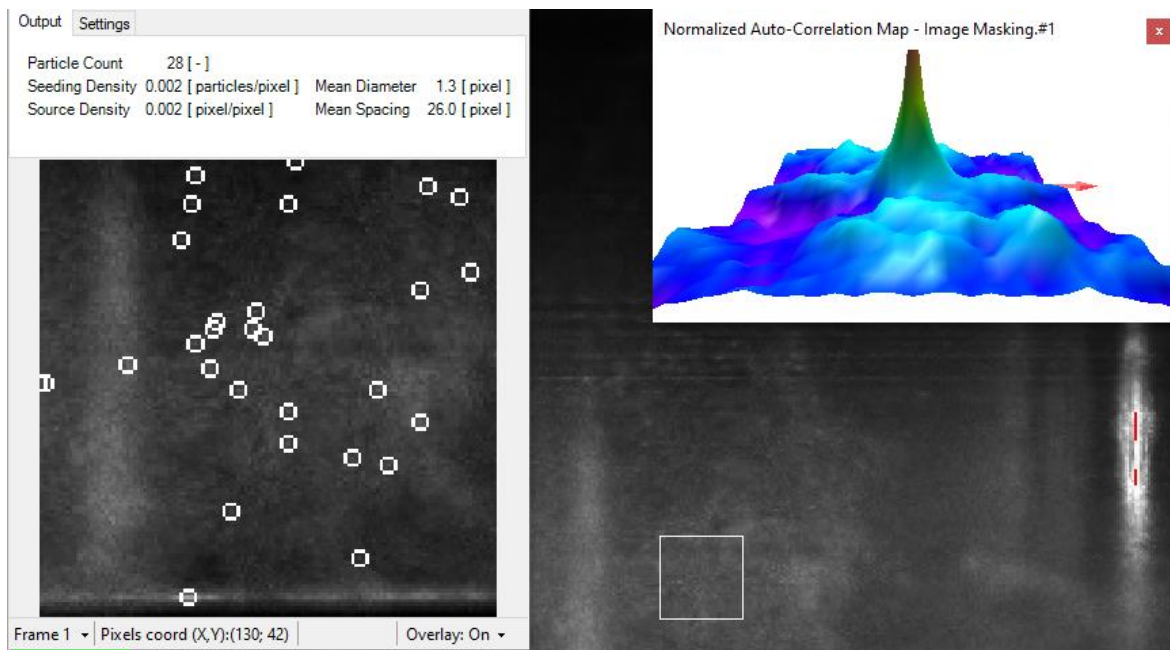
Figure 3.26: cross-correlation analysis on double frame double exposure mode for 128pixels^2 IA and SNR of 3.5 in the omega tumble plane.

The lag in the velocity of the seeded particles and the Stokes number, with respect to the fuel and air flow velocities (calculated individually), can determine how well the particles follow the flow motion.

The velocity lag (U_s) of the selected tracer particles in the continuously accelerating in-cylinder charge (U_s) can be estimated using equation below. The calculations, however, assume that the tracer particles follow a viscous fluid at a low Reynolds number and that the particles are spherical.

$$U_s = U_p - U = d_p^2 \frac{(\rho_p - \rho)}{18\mu} a$$

Equation 3.25

In this case, d_p is the droplets' sizes of the seeding particles, which is 2μm, $ρ_p$ is the density of the DEHS seeding particles which is 981kg/m^3 [131] and ρ is the density of the fuel and air which are 746.1kg/m^3 and 1.254kg/m^3, respectively. μ is the dynamic viscosity of fuel and air which are 0.06Pa.s and 1.81x10^{-5}Pa.s, respectively. The variable a is gravitational acceleration of 9.81m/s^2.

The relaxation time or Stokes No. can be determined using equation below.

$$\tau_s = d_p^2 \frac{\rho_p}{18\mu} \left(\frac{d^2}{\nu} \right)$$
Equation 3.26

Based on the current setup, the velocity lag of the seeded particles following the air flow was 3.6x10^{-14}m/s. The stokes number was 0.0042, which meant that the seeded particles (stokes No. less than unity) followed the flow closely. The expected tracing accuracy error was less than 1% with minimal lag in the velocity. Consequently, the velocity lag of the seeded particles following fuel flow was 2x10^{-11}m/s. The stokes number was 1.3+10^{-6}. This confirms that the seeded particles followed the fuel droplets with minimum velocity lag, with again a tracing accuracy of less than 1%.

The seeding density inside the selected IAs varied depending on the type of stroke, which was heavily influenced by the in-cylinder temperature and pressure conditions. The seeded particles were more scattered in the intake stroke compared to compression stroke. In the omega-tumble flow, with the SNR set to 3.5, the average number of detected particles at bottom dead centre (BDC) for 128pixels x 128pixels IA size and 16pixels x 16pixels IA size were 30 and 7, respectively. In the tumble flow, with the SNR set to 2.5, the average number of detected particles at bottom dead centre (BDC) for 128pixels x 128pixels IA size and 16pixels x 16pixels IA size were 190 and 8, respectively.

It is worth noting that when the fuel broke up into droplets, they scattered light which was also picked up as signals. These fuel droplets were thus also acting as seeded particles in the flow field. As a result, post-fuel injection, the seeding density in the flow field generally increased.

Finally, the mean velocity (μ_u) and TKE (k) were calculated using the following equations, where u and v are directional components of velocities of the tracers and N was the number of samples.

Mean velocity: $\mu_u = \frac{1}{N}\sum u_n$ Equation 3.27

Variance: $\sigma_u^2 = \frac{1}{N-1}\sum u_n - {\mu_u}^2$ Equation 3.28

Standard deviation: $\sigma_u = \sqrt{\sigma_u^2}$ Equation 3.29

TKE: $k = \frac{3}{4}(\sigma_u^2 + \sigma_v^2)$ Equation 3.30

3.2.2.2.7 Limitations and Uncertainties

In addition to the noise generated by the distortion from the curved edges of the optical liner, the highly fuel-dense region of the spray in the image plane had oversaturated the images. An example is provided in Figure 3.27, where the red area is oversaturated by the un-broken fuel spray at 1.9ms after start of injection (ASOI). The prevention of the oversaturation was unavoidable, as a result of which no signal was detected in these areas, resulting in blank regions in the profiles of the accumulated data.
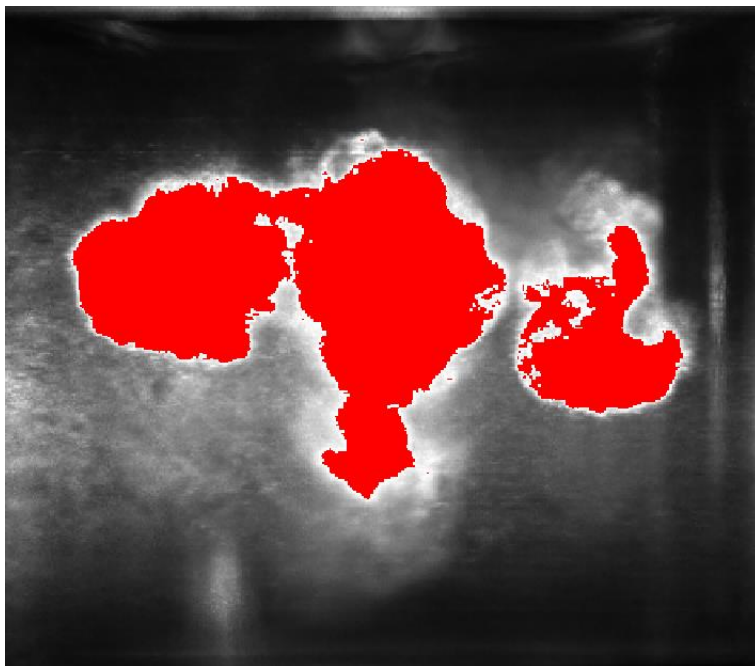
Figure 3.27: representation of over-saturation caused by the un-broken main spray in the image plane

There are uncertainties however, associated with the actual shape of the un-broken spray and the boundary between the fuel spray and the surrounding charge, which cannot be interpreted from the PIV results by merely observing the blank regions. It

must therefore be noted that the blank regions are a rough indication of the unbroken spray and not an actual representation of the global spray structure. Note that at this point, prior to the fuel spray breakup, the seeded particles will be tracing the air flow. Once the spray atomises into smaller droplets, the seeded particles would follow the air-fuel mixture, and the fuel droplets would also be detected as tracers.

One of the major limitations associated with high-speed PIV measurements was the lack of control of the dwell time or time difference between laser pulses, as cycle-resolved high-speed PIV could only be carried out using a fixed frame rate. Consequently, the temporal resolution was worse than low frequency PIV which provides more flexible control of the laser PWs and time differences. In order to tackle this limitation, large IAs had to be used to process the maximum flow velocity, resulting in reduced dynamic range of the velocity measurement.

Another limitation with cycle-resolved high-speed PIV measurements is the lack of consistency in the seeding density at varying strokes of the engine, caused by constant changes in in-cylinder pressure and temperature. To resolve this, a time-consuming process of gauging the PIV density at all engine crank angle positions, in order to determine the sufficient seeding density for the selected minimum IA, had to be undertaken.

Finally, there were variations in the light scattered by the fuel particles between the measurement planes of tumble plane and omega tumble plane. This was due to the orientation of the laser sheet, and its interaction with the thick curved glass liner. One way to avoid this variation with the laser scatter is to direct the laser source from the 45° mirror placed underneath the extended piston. This way, the laser sheet could be emitted from the optical piston crown, thereby eliminating large distortions due to the laser refracted through the curved glass liner. This technique is suggested in [132], [133].

3.3 Summary

The methodologies of the experimental techniques performed have been described in this section. This has also included details of the design logic where applicable, specifications of the diagnostic tools used and the tested injection parameters.

The mass measurements, high-speed imaging, design and commissioning of the constant volume spray chamber and setup of the PDA system were employed for the spray characterisations. The corresponding results from these experiments are discussed in Chapter 4.

The commissioning and setup of the optical GDI engine along with its data acquisition setup, auxiliaries, software tools, and the setup of the PIV system were used to obtain data of the in-cylinder charge characteristics using a variation of the injection strategies. The results obtained from these setups are subsequently discussed in Chapter 5.

Chapter 4.   Spray Characterisation and Droplet size Distribution of a High-pressure Gasoline DI Injector

4.1 Introduction

The spray characteristics of single and split injection strategies were investigated using a solenoid actuated, high-pressure DI injector. This was done in the efforts to help tackle the challenges faced with achieving ideal mixture formation, suitable for the stratified charge operation. Single injections were also investigated in this case to expand the understanding of the effects of injection pressures and duration (as determined by the PW) on the spray characteristics.

The key measurement equipment and techniques used are detailed in Chapter 3. The injection quantities for varying pressures, PW combinations and dwell times, were analysed. High-speed imaging was used to perform macroscopic characterisations of the sprays. This consisted of analysing the penetration lengths and spray angles. PDA measurements were performed to compare the rear plume's droplet characteristics using the single and split injections with varying dwell times and split ratio. These measurements were focused in the near-nozzle region (11mm downstream) and at various axial locations downstream from the injector.

The chapter is structured as follows. The discussions of the spray characterisations are split into four parts. The first part consists of the discussions of the injected masses of the single and split injections with various injection pressures, PWs, dwell times and split ratios. In the second part, the effects of high injection pressures on single and split injections' macroscopic spray characteristics are investigated using the high-speed images. The effects of the split ratios and dwell times of split injections on the velocities and droplet sizes at various distances downstream of the injector are discussed in the third section. The fourth part provides a summary of the investigation, whereby key findings are outlined.

4.2 Studies of Injection Mass Measurements

4.2.1 Single Injections

The average injection masses of the single injections at varying PWs and injection pressures were measured. This was done to investigate the effects of small PWs (operation in the ballistic zone) and large PWs on the injected quantities at varying injection pressures.

The effects of increasing PWs and injection pressures on the injected quantity, for the single injection case, are presented in Figure 4.1. The increase in the average masses for the short PWs in the range of 0.3ms to 0.5ms is non-linear, whereby the rate of increase is initially high and is dampened with increasing PW. For the larger PWs, between 0.5ms to 3ms, the increase in the injected quantity is linear.
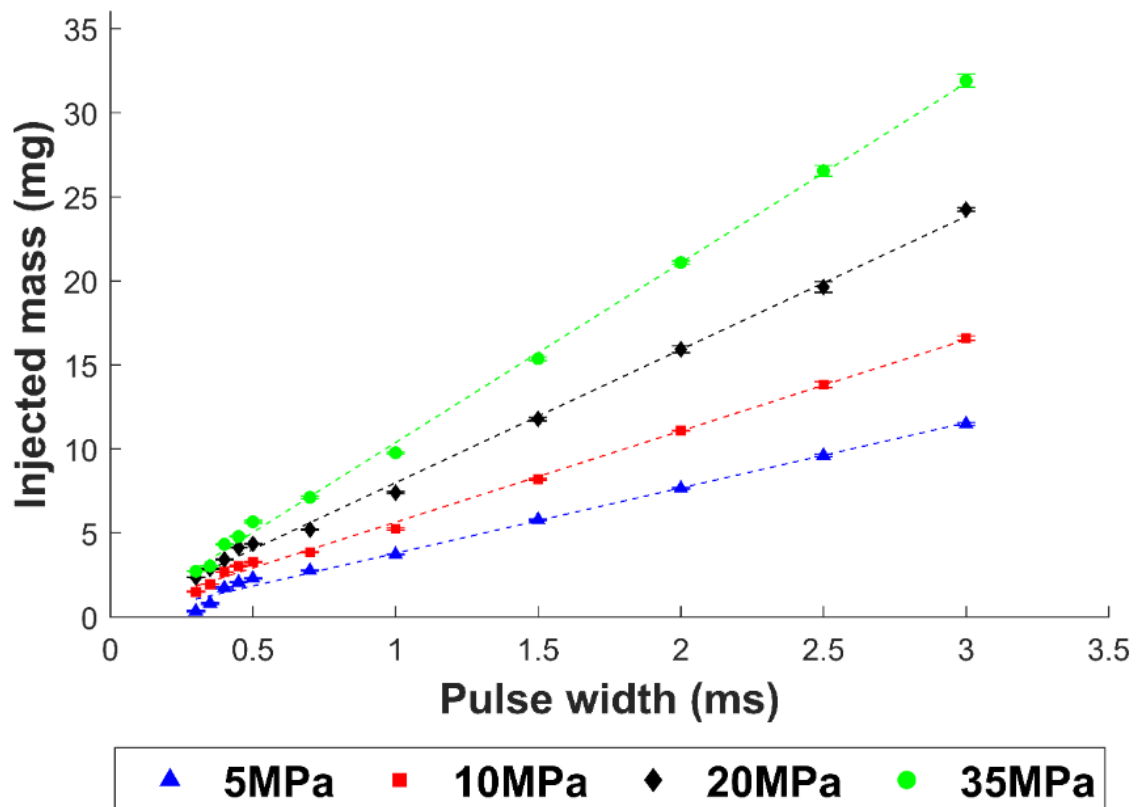
Figure 4.1: effects of increasing PWs and pressures on the injected quantity.

This trend is consistent with all injection pressures tested. It suggests that the injection momentum during the start of injection is large due to the opening event of the valve, which is why the injection quantity increases at a higher rate with the short PWs tested. Increasing the PW allows the injection momentum to stabilise over time

as the spray reaches the steady state region, which is why a linear increase is observed for the larger PW cases. This implies that the injection momentum could be stabilised after 0.5ms ASOI. Mitroglou et al., [134] had reported that a stable and repeatable gasoline spray structure was achieved for injection durations greater than 0.9ms when using injection pressures of up to 12MPa. The steady state regions for a variation of PW are further explored via the PDA measurements in section 4.4.

The average injected mass also increases with the increase in the injected pressure, with the maximum quantity measured at 35MPa rail pressure and 3ms PW. As the fuel rail pressure increases, so does the injection momentum. As a result, the large momentum forces more fuel through the nozzles. This is at a cost of larger error bars associated with higher injection pressures. Fluctuations in the fuel rail pressure of - 10bar was observed in the pressure gauge installed upstream of the high-pressure diaphragm pump, when operating at injection pressure of 35MPa. This variation in the pressure would have subsequently caused variation in the injected quantity, hence the large standard deviation errors observed.

Regarding the injection control Payri et al., [135] reported that the dispersion of Diesel droplets is higher with their injection pressure of 200MPa when compared to 100MPa, which they related to increased difficulty in the injection control. This is because of the increased pressure waves attributed to large pressures, which affected the shot-to-shot variability. A similar effect can be seen here judging by the larger error bars.

4.2.2 Split Injections

The differences in the injection quantity at varying dwell times and the corresponding single injections are analysed in this section. The purpose is to obtain some indication of the solenoid injector's needle behaviour and the interaction of the injection events for the split injection cases with varying dwell times using short PWs. Figure 4.2 shows the effects of dwell times and split ratios on the average injected quantities. Note that a dwell time of zero represents single injections.
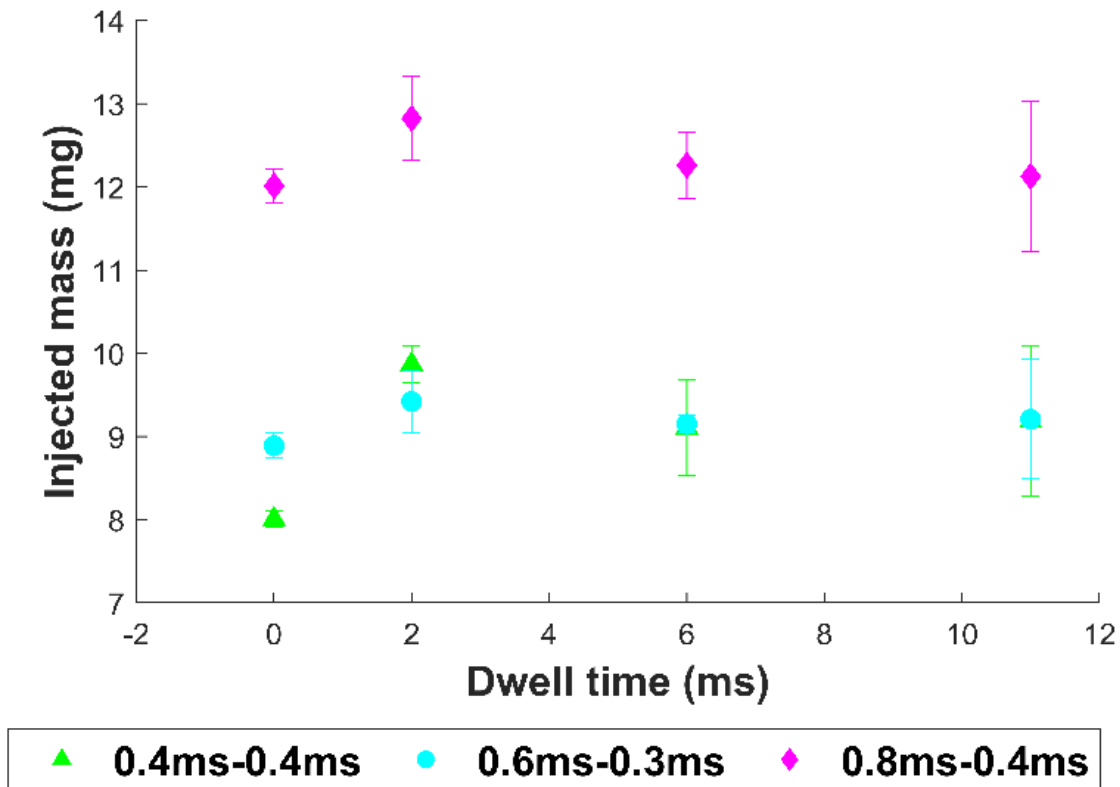
Figure 4.2: effects of dwell times and split ratios on the average injected quantity for the split injection cases and single injections (dwell time=0) for a rail pressure of 35MPa. The PW combinations represent 2:1 and 1:1 split ratios.

When observing the injected quantities from the split cases, the data indicates that the highest quantity of the fuel was measured for the shortest tested dwell time of 2ms. This is the case for all PW combinations and split ratios tested. For dwell times greater than 6ms, the injected quantities are similar.

One reason proposed for the larger quantity of the fuel measured at 2ms dwell time was that the needle had not closed fully prior to the start of the second injection. As reported by Wood, A. [88], for the short dwell times in the range of 0.35ms and 1ms, the eddy currents from the end of the first injection had remained in the solenoid and did not dissipate by the start of the second injection. This led to advanced injector opening for the second injection period, thereby increasing the fuel mass delivery.

To better understand if this is the case with the current injector, the current and voltage profiles applied to the injector for both 0.4ms-0.4ms and 0.8ms-0.8ms PW combinations, using a dwell time of 2ms, are shown in Figure 4.3 (the axes values have been removed do to the confidential nature of the data). Both cases show a

distinctive gap in the transient current profile between the end of the first injection and start of the second injection, confirming that the valve was commanded to shut for the duration of the dwell time.

a.

b.
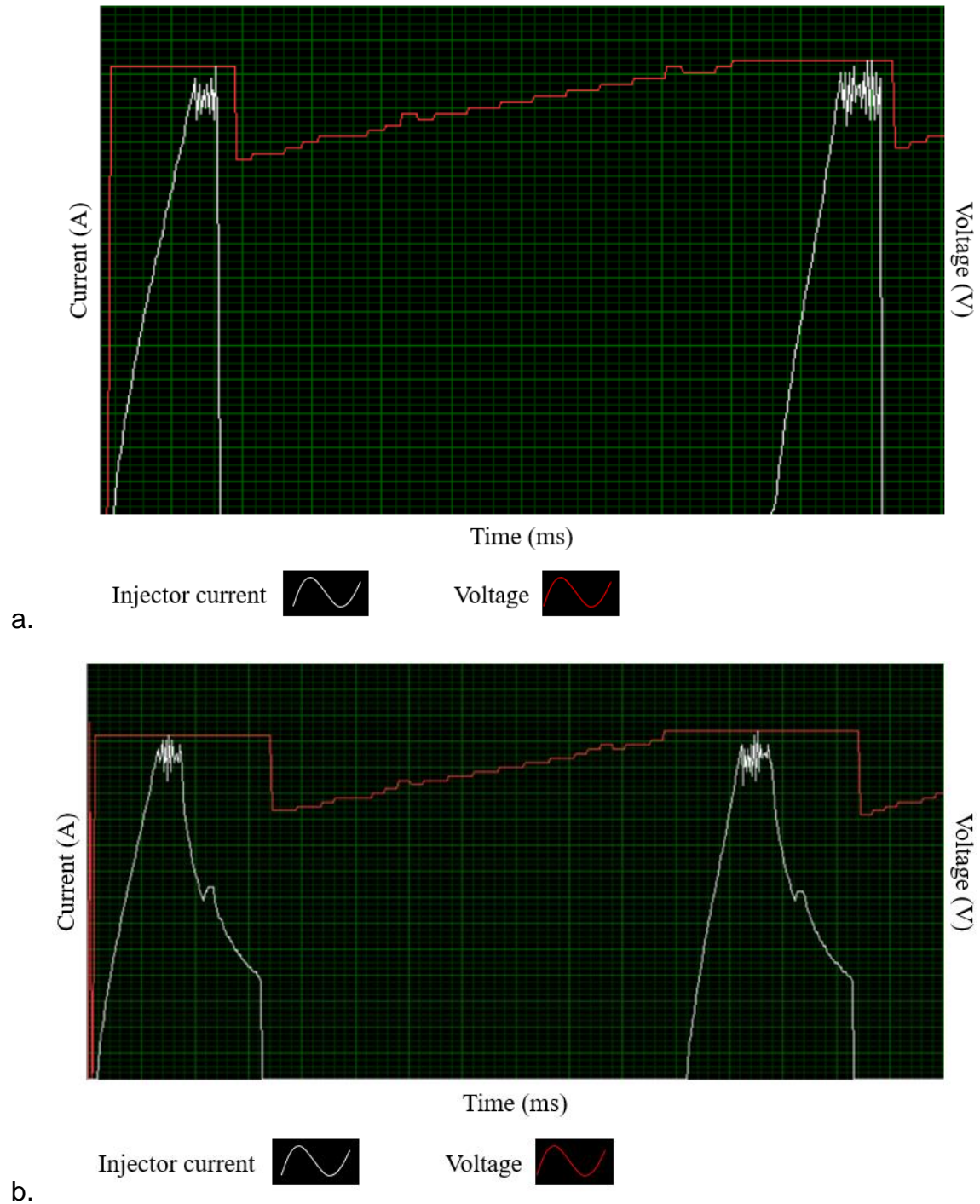
Figure 4.3: current-voltage profiles for PW combinations of: a. 0.4ms-0.4ms and b. 0.8ms-0.8ms. The dwell time settings for both profiles are 2ms. The white and red trend lines represent the current profile and the voltage profiles, respectively.

High-speed images of the tested cases, performed at 20KHz, had further revealed that the start of the second injection had occurred after the specified dwell time. The current high-speed images and the current and voltage profiles showed that the injector needle opening for the second injections occurred after the specified dwell time. However, it is not entirely clear how the needle lift would have been affected by the interactions of the two injections.

In addition, a number of studies have observed tip wetting effects [31] [32] [136]. Upon the injector closing event, Hélie, J. et al., [31] observed large ligaments of fuel formed at the tip of the nozzles resulting in tip wetting. This effect was intensified by the large injection pressures. High-speed images of the flow field by the end of injections presented in Figure 4.4b, however, do not indicate any obvious dripping effects or tip wetting effects. While this indicates that the effects of tip wetting on the injected quantity could be negligible, macroscopic studies would help in observing any formation of ligaments towards the end of injections.

The primary reason for the larger quantity measured with the short dwell time thus points towards the injected fuel interacting with each other in the flow field. For the measurements performed under ambient atmospheric conditions, the fuel prior to the start of the second injection is still in the vicinity of the injector, as seen in Figure 4.4 and Figure 4.5. As a result of this, the injected fuel from the first injection and the tip of the spray plumes are seen to interact, which would affect the droplet atomisation of the second injection, as observed in the following section. These combined effects thus result in higher injected quantity measured, when compared to larger dwell times.

For dwell times larger than 6ms, there is no dramatic change in the injected mass. This indicates that the dwell time is large, providing sufficient time for the first injection to propagate away from the vicinity of the injector. The interactions between the two injection events would be alleviated, thereby reducing the chances of measuring coalesced droplets collected in the beaker.
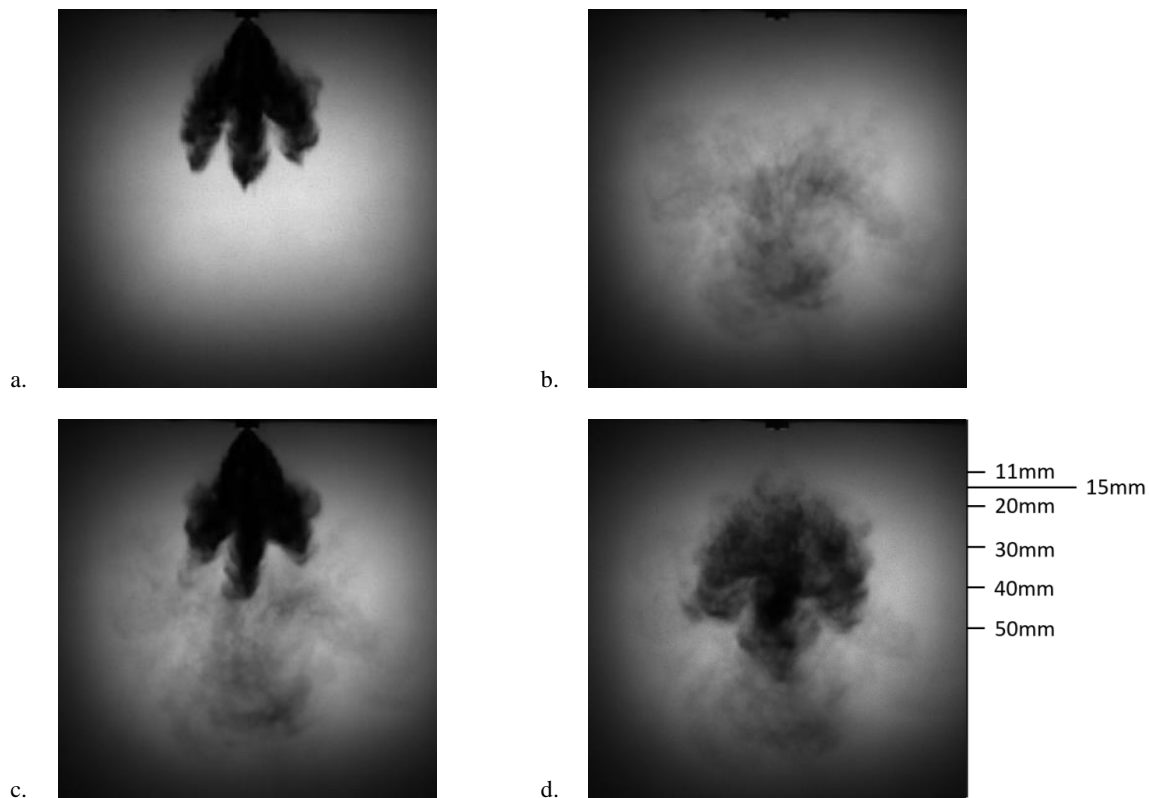
Figure 4.4: images of the flow field for 0.4ms-0.4ms PWs, dwell time of 2ms and injection pressure of 35MPa. The images represent the flow field at a. end of first injection, b. start of second injection, c. end of the second injection and d. 0.45ms after end of second injection (EOI2).

The trend in Figure 4.2 also shows that the overall injected quantities for all the split cases and dwell times tested are generally larger than the single injections. This is caused by the ballistic region repeated twice with the split injections using short PW combinations, which leads to the high mass flow rate initially upon the valve's opening. The injection mass flow rate during the start of injection is large (as observed in Figure 4.1) since the injector is operating in the ballistic region. Increasing the PW causes a reduction in the mass flow rate past the ballistic region, as the spray reaches a steady state region. This is why a linear increase is observed for the larger PW cases. It is this repetition of the injection in the ballistic zone associated with the split cases using short PWs, that leads to higher injected quantity when compared to the single injections.

Additionally, the highest relative peak in the injection quantity at 2ms dwell is observed for the short PW combination of 0.4ms-0.4ms, as the PW is primarily operating in the ballistic region. The short PWs are also sensitive to the valve's

motion. It was observed in the high-speed images that for 0.4ms PW, the spray was attached to the injector tip for at least 100µs after end of injection (EOI). This was not observed for the larger PWs of 0.6ms and 0.8ms.
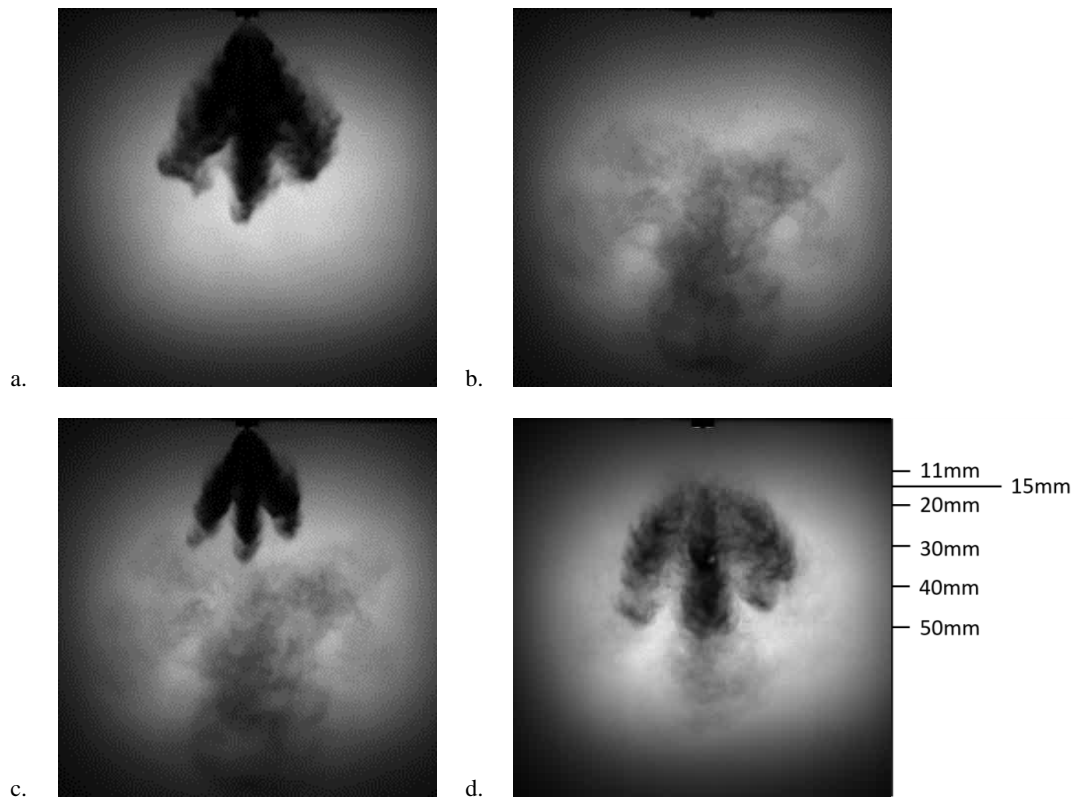
Figure 4.5: images of the flow field for 0.6ms-0.3ms PWs, dwell time of 2ms and injection pressure of 35MPa. The images represent the flow field at a. end of first injection, b. start of second injection, c. end of the second injection and d. 0.45ms after EOI2.

A possible reason for this occurrence is the sudden drop in the peak current, which interrupted the development of the current over time for the short PW as observed in the valve profile (Figure 4.3a). This sends a sudden command for the valve to shut, instead of a progressive drop in the current and therefore a progressive closing of the valve (Figure 4.3b.). In addition, a second shorter peak in current observed with the larger PW combination is missing from the valve profile of the short PW of 0.4ms. This indicates that the short PW does not allow the development of the full current profile before the rapid closing of the injector valve. As such, the sudden drop in current commands the valve to shut, but the closing of the valve could be heavily affected by the large forces of the fuel due to the high injection pressure, which would resist the closing of the valve. The untimely closing of the valve therefore

would have affected the detachment of the spray from the injector tip, subsequently affecting the injected quantity.

This effect was also observed by Mouvanal, S., [32]. Due to the sudden closing of the valve, the inertia force was found to be predominant in the fuel flow, which was injected at 15MPa. As a result, the fuel was injected for a longer duration with lower momentum. As a higher injection pressure was employed in the current study, the inertia forces are greater which means increased resistance against the closing of the valve. This explains why the fuel would have remained attached for a large duration after EOI.

The reason for the higher relative peak in the injected quantity for the short PW combinations observed at 2ms dwell time is thus due to the combination of the delayed detachment of the main spray tip after EOI (independent of the dwell time) and the increased rate of interactions between the two injection cases (dependent on the dwell times).

Observing the standard deviation error bars, the largest error bars in the injected quantity are observed for the largest dwell time of 11ms. This is because the large dwell time would allow sufficient time for the fuel from the first injection to evaporate prior to the start of second injections, preventing some droplets from being accumulated in the beaker during the measurements. Some evaporated fuel therefore affected the measured injected quantity per test cycle, as the rate of vapourisation varied shot-to-shot due to the short PWs employed.

Payri et al., [135] reported that the shot-to-shot variability for the pilot/post diesel injection was dependent on both the transitory characteristics and the dwell times for the post injections due to internal pressure waves. This was observed when short dwell times in the range of 200µs to 650µs were employed, with pressures of up to 200MPa. They thus found the shorter post injection difficult to control due to the impact of the pressure waves (which is dependent on rail pressure) on the valve's behavior. The relatively large standard deviation bars observed with the 2ms dwell case, when compared to single injections, suggest that the internal pressure waves had affected the second injections, even when a larger dwell time was employed. In other words, the shot-to-shot variations would have been a factor in the large standard deviations measured with dwell times larger than that employed in [135].

4.3 Studies of Penetration Lengths and Spray Angles

4.3.1 Single Injections

The effects of increasing pressure on the single injections' spray characteristics, at 1.5ms PW, are investigated. Figure 4.6 represents the effects of increasing injection pressure on the average penetration length. The measured penetration length is the length of the fully developed spray 1.5ms ASOI. A PW of 1.5ms is employed for investigation as this is a typical PW employed in engines to achieve a homogenous charge at WOT and engine cruise speeds.
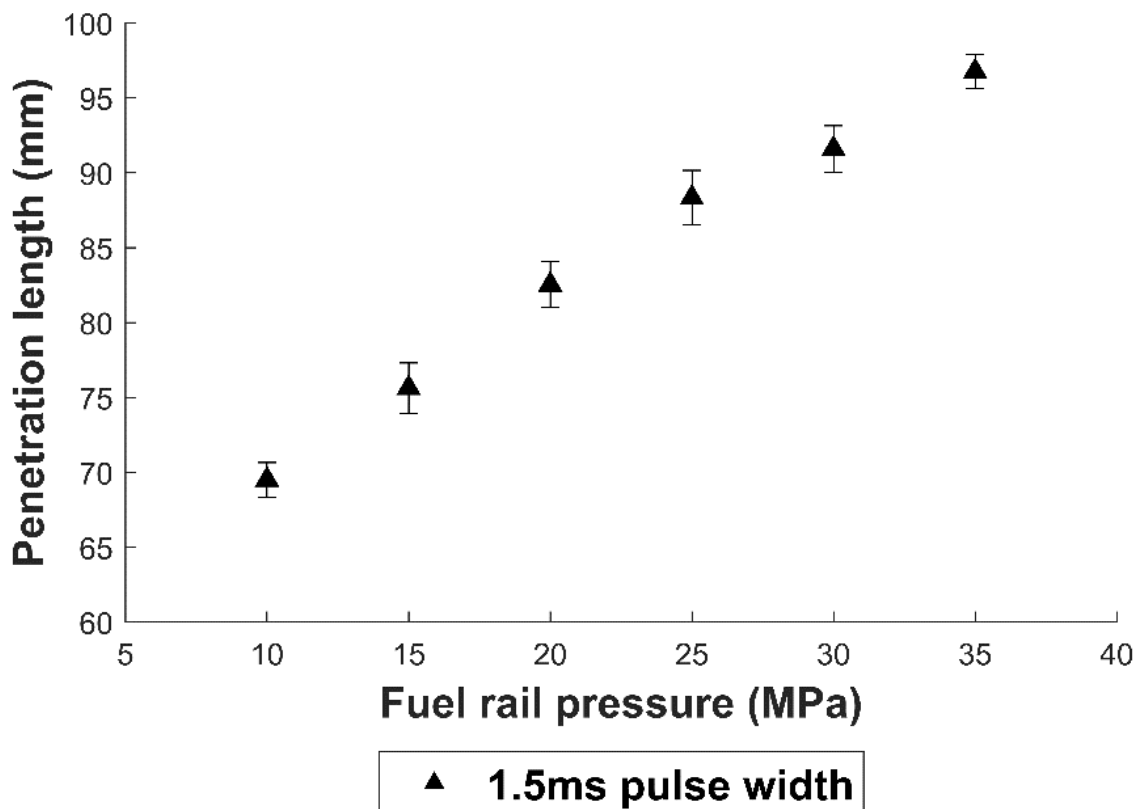
Figure 4.6: the effect of rail pressures on the main tip penetration for single injections using 1.5ms pulse width. The penetration lengths were measured 1.5ms ASOI, using high-speed images at 20KHz. The error bars represent standard deviations in the penetration lengths.

The average penetration length of the fully developed spray increases with increasing rail pressure, with the maximum observed at 35MPa pressure. The increase in the average penetration length is almost linear for pressures ranging between 10MPa and 25MPa.

For the higher rail pressures, this increase in the penetration length is somewhat dampened. This suggests that past 25MPa injection pressure, the extent of the axial spread of the spray is reduced past a threshold injection pressure, which in the current case is 25MPa. This was also observed in [83], whereby the rate of increase in the penetration length had diminished with increasing injection pressure.

The possible reasons for this occurrence are as follows. Firstly, with increasing pressure, the fuel droplets face large shear forces which resist the spray propagation. This also causes the droplets at the edges of the plume to detach from the plume, which then possess reduced velocity. Secondly, high injection pressure is associated with the improved atomisation rate. As such, the combined effects of the reducing mass of the droplets as they undergo phases of atomisation, and the large shear forces resisting the spray's motion are suspected to affect the spray penetration lengths.

The penetration length for the 35MPa pressure however, shows a greater increase than would be expected, especially since the increase is dampened past 25MPa. The reason for this is discussed below.

Figure 4.7 shows the rate of increase in the penetration length over time for varying rail pressures. The initial rate of increase in the average main tip penetration length until 0.6ms ASOI is high, and is reduced past 0.6ms ASOI. This is true for all tested pressures. The trend confirms that the initial momentum of the fuel is high once the needle is opened. The momentum thereafter stabilises past 0.6ms ASOI, after which the spray develops more steadily at a reduced rate.

The average main tip penetration length, after 1.4ms ASOI (indicated with a dashed black line in Figure 4.7), increases slightly. The images of the spray development at 20MPa and 35MPa, from 1.3ms ASOI onwards, are presented in Figure 4.8 and Figure 4.9 respectively. Observing the spray images, the spray detaches from the injector's tip at 1.5ms ASOI for both pressures. This explains the continued increase in the main tip penetration length past 1.4ms ASOI. The PW was set to 1.5ms and the current-voltage profile setting was as per the manufacturer's current-voltage profile. These images indicate that this particular injector's valve shuts slightly earlier than the specified 1.5ms PW. Due to the greater momentum for 35MPa, the spray

penetrated much further. This is why the larger penetration length for the injection pressure was observed in Figure 4.6.

The error bars also get larger with increasing rail pressure and increasing time ASOI. The former is likely to be caused by increasing pressure fluctuations in the fuel flow as injection pressure increases, as discussed earlier. The latter could be caused by the entrainment effects as the spray develops, whereby distinct vortices are formed due to the increasing aerodynamic effects forming a shear layer between the surrounding air and the fuel. This affects the consistency in the trend of the penetration length, hence the larger errors.
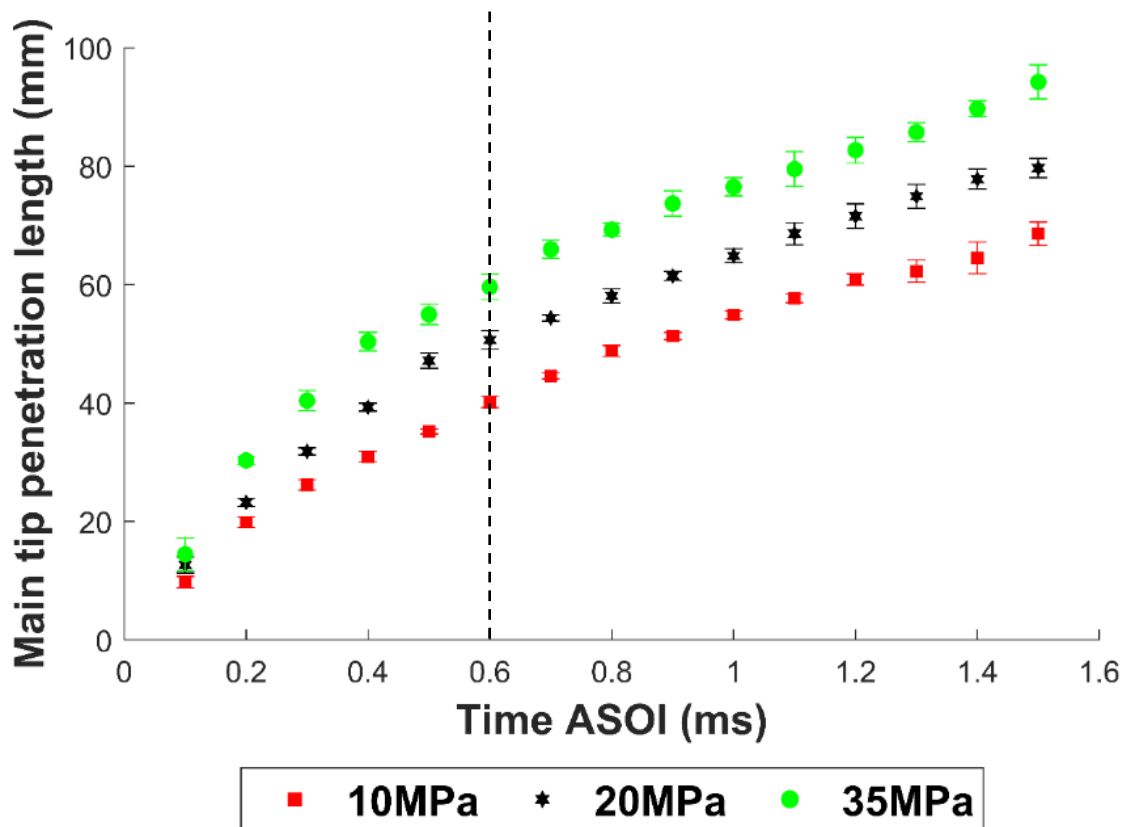
Figure 4.7: rate of increase in the penetration length for three different rail pressures with 1.5ms pulse width. The error bars represent standard deviations in the penetration lengths.
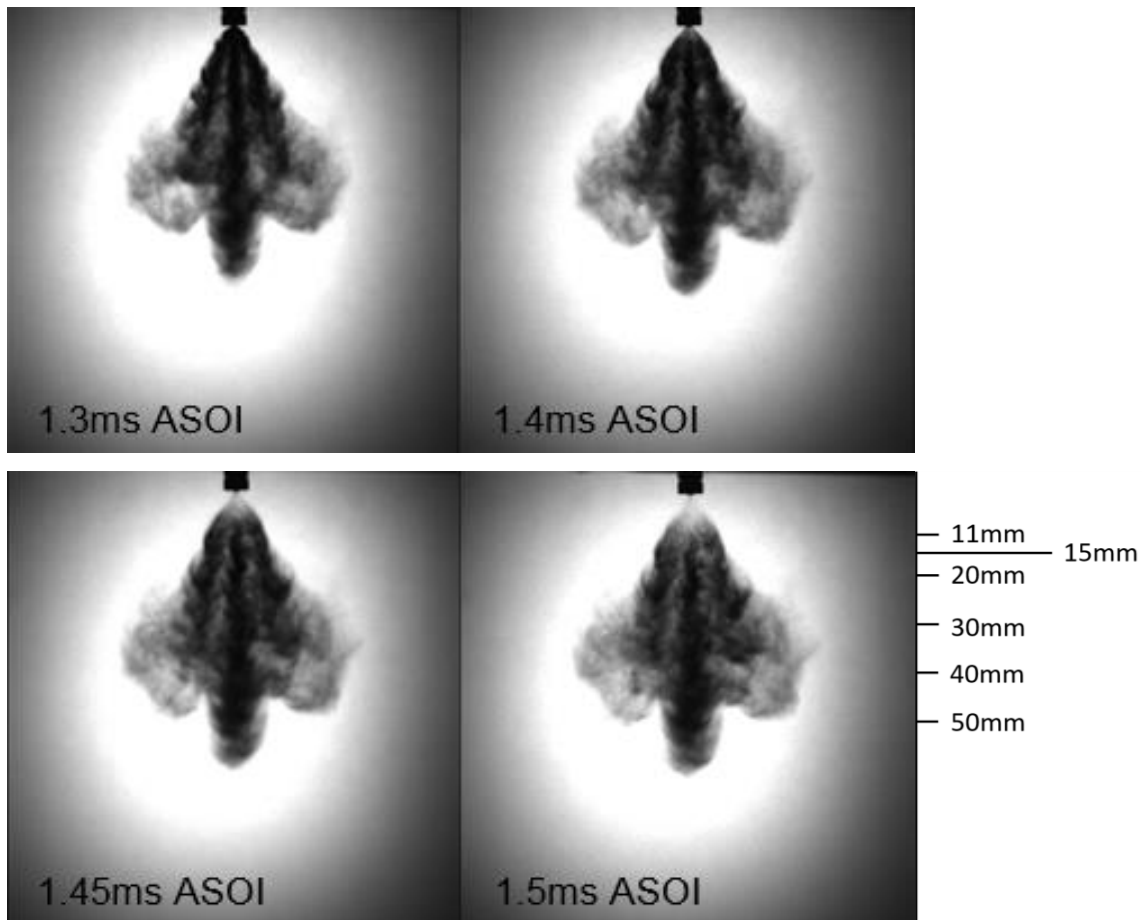
Figure 4.8: high-speed images (performed at 20KHz) of the spray development towards the end of injection for injection pressure of 20MPa and 1.5ms PW.
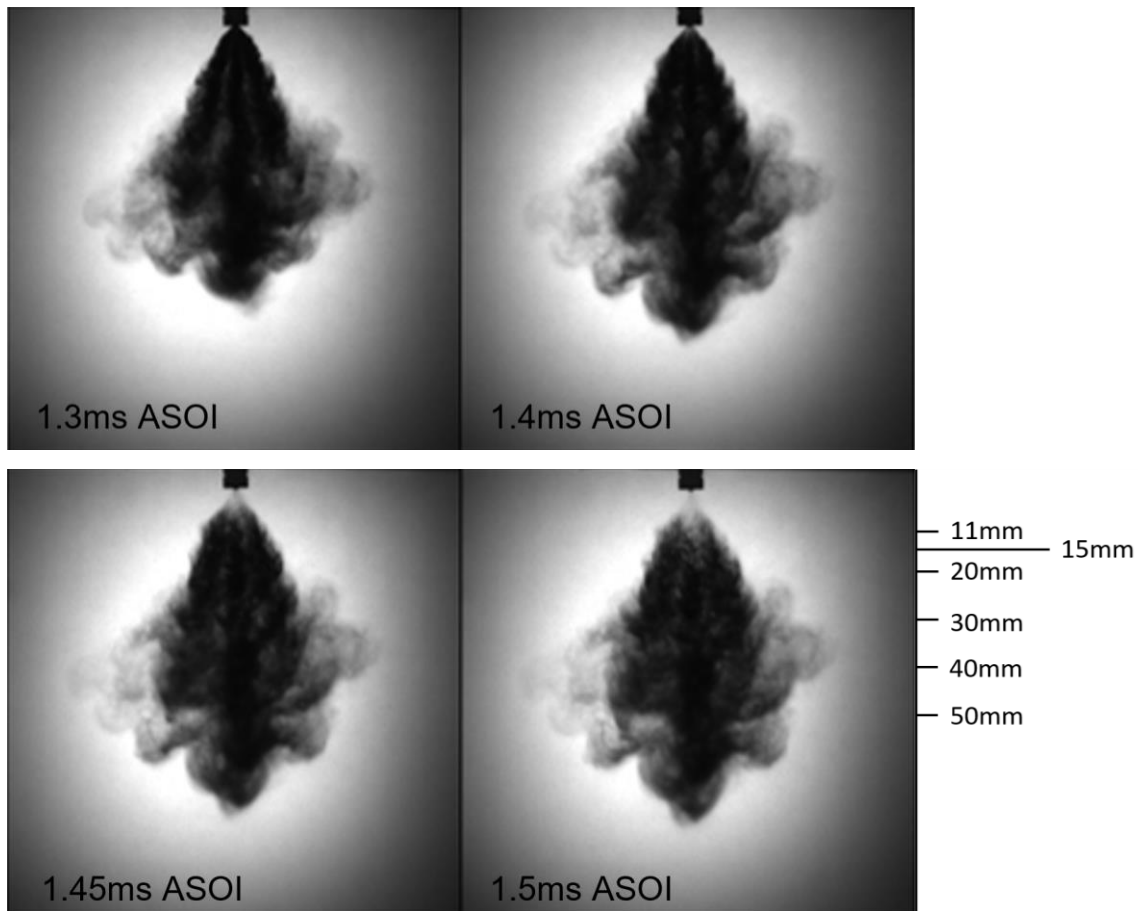
Figure 4.9: high-speed images (performed at 20KHz) of the spray development towards the end of injection for injection pressure of 35MPa and 1.5ms PW.

The effect of increasing pressure on the GDI spray angle is presented in Figure 4.10. The average GDI spray angle increases with increasing fuel rail pressures. This is due to the increasing radial component of the droplets' momentum stemming from the high injection pressures. The standard deviation error bars are significantly large which implies that the GDI spray angles vary extensively per injection case. The reason for this is the large spray liquid variability [137] which increases with increasing pressure. This is due to increased atomisation rates with increasing injection pressures, which results in variations in the radial spread of the sprays.
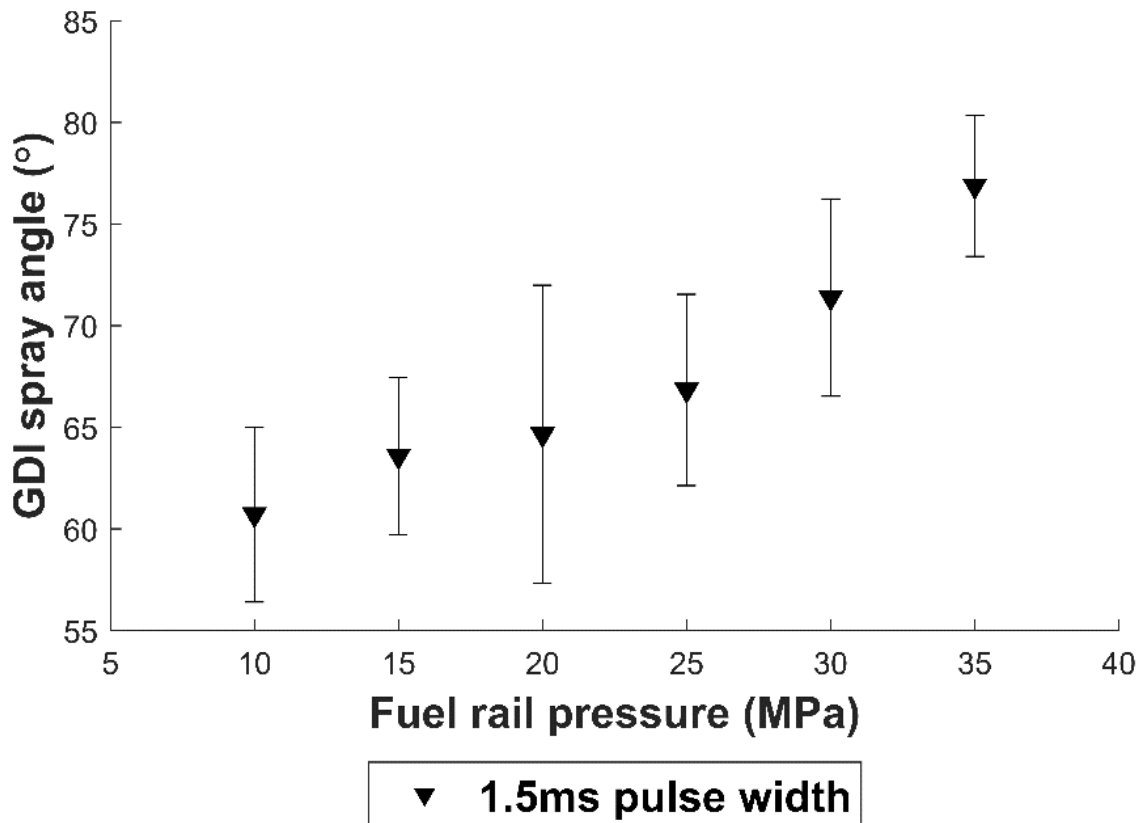
Figure 4.10: the effect of rail pressures on the GDI spray angles for single injections using 1.5ms pulse width. The spray angles were measured 1.5ms ASOI, using high-speed images at 20KHz. The error bars represent standard deviations in the penetration lengths.

4.3.2 Split Injections

The effects of first injections on the second injections' penetration lengths and spray angles, for varying split ratios, dwell times, PW sizes and pressures are discussed in this section.

4.3.2.1 Penetration Lengths

Figure 4.11 and Figure 4.12 present the effects of increasing dwell times on the average percentage decrease in the penetration lengths between the first and second injections for rail pressures of 20MPa and 35MPa, respectively. In this case, the differences between both injections' penetration lengths were determined before being averaged over ten cycles.
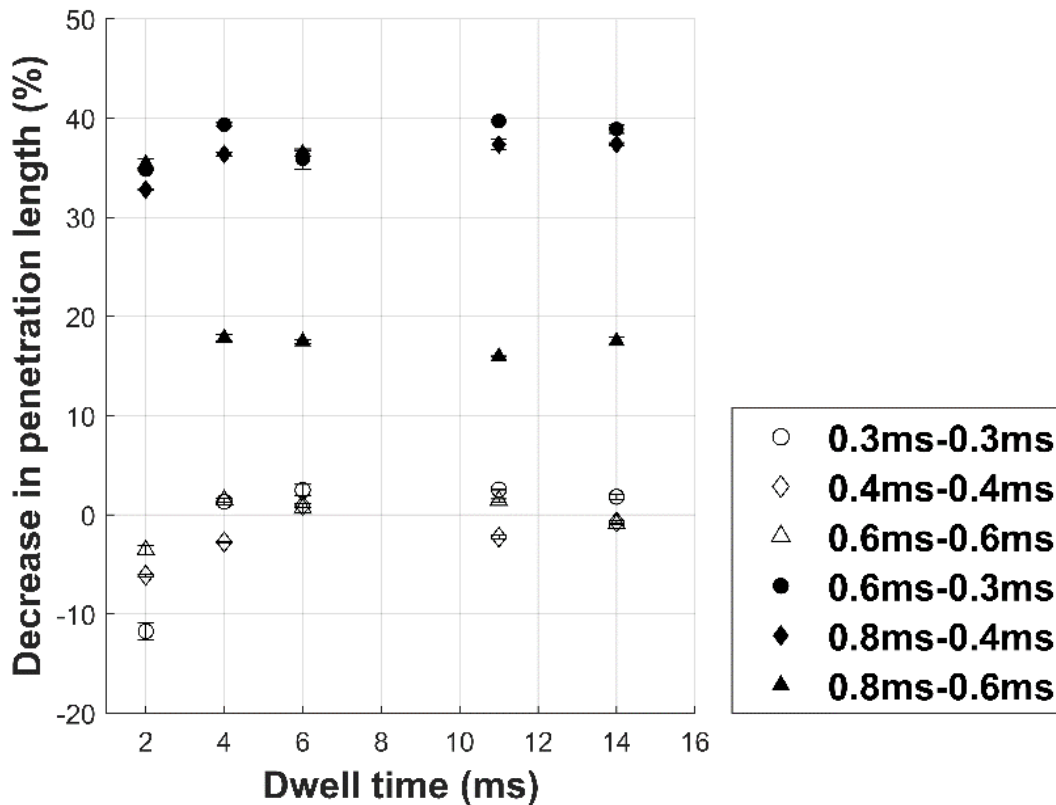
Figure 4.11: percentage decrease in the penetration lengths between first and second injections measured at 20MPa injection pressure, for increasing dwell times. The filled data plots represent 2:1 split ratio, while the unfilled data plot represent 1:1 split ratio.

Observing all 1:1 split ratios for both rail pressures, the penetration lengths of the second injections generally increase for dwells less than 6ms, as interpreted by the negative percentage reduction in the penetration lengths. This is indicative of the slip stream effects from the first injection events, whereby the droplets from the second injections are encouraged to accelerate through the flow field generated by the first injections.

The effect is most pronounced for 2ms dwell and is alleviated with increasing dwell time, as observed by the higher magnitude of the percentage reductions. Short dwell times allow the droplets from the first injection to still be in the vicinity of the flow field prior to the start of the second injection. In this case, the slip stream strength would be more pronounced when compared to larger dwells.
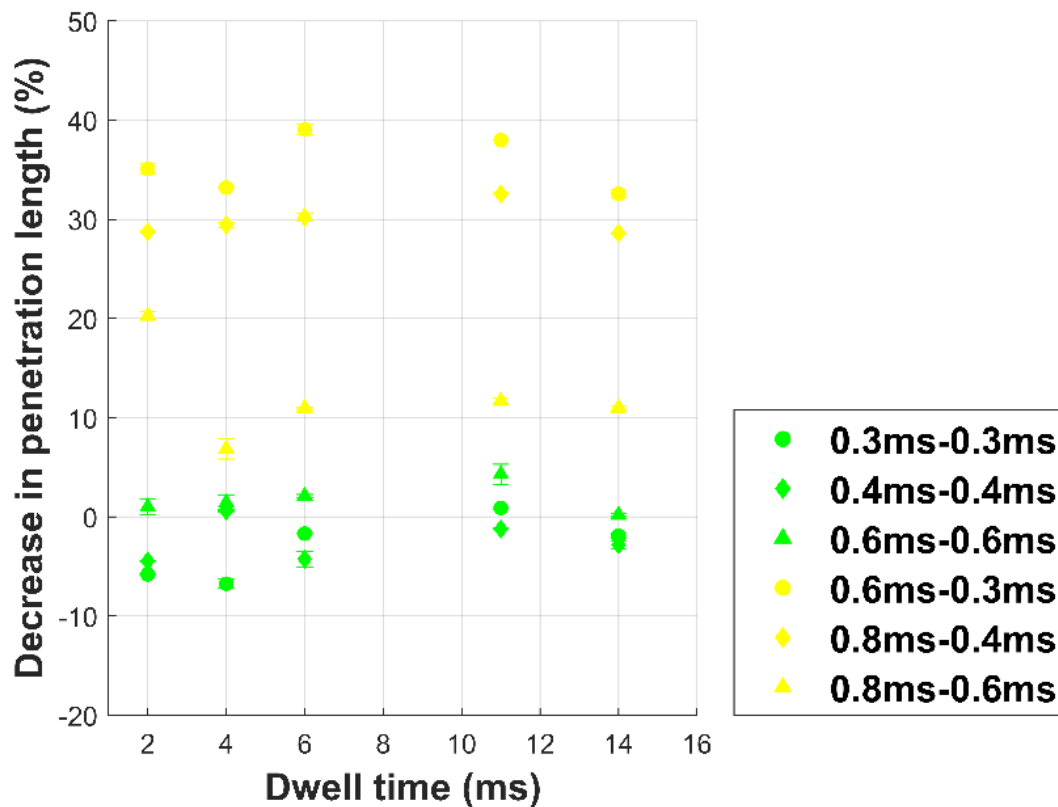
Figure 4.12: percentage decrease in the penetration lengths between first and second injections measured at 35MPa injection pressure, for increasing dwell times. The small split ratios are presented as green data points and large split ratios which are presented as yellow data points. The data points which lie in the negative y-axis region indicates an increase in the stated parameters.

A similar observation was made by Wood. A. [88], when employing 0.5ms-0.5ms PW combination, with dwells ranging between 250µs and 500µs, using a solenoid injector. He found the penetration length to be of a similar order of magnitude as the single injection with 1ms PW. The reason for this was stated to be the entrainment of the second injection, caused by the wake of the first injection, which reduced the shear forces generated on the second spray and caused it to accelerate. However, with such a short dwell time, this led the two sprays to combine further downstream, which is alleviated when using large dwell times greater than, and equal to 2ms.

In addition to split cases, another feature that increased the penetration length is 1) reduction in the initial fuel density and 2) increase in the initial fuel temperature, as was reported by Zhou et al., [138], using 15MPa injection pressure. These effects can increase the entrainment effects.

For dwell times larger than 6ms, the penetration lengths for both injection events are similar judging by the negligible percentage reduction. This implies that the large dwell times have negligible effects on the global axial spread of the second injections as the droplets from the first injection have more time to propagate away from the flow field prior to the start of the second injection. This can be visualised by the spray images presented in Figure 4.13. For the dwell times of 6ms and less, there is still a significant amount of fuel from the first injection present in the vicinity of the injector's tip by the end of the second injection.

A notable difference in the trends between the two injection events is that the extent of increase in the second injection's penetration length is reduced with increasing injection pressure. This is referring to the data points for the 2ms dwell case, whereby the percentage penetration length decrease has reduced for all data points for the 35MPa injection pressures, when compared to 20MPa pressure. Although the atomisation rate is improved with higher pressures as is commonly known, greater quantity of the fuel is injected. These features seem to generate drag forces against the propagation of the second injections, instead of encouraging their axial spread. This effect is also observed for the larger PW combination of 0.6ms-0.6ms under the same injection pressure and with the same dwell times, also indicating that greater injected quantity increases the spray resistive forces.

For all 2:1 and 1.33:1 injection ratios meanwhile, the penetration lengths of the second injections are smaller than their corresponding first injections (Figure 4.11 and Figure 4.12). This is because of the reduced amount of fuel injected in the second injection with their shorter PWs.
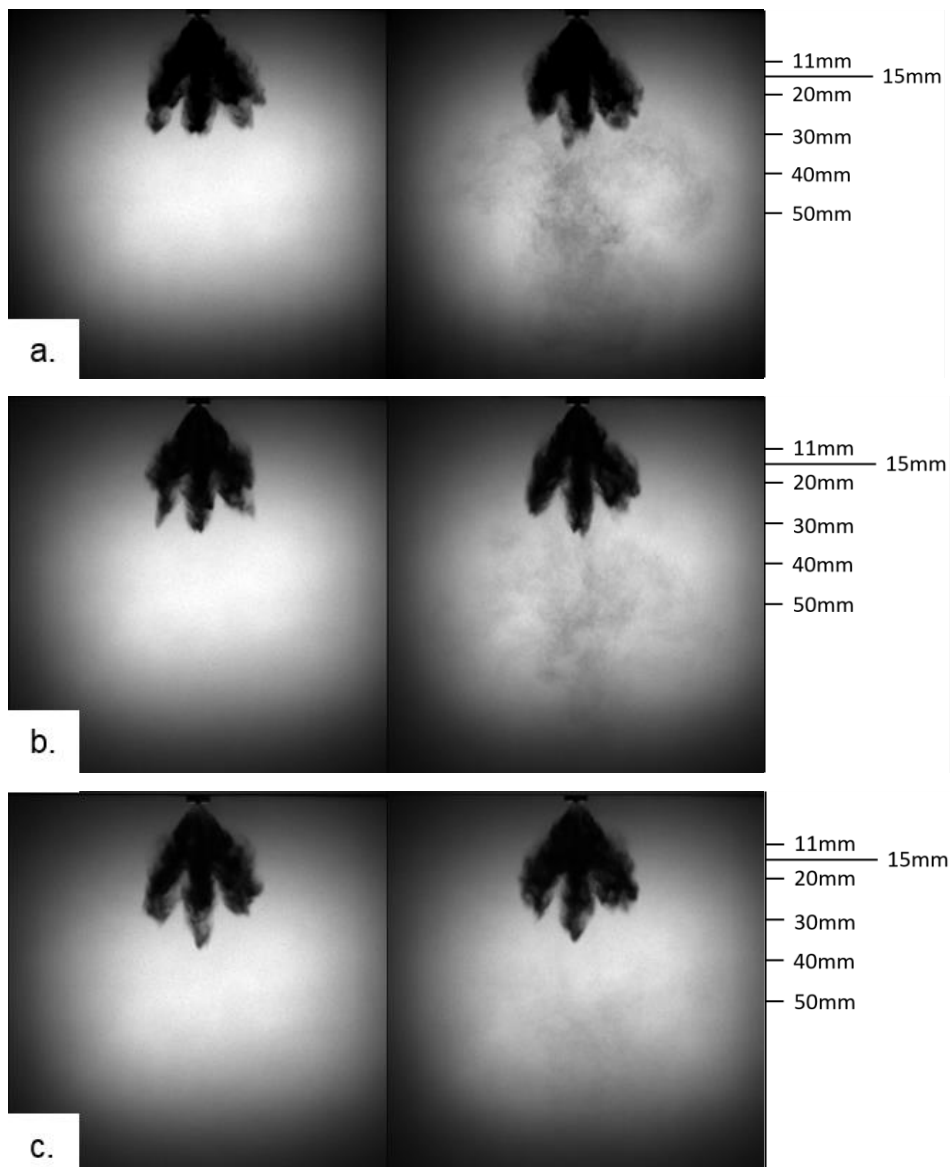
Figure 4.13: Spray images at the end of first injection (left) and end of second injection for PW combination of 0.3ms-0.3ms, 35MPa rail pressure and dwell times of a. 4ms, b. 6ms and c. 11ms.

The second injections' penetration lengths from the large split ratios are therefore compared against the equivalent PW of the single injections. The analysis is performed on 35MPa pressure cases tested, as this is the maximum pressure whose spray characteristics are of key interest for this project.

The percentage differences in the penetration lengths, PL (equation below) for increasing dwell time between the single injection and the second injection are presented in Figure 4.14. These are for PW combinations of 0.6ms-0.3ms (blue circle), 0.8ms-0.4ms (pink diamond) and 0.8ms-0.6ms (green triangle).

$$\text{PL decrease (\%)} = \frac{\text{PL}_{\text{single}} - \text{PL}_{\text{2nd inj}}}{\text{PL}_{\text{single}}} \times 100 \qquad\qquad \text{Equation 4.1}$$

Note that the single injection's PW compared here is equivalent to the second injection's PW. The trend indicates the differences in the penetration lengths between injection into atmospheric environment (single injection) and injection into a fuel rich environment generated by the first injection (effect of first injection on the second injection's PL).
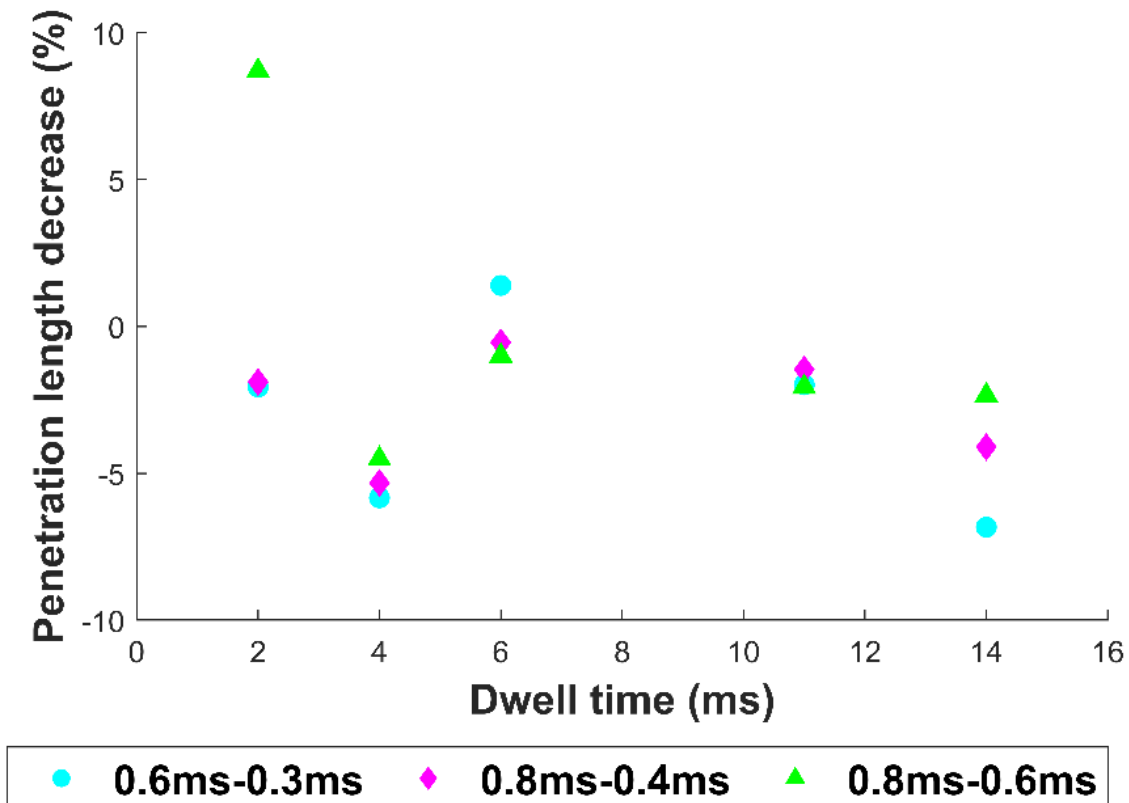
Figure 4.14: effects of increasing dwell time on the spray penetration length.

When compared to single injections of the same PWs, the second injections' penetration lengths generally increase for all PWs and dwell times when using large split ratios, with the injection pressure of 35MPa. The trend suggests that the second injection has higher axial momentum compared to single injections, which is somewhat aided by the flow field generated by the first injection. The result is slip streaming of the second injection past the first injection, whereby the flow field produced by the wake of the first injection generates a high momentum region.

Most of the data points in Figure 4.14 for all three PWs show similar extent of increase in the penetration lengths for each dwell time tested. This is the case

irrespective of the differences in the split ratio or PW combinations. This suggests that the first injection affects the flow field significantly and controls the axial spread of the second injection. The penetration of the second injection becomes independent of the split ratio at this pressure.

The exceptions are 2ms and 11ms dwell times. With the 2ms dwell time, the lower split ratio of 0.8ms-0.6ms (1.33:1) shows a decrease in the penetration length compared to the 2:1 split ratio. The axial momentum of the second injection is reduced with larger quantity injected in the second injection and smaller dwell time, compared to the 2:1 case. This could be the result of increased drag in the flow field generated by the first injection, especially with limited time preventing the first injection from propagating far downstream prior to the start of the second injection.

A similar observation was also made in the experimental studies by Martin et al., [139] when using an outward opening Piezo injector, with the dwell times ranging between 0.75ms to 4ms. They observed that the penetration length of the second injection had decreased, which was stated to be independent of the chamber pressure. They related this to the high phase density occurring due to cooling and evaporation along with the collision events between the two injection events.

The error bars for the short PW combination of 0.6ms-0.3ms are in the range of 3% and 6.3%, with the largest error bar of 6.3% observed for the 11ms dwell case. For the larger PWs cases of 0.8ms-0.4ms, the error bars fall in the range of 3.2% and 7%, with the largest error bar observed for 4ms dwell time. For the small split ratio of 1.33:1, the error bars are in the range of 2.2% and 9.3%, with the largest error bar again corresponding to 4ms dwell time. The error bars, just like the percentage decrease in the penetration lengths, are similar for each dwell time for all three split ratios, particularly at short dwells. This verifies that the second injection's penetration length is independent of the split ratios to an extent. It is however reported in [88] that such large dwell times employed in the current study poses difficulties with regards to the reproduction of reliable second injections. When employing large dwells, the cyclic variability in IMEP can therefore partly be affected by this.

4.3.2.2 GDI Spray Angles

The ideal flow field using the split injection strategy for stratified charge operation are global pre-mixed homogenous charge with early first injection, and local stratified charge with a compact spray structure achieved from the second injection. This section evaluates the effects of the first injection and increasing pressure on the extent to which the spray from the second injection spreads radially.

For the rail pressure of 35MPa, observing all 1:1 split ratios (Figure 4.15), there is a general reduction in the second injections' spray angles compared to the first injections. This effect is more pronounced with the large PW of 0.6ms. Although the injection momentum is high for both PWs due to the high rail pressure, the radial spread of the second injection is reduced while the penetration lengths had increased (for short dwells). The reduction in the spray angle for small dwell times suggests that the spray from the first injections resist the radial spread of the second injections.
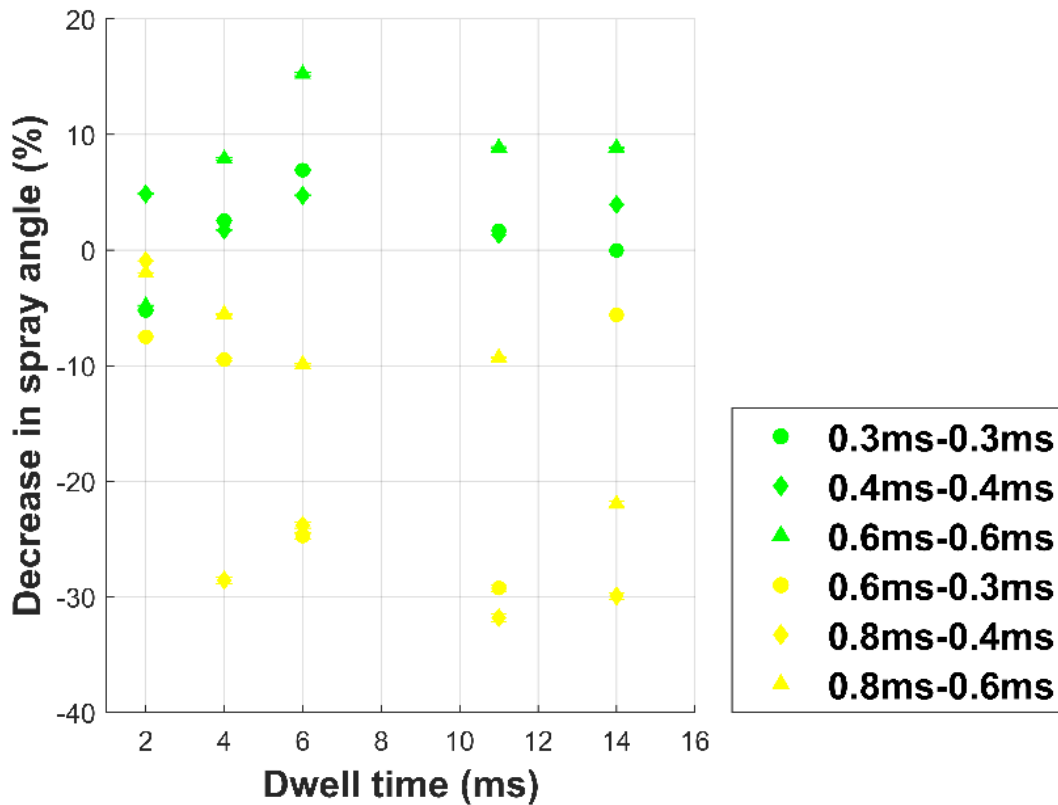
Figure 4.15: percentage decrease in the GDI spray angle between first and second injections at 35MPa for small split ratios presented as green data points and large split ratios which are presented as yellow data points. The data points which lie in the negative y-axis region indicates an increase in the stated parameters.

Observing the larger split ratios (Figure 4.15), the spray angles of the second injections are larger than the first injections across all PWs, albeit the PW of the second injection being shorter. Past 6ms dwell time, the angles increase with increasing dwell times too.

To better understand this trend, the percentage differences in the GDI spray angle (SA) for increasing dwell time between the single injection and the second injection of the split cases (equation below) are presented in Figure 4.16. These are for the larger spit ratios with PW combinations of 0.6ms-0.3ms, 0.8ms-0.4ms and 0.8ms-0.6ms.

$$SA\ decrease\ (\%) = \frac{SA_{single} - SA_{2nd\ inj}}{SA_{single}} \times 100$$
Equation 4.2

The trend indicates the difference in spray angles between injection into atmospheric environment (single injection) and injection into a fuel rich environment generated by

the first injection (effect of first injection on the second injection's SA)
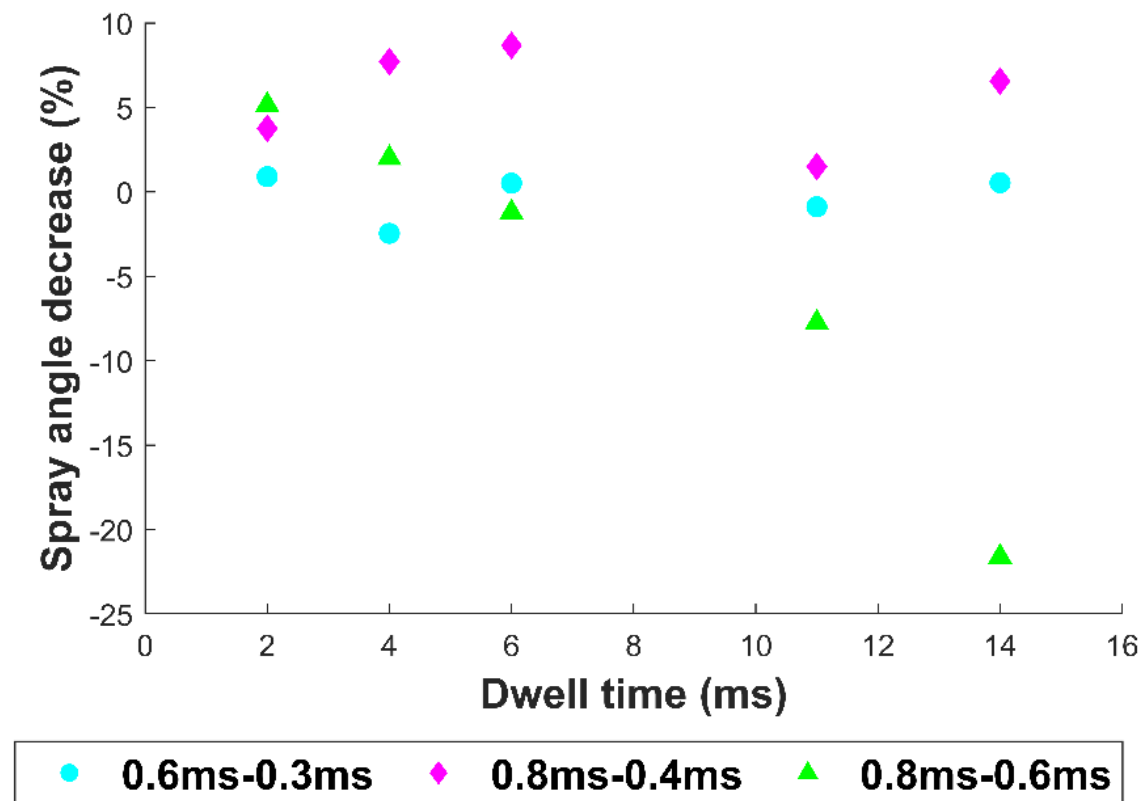
Figure 4.16: effect of increasing dwell time on the GDI spray angle.

There is minimal impact on the radial spread of the second injection for the short PW of 0.6ms-0.3ms. This implies that for the short PW combinations, the radial spread is hardly affected by the changes in the ambient conditions and therefore different dwell times to an extent. Meanwhile, for this PW combination, the penetration length of the second injection in Figure 4.14 was observed to increase across all dwells. This suggests that the axial momentum of the second injection, generated by the wake of the first injection, is more predominant than the radial momentum for the short PWs.

For the larger PW of 0.4ms, the spray angles across all dwells are generally reduced. The reduction is most pronounced for dwell of 6ms or less. In this case, the second injection's penetration length had increased at this PW and shorter dwells. It could be deduced from these trends that for the PW combination of 0.8ms-0.4ms, most of the droplets from the second injection spread axially, keeping it compact radially. The effects of the larger first PW are most likely to dominate the spray characteristics here, generating resistance against the propagation of the radial spread.

For the larger PW case of 0.8ms-0.6ms, the spray angle of the second injection is reduced for dwell of 4ms or less, but increases significantly for the larger dwells past 6ms. In this case, increasing dwell thus encourages both radial and axial spread of the second injection. This could be due to the alleviated resistance from the droplets in the vicinity of the second injections when using short dwell times.

When compared to the 2:1 case of 0.8ms-0.4ms PW, the 1.33:1 injection ratio exhibits small differences in the percentage penetration length decrease with increasing dwell time, especially past 6ms. Its spray angles of the second injection on the other hand increase with increasing dwell time. This trend suggests that increasing the dwell provides the flow from the first injection sufficient time to propagate downstream. This in turn reduces the drag effects, noted earlier for short dwell, of the first injections on the second injection. Most of the spread of the second injection is therefore concentrated radially, thereby encouraging larger spray angle with minimum impact of the increasing dwell time on the penetration length at this split ratio.

The error bars for the 2:1 split-ratio of 0.6ms-0.3ms and 0.8ms-0.4ms range from 3.1% to 4.8% and 3% to 4.3%, respectively. For the small split ratio of 1.33:1, the error bars are in the range of 5% and 12.7%, with the largest error bar corresponding to 11ms dwell time. Such a large error bar suggests that the second injection's spray angle for 11ms dwell time could potentially increase. Overall, the error bars of the small split ratios are larger than the 2:1 split cases. This indicates the inconsistencies of the second injection's radial spread pertaining to the small split ratio, in spite of the greater radial spread of the second injection observed here.

The large error bars can be attributed to the large shot-to-shot variability due to the combination of the transitory characteristics related to the sizes of the PWs and internal pressure waves, as was reported by Payri et al., [135].

In summary, the results generally show that for the large split ratio of 2:1, the axial spread of the second injection persists, while the spray remains radially compact at sufficiently small dwells. A smaller split ratio on the other hand encourages the radial and axial spread of the second injection, with large shot-to-shot variations both radially and axially.

4.4 Studies of Droplet sizes and velocities

The results presented here are those obtained from the PDA measurements, discussed in the methodology, Section 3.1.4.

The axes and points of measurements in the flow field are indicated in Figure 4.17. The focus of the study was to characterise the droplets in the core of the rear plume. The measurements were therefore performed along the axis of the rear plume, as indicated in Figure 4.17b. The elevations (z-coordinates) tested were 11mm (also referred to as near-nozzle region), 15mm and 20mm for the 0.4ms PW. The elevations measured with larger PWs also included 30mm and 40mm downstream of the injector tip.

a.   b.
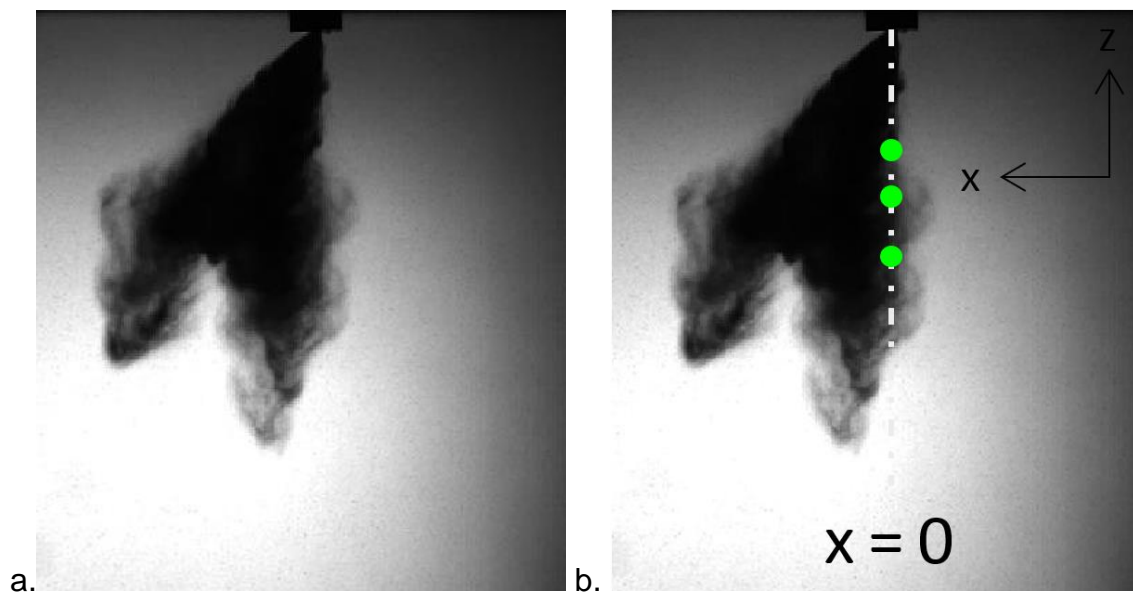
Figure 4.17: representation of the measurement points in the flow field for the 0.4ms PW. Image a. is the spray captured using back-light imaging at the end of injection for the 0.4ms PW and 35MPa injection pressure. Image b. represents the control volumes (green dots) positioned in the core of the rear plume for elevations of 11mm, 15mm and 20mm downstream of the injector.

The uncertainties in velocities presented in the results are the standard deviations of the measured droplet velocities. The uncertainty in SMDs were calculated using the ratio between the CoV of D_i^3 and D_i^2 as defined below:

$$\text{SMD uncertainties} = \frac{\left(s_D(D_i^{\;3}) / \overline{D_i^3} \right)}{\left(s_D(D_i^{\;2}) / \overline{D_i^2} \right)}$$

S_D in this case is the standard deviation and D_i is the measured droplet size. The SMD uncertainty calculation has no unit.

Furthermore, as was observed in the earlier investigations of the injection quantity and macroscopic spray characterisation, 14ms dwell time was generally too large a dwell for there to be any impact on the second injections. 14ms dwell time was therefore not investigated in this section.

4.4.1 1:1 Split Ratio

For the 1:1 split ratio, the spray characteristics from the PDA measurements, for the PW combination of 0.4ms-0.4ms, are investigated. The total PW of the single injection was 0.8ms and the dwell times analysed are 2ms and 6ms.

Less than 100 drop counts were detected for the 11ms dwell case, which were deemed insufficient for data validation purposes. This was because 11ms dwell time provided the droplets from the first injection sufficient time to propagate away from the vicinity of the injector. As a result, the drop counts in the second injection were significantly less due to the reduced interaction with the first injections.

4.4.1.1 Analyses of the Droplet Velocities

Figure 4.18a. and b. represent the average velocities and overall drop counts respectively, across varying axial locations in the core of the rear plume (Figure 4.17). The data is the average of the total droplets crossing the measurement volume each test cycle, for the 50,000ms AT, and so include both injection events.

11mm downstream of the injector, the average velocities for the split cases are higher than the single injection event, with the largest dwell time of 6ms possessing the highest average velocities at this position. The average velocities for the split cases at 20mm elevation decrease to stagnation however. The corresponding drop counts 11mm downstream for all test cases are generally similar, with a slightly lower drop count measured for the 6ms dwell time.

a.

b.
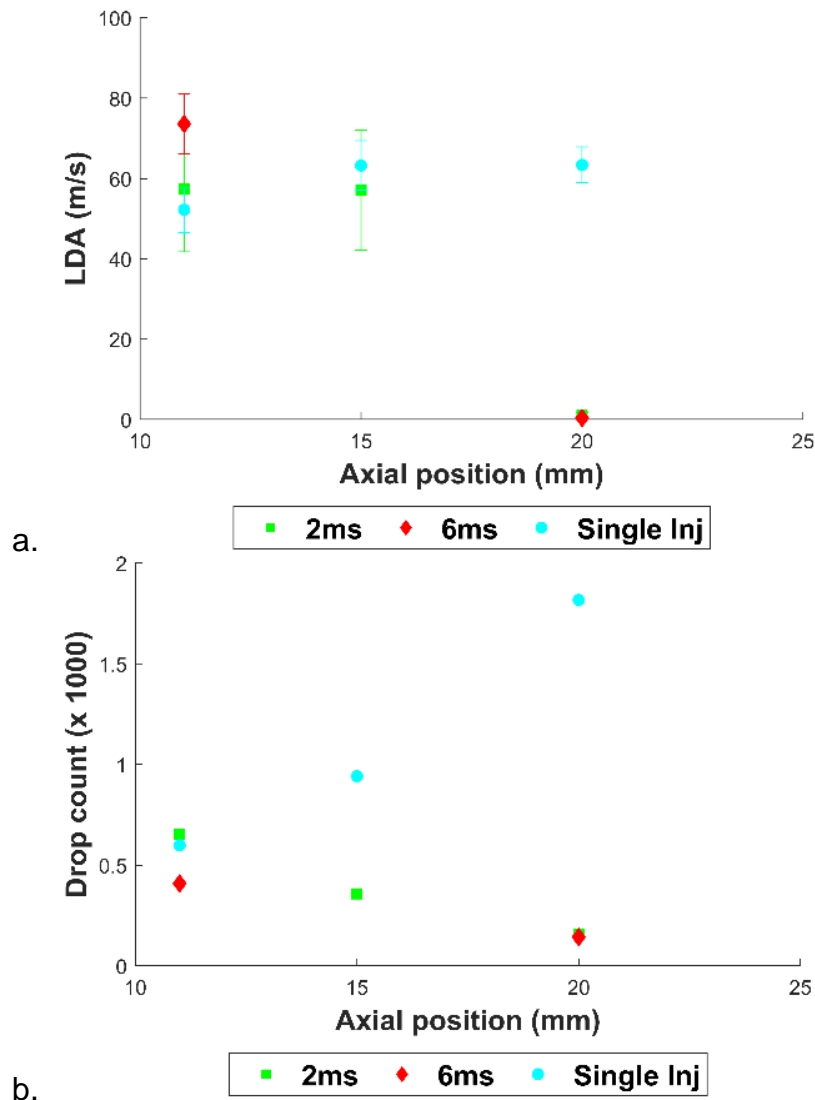
Figure 4.18: axial trends of the droplets inside the plume's core representing a. droplets velocities with the standard deviation error bars and b. drop counts along various distances downstream of the injector. The PW combination is 0.4ms-0.4ms for the tested split cases and the PW for the single injection is 0.8ms.

To further understand these trends, Table 4.1 provides the averaged velocities and drop counts for the first and second injections, for both dwell times tested 11mm downstream. The transient trends of the velocities and the mean velocities for the three tested cases at this elevation are subsequently presented in Figure 4.19.

The transient trend in velocities (Figure 4.19a.) shows a large number of droplets in the second injection event which possess low velocities, in the range of -20m/s to 20m/s, when compared to the first injection. These velocities are observed from the start of the second injection. The low droplet velocities in the first injection event are detected towards the end of the first injection, which are in fact low in number. One

reason for this is the effect of the sudden valve's closing event towards the end of the first injection, which reduced the pressure due to the throttling effects [140]. This causes deceleration of the droplets prior to exiting the nozzle, which is possibly why the low droplet velocities were detected towards the end of the first injection.

Table 4.1: average velocities, their corresponding standard deviation (S_D) uncertainties, and drop counts measured at two injection events for dwell times of 2ms and 6ms, 11mm downstream of the injector for the 0.4ms-0.4ms PW combination.

Dwell time (ms)	1st injection average velocity (m/s)	S_D uncertainty (m/s)	2nd injection average velocity (m/s)	S_D uncertainty (m/s)	Drop count - 1st injection	Drop count - 2nd injection
2	75.6	30.8	58.7	35.0	156.0	495.0
6	74.5	28.3	72.2	31.8	212.0	195.0

Upon the valve's opening for the second time after 2ms dwell, there are greater number of low velocity droplets, in the range of -20m/s to 20m/s. Some of these droplets are even detected prior to the start of the second injection. In addition, the drop counts have now more than tripled, when compared to the first injection, albeit the PW being kept the same.

This suggests that a number of droplets in the control volume in the second injection event would be those originating from the first injection, which would have been recirculating (as can be interpreted by the large negative velocities) and had propagated towards the vicinity of the injector tip prior to the start of the second injection. It is suspected that high injection pressure would intensify the recirculation velocity. This could cause some droplets, particularly those at the edges of the plume, to travel upwards and close to the injector tip. This phenomenon would have thus led to the reduced average velocity and larger drop counts measured in the second injection event for the 2ms dwell time (Table 4.1).

Figure 4.19: transient trends of the droplet velocities measured 11mm downstream of the injector for a. 2ms dwell case, b. 6ms dwell case and c. single injections. The PW combination is 0.4ms-0.4ms for the tested split cases and the PW for the single injection is 0.8ms. The black trend line represents the average droplet velocities.

The recirculating droplets close to the injector tip has been stated to form fuel films on the nozzle, as reported by Medina et al., [33]. A shear layer is formed between the injected fuel and the ambient gases inside the chamber, which is caused by a complex mixing process that generates air entrainment and mixture between the liquid and vapour phases of fuel with the air. When the mixing occurs, vortices of fuel droplets and vapour are formed, which re-entrain fuel and air back into the bulk flow. This could be the sources of the droplets detected with large negative velocities in the control volume. Those droplets that manage to escape the vortices end up being deposited on the injector tip due to the low-pressure zones formed near the nozzle exit [33].

Contrary to this trend, a dwell time of 6ms shows similar velocity profile (Figure 4.19b.) along with similar averaged velocities and drop counts for the two injection events (Table 4.1). This suggests that a dwell time of 6ms is sufficiently large, allowing droplets from the first injection to propagate away from the vicinity of the injector prior to the start of the second injection. This would minimise interactions between the two injection events, but not completely eliminate it.

The droplets with near-zero velocities are again slightly larger in number in the corresponding second injections, when compared to first injections. The presence of these low velocity droplets throughout the second injection implies that even with such a large dwell time, there is the possibility of droplets from the first injection interacting with the second injections, albeit significantly lower in number than those observed in the second injection after 2ms dwell time.

There is a consistency in the trend of the low velocity droplets being observed towards the end of the first injection for both dwell cases tested. This repeated behaviour confirms the effect of the valve closing on the droplets' exit velocities.

Another possible reason for the occurrence of the near zero velocities in both injection events is the likelihood of the droplets detected in this region travelling perpendicular to the plume's direction of motion. This is most likely caused by the large injection pressure, which would cause the droplets to travel with both high radial component and axial component of momentum upon the droplets exit from the nozzles. The low velocity region is also present in the single injection case (Figure

4.19c.), but the frequency of this occurrence is large, which alleviates the large fluctuations in the average velocity profiles, when compared to the split cases.

This effect was also observed by Jiang et al., [141] in their studies using 20MPa injection pressure. They found that smaller particles had a wide range of plume perpendicular velocity close to the injector, while the largest particles that possessed greater momentum continued along the direction of the plume with low transverse velocities. The smaller droplets had responded to the turbulent entrained airflow time scales more readily than the large drops.

However, while this phenomenon is possible, the fact that the low velocities measured towards the end of the first injection indicates that there is a high likelihood of these detected droplet velocities being caused by the valve's closing events. The larger number of droplets with high negative velocities detected in the second injection, along with the greater drop counts, points toward the interaction of droplets from the first injection with the second injections.

Another observation in the transient trend is the similarities in the second injections' droplet arrival times for both dwell times tested 11mm downstream. The droplets arrive around 0.9ms after the end of the specified dwell time for both dwell cases. This consistency further confirms the lack of needle bounce and the interference of the eddy currents from the first injection on the valve opening time of the second injection, which was observed by Wood, A, [88] using shorter dwell times. The similar arrival times indicate repeatable start of injection times for the solenoid injector, which can be achieved at a minimum dwell time of 2ms.

This however, could be seen as a disadvantage as the repeatable events of the valve's full opening and closing effects would impact the droplet sizes, as is observed in the following section. On the other hand, Moiz et al., [74], found that using a split PW combination of 0.3ms-1.2ms, with a dwell time of 0.65ms, helped achieve a higher quasi-steady lift-off length, which increased the entrainment effects of the surrounding oxygen in the flame region and led to leaner combustion, when compared to a shorter dwell time of 0.5ms.

These effects would be intensified when employing larger dwells of 2ms, which would provide sufficient time for the entrainment of the surrounding charge with the atomised droplets from the first injections, prior to the start of the second injection. A

potential drawback however would be reduced momentum of the droplets from the first injections towards the end of the dwell time, which could affect the rate of entrainment. As such, 6ms dwell time would be less favourable in generating a well-mixed lean mixture, with high entrainment rate, when compared to 2ms dwell time.

The trend in velocities for the split cases 20mm downstream changes considerably. The transient trends in velocities at this elevation are provided in Figure 4.20 and the averaged velocities and drop counts for both injection events are provided in Table 4.2.

Table 4.2: average velocities, their corresponding S_D uncertainty, and drop counts measured at two injection events for dwell times of 2ms and 6ms, 20mm downstream of the injector for the 0.4ms-0.4ms PW combination.

Dwell time (ms)	1st injection average velocity (m/s)	S_D uncertainty (m/s)	2nd injection average velocity (m/s)	S_D uncertainty (m/s)	Drop count - 1st injection	Drop count - 2nd injection
2	-0.4	0.8	1.6	1.8	36.0	120.0
6	-0.2	1.1	0.7	1.0	41.0	141.0

For both split cases, the droplets from the first injection are generally recirculating upwards towards the injector, indicating heavy recirculation region at this point. This is represented by the large number of droplets in the negative velocity region (Figure 4.20 a. - b.). It is suspected that the plume axis is slightly deflected towards the x co-ordinate of the injector axis (Figure 4.17), so the droplets measured at this position would be slightly offset from the core of the plume being studied 20mm downstream. However, these droplets seem to create a slip-stream region whereby the droplets from the second injection are accelerated, judging by the higher overall velocities in the second injection event. This indicates that the droplets from the first injection not only creates a region where the droplets from the second injection are encouraged to accelerate, but also causes the angle of the second plume to reduce slightly, as was also reported in section 4.3.2, whereby a reduction in the second injection's spray angle was observed. This is independent of the dwell time, as both dwell times

indicate a similar transient trend. These larger velocities in the second injections would also enhance the entrainment rate of the surrounding charge and generate a lean pre-mixed mixture prior to the start of the second injection [74] along with a sufficiently large dwell time.

A similar trend was observed by Wood, A, [88], when short dwell times in the range of 0.35ms to 1ms were employed. The author observed that at an axial distance of 10mm from the injector tip, both injection events presented a similar velocity profile. Further downstream, there was an increase in the maximum velocity observed for the second injection, which was stated to be caused by entrainment from the wake of the first injections. This consistency in the trends suggests that the slip streaming effects from the first injections are even considerable when large dwells of up to 6ms are employed, which could even affect the flow characteristics and mixture formation inside the combustion chamber, when employing the first injection in the intake stroke and subsequent injections in the compression stroke.

Observing the trends in the single injection, the overall drop counts increase 20mm downstream, compared to 11mm and 15mm elevations. The average velocities along the axial distance are similar, with a slight increase in the velocity 20mm downstream when compared to the near nozzle region. This suggests that 11mm downstream, with the large PW, the highly fuel dense region near the nozzle made it difficult for all the droplets to be detected. As the optical detection is improved further downstream, greater number of droplets are measured in this region. This indicates that the detection 11mm downstream possesses some difficulties in representing the actual droplet density.

It was reported in [141] that both the validation rate and average data rate had increased with increasing distance away from the injector tip, due to the increased signal strength. In addition, the data rate in the plume centre was reported to be the highest, with the cost of reduced validation rate due to the dense spray obscuring the optical paths. As a result, the slightly larger droplet velocities observed 20mm downstream, when compared to 11mm downstream, could be due to the improved optical strength further downstream. This means that the accuracy in the actual average velocity in the near nozzle region could be affected.

Figure 4.20: transient trends of the droplet velocities measured 20mm downstream of the injector for a. 2ms dwell case, b. 6ms dwell case and c. single injections. The PW combination is 0.4ms-0.4ms for the tested split cases and the PW for the single injection is 0.8ms. The black trend line represents the average droplet velocities.

4.4.1.2 Analyses of the Droplet Sizes

Figure 4.21 represents the SMDs (D32) of the droplets across varying axial locations in the plume investigated.
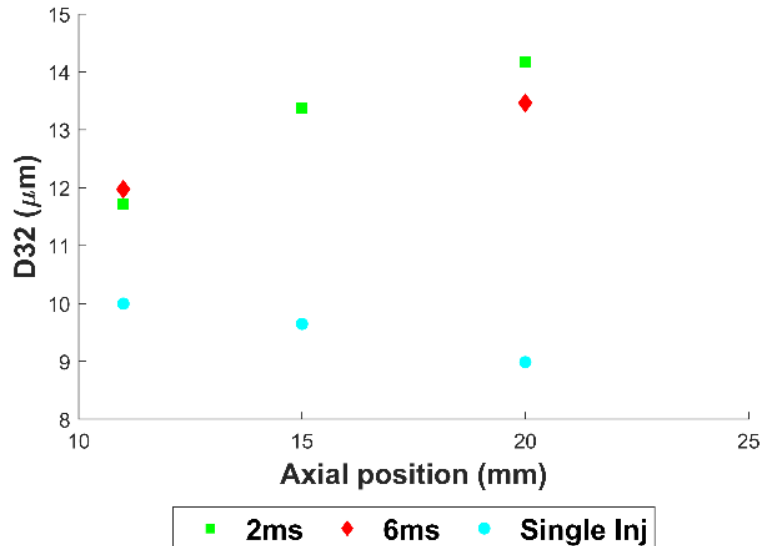
Figure 4.21: axial trend in the SMD (D32) of the droplets inside the plume's core, measured along various distances downstream of the injector. The PW combination is 0.4ms-0.4ms for the tested split cases and the PW for the single injection is 0.8ms.

The trend shows that the droplets injected in a single injection event are generally smaller across all elevations. Additionally, while the SMDs for the single injections decrease with increasing axial distance, the SMDs for the split cases increase.

To understand the physical mechanisms causing this trend, we analyse the transient trends in the droplet sizes for all injection cases tested. Table 4.3 and Table 4.4 provide the SMDs and SMD standard deviations for the first and second injections, 11mm downstream and 20mm downstream, respectively. The transient trend of the droplet sizes and the average droplet sizes for the three tested cases are presented in Figure 4.22 and Figure 4.23, 11mm and 20mm downstream of the injector, respectively.

Table 4.3 and Table 4.4 show that for the elevations of 11mm and 20mm, the SMD of the first injections are of similar order of magnitude as the single injection. This indicates that the variation in PWs or the injected quantity has little effect on the droplet sizes close to the injector. The droplet sizes at this elevation could be primarily governed by the high injection pressure.

Table 4.3: SMD and the corresponding uncertainties in SMDs measured at two injection events for dwell times of 2ms and 6ms, 11mm downstream of the injector for the 0.4ms-0.4ms PW combination.

Dwell time (ms)	1st injection SMD (μm)	SMD uncertainties	2nd injection SMD (μm)	SMD uncertainties
2	11.8	1.7	17.9	2.3
6	10.2	1.5	13.5	1.5

The SMD and the corresponding uncertainty for the second injections increase considerably for the 2ms dwell case, when compared to the first injection event. Observing the transient trend in the droplet sizes for this dwell case (Figure 4.22a.), larger number of droplets are observed in the range of 15μm to 30μm in the second injection event, which have caused the SMD to increase in comparison.

The larger SMD in the second injection can be correlated with the large number of droplets that possessed high negative velocities observed in the second injections (Figure 4.22 a. - b.). The larger SMD in the second injection can thus be attributed to the droplets from the first injection present in the control volume during the second injection, which would interact with other droplets. This would subsequently cause the droplets from both injection events to coalesce with each other and form larger droplets overall.

This is contrary to the observations made in [88]. They observed that the number of large droplets for the second and subsequent injections had been greatly reduced due to the faster opening of the valve with split injection strategies, when employing short dwells times. A steady state spray was achieved more rapidly than for a comparable single injection. One disadvantage with using large dwell times greater than 2ms therefore is the absence of the eddy current from the first injection advancing the second injection and the effect of the valve bounce on the second injection, which had resulted in overall reduced droplet sizes.
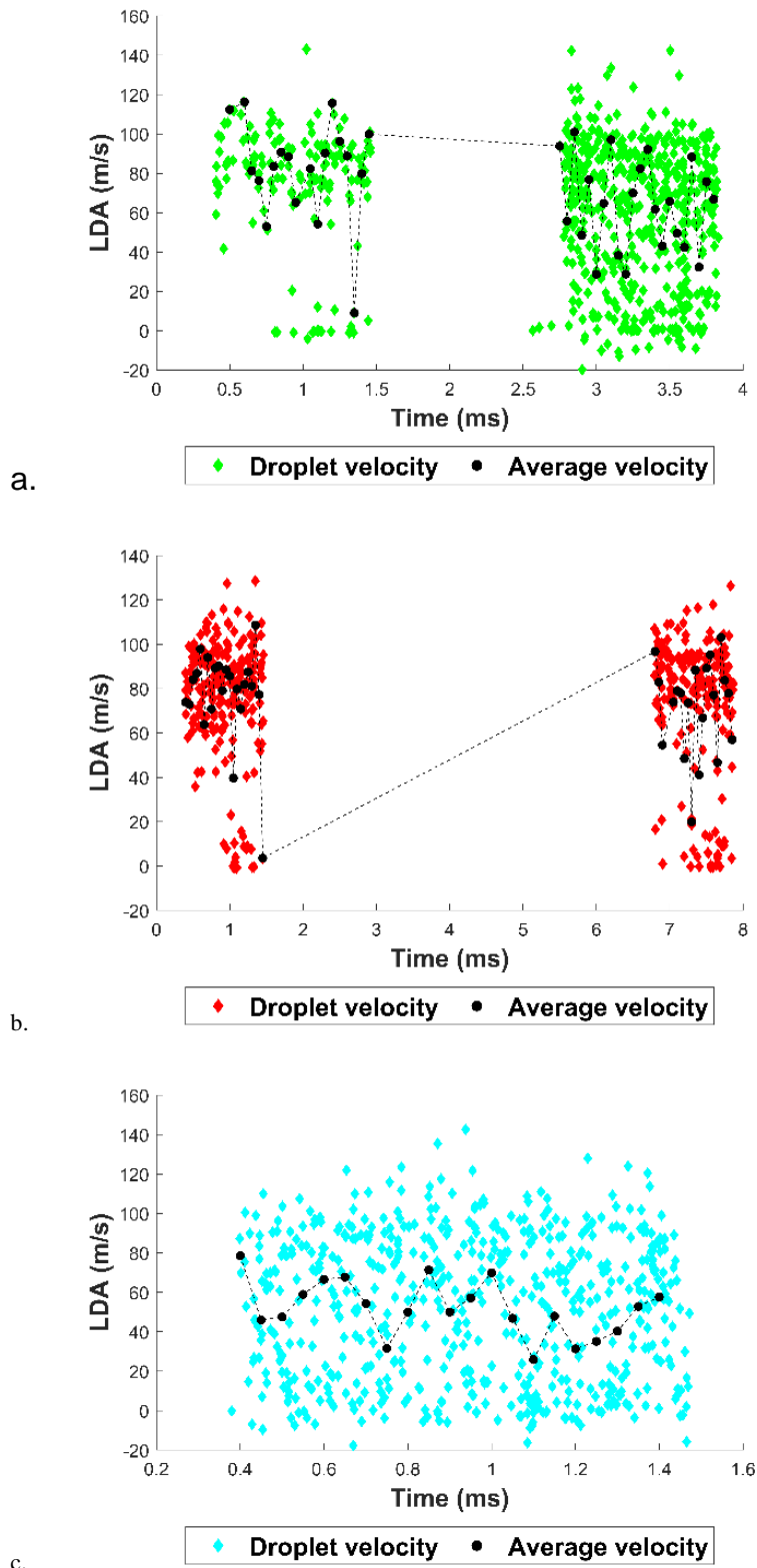
a.

b.
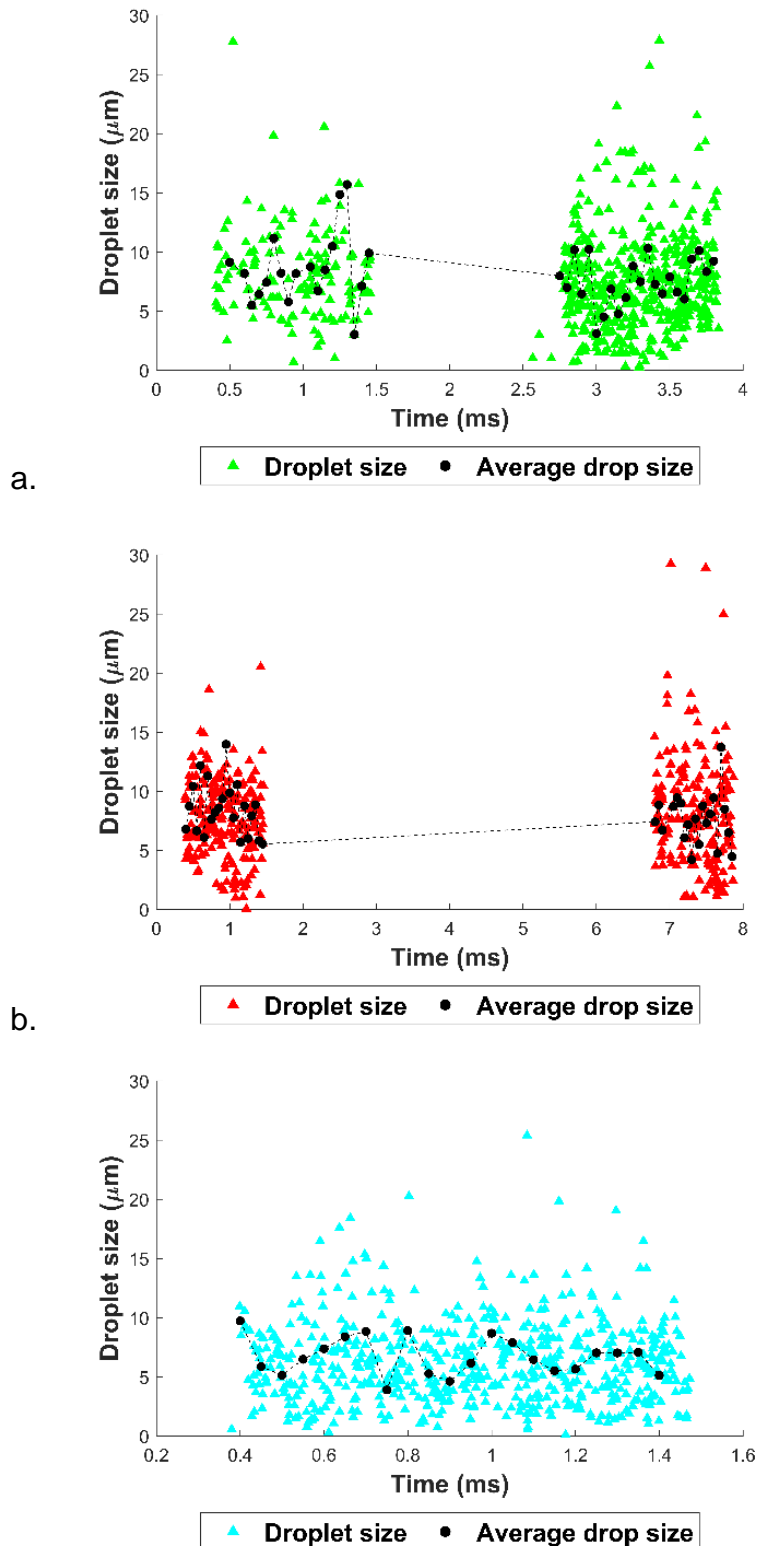
c.

Figure 4.22: transient trends of droplet sizes measured 11mm downstream of the injector for a. 2ms dwell case, b. 6ms dwell case and c. single injections. The PW combination is 0.4ms-0.4ms for the tested split cases and the PW for the single injection is 0.8ms. The black trend line represents the average droplet sizes.

When observing the transient trends of the droplet sizes in the first injection, the average droplet sizes increase towards the end of the first injection. This is the region where the low velocity droplets were observed, which was stated to be affected by the closing period of the solenoid valve. It can thus be deduced that along with the reduction in the exit velocities towards the end of the first injection, the droplet sizes are also affected.

Mouvanal, S. [31] and Medina et al., [33] observed that the end of injection event had led to tip wetting, with large droplets settled at the tip of the injector caused by the large surface tension forces and reduction in pressure due to the throttling effect. These effects had formed large droplets and ligaments. While macroscopic visualisation close to the injector tip was not performed in the current study, the subsequent large droplets measured towards the end of the first injection event, 11mm downstream of the injector, could be correlated to the reduced pressure of the droplets prior to exiting the nozzle during the closing event, potentially forming large droplets.

The SMD for the 6ms dwell case is also observed to increase in the second injection event, but to a lesser extent compared to the shorter dwell case. This is again owing to potential interactions between the droplets from the two injection events. The reduced number of these large droplets and the reduced number of low velocities in the transient profiles of the second injections (Figure 4.22b.), when compared to those measured with 2ms dwell, can be attributed to the lesser increase in the SMD in the second injection event (Table 4.3). This is also indicated by the lower SMD uncertainty in the second injection compared to that measured during the shorter dwell case.

The increase in SMD in the second injection is also observed 20mm downstream, for both dwell times, albeit the general increase in the velocities of the second injections observed at this elevation. This suggests that the interaction between both droplets is significant, especially since the droplets from the first injection would be stagnating or recirculating with low velocities in this region by the start of the second injections, as represented in the high-speed images in Figure 4.4 and the recirculation velocities measured in Figure 4.22a. - b.

In addition, one would expect the droplet sizes further downstream to decrease owing to phases of atomisation, as observed for the corresponding single injection case. The lack of similar characteristics observed with the split injection confirms that the larger measured SMDs in Figure 4.21 are mainly owing to droplets coalescing.

The transient trends in the droplet sizes for the single injection case at 11mm and 20mm presented in Figure 4.22c. and Figure 4.23c. respectively, indicate minor fluctuations in the average droplet sizes during the measurement period. The corresponding SMD uncertainties 11mm and 20mm downstream are 1.9 and 2 respectively. This trend, along with the variation in SMD with increasing axial distance suggests that the droplet sizes decrease uniformly with increasing distance downstream. This is indicative of the phases of atomisation that the droplets would be undergoing as they propagate further downstream and face large shear forces which break the droplets up further.

Table 4.4: SMD and the corresponding uncertainties in SMDs measured at two injection events for dwell times of 2ms and 6ms, 20mm downstream of the injector for the 0.4ms-0.4ms PW combination.

Dwell time (ms)	1st injection SMD (μm)	SMD uncertainties	2nd injection SMD (μm)	SMD uncertainties
2	9.0	2.0	15.0	3.5
6	10.4	1.6	14.4	1.9

a.

b.
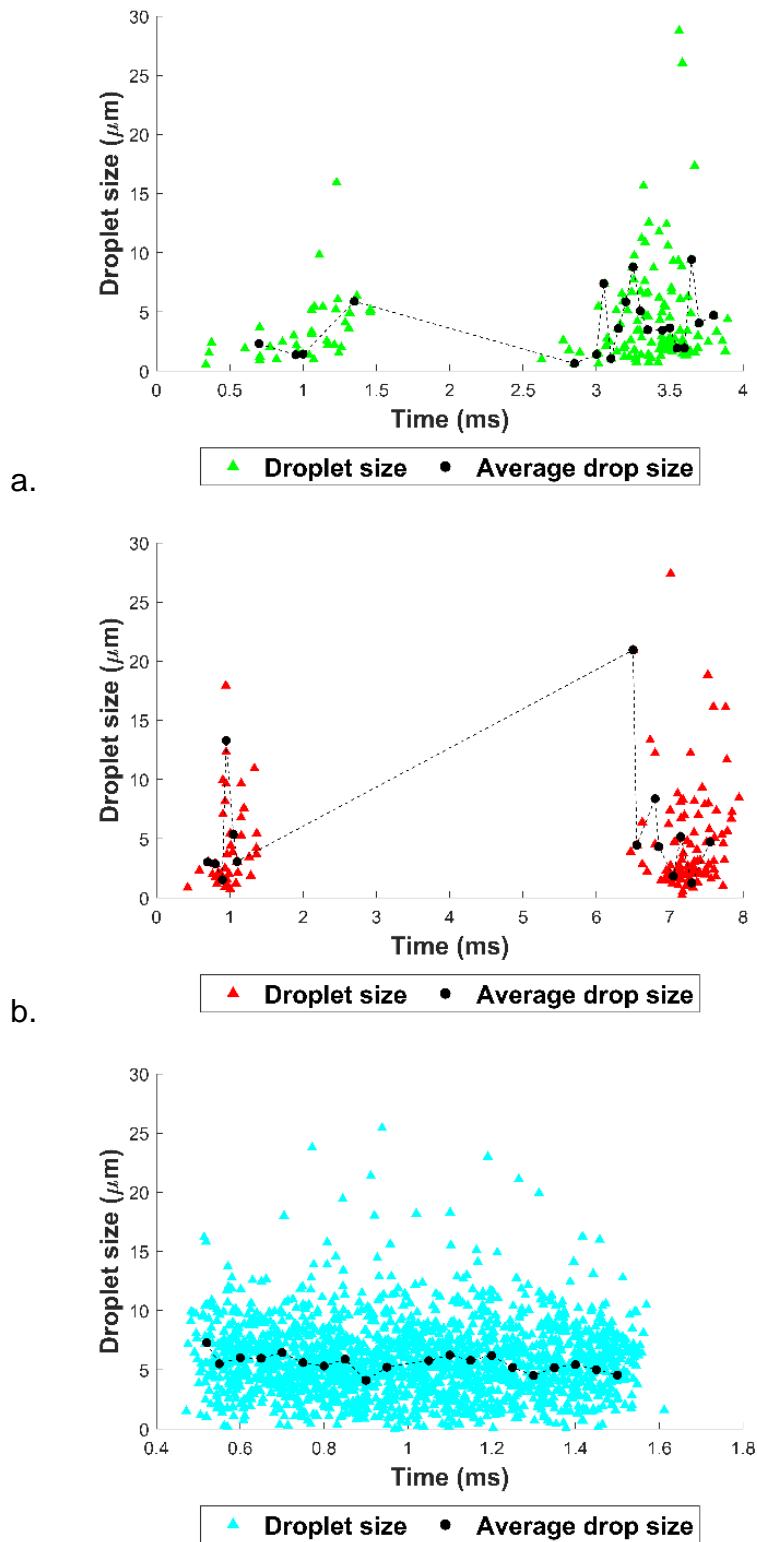
c.

Figure 4.23: transient trends of droplet sizes measured 20mm downstream of the injector for a. 2ms dwell case, b. 6ms dwell case and c. single injections. The PW combination is 0.4ms-0.4ms for the tested split cases and the PW for the single injection is 0.8ms. The black trend line represents the average droplet sizes.

4.4.2 2:1 Split Ratio

The effects of a larger first PW with a split ratio of 2:1 (0.8ms-0.4ms) are analysed at varying distances downstream of the injector. The variation in the spray characteristics are analysed for increasing dwell times, from 2ms to 11ms. These characteristics are compared against single injections, with the PW of 1.2ms equating to the total PW of the split injection.

4.4.2.1 Analyses of the Droplet Velocities

The trend of the droplet average velocities, increasing distance downstream from the injector tip, in the rear plume of the spray are presented in Figure 4.24. These measurements represent the average velocities of droplets measured over 50000ms AT.
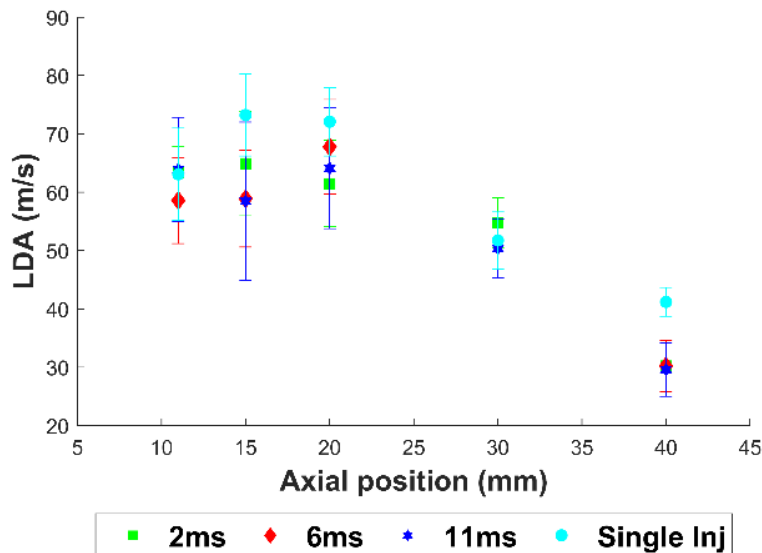
Figure 4.24: axial trend in the average velocities (LDA) of the droplets in the rear plume's core, for single and split cases, measured along various distances downstream of the injector. The error bars represent the standard deviation of the measured velocities. The PW combination is 0.8ms-0.4ms for the tested split cases and the PW for the single injection is 1.2ms.

The trend indicates similar droplet mean velocities along with the corresponding error bars between the injection strategies and varying dwell times. This is true for all elevations tested. The highest axial velocity regions are between 11mm and 20mm downstream of the injector, with the highest overall velocities observed for the single injection case.

To investigate these trends further, Table 4.5 provides the differences in the mean velocities, corresponding standard deviations and drop counts for the two injection events and the three tested dwell times 11mm downstream. Figure 4.25 provides the transient trends of the velocities for the four tested injection cases, with the black dotted line indicating the average velocity.

Table 4.5: average velocities, their corresponding S_D uncertainty, and drop counts measured at two injection events for dwell times of 2ms, 6ms and 11ms, 11mm downstream of the injector for the 0.8ms-0.4ms PW combination.

Dwell time (ms)	1st injection average velocity (m/s)	S_D uncertainty (m/s)	2nd injection average velocity (m/s)	S_D uncertainty (m/s)	Drop count - 1st injection	Drop count - 2nd injection
2	59.8	32.4	66.6	33.4	491.0	386.0
6	53.4	34.3	72.7	26.8	568.0	248.0
11	54.9	32.8	70.0	32.9	435.0	219.0

Table 4.5 shows higher average velocities for the second injections for all dwell times, compared to the first injections. These velocities, corresponding to the shorter second PW, are comparable to the average velocities observed with the first injections using 1:1 split ratio (Table 4.1). This suggests that 11mm downstream, there are negligible effects of the larger first injection and dwell times on the velocities of the droplets from the second injections, as the measured velocities in the near-nozzle region are primarily driven by the high momentum region using the high injection pressure close to the injector.

The average velocities of the 0.8ms PW in the first injection are lower when compared to the shorter PW of 0.4ms. Observing the transient trends for all dwell times (Figure 4.25a. - c.) greater number of droplets in the low velocity region in the range of -20m/s to 20m/s are detected throughout the first injection period. This indicates the possibility of large number of droplets possessing velocities perpendicular to the plume's direction of travel as well as recirculating droplets from the plume's edges (judging by the high negative velocities).

The fact that such a large number of droplets with the low velocities are observed in the first injection suggests that the larger the PW, 1) the larger the number of droplets travelling in the direction perpendicular to the plume and 2) greater the likelihood of recirculating droplets at the plume's edges travelling back in to the control volume, which is the plume's core. The latter is potentially caused by the greater resistive forces, resisting the propagation of the small droplets at the spray's edges under ambient conditions. This would force some of the droplets at the edges to recirculate back towards the centre of the plume. The resistance forces seem to increase with both large injection pressure and large PW. This is possibly because of the momentum transfer between the large injection momentum and the surrounding flow field. The overall velocity range between the two injection events however, are comparable.

Furthermore, due to the larger first PW, the transient trend in velocity was expected to have less fluctuations in velocities after a certain time after start of injection once the steady state region of the spray was achieved [135]. The standard deviations are in fact comparable for all PWs tested at this elevation. The main source of the large uncertainties are suspected to be the large pressure waves, increasing the shot-to-shot variability [135] and resulting in large fluctuations in the droplet velocities, independent of the PW.

Additionally, the error bar for the single injection case with a PW of 1.2ms is 33.3m/s, which is comparable to the split cases in both injection events. The transient trend of the velocity (Figure 4.25d.) shows a consistent trend in velocities ranging between 0 and 120m/s. The magnitude of this error bar is also comparable to that measured 11mm downstream for the 0.8ms PW in Figure 4.18, whose standard deviation error was 35.6m/s. The similarity in the standard deviation values makes the transient steady-state region, typically achieved with large PWs, difficult to detect at least in the near-nozzle region, 11mm downstream.
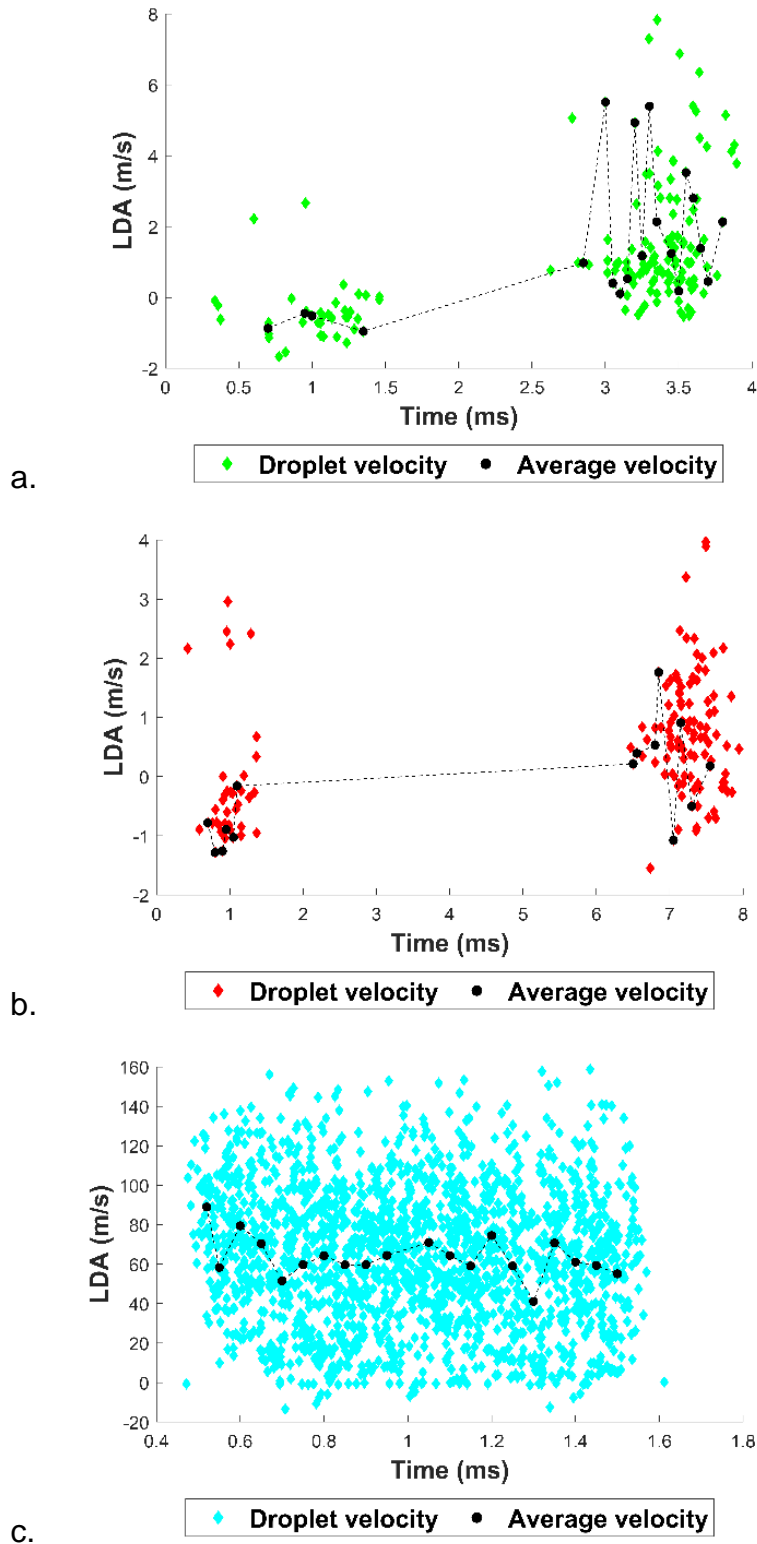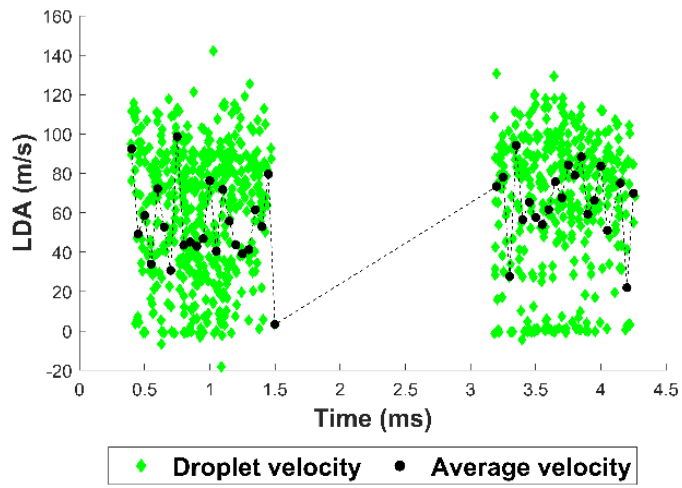
a.
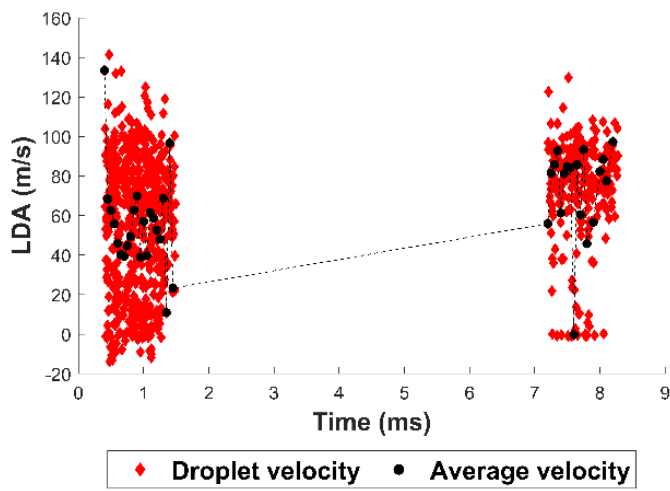
b.
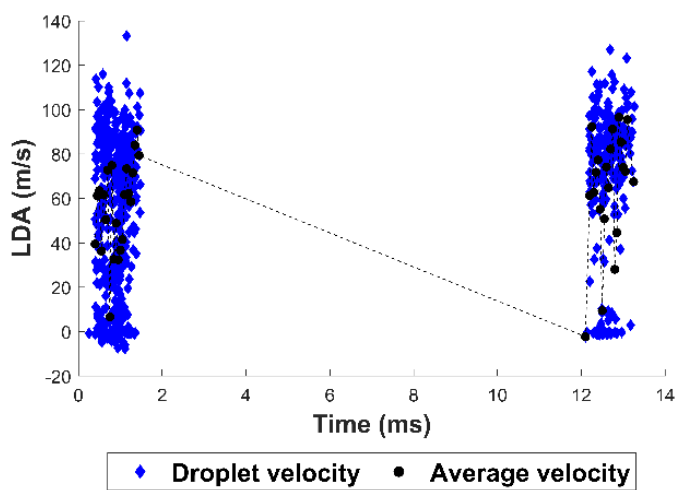
c.
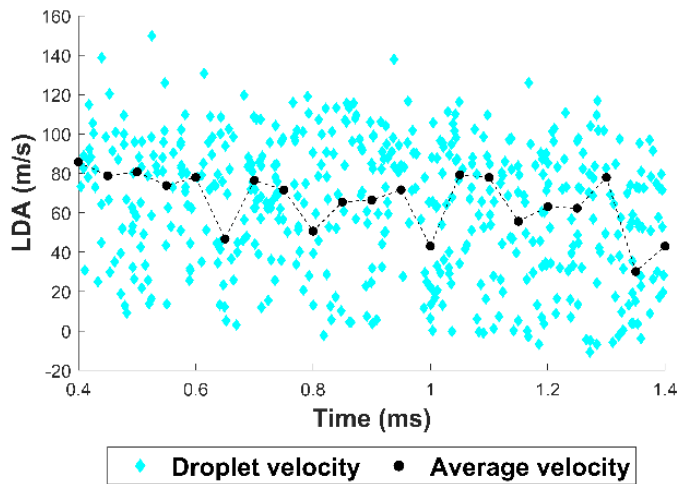
d.

Figure 4.25: transient trends of the droplet velocities measured 11mm downstream of the injector for a. 2ms dwell case, b. 6ms dwell case, c. 11ms dwell case and d. single injections. The PW combination is 0.8ms-0.4ms for the tested split cases and the PW for the single injection is 1.2ms. The black trend line represents the average droplet velocities.

40mm downstream of the injector, the average velocities decrease for all cases, along with the corresponding uncertainties (Figure 4.24). Table 4.6 provides the differences in the mean velocities, corresponding standard deviations and drop counts for the two injection events and the three tested dwell times 40mm downstream of the injector.

Figure 4.26 provides the transient trends in velocities for the four tested injection cases, with the black dotted line indicating the average velocity.

It is worth noting here that a distinctive band of low velocity droplets, in the transient velocity profiles of the first injections are observed throughout the injection durations. This band is more distinctive than the transient profile observed 11mm downstream for this PW. A similar observation was made by Zhou et al., [137], using injection pressures of up to 10MPa, and injection durations in the range of 0.56ms to 0.8ms. They stated that the variation in the liquid fuel distribution (which would consist of large droplets) along the injection direction is greater than that perpendicular to the injection direction. With the downstream development of the spray, these variations in the spray edge increased and the variations perpendicular to the injection direction become more apparent. It is believed that the clear band of low velocity droplets

observed in the first injection 40mm downstream indicate a more obvious segment of droplets travelling in the direction perpendicular to plume.

At this elevation, the average velocities in the second injections generally reduce to stagnation. This indicates the furthest point at which the droplets propagate before recirculating, when injected at 0.4ms PW. The calculated average penetration length of this PW was 40mm, with a standard deviation of ±1.5mm.

Observing the drop counts 40mm downstream in Table 4.6, the higher the dwell time, the lower the drop counts measured in the second injection event. This was also observed 11mm downstream (Table 4.5). This confirms that the interaction of the droplets from the first injections reduce progressively with increasing dwell, as they have more time to propagate away from the vicinity of the flow field prior to the start of the second injections.

Table 4.6: average velocities, their corresponding standard deviation uncertainties, and drop counts measured at two injection events for dwell times of 2ms, 6ms and 11ms, 40mm downstream of the injector of the injector for the 0.8ms-0.4ms PW combination.

Dwell time (ms)	1st injection average velocity (m/s)	S_D uncertainty (m/s)	2nd injection average velocity (m/s)	S_D uncertainty (m/s)	Drop count - 1st injection	Drop count - 2nd injection
2	41.7	25.1	9.7	2.5	1024.0	3274.0
6	39.5	26.3	2.5	1.0	953.0	1386.0
11	42.0	24.4	1.1	0.7	1171.0	380.0
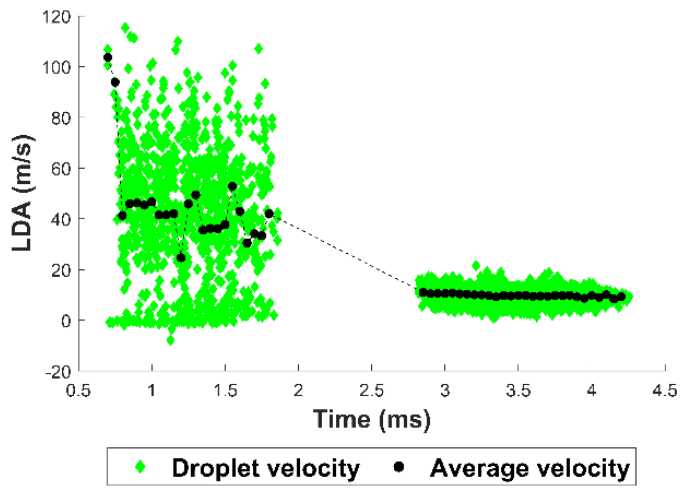
a.
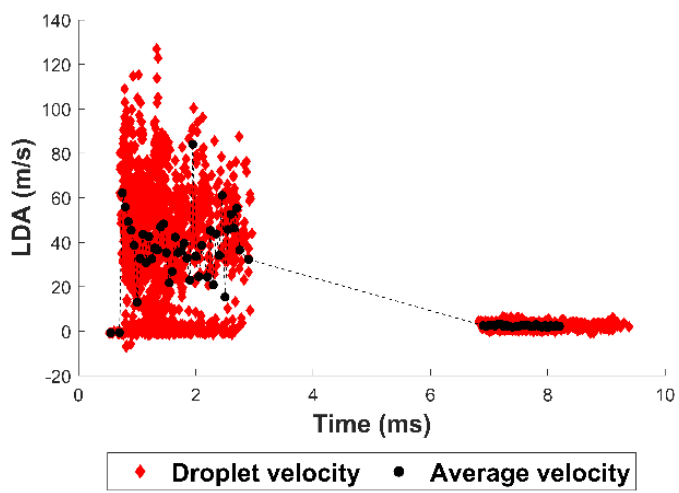
b.
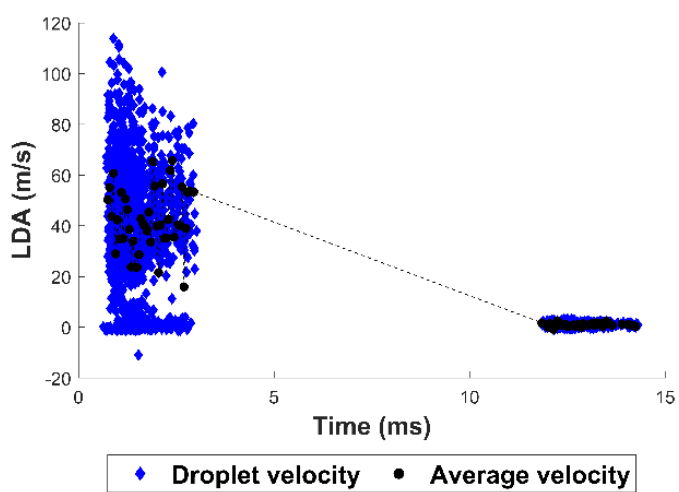
c.
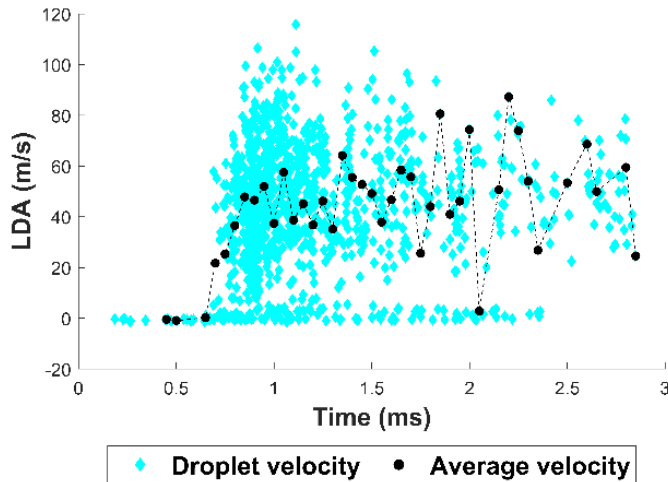
d.

Figure 4.26: transient trends of the droplet velocities measured 40mm downstream of the injector for a. 2ms dwell case, b. 6ms dwell case, c 11ms dwell case and d. single injections. The PW combination is 0.8ms-0.4ms for the tested split cases and the PW for the single injection is 1.2ms. The black trend line represents the average droplet velocities.

4.4.2.2 Analyses of the Droplet Sizes

Figure 4.27 represents the SMDs (D32) of the droplets across varying axial locations in the plume. The data is the average of the total droplets crossing the measurement volume each test cycle, for the 50,000ms AT, and so include both injection events.
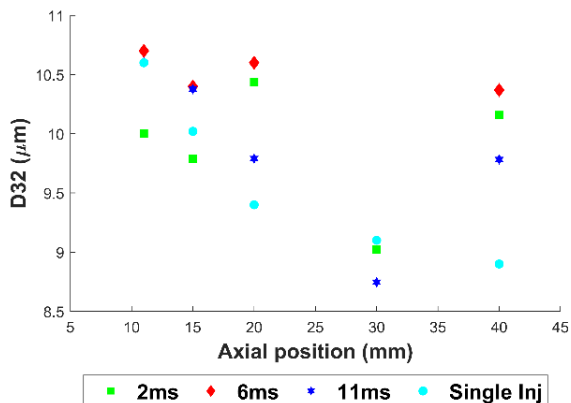
Figure 4.27: axial trend in the SMD (D32) of the droplets inside the plume's core, measured along various distances downstream of the injector. The PW combination is 0.8ms-0.4ms for the tested split cases and the PW for the single injection is 1.2ms.

Contrary to the axial trend in the SMD observed for the 1:1 split ratio, the SMDs for all cases injected using a 2:1 split ratio generally decrease with increasing distance downstream of the injector. The lowest rate of reduction in the SMD with increasing

distance downstream, is associated with the split case with 6ms dwell time. Near the injector, between 11mm and 20mm, the smallest SMD is associated with the 2ms dwell time. In spite of the greater rate of interaction of droplets between the two injection events at the short dwell time, the rate of atomisation seems to be high.

The results 40mm downstream indicate large increase in SMDs for the split cases, while the droplets from the single injection continue to decrease. Diminished radial and axial momentum here could increase the likelihood of the droplets' coalescence between the two injection events or from the low-velocity vortices generated, especially since the ambient pressure is low.

Table 4.7 and Figure 4.28 further provide the SMD for the two injection events and transient trends of drop sizes, respectively, 11mm downstream. Upon a closer look at the differences in the SMDs between both injection events provided in Table 4.7, the SMDs measured in the second injections are larger than the first injection. This is also accompanied by larger error bars in SMDs, with the exception of the 11ms dwell time. These higher second injection droplet sizes are also characteristic of the 0.4ms PW, as the sizes are similar to the SMDs measured in the first injection event with the 1:1 split ratio (Table 4.3). These features further confirm the effect of the closely spaced valve's opening and closing times on the droplet momentum and subsequently their droplet sizes.

Furthermore, observing the transient trends for all dwells in Figure 4.28a. - c., the second injections exhibit greater number of droplets in the range of 15μm to 35μm. This variation in the drop sizes between the two different PWs further suggests that the droplets from the short PWs suffer from poorer atomisation, observed close to the injector tip, when compared to the larger PWs, owing to the opening and closing events of the valve within a short time.

Table 4.7: SMD and the corresponding uncertainties in SMDs measured at two injection events for dwell times of 2ms, 6ms and 11ms, 11mm downstream of the injector of the injector for the 0.8ms-0.4ms PW combination.

Dwell time (ms)	1st injection SMD (µm)	SMD uncertainties	2nd injection SMD (µm)	SMD uncertainties
2	9.2	1.6	10.8	2.3
6	9.6	1.8	12.3	2.3
11	10.1	1.7	11.3	1.7

a.

b.
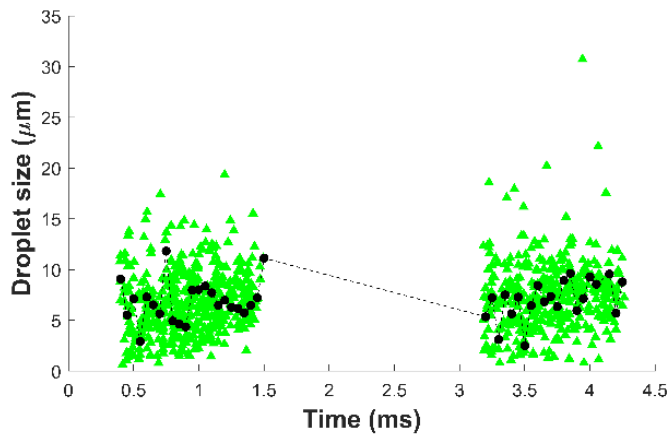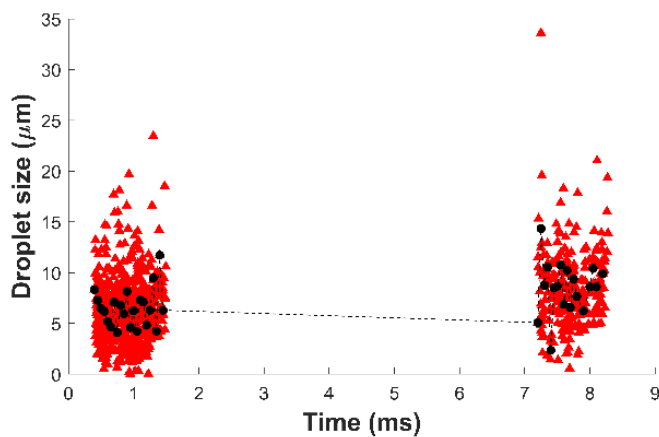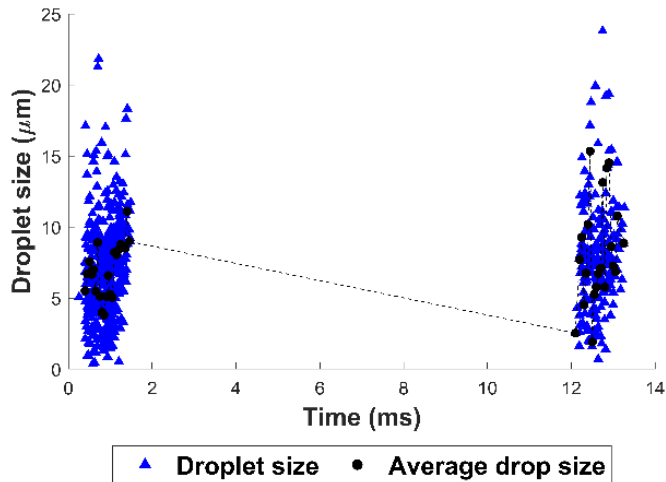
c.
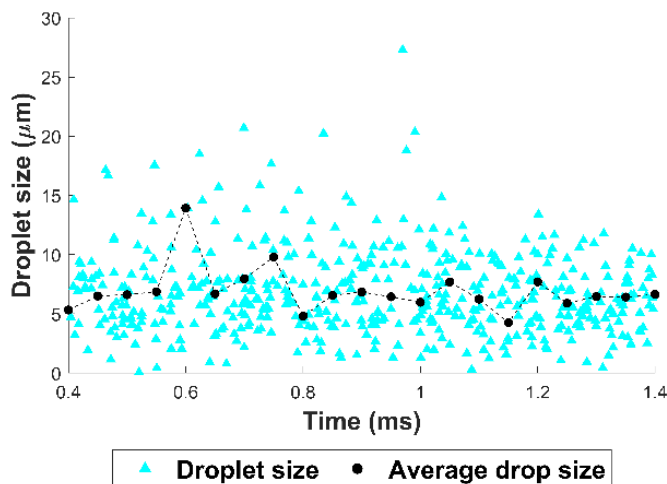
d.

Figure 4.28: transient trends of droplet sizes measured 11mm downstream of the injector for a. 2ms dwell case, b. 6ms dwell case, c. 11ms dwell case and d. single injections. The PW combination is 0.8ms-0.4ms for the tested split cases and the PW for the single injection is 1.2ms. The black trend line represents the average droplet velocities.

The second injections' SMDs 40mm downstream (Table 4.8) are still larger than the corresponding first injections. These sizes have also superseded the SMDs measured 11mm downstream for the shorter second PW.

Observing the transient trends in the droplet sizes for all the split cases, the average droplet size trend in the second injections increase with increasing time ASOI, in spite of the near-zero droplet velocities measured here (Figure 4.29a. - d.). This trend is in fact independent of the dwell times. When comparing the SMD between

2ms and 11ms (Table 4.8), the drop sizes increase for the second injection event to similar magnitudes, even though the drop counts in the second injections for the larger dwell time are reduced. The trends suggest that the droplet sizes increase owing to coalescence between the stagnated or low momentum droplets in the second injection events.

The average drop size trend for the single injections 40mm downstream shows a distinct increase in the average drop sizes towards the end of injection, when compared to 11mm downstream. Observing the corresponding velocity trend (Figure 4.29d.) there are large velocity fluctuations towards the end of the injection. These two trends suggest that during the valve's closing period, the droplet velocities towards the end of injections are heavily affected. 40mm downstream, where the droplets would have undergone maximum atomisation, the fluctuations in the velocities and droplet sizes indicate the possible effect of tip wetting, which would have generated the formation of ligaments and large droplets, but with low momentum, caused by the reduction in injection pressure during the throttling effects as the valve closes. This trend is not only observed with the single injections, but for all the PW combinations tested at this elevation (Figure 4.29a. – c.). As such, this far downstream, the valve closing effects on the droplet sizes particularly, become apparent.

This increase in the droplet sizes in the valve's closing period was also reported by Hélie e. al., [31]. They observed systematic long and hollow liquid coronas during the valve's closing event. Their observation of the evolution of these features showed a film collapse which generated big drops, mostly far from the nozzle. While tip wetting is not captured in the current high-speed images, the common observation of these phenomena reported by various literature discussed in this paper [32] [31] [33] [140], suggests that the increasing drop sizes towards EOI could be affected by the nozzle closing period and the subsequent tip wetting. Additionally, it is suspected that the smaller droplets would have propagated away from the plume's core, much closer to the injector's tip. Majority of the large droplet sizes have stated to propagate axially with low momentum [137], which is what has potentially been captured 40mm downstream.

Table 4.8: SMD and the corresponding uncertainties in SMDs measured at two injection events for dwell times of 2ms, 6ms and 11ms, 40mm downstream of the injector of the injector for the 0.8ms-0.4ms PW combination.

Dwell time (ms)	1st injection SMD (µm)	SMD uncertainties	2nd injection SMD (µm)	SMD uncertainties
2	11.9	1.5	12.4	2.5
6	12.9	2.0	14.2	1.9
11	12.4	1.6	13.1	1.6
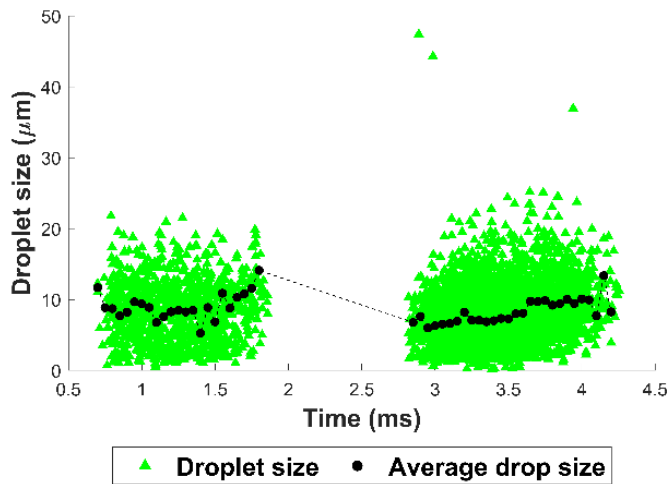
a.
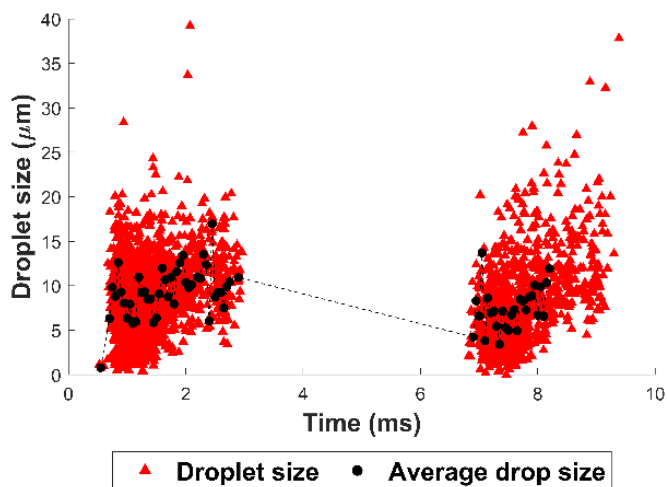
b.
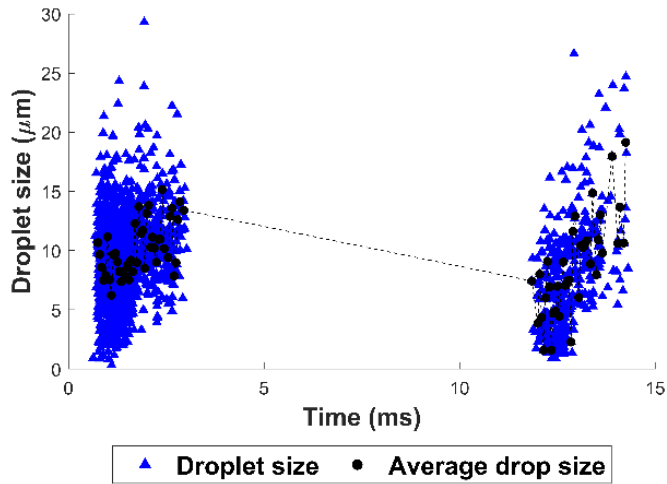
c.
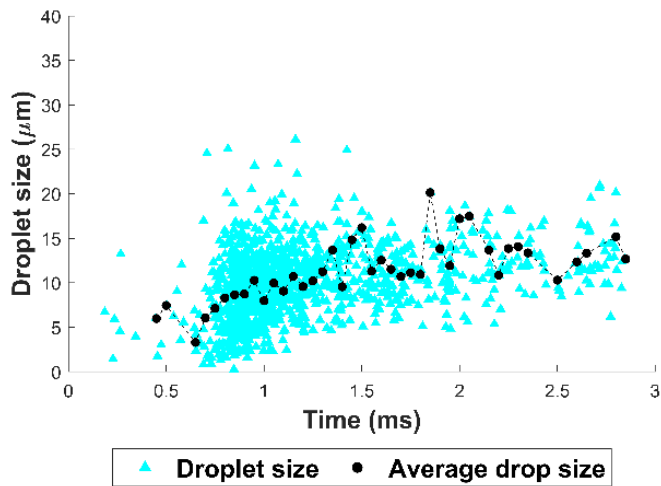
d.

Figure 4.29: transient trends of droplet sizes measured 40mm downstream of the injector for a. 2ms dwell case, b. 6ms dwell case, c. 11ms dwell case and d. single injections. The PW combination is 0.8ms-0.4ms for the tested split cases and the PW for the single injection is 1.2ms. The black trend line represents the average droplet velocities.

4.5 Summary

The key findings of the single injections' studies discussed in this chapter are as follows:

- The single injection quantities increased at a higher rate when the PW was less than 0.5ms. Increasing the PWs over 0.5ms allowed the injection momentum to stabilise over time. Thus, a linear increase in the injected quantity was observed for the larger PWs.

- The rate of increase in the penetration length reduced for injection pressure greater than 25MPa.

- The rate of increase in the penetration length at the start of injection until 0.6ms ASOI (After the Start of Injection) was large, which suggests that the injection momentum at the start of injection is high and stabilises progressively.

- The error bars in the penetration lengths increased with increasing rail pressure and increasing time ASOI. The former was caused by increased internal pressure fluctuations in the fuel rail, which affected the shot-to-shot variability. The latter was caused by the entrainment effects as the spray developed. In this case, vortices were formed by a shear layer formed between the surrounding air and the fuel, which increased the aerodynamic drag. This affected the consistency in the trend of the penetration length, hence the larger errors.

The key findings of the split injections' studies discussed in this chapter are as follows:

- The highest quantity of the total fuel injected was found with the shortest tested dwell time of 2ms for a given total injection duration as measured by the sum of split injection PWs. This was caused by the fuel prior to the start of the second injection being present in the vicinity of the injector and interacting with the tip of the second injection. These interactions had increased the droplet sizes. With low chamber pressures, the interactions between the droplets from different injection events, using short dwell times, can affect the

atomisation rates, mixture formation and subsequently the emissions of particulates.

- The highest relative peak in the injection quantity at 2ms dwell was attributed to the short PW combination of 0.4ms-0.4ms. High speed images revealed that the spray was attached to the injector tip for at least 100µs after EOI. This was due to the sudden closing of the valve, which interrupted the development of the peak current over time. The sudden drop in current commanded the valve to shut, but the high injection pressure had likely resisted the closing of the valve. The delayed detachment would have thus affected the injected quantity.

- At 35MPa injection pressure, the dwell time, split ratios and the flow field from the first injection all influenced the spray characteristics of the second injections. The penetration lengths of the second injections had generally increased for all the dwell times, PWs and split ratios tested, when compared to the single injections. The flow field from the first injection created a high momentum region, encouraging slip-streaming of the second injection, particularly when small dwell times were employed.

- Slip stream effects were observed for all split cases further downstream from the injector tip, whereby the droplets from the second injection possessed higher overall velocities in the second injection event. The droplets from the first injection did not only form a region where the droplets from the second injection had accelerated through, but had also caused the angle of the second plume to reduce slightly.

- For both 1:1 and 2:1 split ratio, the axial spread of the second injection persisted, while the spray remained radially compact for dwell times shorter than 6ms. The first injection and high rail pressures resisted the extent to which the second spray had spread radially.

- The average droplet sizes had increased towards the end of the injection for all tested cases. The corresponding droplet velocities had reduced. This was due to the valve's closing effects, which has been reported to inject ligaments and large droplets with low momentum by a range of previous studies.

- Upon the valve's opening for the second time after 2ms dwell, greater number of low velocity droplets were observed, particularly in the near nozzle region (11mm downstream). This had occurred due to a combination of recirculating droplets and droplets with plume perpendicular velocities being captured. The former is stated to have been intensified by the high injection pressure, which could cause some droplets, particularly those at the edges of the plume, to travel upwards and close to the injector tip. This increases the likelihood of a fuel film being accumulated on injector tip as well as affecting the momentum of the injected droplets. This effect was alleviated with 6ms dwell and intensified with larger PW.

- Large fluctuations in velocities observed with both short and large PWs were due to the large pressure waves in the injector and the pipe from the common rail, thereby increasing shot-to-shot variability.

- SMDs for the shorter PW of 0.4ms were generally larger than 0.8ms PW. Droplets in this case are affected by closely spaced opening and closing events of the solenoid valve.

While the current tests revealed interesting spray phenomena, it is important to remember that the spray variabilities in an operating engine increase. By realising the more stable and repeatable structures under ambient atmospheric conditions, appropriate injection strategies can thus be employed in the engine to reduce the relative spray variations and thereby fluctuations in IMEP and the peak in-cylinder pressure. Additionally, the gas-phase flow field within the cylinder is not simply overwhelmed by the spray events, but can influence the spray propagation itself as well as the vapor-phase fuel distribution.

The next stage of study is therefore to employ the split injection strategies using the same injector, in a single-cylinder optical GDI engine. It is proposed that the interaction of droplets from the split injections could be alleviated inside the cylinder due to the higher in-cylinder pressure, which would encourage greater entrainment but also greater resistance against the propagating droplets. High-speed PIV measurements can help reveal these phenomena in order to realise the optimum stratified charge using a split injection strategy and a solenoid actuated injector.

Chapter 5.   In-cylinder Flow and Mixture Formation in a GDI Engine via High-speed PIV

5.1 Introduction

The effects of the injection strategies on the velocity vectors and turbulence levels in the flow field throughout the cycle are discussed in this chapter. These studies are performed in an attempt to understand the effects of injection strategies (single Vs. split), injection timings and split ratios on the mixture formation and charge stratification. The key diagnostic tool used here was high-speed PIV, with the methodology described in Section 3.2.2.

Note that this part of the study is not an extension of the studies of the spray characterisation performed in the constant volume spray chamber and discussed in Chapter 4 of the Thesis. It should be reviewed as a separate study.

While a homogeneous-stratified charge, with a fuel rich mixture close to the spark plug, is essential for engine idle and part-load conditions, it is also crucial to avoid liquid fuel deposition on the chamber surfaces along with achieving high rate of spray atomisation. These features have been used to minimise the formation of PN in GDI engines [142]. Further studies are necessary in minimising PN emissions under low-load conditions as these emissions have exhibited high sensitivity to load at low engine speeds for all injection timings [33]. These effects have been taken into consideration and part of the focus of the current investigations is to determine injection parameters that would aggregate surface impingements along with ways to overcome them.

The effects of split injections with short dwells (both injections in the intake stroke) and large dwells (second injections in the compression strokes) on the charge formation are discussed in detail in this chapter. In this case, Gainey et al., [71] reported that achieving thermal stratification via the fuel injected in the compression stroke is sensitive to both the combustion chamber geometry and the injector spray angle. The compression stroke injection's capability at enhancing thermal stratification is strongly related to the region in the cylinder that is targeted by the spray. In addition, differences in the vortex positions influences the difference in the flow direction at the position of the spark plug [143].

Priyadarshini et al., [144] have stated that mixture stratification increases by retarding the second injection, which can also be used to control autoignition timing and the combustion phasing. For instance, ignition in the fuel rich zones is stated to drive the sequential ignition process of the leaner zones in the rest of the flow field. The sources of the bulk heat release are the zones with the highest fuel mass concentration.

Another advantage of delaying the injection timing is improved wall impact strength and stronger tumble flow in the cylinder, as reported by Wang et al., [84]. These two features have the potential to reverse the natural diffusion law of fuel and improve the in-cylinder mixing effect.

Taking all of these previous studies and findings into account, the discussions in this chapter are split into three key parts. The first part includes discussions of the velocity vectors, TKE contours and maps of standard deviation in velocities for early and late single injections in the intake stroke. This is followed by a comparison of the large split ratio (75%:25%) and small split ratio (25%:75%) on the mixture formation. In this case, all injection events occur in the intake stroke. The third part consists of evaluating the effects of a first injection in the intake stroke and delayed second injections with sweeps across the compression stroke. In this case, the split ratio of 75%-25% is kept constant in the study.

5.2 Single Injections

The effects of the single pulse injection timing during the intake stroke on the in-cylinder flow field are investigated in this section. The first test case is an early single injection at the start of the intake stroke, which is compared against a single injection close to the end of the intake stroke. Table 5.1 provides an overview of the injection parameters tested and Figure 5.1 provides a schematic of the timings with respect to the gas exchange TDC. The corresponding injection quantity is determined using the linear relationship between large PWs (from 0.5ms to 3ms) and injected quantity measured at 35MPa injection pressure (Figure 4.1 in section 4.2).

Table 5.1: test parameters and timings for both early single injection of SOI 310˚CA and late single injection of SOI 200˚CA.

Injection pressure (MPa)	SOI (˚CA bTDC)	PW (ms)	Injected quantity (mg)
35	310	2.5	26.4
35	200	2.5	26.4

The injection in the intake stroke would provide sufficient time for the fuel to atomise and interact with the surrounding charge. The former case of SOI 310˚CA bTDC would determine the mixture evolution and the spray's interaction with the surrounding charge during the cycle when the fuel is injected at the beginning of the intake stroke. The latter case of 200˚CA bTDC was investigated to evaluate the effects of the injection close to the end of the intake stroke.
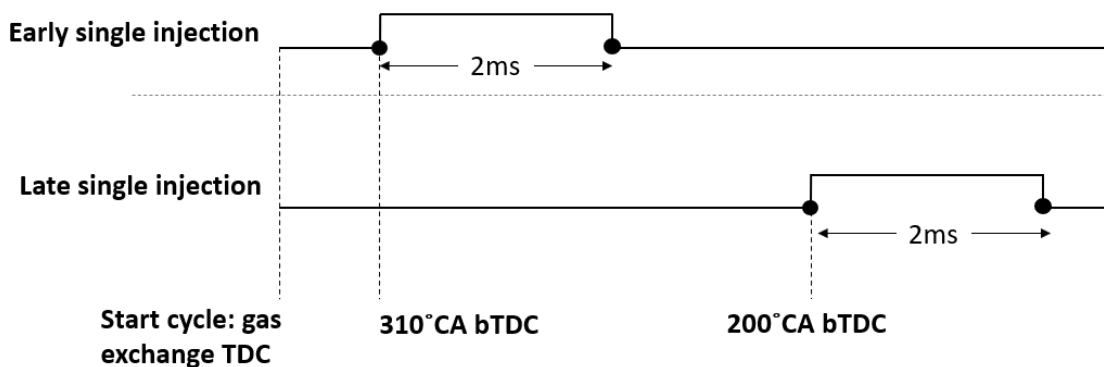
Figure 5.1: schematic representing the differences between the two single injection timings with respect to the gas exchange TDC.

5.2.1 Effects of Single Injection Timings on the Engine's In-cylinder Gas Properties

Figure 5.2 presents the measured pressure traces averaged over 300 cycles for the motored case (without injection), and the two tested injection cases of SOI 310˚CA bTDC and SOI 200˚CA bTDC. The measurements were performed under cold-flow conditions, so the peak pressures are not representative of the combustion conditions. Nevertheless, an indication of the injection strategy on the in-cylinder pressure can be achieved with the current measurements.

The traces indicate that the single injection timings at varying sweeps in the intake stroke has negligible effect on the average peak pressures at TDC, as they are similar under similar loads, which are presented in Table 5.2. Both injection cases tested however, show lower average peak pressures when compared to that for the motored case. This is because the fuel entering the cylinder lowers the in-cylinder temperature. As a result of this, the overall average peak pressure is reduced by 1bar for the single injection cases, when compared to the motored case.
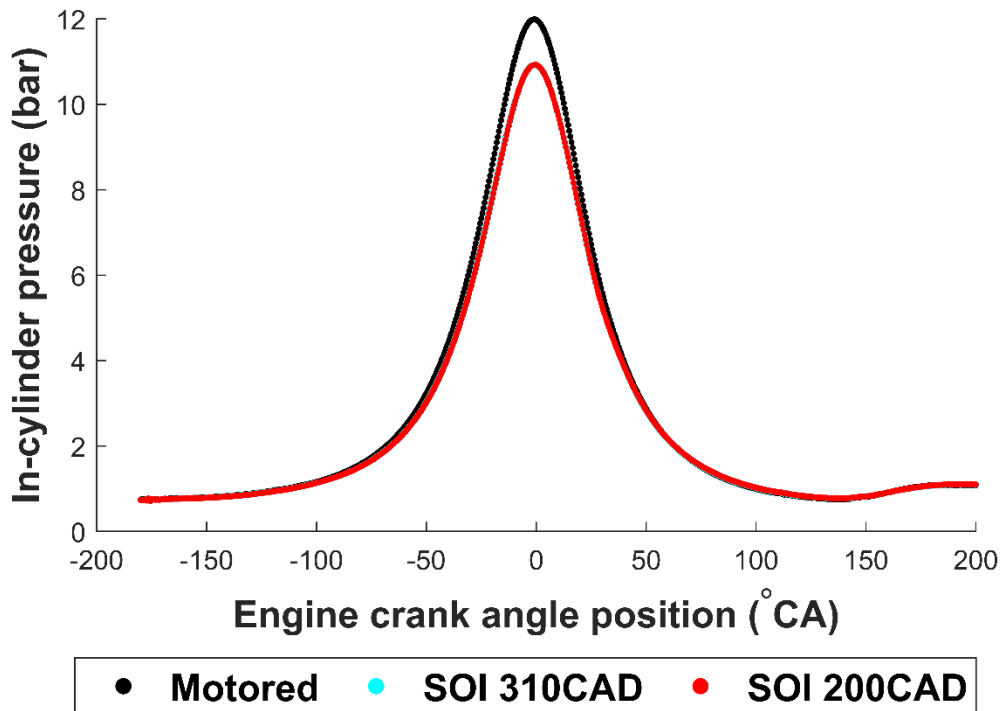
Figure 5.2: averaged in-cylinder pressure traces for the intake and compression strokes for three test cases of 1) motored, 2) early single injection of SOI 310˚CA and 3) late single injection of SOI 200˚CA. The in-cylinder pressure at each engine crank angle are averaged over 300 recorded cycles.

Table 5.2: recorded test conditions for the three test cases.

SOI (˚CA bTDC)	Average MAP (bar)	Inlet temperature (˚C)	Coolant temperature in/out (˚C)	Oil temperature in/out (˚C)	Ambient pressure (˚C)
Motored	0.74	27.1	56.4 / 55.4	41.2 / 42.3	1.016
310	0.74	29.8	49.5 / 49.4	37.8 / 38.4	1.018
200	0.73	30.8	50.4 / 50.2	39.5 / 40	1.019

Figure 5.3 represents the logarithmic relationship between the in-cylinder pressure and volume for all the tested cases. Log(V) was derived using the following equation:

$$\log V = \log\left(V_c + \frac{\pi.B^2}{4}.c\right) \qquad\qquad \text{Equation 5.1}$$

$$\text{where } c = \frac{S}{2}.(R + 1 - \cos x - R^2 - \sqrt{\sin x^2}) \qquad\qquad \text{Equation 5.2}$$

In this case, V_c was a factor of the displaced volume (454cc) and compression ratio (10.51), B and S were the bore (82mm) and stroke (86mm) respectively, R was the conrod length (144mm) divided by half of the stroke and x was the engine position measured in radians.

The corresponding polytropic constants are provided in Table 5.3, which represents the rate of pressure rising in the compression stroke. The trend is similar to the peak pressures observed. The polytropic constants for the two injected cases are similar, suggesting that the injection times in the intake stroke, and therefore the variations in the fuel distribution in the combustion chamber, has negligible impact on the rise of the in-cylinder pressure throughout the compression stroke. The polytropic constant of the compression process was reduced slightly by the fuel injection due to the charge cooling effect of the liquid fuel, which lowered the in-cylinder pressure and temperature.
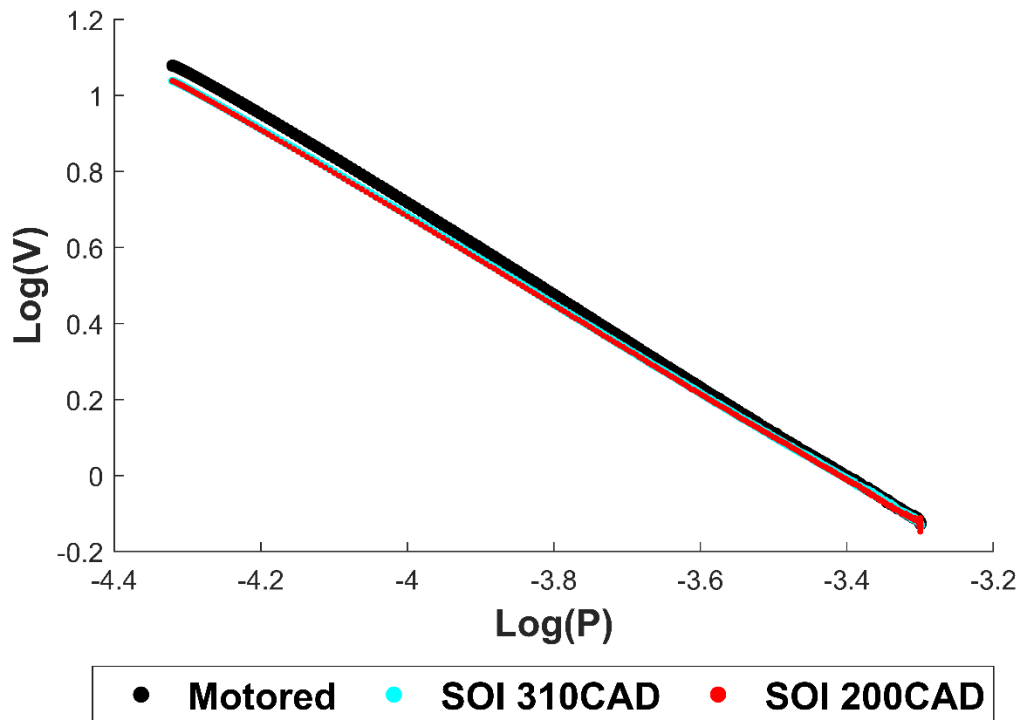
Figure 5.3: relationships between Log(P) and Log(V) recorded during the compression stroke for the three test cases.

Table 5.3: polytropic constants for three test cases derived from the Lop(P) - Log(V) trends measured in the compression strokes.

SOI (˚CA bTDC)	Polytropic constant, n
Motored	1.19
310	1.15
200	1.15

5.2.2 Effects of Early Single Injection on the Flow Field

Ensemble-averaged velocity vectors during the injection period of SOI 310˚CA bTDC, are presented in Figure 5.4. For direct comparison purposes, the velocity vectors in the tumble plane are presented in the left column, and the corresponding velocity vectors in the omega tumble plane for the same engine positions, are provided in the column on the right-hand side. The blank white regions occur due to a lack of signal caused by the oversaturation of the image as the laser comes into contact with the fuel dense regions in the image plane, as discussed in the methodology in section 3.2.2. This region however also provides an indication of the global shape of the main spray structure.

Figure 5.4a. – c. in the tumble plane show that upon injection, the fuel impinges on the piston's surface directly and continues to impinge on the surface throughout the injection period. Due to the piston being so close to the injector, the injected fuel does not develop into a global spray structure as majority of the fuel is impinged on the surface of the piston, as seen clearly in the tumble plane.

As the plumes are directed towards the left-hand side (LHS) of the tumble plane with the high injection pressure, the tip of the spray bounces off the piston's surface upon contact. This subsequently transfers the high momentum to the surrounding charge which moves upwards and towards the LHS of the liner, as represented by the high velocity vectors towards the LHS of the plane (Figure 5.4a.).

Tumble plane	Omega tumble plane
a. 10˚CA ASOI (299˚CA bTDC)	10˚CA ASOI (299˚CA bTDC)
b. 15˚CA ASOI (294˚CA bTDC)	15˚CA ASOI (294˚CA bTDC)
c. EOI (292˚CA bTDC)	EOI (292˚CA bTDC)

Vector color (min: 0.0299999993294477 max: 30) Variable(X): U Variable(Y): V Unit: m/s

| 30.000E-3 | 3.0270 | 6.0240 | 9.0210 | 12.018 | 15.015 | 18.012 | 21.009 | 24.006 | 27.003 | 30.000 |
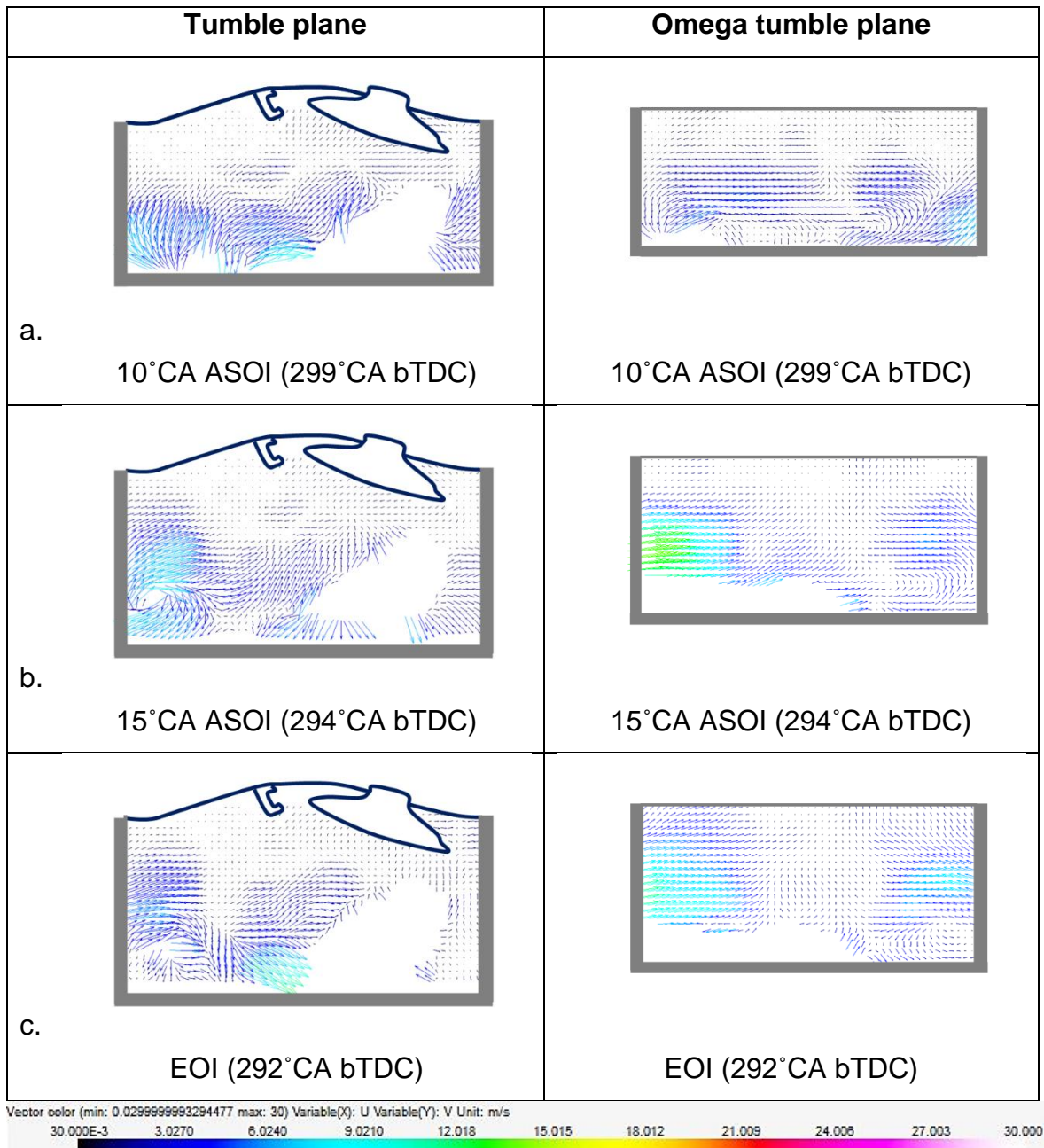
Figure 5.4: ensemble averaged velocity vectors for SOI 310˚CA bTDC and 35MPa injection pressure representing data over the injection period. The planes of measurements are indicated in the top row, and the engine positions are labelled underneath each corresponding velocity vector profile.

As the intake stroke develops, a small eddy with high local mean velocity starts to form on the LHS of the cylinder liner and the piston's surface in the tumble plane (Figure 5.4b.). This occurs due to the impingement of the fuel on the piston's surface, which forces the fuel and the surrounding charge to create eddies and rotate in the clockwise direction in the vicinity of the liner. This phenomenon would

typically encourage interactions between the impinged fuel droplets/ligaments with the surrounding charge in this region.

The eddy persists throughout the injection duration. The dense velocity vectors in the eddy by EOI suggests that the charge entrained within the eddy, which had possessed high local mean velocity, could have enabled fuel dense pocket to be entrained with the surrounding charge.

The lack of signal on the LHS of the omega tumble plane is due to the fuel dense region oversaturating the image plane. Generally, the local mean velocities in this plane are larger when compared to the tumble flow plane, particularly at 15°CA ASOI and EOI. This is the result of the main spray pushing the surrounding charge away from it. This effect causes the formation of local eddies towards both sides of the liner in this plane, while the charge above this eddy possesses high mean velocity.

Figure 5.5 provides ensemble-averaged velocity vectors throughout the rest of the intake stroke, after EOI, in both tumble plane (LHS column) and omega tumble plane (RHS column). As the intake stroke develops, the eddy observed on the LHS of the liner in the tumble flow plane grows. A similar feature is also observed in the omega tumble plane (Figure 5.5a.). Judging by the lack of signal received in this region, the core of these regions contains un-vapourised fuel that had bounced off the piston and was transported towards the LHS of the liner, as stated earlier. It turns out that the eddy entrained more fuel which bounced off the piston's surface, instead of increased interactions with the surrounding charge.

The fuel rich region is then broken down and interacts with the surrounding charge much later in the intake stroke (Figure 5.5b. - c. tumble plane), forming large eddies in the centre of the cylinder with high local mean velocities. This fuel-rich charge intensified the tumble flow in the counter-clockwise direction for the rest of the intake stroke, as indicated by the distinct eddies formed underneath the high local mean velocity region. In the omega tumble plane meanwhile, the breaking down of the fuel-rich region forms much weaker vortices compared to those formed in the tumble plane, judging by the low magnitudes of the velocity vectors in the flow field towards the end of the intake stroke (Figure 5.5b. - c). This is because the high plume angle directed in the tumble plane generates a higher tumble charge motion compared to the charge motion in the cross-flow plane.

Tumble plane	Omega tumble plane

a. 270°CA bTDC — 270°CA bTDC

b. 240°CA bTDC — 240°CA bTDC

c. 230°CA bTDC — 230°CA bTDC

Vector color (min: 0.0299999993294477 max: 30) Variable(X): U Variable(Y): V Unit: m/s

30.000E-3 3.0270 6.0240 9.0210 12.018 15.015 18.012 21.009 24.006 27.003 30.000
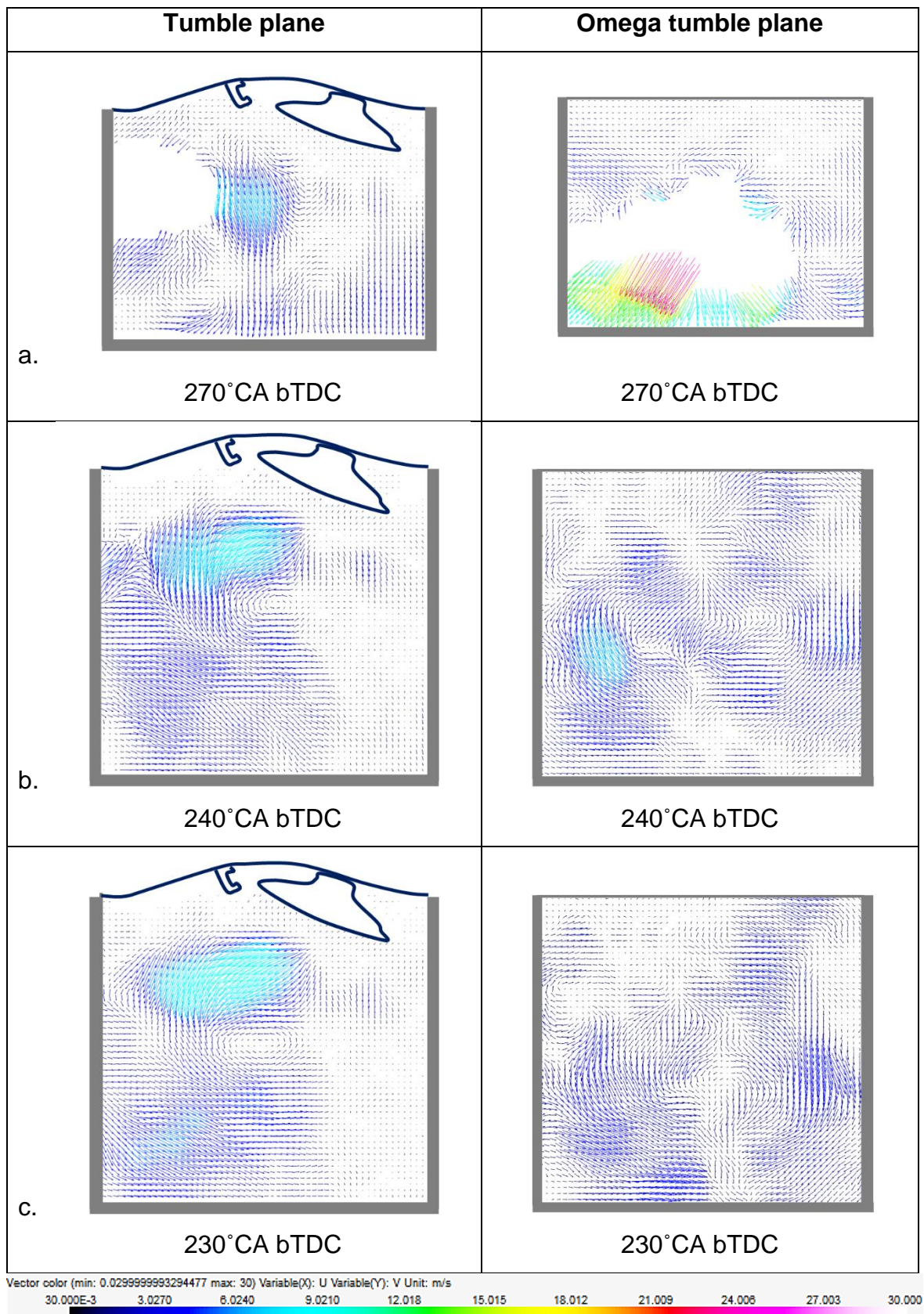
Figure 5.5: ensemble averaged velocity vectors for SOI 310°CA bTDC representing remainder of the intake stroke post-injection.

Figure 5.6 provides ensemble-averaged velocity vectors throughout the compression stroke for SOI 310˚CA bTDC case. This data represents the effects of EOI on the flow-field of the tumble and omega-tumble planes for the remainder of the cycle.

As observed in both planes, the overall magnitude of velocity of the flow has weakened across the planes. Close to TDC (Figure 5.6c.), the charge is getting pushed upwards caused by the piston's upwards motion. The densely populated velocity vectors observed near the piston's surface indicate that the charge in the vicinity of the piston's surface is being affected by the piston motion the most. This is interpreted from the large velocity vectors, which are densely populated near the piston's surface and pointing upwards towards the cylinder head as the piston moves upwards. The results suggest that the charge motion is affected by the piston's motions, particularly near the surface of the piston.

It is also believed that due to the piston surface impingement, a considerable amount of fuel would be settled on the piston's surface throughout the cycle. As a result, close to TDC, the characteristics of the flow-field would be a thick fuel film settled on the liner along with a weak flow field with low bulk flow motion in the vicinity of the spark plug. These features would adversely affect the combustion stability, with a potential likelihood of pool fire whose flame would be attached to the piston's surface, as was reported by Stevens et al., [39].

A similar observation was also made by Kim et al., [142] whereby with injection timings of 285°CA bTDC and earlier, pool fires had formed on the piston top judging by the high fluorescence intensity from their LIF measurements, with the same engine speed of 1200rpm and WOT condition. This had occurred due to the piston top being in the vicinity of the injector tip during injection. The result was a thick liquid fuel film accumulated on the piston surface. In addition to this, larger soot primary particles and a variety of soot aggregate sizes were observed as the pool fire persisted through the expansion stroke. They attributed this to the observations of soot formation occurring under a variation of ambient pressure condition, large soot residence time within the flame, and high soot oxidation later in the exhaust stroke.

Tumble plane	Omega tumble plane

a. 180°CA bTDC — 180°CA bTDC

b. 70°CA bTDC — 70°CA bTDC

c. 50°CA bTDC (nearing TDC) — 50°CA bTDC (nearing TDC)

Vector color (min: 0.0299999993294477 max: 30) Variable(X): U Variable(Y): V Unit: m/s
30.000E-3 3.0270 6.0240 9.0210 12.018 15.015 18.012 21.009 24.006 27.003 30.000
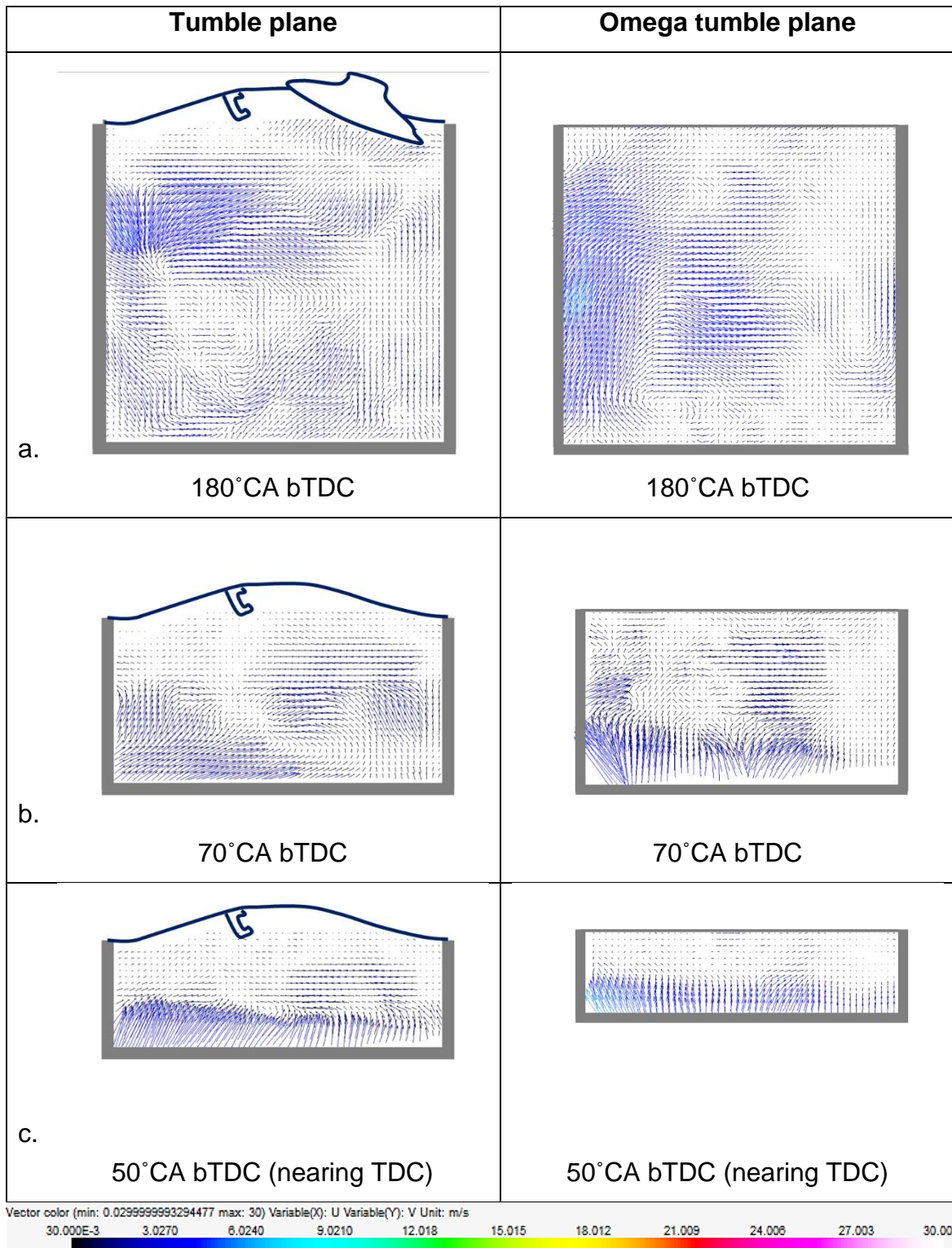
Figure 5.6: ensemble averaged velocity vectors for SOI 310°CA bTDC representing remainder of the compression stroke.

5.2.3 Effects of Late Single Injection on the Flow Field

Ensemble-averaged velocity vectors during the injection period for the late single injection case of SOI 200°CA bTDC in both tumble and omega tumble planes, are presented in Figure 5.7.

Upon injection, local eddies are formed across the edges of the spray as the high injection momentum of the fuel displaces the surrounding charge that possesses lower velocities. This interaction is particularly dramatic at the head of the spray (tumble plane), where peak velocity vectors exceeding 18m/s are observed (Figure 5.7a.), which is also reflected in the corresponding omega tumble plane. This is caused by the propagation of the wide head of the spray, which thereby forces the surrounding charge away from it. During this interaction, there is high momentum transfer taking place, over a large surface area (head region), between the injected fuel and the charge in the vicinity. As a result, the local TKE contours in this region are of the order of magnitude of 170m^2/s^2 (Figure 5.8a.), which indicates large velocity fluctuations per cycle.

The peak velocity vectors and TKE contours at the spray's head should theoretically be consistent, or even increase, for the injection duration past 5°CA ASOI until EOI, due to the high injection pressure and large PW introducing increasing amount of fuel into the cylinder. This would be the case however, if the spray was injected under ambient atmospheric conditions. In the current case, the surrounding charge affects the spray propagation. Due to the reduced pressure difference between the injected fuel and surrounding charge, the peak velocity vectors with increasing injection duration are not observed.

The charge that was being pushed away with high velocity at 5°CA ASOI, starts to form a recirculation region with vortices travelling in the counter clockwise direction at the head of the spray in the tumble plane (Figure 5.7b.). The magnitude of the velocity vectors of the charge within the recirculation zone has reduced in this process, as a result of the changing directional components of the tracer particles. Along with this, the width of the spray is visibly reduced. This is because the recirculation zone causes the fuel dense region at the head of the spray to break up, enabling entrainment of the fuel droplets, broken away from the spray head, with the charge at this location.

Tumble plane	Omega tumble plane
a. 5˚CA ASOI (195˚CA bTDC)	5˚CA ASOI (195˚CA bTDC)
b. 10˚CA ASOI (200˚CA bTDC)	10˚CA ASOI (200˚CA bTDC)
c. EOI (182˚CA bTDC)	EOI (182˚CA bTDC)

Vector color (min: 0.0299999993294477 max: 30) Variable(X): U Variable(Y): V Unit: m/s

| 30.000E-3 | 3.0270 | 6.0240 | 9.0210 | 12.018 | 15.015 | 18.012 | 21.009 | 24.006 | 27.003 | 30.000 |
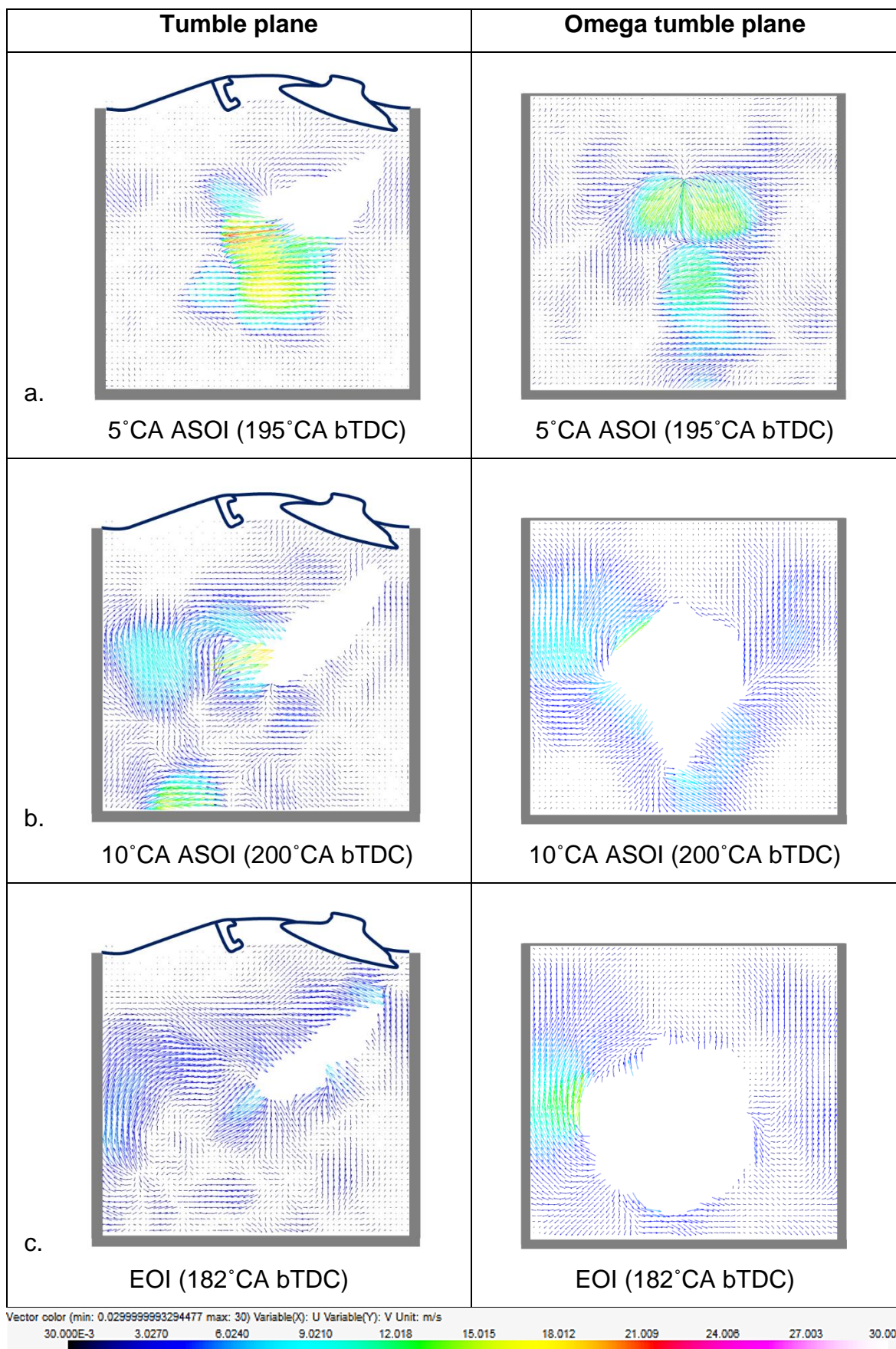
Figure 5.7: ensemble averaged velocity vectors for SOI 200˚CA bTDC representing data over the injection period.

Tumble plane	Omega tumble plane
a. 5˚CA ASOI (195˚CA bTDC)	5˚CA ASOI (195˚CA bTDC)
b. 10˚CA ASOI (200˚CA bTDC)	10˚CA ASOI (200˚CA bTDC)
c. EOI (182˚CA bTDC)	EOI (182˚CA bTDC)

Follow Contours Scalar Map (min: 0 max: 200) Variable: TKE Unit: (m/s)²

10.00   30.00   50.00   70.00   90.00   110.0   130.0   150.0   170.0   190.0
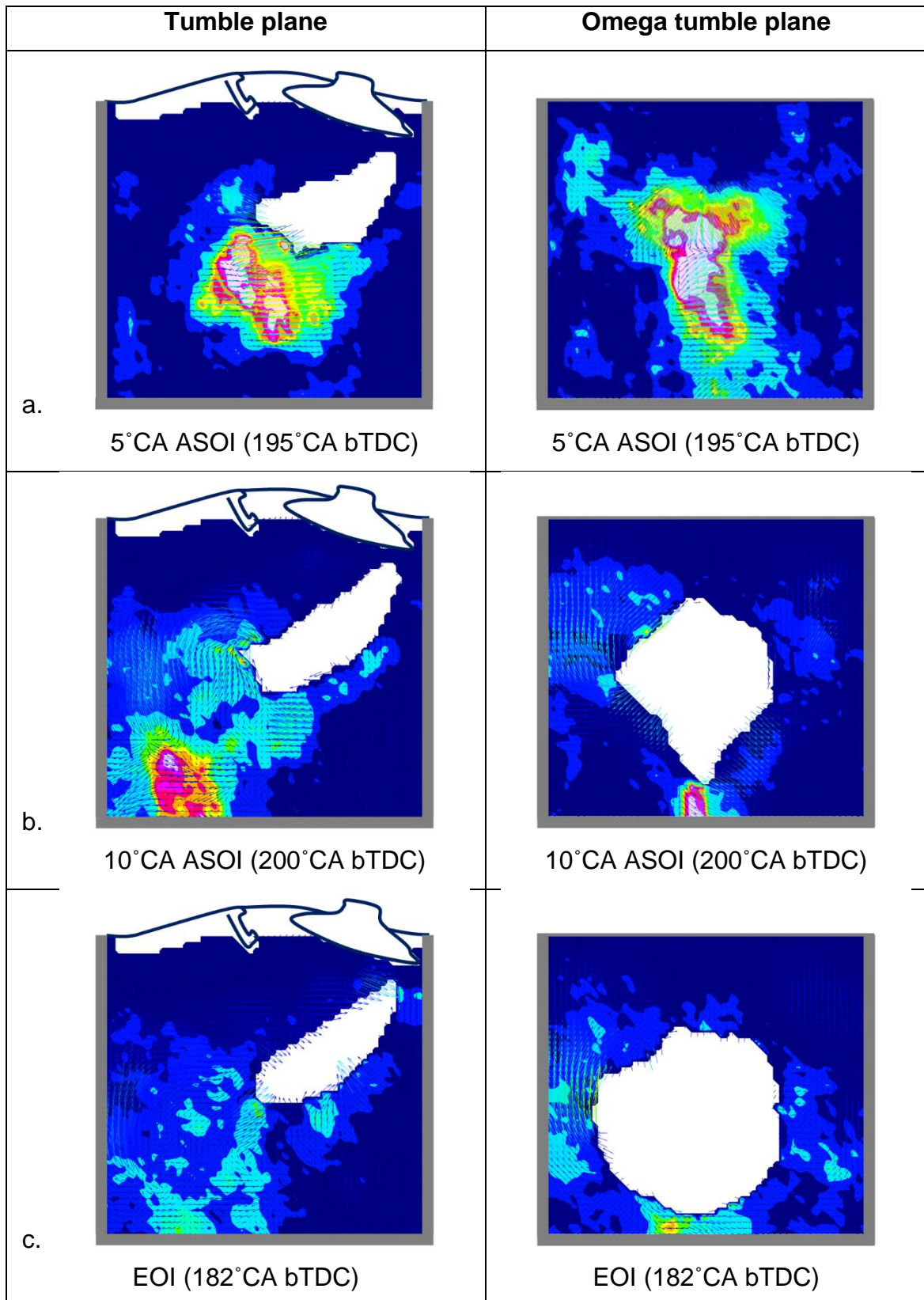
Figure 5.8: averaged TKE contours for SOI 200˚CA bTDC representing data over the injection period.

It is worth noting here that the area of the oversaturated region in the omega tumble plane in Figure 5.7b. is much larger than that in the tumble plane for the same engine position. This is caused by the differences in the light scattered by the droplets. In the omega tumble plane, the light scattering caused by the fuel rich region in the image plane expands the oversaturated region. The structure of the oversaturated region with the lack of PIV signal therefore appears to be greater in comparison. As a result, a direct comparison of the main spray's evolution in both planes should not be made. A direct comparison of the raw images and the data indicated that the oversaturated region in the tumble flow is the better representation of the actual global spray structure.

By EOI (Figure 5.7c.), the vortices at the head of the spray grow and break up the edges of the main spray structure, judging by the reduced area of over-saturated signal from the main spray in the tumble plane. These vortices resist further propagation of the main spray structure both axially and radially, which appears to have been reduced in width. By this time, the velocity vectors are more uniform globally, with reduced velocity magnitudes, when compared to the start of injection, all while the piston is still on its way to BDC. The peak TKE contours have also reduced significantly by EOI (Figure 5.8c.), with a larger region at the head covered by relatively high local TKE contours. The reduction in the peak velocities and TKE levels of the eddies is mainly caused by the growth of the eddy.

This phenomenon confirms that even though the injection pressure and PWs are both relatively large, the surrounding charge at part-load conditions can still induce sufficient resistance against the propagation of the spray, that too during the intake stroke when the in-cylinder pressure traces are low (Figure 5.2). The main cause of this is the momentum transfer taking place between the injected fuel at high pressure and the charge in the vicinity of the global spray structure.

These characteristics however indicate alleviated interactions between the fuel and piston surface, along with the cylinder liner. On the contrary, Wang et al., [84] observed a stronger wall impingement jet produced by delaying the injection timing in the intake stroke, albeit with improved overall mixture uniformity. This alleviated the fuel impingement on the piston's surface. Meanwhile, Kim et al., [142] found that the pool fires had developed mostly from the cylinder liner wall with the injection

timings between 180°CA bTDC and 250°CA bTDC, when running at 1200rpm WOT conditions with an injection pressure of 15MPa. In addition, there was a lack of soot particles detected with SOI 250°CA bTDC, both within the flame and at the exhaust locations due to the low level of pool fires. The liner wetting had reduced however, when the injection was executed at more advanced timings in the intake stroke due to the higher ambient gas density and temperature. In the current case, no liner wetting is observed altogether even under the low load condition. This is the result of increased resistance against the spray propagation, which is caused by the momentum transfer from the spray with high injection pressure to the surrounding charge.

Figure 5.9 and Figure 5.10 represent the ensemble averaged velocity vectors and TKE contours respectively, of the flow field in the compression stroke, after the end of injection. As the main spray collapses, vortices with high velocity vectors in the tumble plane, moving in the counter clockwise direction, are largely distributed in the centre of the flow field (Figure 5.9a.). These vortices with high local mean velocities and TKE contours are formed due to 1) the collapse of the fuel-dense spray with high injection momentum, which now contains a fuel rich charge and 2) the rise of the in-cylinder pressure from the start of the compression stroke. The high local velocities are observed in both the tumble and omega tumble planes, at the tip of the spark plug. It is suspected that these eddies are part of one large vortical structure formed as the main spray collapsed and transferred momentum to the surrounding charge.

As the compression stroke develops (Figure 5.9b. - c.), the high velocity vortices in the tumble plane persist all the way to near TDC. Interestingly however, the movement of the piston and variation in the in-cylinder pressure does not dislocate the position of this high-velocity region in the tumble plane, while these properties do tend to impact the high local mean velocity charge in the omega tumble plane. This implies that greater variations in the flow field are induced in the omega tumble plane, when compared to the tumble plane.

Tumble plane	Omega tumble plane
a. 120˚CA bTDC	120˚CA bTDC
b. 80˚CA bTDC	80˚CA bTDC
c. 50˚CA bTDC (nearing TDC)	50˚CA bTDC (nearing TDC)

Vector color (min: 0.0299999993294477 max: 30) Variable(X): U Variable(Y): V Unit: m/s
30.000E-3 3.0270 6.0240 9.0210 12.018 15.015 18.012 21.009 24.006 27.003 30.000
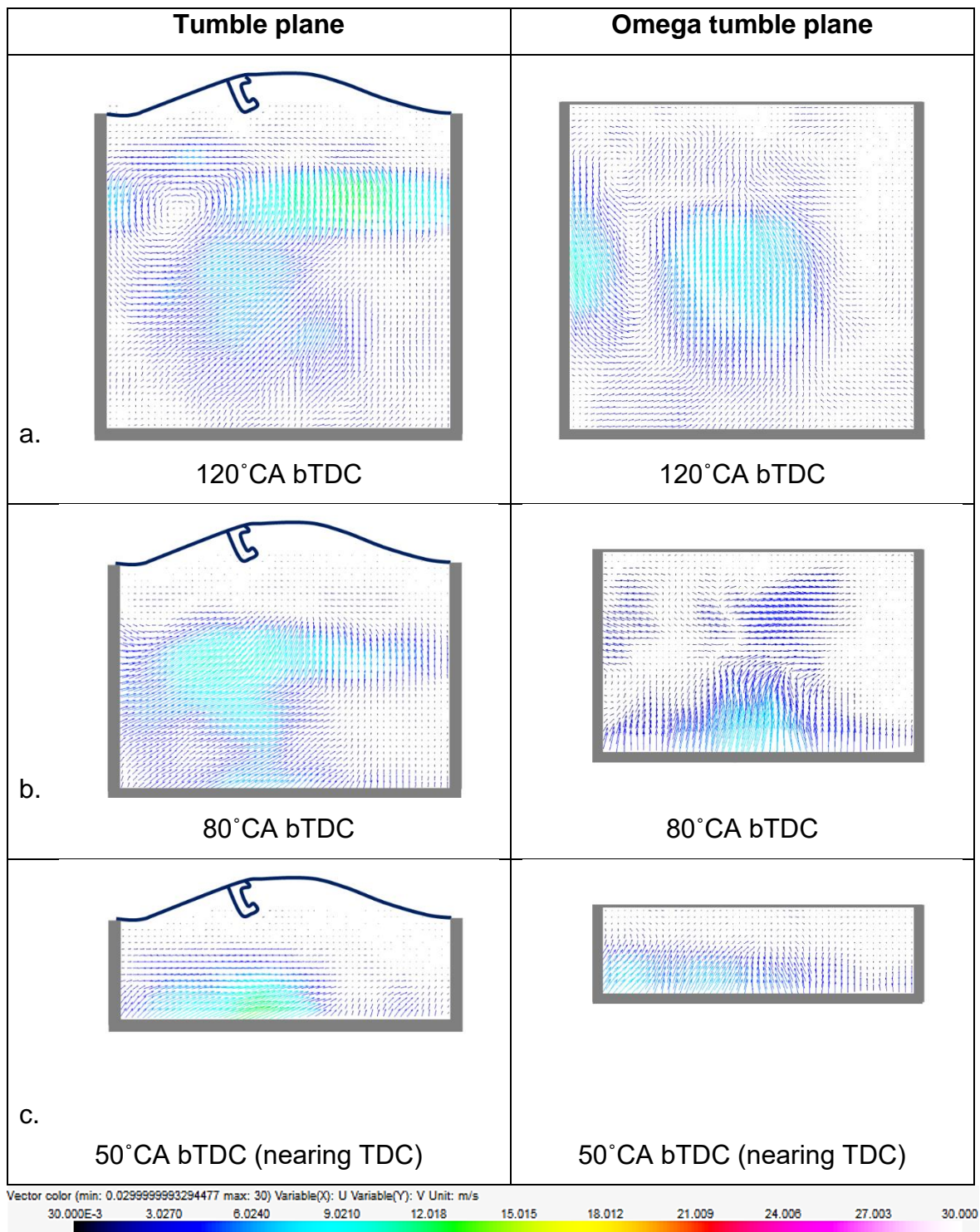
Figure 5.9: ensemble averaged velocity vectors for SOI 200˚CA bTDC representing data during the compression stroke.
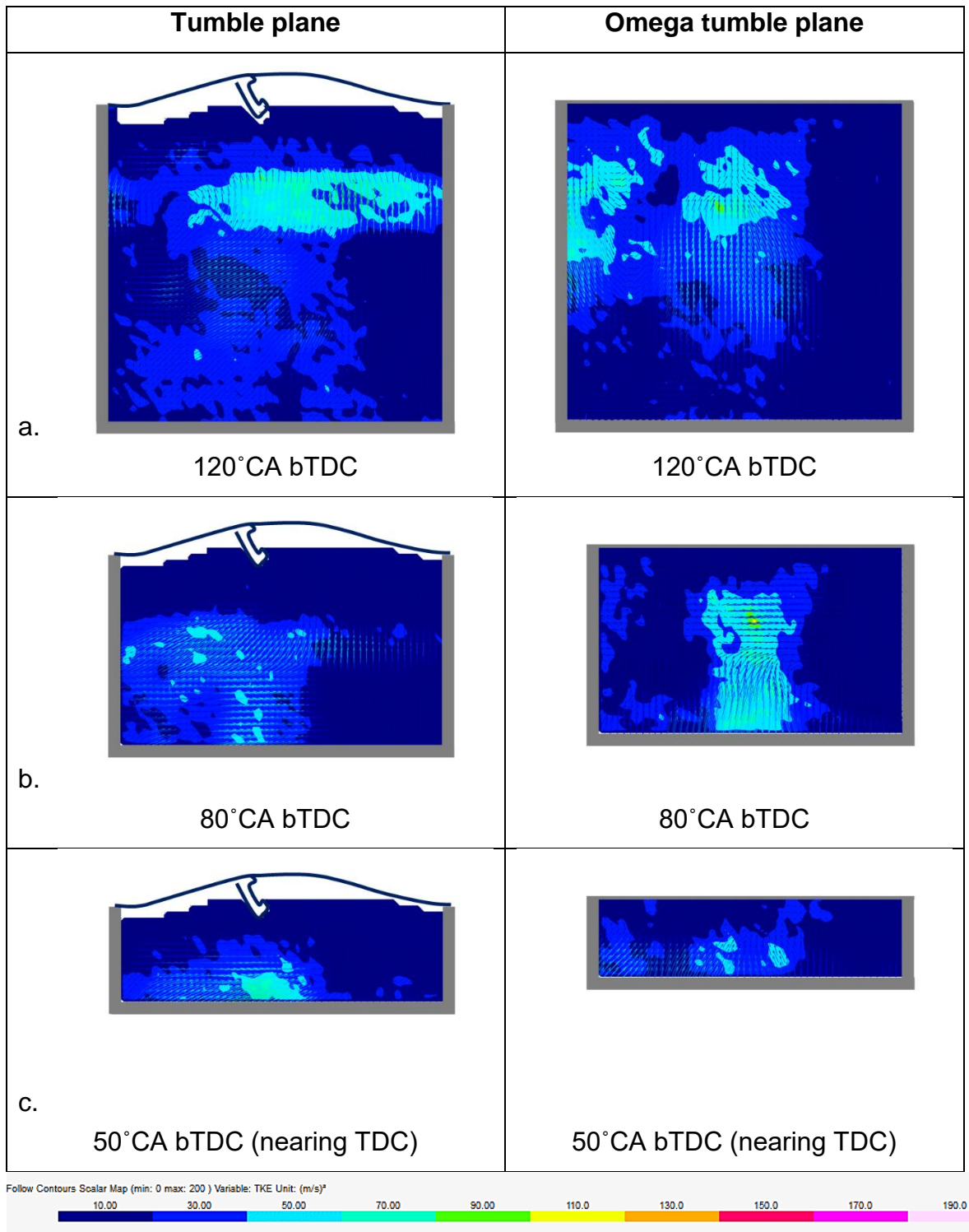
Figure 5.10: averaged TKE contours for SOI 200˚CA bTDC representing data during the compression stroke. The planes of measurements are indicated in the top row, and the engine positions are labelled below each corresponding TKE profile.

Further studies on the effects of these differences on the flame structure would also provide an indication of the sources of its cycle-cycle variabilities. It was stated by Szybist et al., [36] that the initial flame development was the most crucial feature that affected the cycle-to-cycle variations. This was due to the high sensitivity towards a number of factors, including laminar flame speed which dominates the combustion rate, and turbulent flame propagation stage which is predominant only after the flame kernel is sufficiently large so that it can be influenced by multiple turbulent eddies simultaneously. Fuels with high flame speed increase the rate of development of the early flame kernel, which makes them less susceptible to the stochastic cycle-to-cycle differences in turbulence and ultimately result in stable combustion.

Near TDC (Figure 5.9c.), the velocity vectors of the charge on the surface of the piston are large, with the order of magnitude of around 10m/s. In the tumble plane, this high local mean velocity region is located closer to the exhaust valves and far from the spark plug. This is also reflected by the high TKE contours directed towards the exhaust valves in Figure 5.10c. It is suspected that upon ignition, these charge properties would cause the flame kernel to propagate with high velocity towards this region, and could potentially be directed through the exhaust valves, instead of propagating across the combustion chamber.

5.2.4 Effects of Single Injection Timings on TKE levels near TDC

A comparison of the TKE contours near TDC, for both single injection times tested, are presented in Figure 5.11. Observing the early single injection case of SOI 310°CA bTDC, the global TKE levels of the flow field in the tumble plane near TDC in Figure 5.11a. are lower than $10m^2/s^2$. This is because the fuel injected during the early single injection had sufficient time to interact with the surrounding charge, which mostly happened towards the intake stroke as was observed. As such, the high velocity vectors dissipated by the end of the compression stroke, thereby reducing the overall TKE levels. Observing the omega tumble plane on the other hand, the overall TKE levels are slightly higher than the tumble flow plane. It is suspected that these conditions are still too low to support stable flame propagation and combustion.

Tumble plane	Omega tumble plane
a. SOI 310˚CA bTDC Engine position: 50˚CA bTDC	SOI 310˚CA bTDC Engine position: 50˚CA bTDC
b. SOI 200˚CA bTDC Engine position: 50˚CA bTDC	SOI 200˚CA bTDC Engine position: 50˚CA bTDC

Follow Contours Scalar Map (min: 0 max: 200) Variable: TKE Unit: (m/s)²

10.00 30.00 50.00 70.00 90.00 110.0 130.0 150.0 170.0 190.0
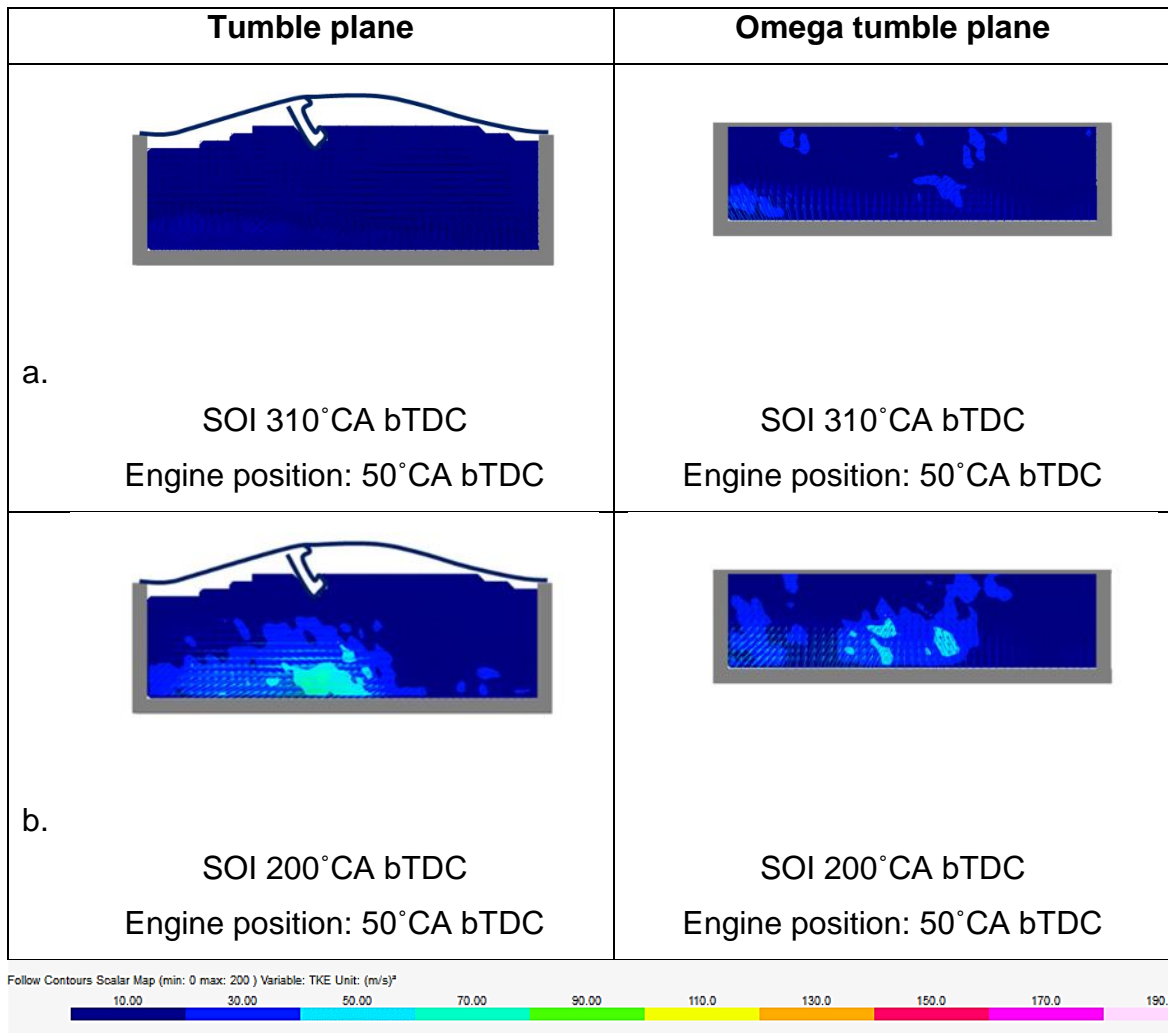
Figure 5.11: averaged TKE contours for SOI 310˚CA bTDC and SOI 200˚CA bTDC representing the turbulence levels in the flow field at 50˚CA bTDC (nearing TDC).

High local TKE contours for SOI 200˚CA bTDC on the other hand, are observed in both planes near the tip of the spark plug. The flow indicates higher turbulence levels in the tumble plane compared to the omega tumble plane. While this flow-field creates a locally turbulent flow field near TDC, which could be favourable for high flame speed, the TKE contours are mostly concentrated near the exhaust valves as discussed earlier. This could adversely influence the direction of the motion of the flame speed.

Another concern regarding the later injection in the intake stroke is tip wetting, which is more sensitive to timescales and injector tip temperature [33]. Medina et al., [33] found that late single injections in the intake stroke reduced the total time taken for tip drying, which was exacerbated by using high injection pressures, as in the current

case. This reduced time for tip drying has increased the PN emissions, which was consistent across the speed ranges of 1000rpm to 2000rpm.

It is also interesting to note that while the local turbulence levels vary visibly between the two injected cases, the difference is clearly not large enough to affect the average peak pressures recorded at TDC, which were comparable for both injection cases.

5.2.5 Cyclic Variations of the Flow Field Close to TDC

The maps of the standard deviation in the velocity measurements close to TDC (50°CA bTDC) for both the tested cases are presented in Figure 5.12. This data provides an indication of the cyclic repeatability of the flow field observed close to TDC.

The low standard deviation in the tumble plane observed for SOI 310°CA bTDC (Figure 5.12a.) suggests consistency in the formation of the weak velocity vector flow field close to TDC and near the spark plug. On the contrary, the large standard deviation of magnitudes of up to 7m/s implies increased cyclic variability in the flow field in the corresponding omega tumble plane for the same engine position.

Meanwhile, the highest standard deviations are associated with the later single injection case of SOI 200°CA bTDC, whereby the velocity magnitudes vary up to 7m/s in both planes. This suggests that although the flow field possesses higher velocity magnitudes near TDC due to the later single injection case, there are greater cyclic variations associated with this. This is most likely due to the largely dynamic flow development which varies across three dimensions, generating large cyclic variations. In other words, the late second injection showed high entrainment rates with high TKE levels and velocity magnitudes which persisted throughout the compression stroke. The high entrainments rate is typically accompanied with the cost of cyclic variations, observed close to TDC.

Tumble plane	Omega tumble plane
a. SOI 310˚CA bTDC Engine position: 50˚CA bTDC	SOI 310˚CA bTDC Engine position: 50˚CA bTDC
b. SOI 200˚CA bTDC Engine position: 50˚CA bTDC	SOI 200˚CA bTDC Engine position: 50˚CA bTDC

Follow Contours Scalar Map (min: 0 max: 20) Variable: StdDev (U) Unit: m/s
1.000 3.000 5.000 7.000 9.000 11.00 13.00 15.00 17.00 19.00
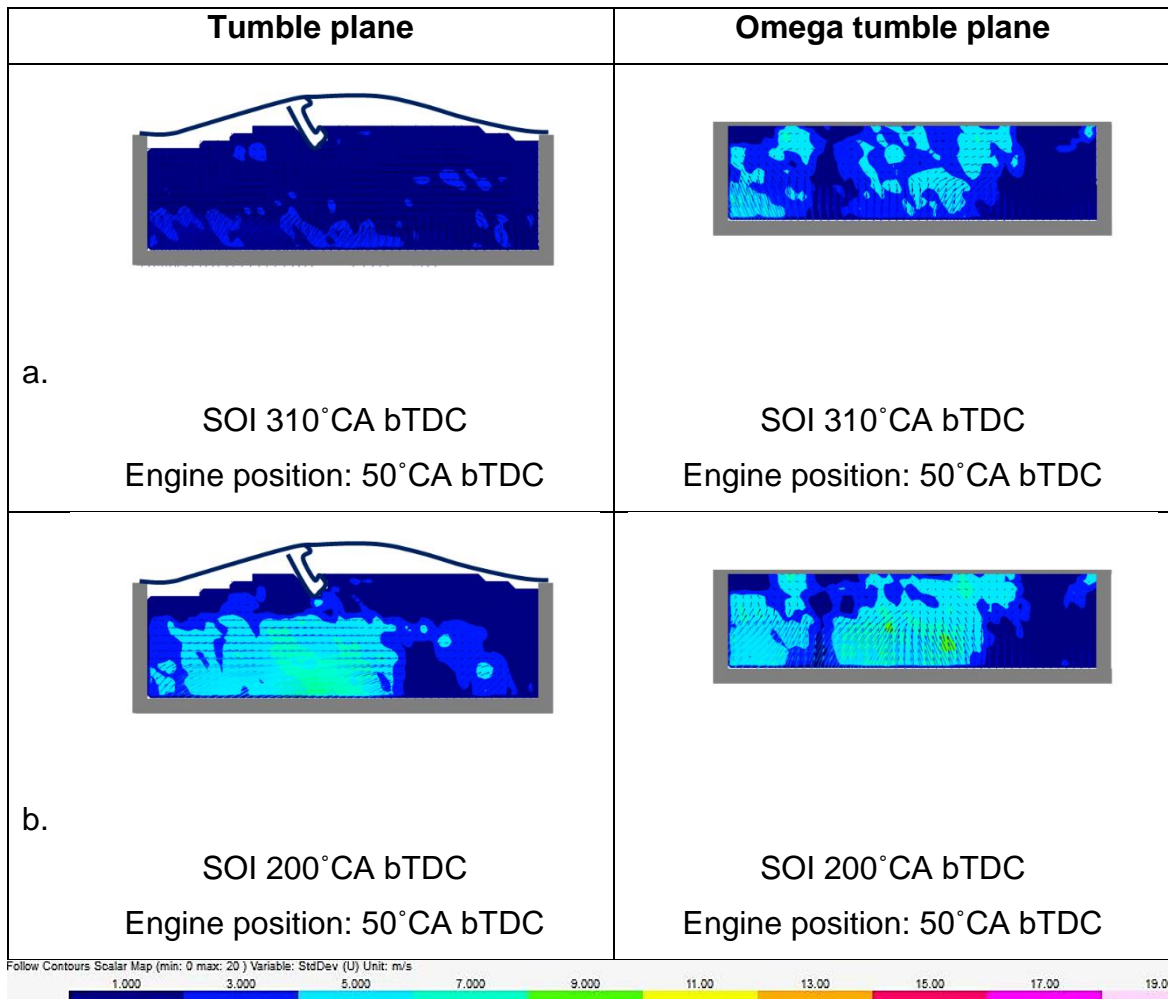
Figure 5.12: maps of standard deviation in velocities for SOI 310˚CA bTDC and SOI 200˚CA bTDC at 50˚CA bTDC (nearing TDC).

5.2.6 Summary

The effects of the single injections at two different times in the intake stroke were investigated in this section. The early single injection case of SOI 310°CA bTDC and the large PW of 2.5ms, was observed to cause significant piston impingement due to the piston being in the vicinity of the injector upon injection. As a result, the flow field in the compression stroke was observed to have been weakened significantly due to inhibited interaction between the main spray structure and the surrounding charge. In addition, the TKE levels near the spark plug were low in the tumble plane.

Due to the piston impingement, it could lead to the formation of fuel film on the piston throughout the cycle, which would in turn cause pool fires. A similar study observed larger soot primary particles and a variety of soot aggregate sizes caused by pool fires, which had persisted through the expansion stroke [142].

A later single injection case of SOI 200°CA bTDC allowed the global spray structure to develop towards the centre of the cylinder, due to the piston position being near BDC. As the spray collapsed, high velocity tumble charge motion in the counter clockwise direction was observed to have been developed. These eddies would most likely be highly fuel-rich, as they replaced the main spray structure upon spray collapse. The high tumble charge motion persisted throughout the compression stroke in the tumble plane, while the overall velocity magnitudes reduced in the omega tumble plane.

Relatively turbulent charge motion, close to TDC, was achieved with this injection timing, whereby the TKE contours were positioned closer to the exhaust valves, albeit with large uncertainties in velocities implying increased cyclic variability. As the injection was relatively early however, it is suspected that the mixture would be homogeneous, instead of generating a stratified charge with a fuel rich cloud close to the spark plug.

Both injection strategies generated the same peak pressure at TDC, albeit the significant variations in the velocity vectors and TKE levels observed throughout the cycle.

5.3 Split Injections

5.3.1 Investigations of Split Ratios on the Flow Field

The effects of early split injections in the intake stroke with varying split ratios are investigated in this section. Table 5.4 and Table 5.5 provide details of the injection parameters tested, respectively. Figure 5.13 presents an overview of the differences in the split ratios and injection timings, in the form a simple schematic. The first injection is maintained at SOI 310°CA bTDC for both cases, with a variation in the injected quantity. The second injection takes place toward the end of the intake stroke. The purpose of studying these parameters was to investigate (1) the effects of the injection timings and (2) the effects of split ratios on the evolution of the in-cylinder charge throughout the cycle and the mixture formation.

Note that the total PW of the split injections is equivalent to the single injection's PW of 2ms. The injected quantity presented was obtained using the linear relationship between the injector's PW and the quantity at 35MPa, as presented in (Figure 4.1 in section 4.2).

Table 5.4: split injections test parameters, timings and split ratios of the early 1st and 2nd injection cases.

Injection pressure (MPa)	SOI1 (°CA bTDC)	Split1 (%)	PW1 (ms)	1st injection quantity (mg)	SOI2 (°CA bTDC)	PW2 (ms)	2nd injection quantity (mg)
35	310	75	1.87	19.7	191	0.63	6.3
35	310	25	0.63	6.3	182	1.87	19.7

Table 5.5: corresponding split ratios and dwell times for the specified injection parameters.

Split 1(%)	Split ratio	Dwell time (°CA)	Dwell time (ms)
75	3:1	128	18
25	1:3	128	18
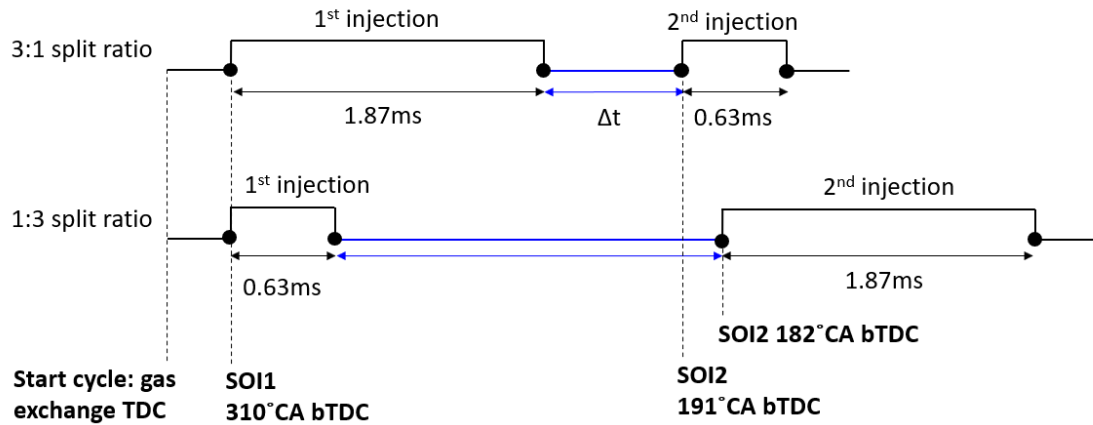
Figure 5.13: schematic representing the differences between the two tested split injection ratios and their timings with respect to the gas exchange TDC.

5.3.1.1 Effects of Early First and Second Split Injections on the In-cylinder Gas Properties

Figure 5.14 provides the in-cylinder pressure traces for the two tested cases. Table 5.6 presents information of the operating conditions for reference.
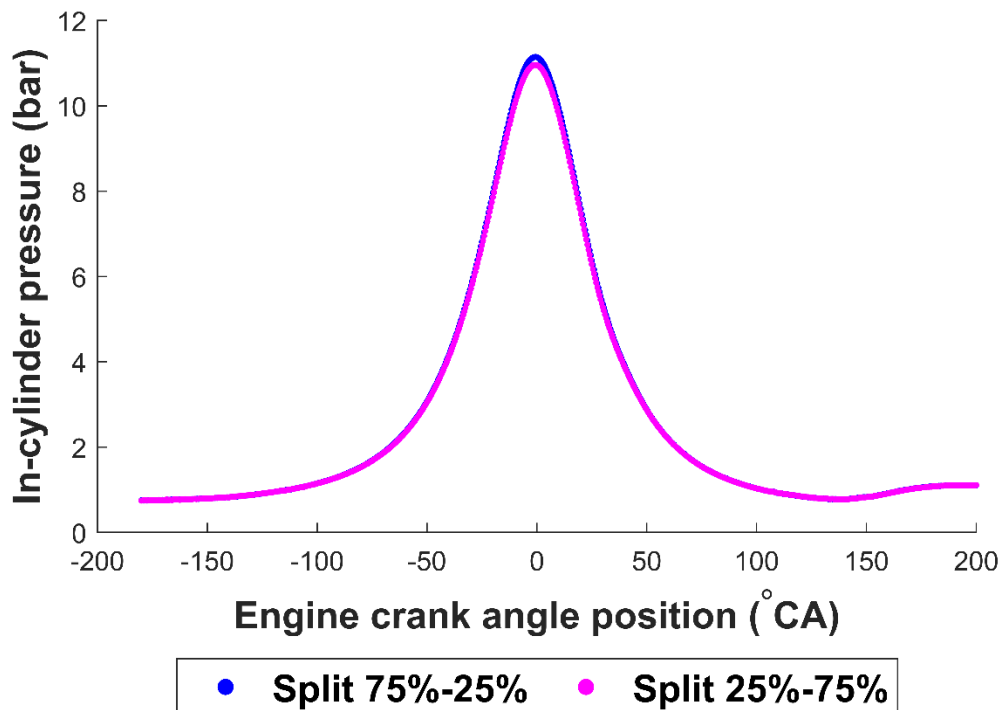
Figure 5.14: averaged in-cylinder pressure traces for the intake and compression strokes for the two tested split cases of varying ratios: 1) split 75% - 25% and 2) split 25% - 75%. The in-cylinder pressure at each engine crank angle are averaged over 300 recorded cycles.

Table 5.6: recorded test conditions for the two split cases tested with the different split ratios, at an injection pressure of 35MPa.

Split1 (%)	Average MAP (bar)	Inlet temperature (°C)	Coolant temperature in/out (°C)	Oil temperature in/out (°C)	Ambient pressure (°C)
75	0.75	30.4	50.2 / 49.9	39.5 / 39.7	1.025
25	0.75	30.2	50.1 / 49.8	39.0 / 39.0	1.026

For a constant load of 0.75bar MAP, a slightly higher average peak pressure at TDC is associated with the 75%-25% split ratio. This is because of the reduced amount of fuel entering the cylinder the second time, when compared to the smaller split ratio. As a result, the temperature and pressure inside the cylinder are higher than the smaller split ratio, whereby the higher second injection's fuel quantity would reduce the cylinder temperature. The difference in the average peak pressure however is as small as 0.2bar.

Interestingly however, the variation in the second injection quantity has negligible effects on the average peak pressure, suggesting that the average peak pressure is primarily affected by the injection timings.

Figure 5.15 represents the logarithmic relationship between the in-cylinder pressure and volume for the tested split injection cases. The corresponding polytropic constants are provided in Table 5.7, which represents the rate of pressure rising in the compression stroke.
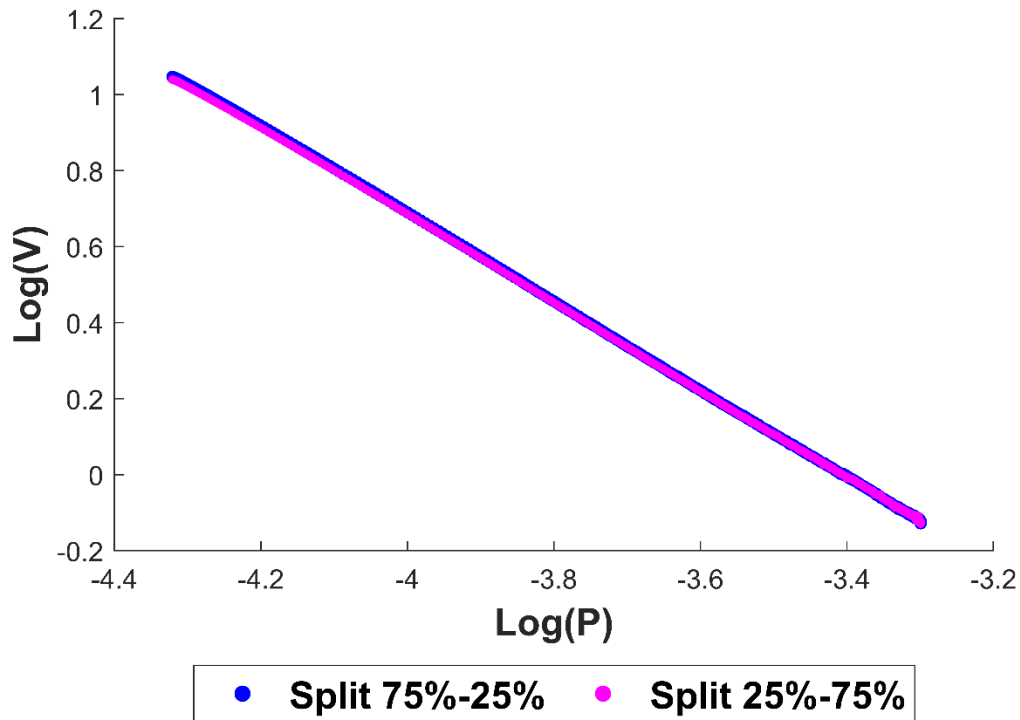
Figure 5.15: relationships between Log(P) and Log(V) recorded during the compression stroke for the two split cases tested with the different split ratios.

The trend indicates that the rate of increase in pressure during the compression stroke is also independent of the split ratio and the second injection quantity. Additionally, the polytropic constants of the split cases and single injections are identical, suggesting that the injection strategy does not have any effect on the rate of pressure increase in the compression stroke, at least under cold-flow conditions.

Table 5.7: polytropic constants for the two tested split cases derived from the Lop(P) - Log(V) trends measured in the compression strokes.

Split1 (%)	Polytropic constant, n
75	1.15
25	1.15

5.3.1.2 Effects of a Large Split Ratio on the Flow Field

The effects of the larger split ratio of 75%-25% on the in-cylinder charge characteristics throughout the cycle are explored in this section. Figure 5.16 provides ensemble averaged velocity vectors during the injection period for the 75%-25% split ratio, measured in the tumble plane (column on the LHS) and omega tumble plane (column on the RHS).

The effects of the first injections in this case are similar to the injection case of SOI 310°CA bTDC. Upon fuel injection, the surrounding charge gets displaced by the high-pressure fuel entering the cylinder, as a result of which the charge surrounding the head of the spray possesses large local mean velocity, as observed in the tumble plane (Figure 5.16a.). Majority of the plumes impinge on the surface of the piston, which would result in heavy piston surface impingement from the first injection.

The momentum transfer between the spray and the surrounding charge at the spray head causes the formation of large vortices, with high local mean velocities, towards the LHS of the piston (Figure 5.16b.). By the end of first injection (EOI1), large eddies are now well developed in this region. Judging by the reduced width of the over-saturated region, it can be deduced that the surrounding vortices, which possess high local mean velocities, start to break off the edges of the main spray, encouraging the entrainment of the atomised fuel droplets. In addition, due to the formation of the large vortices by the EOI1, the high local mean velocities in the plane have dissipated, when compared to 10°CA after start of first injection (ASOI1), caused by the momentum transfer between the spray and the formation of the eddy.

The impinged fuel in the omega tumble flow plane indicates that the surrounding charge is being pushed upwards, causing the formation of counter rotating vortices towards both edges of the liner with high local mean velocities. These vortices gain increasing momentum by the EOI1, judging by the higher velocity magnitudes of the charge within the vortices.

Tumble plane	Omega tumble plane
a. 4˚CA ASOI1	4˚CA ASOI1
b. 10˚CA ASOI1	10˚CA ASOI1
c. EOI1	EOI1

Vector color (min: 0.0299999993294477 max: 30) Variable(X): U Variable(Y): V Unit: m/s

| 30.000E-3 | 3.0270 | 6.0240 | 9.0210 | 12.018 | 15.015 | 18.012 | 21.009 | 24.006 | 27.003 | 30.000 |

Figure 5.16: ensemble averaged velocity vectors for split ratio of 75%-25% and 35MPa injection pressure representing data over the injection period. The planes of measurements are indicated in the top row, and the engine positions are labelled below each corresponding velocity vector profile.

Figure 5.17a. - c. show the effects of the first injection on the ensemble averaged velocity vectors in the flow field prior to the start of second injection. The most notable feature is that upon the collapse of the remainder of the spray from the first injection (the remainder which had not settled on the piston's surface), the eddy that had initially started to form towards the LHS of the liner during the injection period,

grows with high local velocities as seen at 290°CA bTDC. The dense velocity vectors in this eddy implies high charge entrainment, instead of the fuel rich charge as was observed with the single injection case of SOI 310°CA bTDC. Meanwhile, the small but distinct eddies with diminished velocity magnitudes persist in the omega tumble plane at this engine position.

As the intake stroke progresses to 260°CA bTDC, the large eddy in the tumble plane is directed towards the centre of the cylinder. This occurs while the intake valves are open (Figure 5.17c.). It is suspected that the induced air causes further momentum transfer to this eddy, causing it to grow and rotate in the counter clockwise direction, with high velocity magnitude.

In this case, the eddy observed in the tumble plane consumes a large surface area in this plane, as observed by the band of high velocity vectors distributed across the centre of the flow field. This shows that the formation and direction of the eddies are rapidly changing. To elaborate this, while high local mean velocities are observed across the omega tumble plane at 260°CA bTDC, the flow in the tumble plane at this position does not show such a wide area covered by the high velocity vectors. Conversely, the eddy's high velocity region is now in the tumble plane at 240°CA bTDC (Figure 5.17c.), while the flow field in the omega tumble plane indicates a uniform distribution of the low velocity vectors throughout the flow field, albeit with small vortices formed across the flow field. This reveals the highly three-dimensional nature of these vortices, which moves rapidly, in different directions in the flow field. This behaviour would encourage a high rate of entrainment of the fuel droplets with the surrounding charge, producing a global homogenous charge prior to the start of the compression stroke.

The formation of the large eddy in the centre is indicative of the entrainment of the atomised droplets and the surrounding charge, albeit the significant spray-piston interaction. The size of the eddy, distributed across the cylinder in both planes (Figure 5.17c.), suggests that the fuel droplets are transported across the tumble plane in the cylinder, forming a global homogeneous charge prior to the second injection.

Tumble plane	Omega tumble plane
a. 290˚CA bTDC (7˚CA after end of first injection)	290˚CA bTDC (7˚CA after end of first injection)
b. 260˚CA bTDC	260˚CA bTDC
c. 240˚CA bTDC	240˚CA bTDC

Vector color (min: 0.0299999993294477 max: 30) Variable(X): U Variable(Y): V Unit: m/s

30.000E-3   3.0270   6.0240   9.0210   12.018   15.015   18.012   21.009   24.006   27.003   30.000

Figure 5.17: ensemble averaged velocity vectors for split ratio of 75%-25% and 35MPa injection pressure representing data of the flow field after the end of first injection.

Figure 5.18 provides ensemble averaged velocity vectors in both planes for the end of second injection (EOI2), with a short PW of 0.63ms. The immediate observation is

that the flow field by EOI2 is lacking the vortices generated at the tip of the spray, as has been observed with the first injection case in Figure 5.7c. As a result of the PW being so short, the charge in the vicinity has only started to be pushed away in both planes due to the introduction of the injection. By EOI2, the charge in the vicinity of the spray head thus possesses high velocity vectors as it is being pushed towards the LHS of the liner.

It is also worth noting here that the effects of the strong tumble motion observed at 240˚CA bTDC is not visible in this plane. In this case it is difficult to state the extent to which the propagation of the second injection was influenced by the vortices generated prior to SOI2. In the omega tumble plane, the spray head just reaches the image plane by EOI2, displacing the surrounding charge in all directions away from the fuel at high velocities.

Tumble plane	Omega tumble plane
EOI2	EOI2

Vector color (min: 0.0299999993294477 max: 30) Variable(X): U Variable(Y): V Unit: m/s

| 30.000E-3 | 3.0270 | 6.0240 | 9.0210 | 12.018 | 15.015 | 18.012 | 21.009 | 24.006 | 27.003 | 30.000 |

Figure 5.18: ensemble averaged velocity vectors for split ratio of 75%-25% and 35MPa injection pressure representing data for the end of the second injection.

Figure 5.19a. - c. show the effects of the second injection on the remainder of the cycle, which is the compression stroke. The velocity vectors indicate that the due to the short PW of the second injection, the intensity of the tumble vortices reduce progressively by 170˚CA bTDC. The distinct vortices have dissipated by this time

and the overall velocity magnitudes are uniform across the cylinder with magnitudes of around 5m/s.

Conversely the overall velocities are slightly larger in the omega tumble plane with distinct eddies at 170˚CA bTDC. This is indicative of the short quantity of the fuel collapsing and being entrained with the surrounding charge by the start of the compression stroke.

For the rest of the compression stroke, the flow field is relatively weak with diminished vortices. Near TDC (Figure 5.19c.), slightly large velocity vectors are distributed across the piston's surface. This was caused by the mixture being pushed upwards by the piston's motion and the subsequent large in-cylinder pressure trace.

Towards the end of the compression stroke however, distinct vortices with slightly larger local mean velocities are observed in the tumble plane as shown in Figure 5.19b. - c., which is most likely to be formed by the development of the compression stroke, forcing the vortices formed in the omega tumble plane at 170˚CA bTDC to be pushed upwards and rotate in the tumble plane. As a result, at 50˚CA bTDC at the centre region on the surface of the piston, the charge possesses slightly large velocity vectors.

This data suggests that a shorter 2nd injection late in the intake stroke (191˚CA bTDC), seems to form a relatively weak velocity region near TDC at the piston's centre. It is suspected that the fuel would effectively produce a global homogeneous mixture instead of there being a fuel rich charge local to the spark plug. A similar observation was also made by Zheng et al., [70], who reported that the overall mixture homogeneity increases with larger proportions injected in the first injection. The shorter second injection would cause the rich mixture to move away from the spark plug with decreased spray momentum. The effects of a smaller split ratio of 25%-75% are thus discussed in the following subsection.
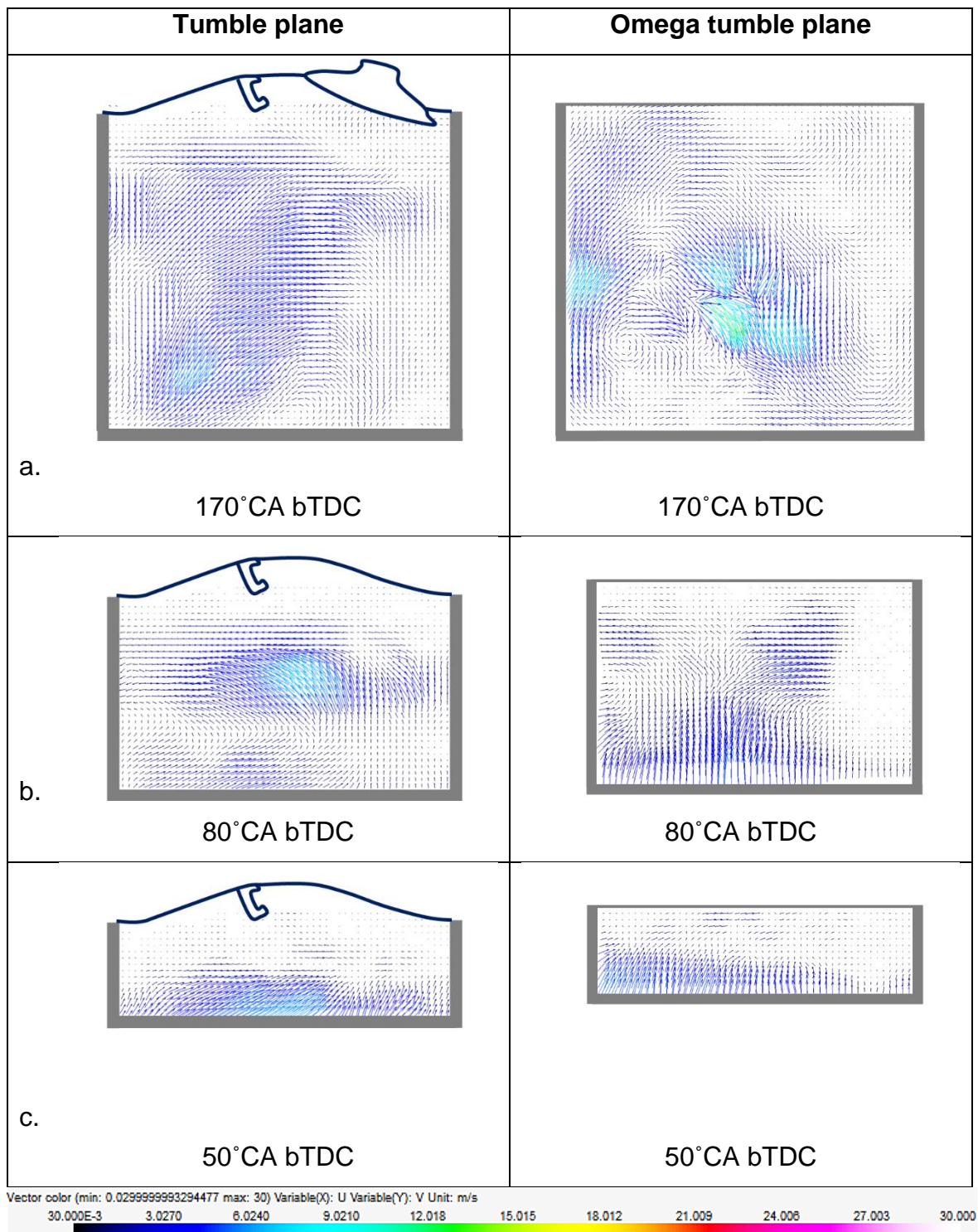
Figure 5.19: ensemble averaged velocity vectors for split ratio of 75%-25% and 35MPa injection pressure representing data of the flow field after the end of second injection.

5.3.1.3 Effects of a Small Split Ratio on the Flow Field

The effects of the small split ratio of 25%-75% (or 1:3) on the in-cylinder charge characteristics are explored in this section. Figure 5.20 provides ensemble averaged velocity vectors during the injection period, measured in the tumble plane and omega tumble plane.

The velocity vectors in the tumble plane reveal that although the fuel is impinged on the piston's surface upon injection, the earlier observation of the vortices formed from the interaction of the plumes with the piston's surface on the LHS is missing here. This is because the PW is a third of the PW tested for the larger split ratio. The short PW has minimum effect on the surrounding charge. By EOI1, the surrounding charge is infiltrating into the tail of the spray, resulting in accelerated spray collapse (when compared to larger 1st PW), as seen in Figure 5.20c. in the tumble flow plane. This indicates that although the injection pressure is high, the difference in the momentum between the spray and the surrounding charge is low, as a result of which the charge is able to interact with the main spray so soon.

The main spray does not reach the image plane in the omega tumble plane by EOI1, as observed by the dense velocity vectors in the flow field and the lack of the oversaturated region. Relatively high velocity vectors are observed on the piston's surface in this plane due to the fuel pushing the charge away from it.

Tumble plane	Omega tumble plane
a.	
2˚CA ASOI1	2˚CA ASOI1
b.	
3˚CA ASOI1	3˚CA ASOI1
c.	
EOI1	EOI1

Vector color (min: 0.0299999993294477 max: 30) Variable(X): U Variable(Y): V Unit: m/s

| 30.000E-3 | 3.0270 | 6.0240 | 9.0210 | 12.018 | 15.015 | 18.012 | 21.009 | 24.006 | 27.003 | 30.000 |
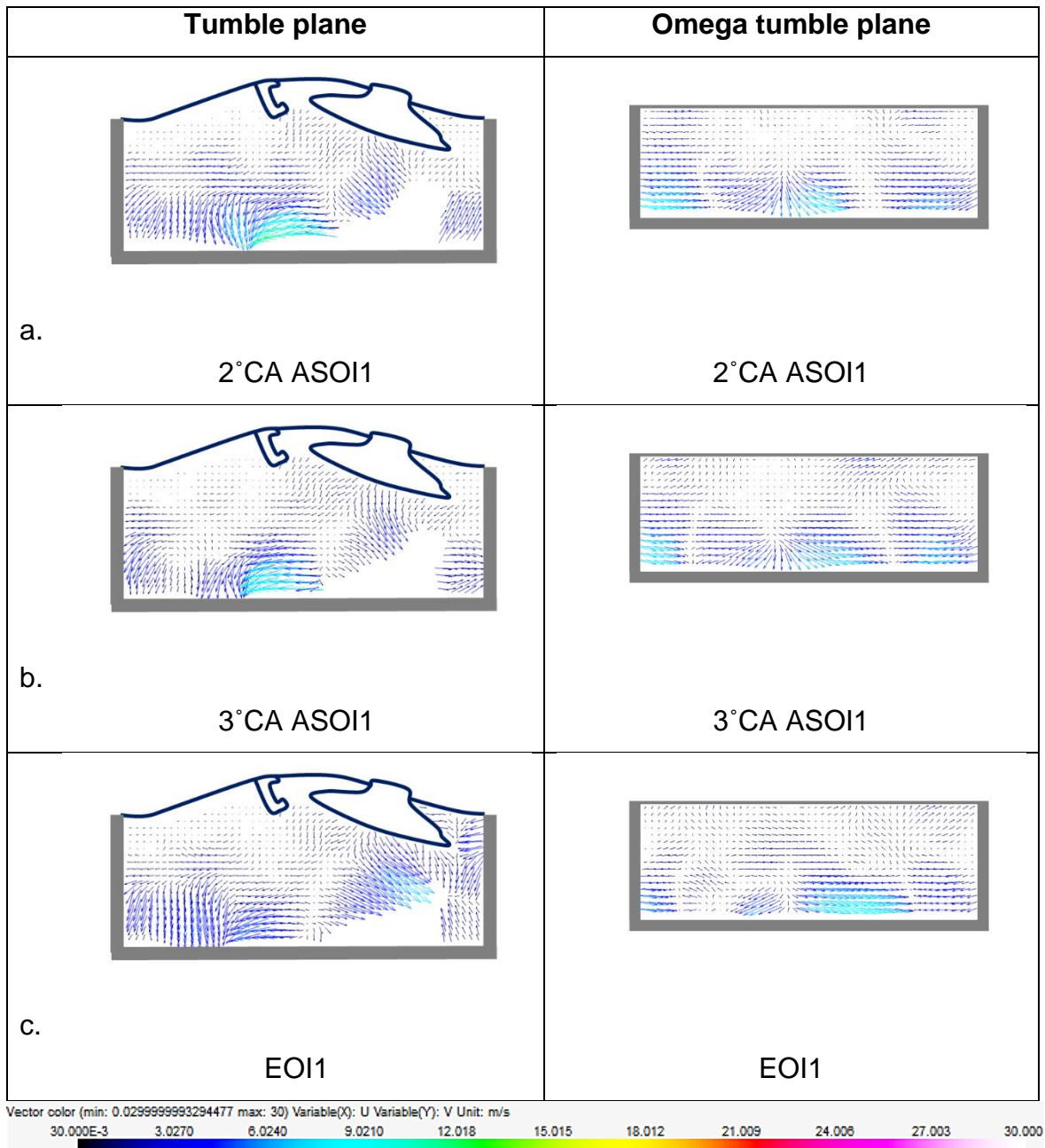
Figure 5.20: ensemble averaged velocity vectors for split ratio of 25%-75% and 35MPa injection pressure representing data over the first injection period.

Figure 5.21 a. - c. show the effects of the first injection on the ensemble averaged velocity vectors in the flow field, prior to the start of the second injection. At this point, it is worth comparing the flow field with the motored case, which would reveal the effects of the short PW on the flow field. Ensemble averaged velocity vectors for the motored case, without injection, are thus provided in Figure 5.22a. - c.

Tumble plane	Omega tumble plane
a. 290˚CA bTDC (7˚CA after end of first injection)	290˚CA bTDC (7˚CA after end of first injection)
b. 260˚CA bTDC	260˚CA bTDC
c. 240˚CA bTDC	240˚CA bTDC

Vector color (min: 0.0299999993294477 max: 30) Variable(X): U Variable(Y): V Unit: m/s

30.000E-3   3.0270   6.0240   9.0210   12.018   15.015   18.012   21.009   24.006   27.003   30.000
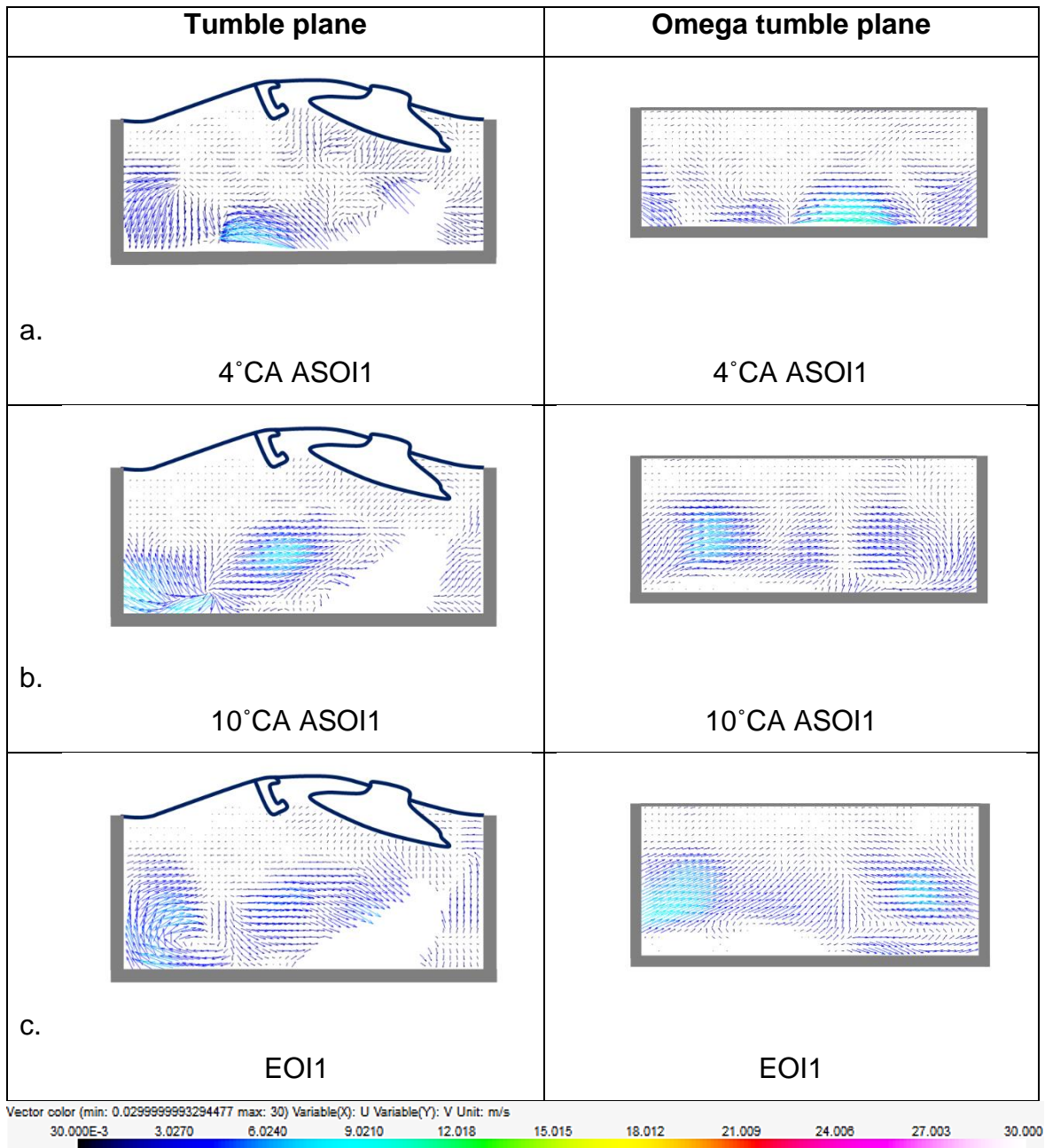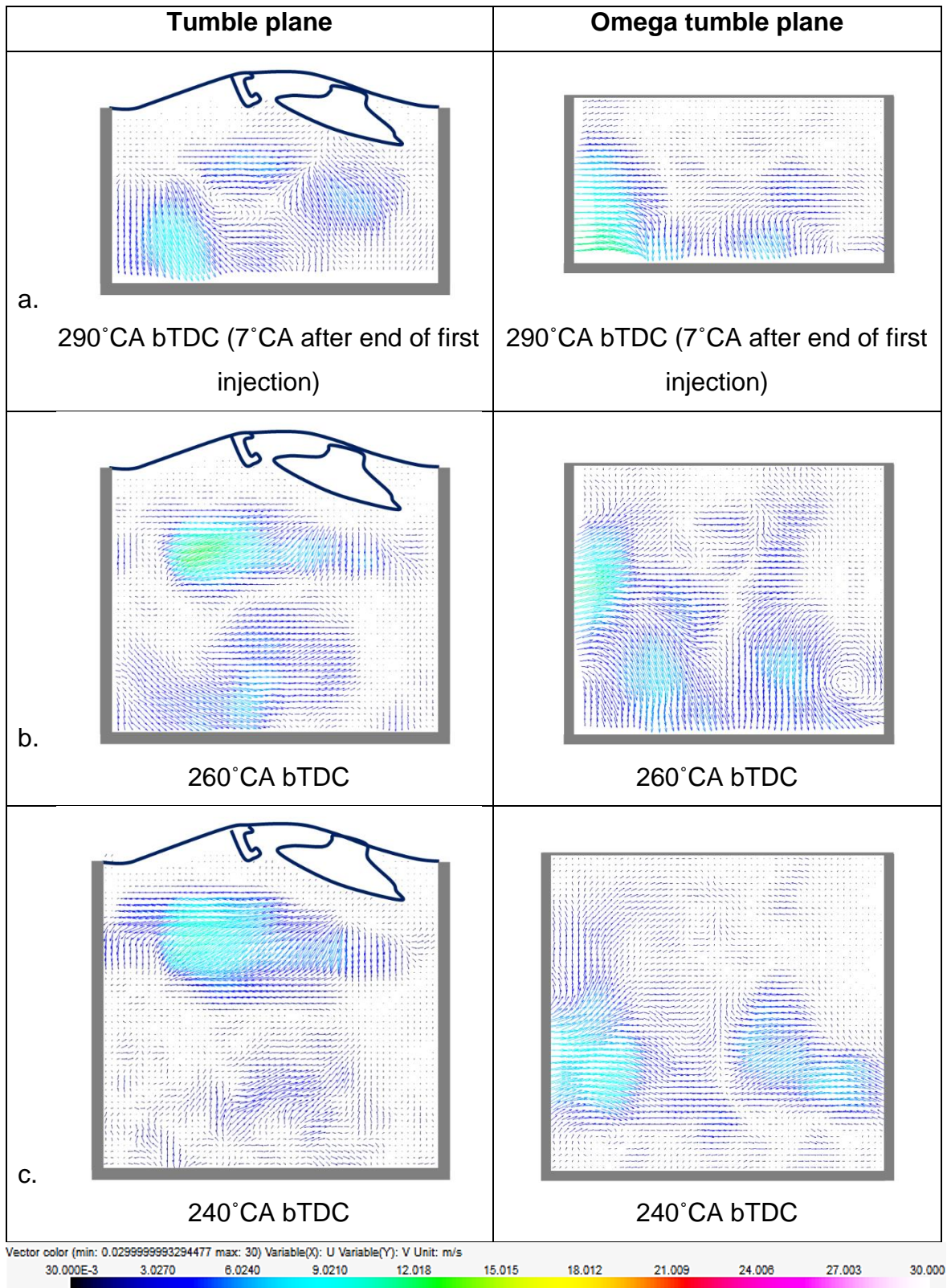
Figure 5.21: ensemble averaged velocity vectors for split ratio of 25%-75% and 35MPa injection pressure representing data after the end of the first injection period.

Tumble plane	Omega tumble plane
a. 290˚CA bTDC	290˚CA bTDC
b. 260˚CA bTDC	260˚CA bTDC
c. 240˚CA bTDC	240˚CA bTDC

Vector color (min: 0.0299999993294477 max: 30) Variable(X): U Variable(Y): V Unit: m/s

| 30.000E-3 | 3.0270 | 6.0240 | 9.0210 | 12.018 | 15.015 | 18.012 | 21.009 | 24.006 | 27.003 | 30.000 |
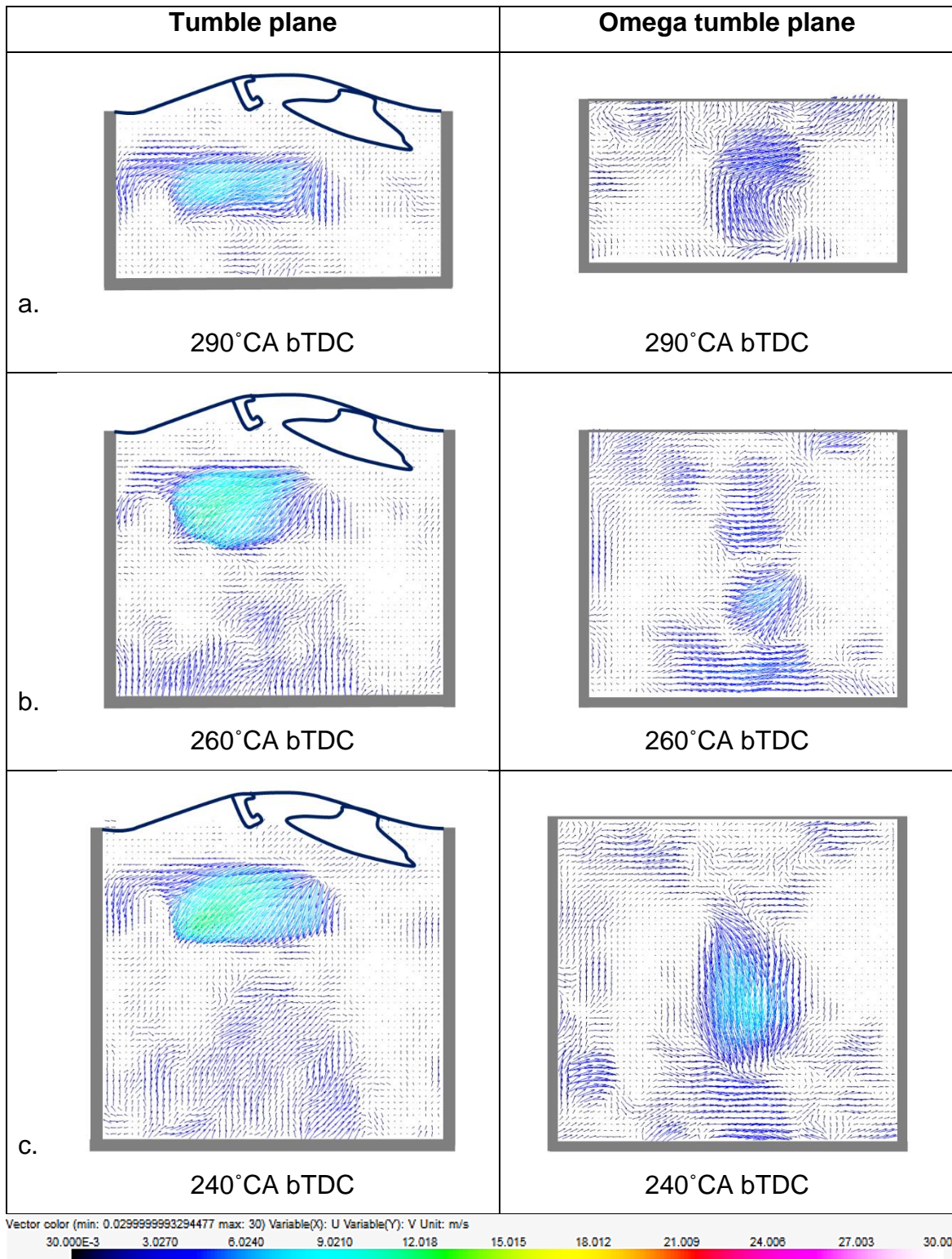
Figure 5.22: ensemble averaged velocity vectors for motored case. The planes of measurements are indicated in the top row, and the engine positions are labelled below each corresponding velocity vector profile.

The high local mean velocity region observed at the centre of the flow-field near the spark plug, observed with the motored case in Figure 5.22a. - c. is the result of the

fresh air charge introduced into the flow field as the intake valves open. The charge possesses high velocity, which upon entering the cylinder, is being directed in the counter clockwise direction of the tumble plane.

When analysing the flow field after the first injection, a similar eddy, with similar velocity magnitude is also present in the flow field, as observed in Figure 5.21b. Below this eddy, there is a weaker eddy formed, which is distinct in Figure 5.21b. This feature at the bottom, which is absent in the data for the motored case, represents the motion of the first injection as the intake stroke develops. It can thus be deduced that the first injection increases the tumble motion slightly, albeit the PW being short. By 240°CA bTDC (Figure 5.21c.), this eddy dissipates as the atomised fuel of small quantity interacts with the surrounding charge in the intake stroke.

Meanwhile, the first injection in the omega tumble plane gives rise to regions with high mean velocity near both edges of the liner, rotating in opposite directions to each other and forming distinct eddies in the plane of the spark plug. These features are absent in the motored cases, which confirms that the source of the high charge velocity is the first injection. By 240°CA bTDC the eddies with high local mean velocities remain in the same position, with the same velocity magnitudes implying negligible effects of the variations in in-cylinder pressure.

The ensemble averaged velocity vectors of the second injection with the larger PW on the surrounding charge and the rest of the cycle are presented in Figure 5.23 and Figure 5.24, respectively. The charge characteristics in this case are similar to those of late single injection at SOI 200°CA bTDC (Figure 5.7). Upon injection, local eddies are formed across the edges of the spray as the high injection momentum of the fuel displaces the surrounding charge. This interaction is particularly dramatic at the head of the spray, where peak velocity vectors are observed in both planes (Figure 5.23a.). This is caused by the propagation of the wide head of the spray, which thereby forces the surrounding charge away from it.

Tumble plane	Omega tumble plane
a. 5˚CA ASOI2	5˚CA ASOI2
b. 10˚CA ASOI2	10˚CA ASOI2
c. EOI2	EOI2

Vector color (min: 0.0299999993294477 max: 30) Variable(X): U Variable(Y): V Unit: m/s

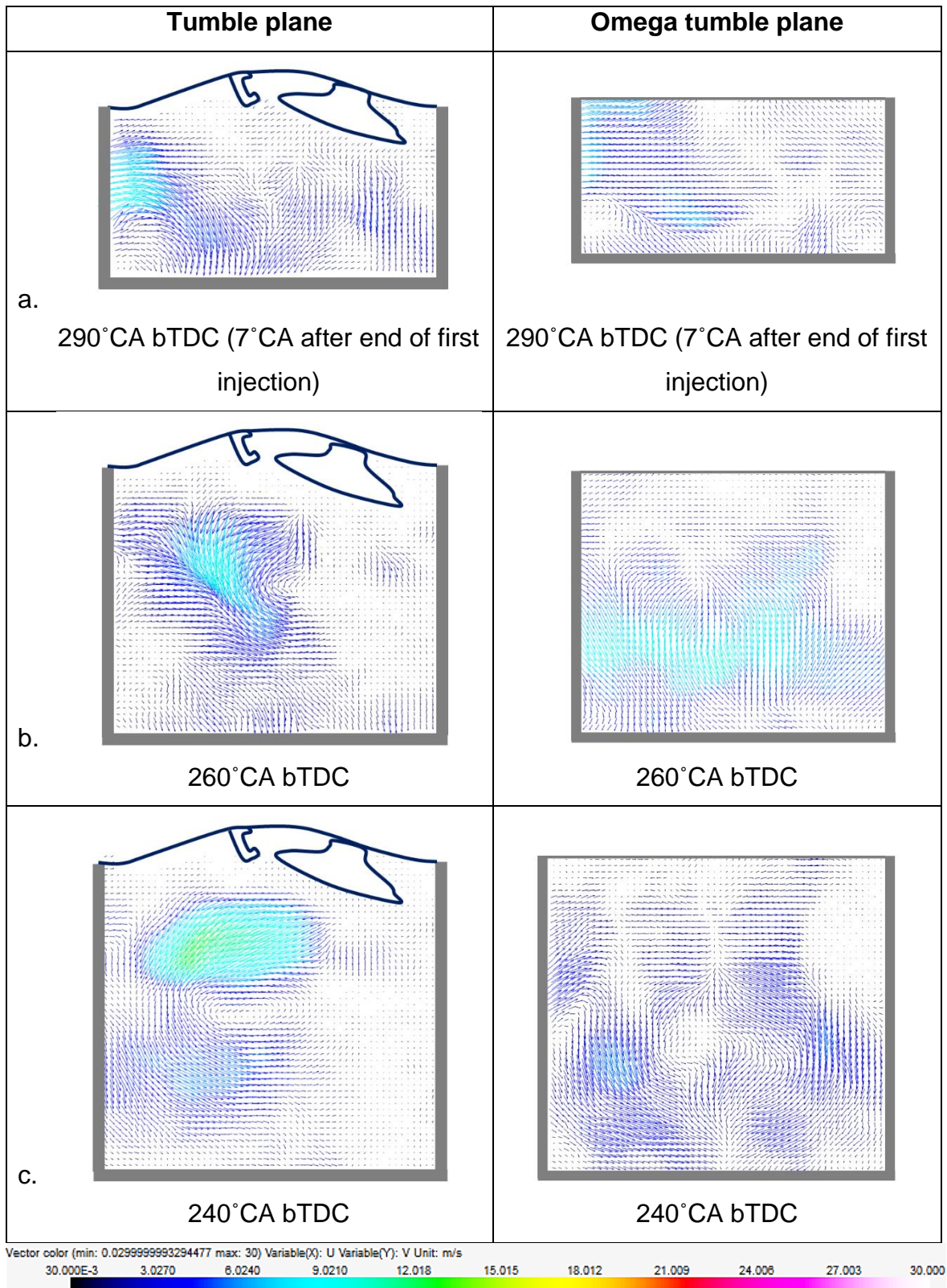30.000E-3   3.0270   6.0240   9.0210   12.018   15.015   18.012   21.009   24.006   27.003   30.000
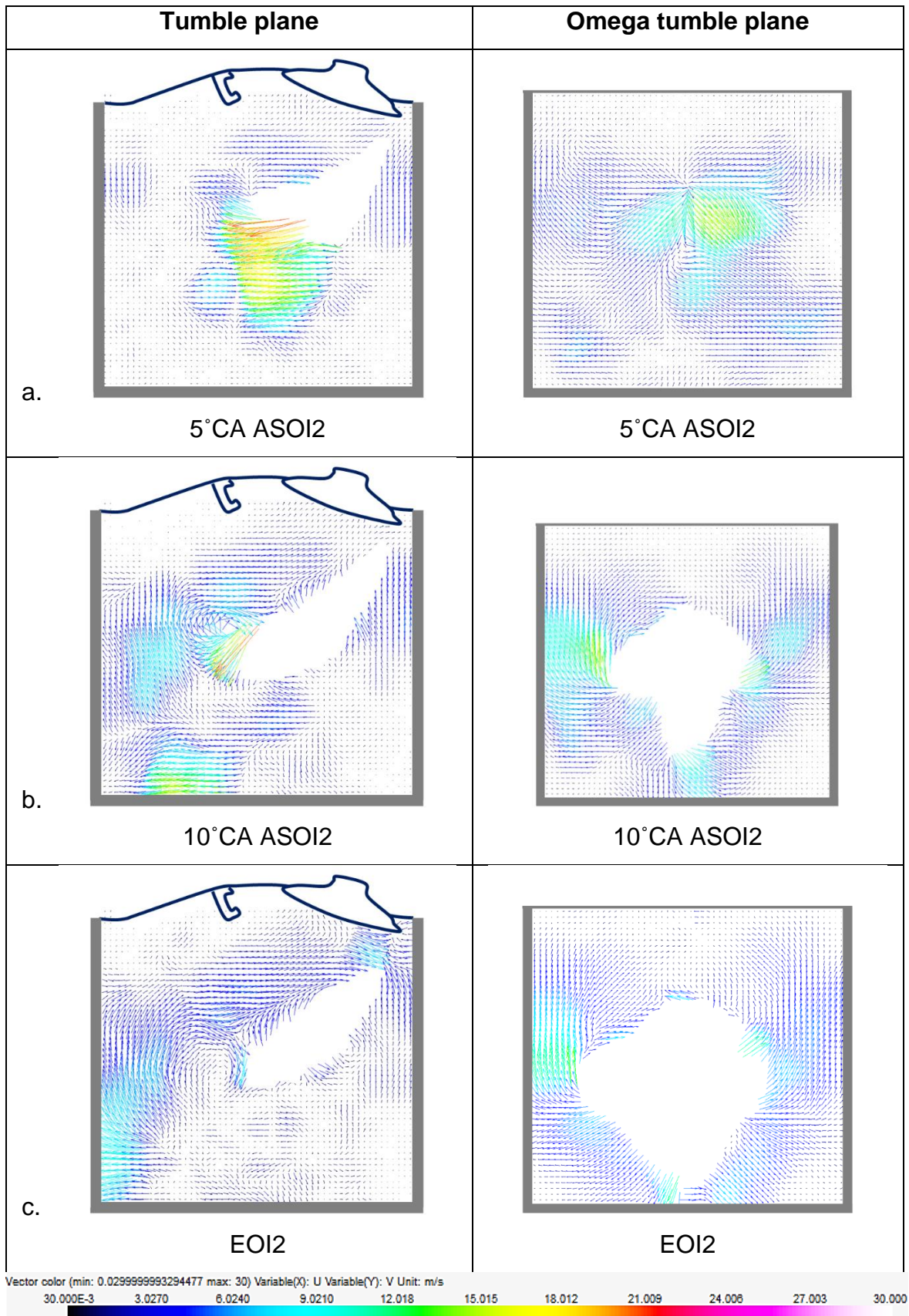
Figure 5.23: ensemble averaged velocity vectors for split ratio of 25%-75% and 35MPa injection pressure representing data over the second injection period.

Tumble plane	Omega tumble plane
a. 170˚CA bTDC	170˚CA bTDC
b. 80˚CA bTDC	80˚CA bTDC
c. 50˚CA bTDC	50˚CA bTDC

Vector color (min: 0.0299999993294477 max: 30) Variable(X): U Variable(Y): V Unit: m/s

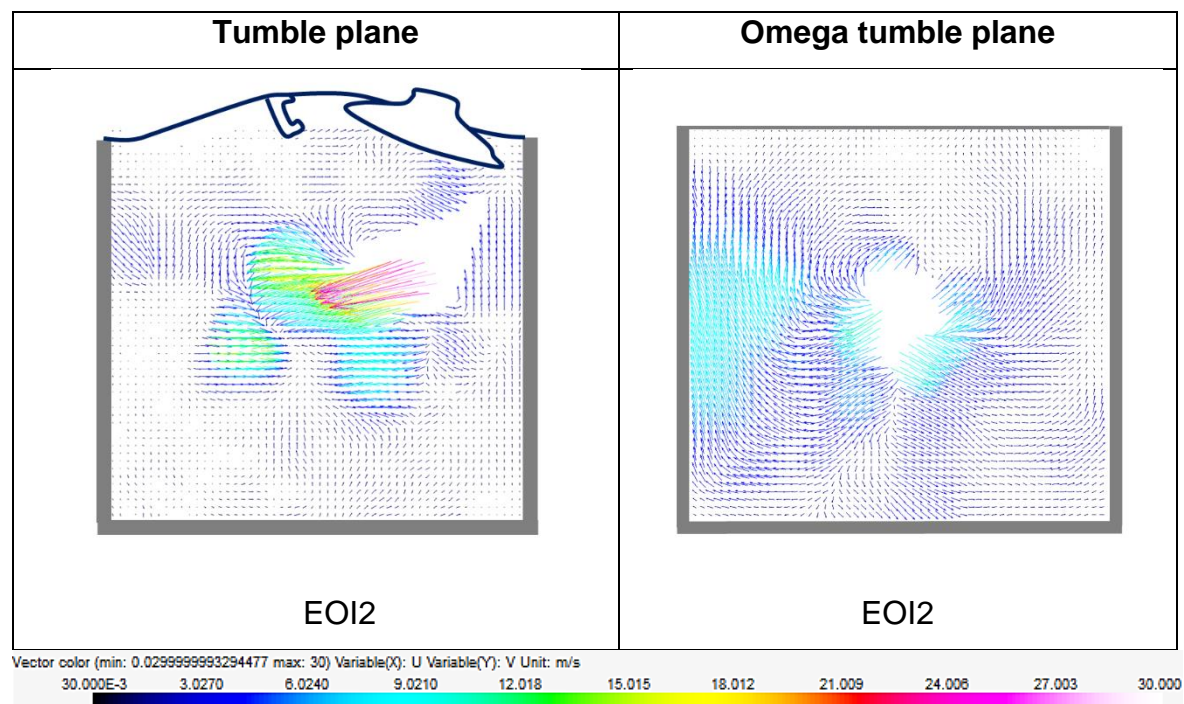| 30.000E-3 | 3.0270 | 6.0240 | 9.0210 | 12.018 | 15.015 | 18.012 | 21.009 | 24.006 | 27.003 | 30.000 |
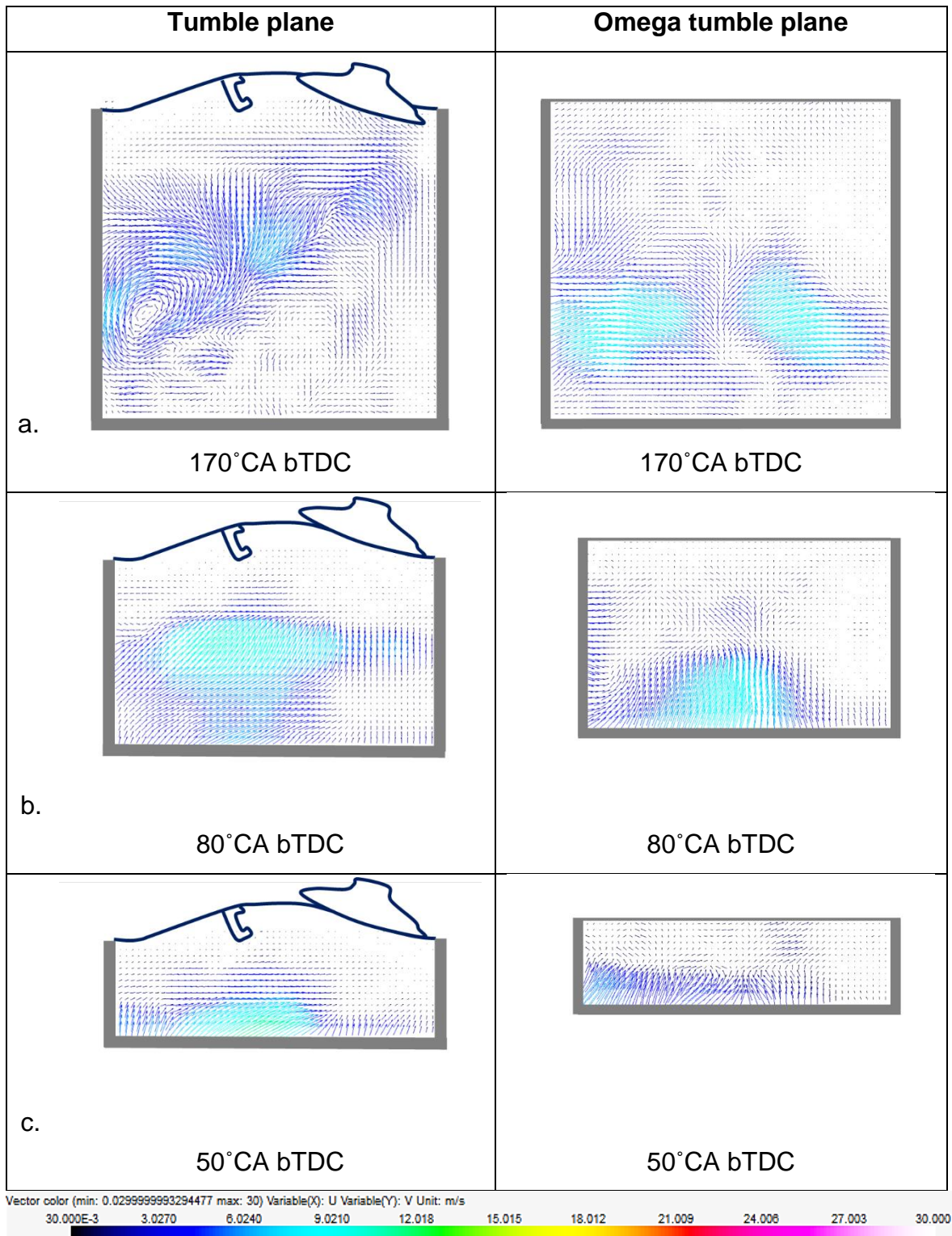
Figure 5.24: ensemble averaged velocity vectors for split ratio of 25%-75% and 35MPa injection pressure representing data after the second injection period.

The charge starts to form a recirculation region, with vortices travelling in the counter clockwise direction at the head of the spray in the tumble plane (Figure 5.23b.). By EOI2 (Figure 5.23c.), the vortices at the head grow and break up the edges of the

main spray structure, judging by the reduced over-saturated area. These vortices resist further propagation of the main spray structure both axially and radially and it appears to have been reduced in width.

In the omega tumble plane meanwhile, the main spray structure simply pushed the surrounding charge away from it as the surface area of the oversaturated region grows progressively in the image plane.

After injection, as the main spray collapses, vortices with high velocity vectors are largely distributed across both planes (Figure 5.24a.), with higher velocity magnitudes observed in the omega tumble plane, compared to the tumble plane. By 80°CA bTDC, the vortices in the tumble plane disappear, replaced by an envelope of high velocity charge. This is also reflected in the corresponding omega tumble plane. This suggests that the larger second injection has had sufficient time to break up but generates strong tumble motion in the compression stroke. The high velocity region persists to near TDC (Figure 5.24c.), generating potentially favourable conditions for the growth of the flame kernel with high equivalence ratio.

5.3.1.4 Effects of Split Ratios on TKE levels near TDC

Local TKE contours near TDC for large and small split ratios in both tumble and omega tumble planes are presented in Figure 5.25a. - b. The overall TKE levels are higher for the small split ratio of 25%-75% in both planes, in spite of the diminished vortices halfway through the compression stroke observed earlier. For the large split ratio on the other hand, the flow field is uniformly laminar towards TDC. This generates unfavourable conditions for the fast flame propagation upon ignition.

The high TKE levels with the small split ratios on the other hand are observed because of the direct injection of the large amount of fuel late in the intake stroke, which results in sufficient time for fuel break up, but with large local TKE levels in the flow field resulting from the on-going momentum transfer from the fuel to the surrounding charge and the on-going entrainment effects between the atomised fuel and charge.

Tumble plane	Omega tumble plane
a.	
Split 75%-25% Engine position: 50˚CA bTDC	Split 75%-25% Engine position: 50˚CA bTDC
b.	
Split 25%-75% Engine position: 50˚CA bTDC	Split 25%-75% Engine position: 50˚CA bTDC
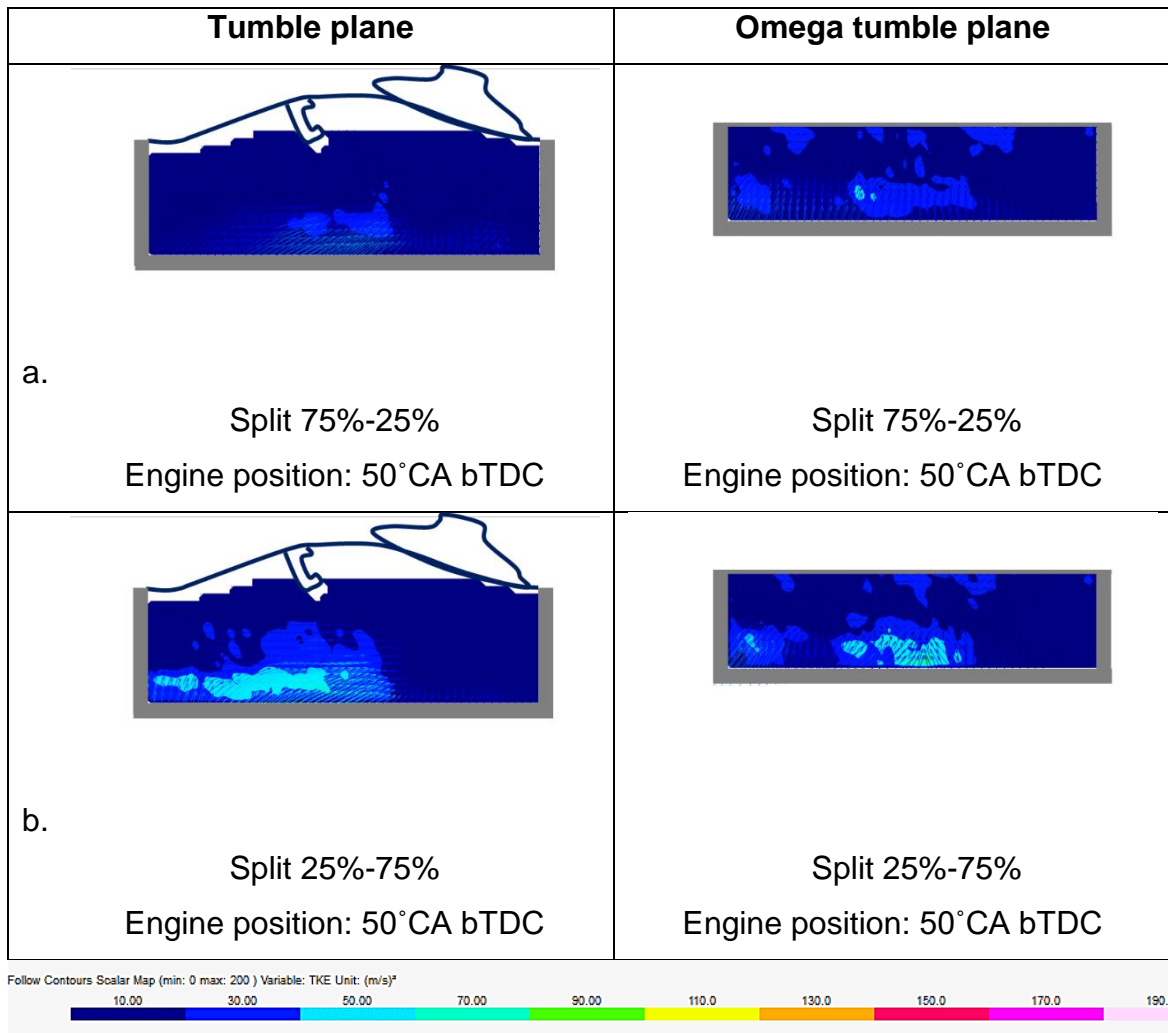
Figure 5.25: averaged TKE contours for split 75%-25% and split 25%-75% representing data near the spark plug at 50˚CA bTDC (nearing TDC).

The large TKE contours near the spark plug would be favourable for flame propagation, but if they were concentrated more centrally in the flow field or distributed across the flow field. This would encourage the development and transportation of the flame kernel across the cylinder. The large TKE contours formed near the exhaust valves suggests potentially favourable conditions for the growth of flame kernel, but also suggests that the transportation of the flame kernel could be affected adversely by the opening of the exhaust valves. The same characteristics were also observed for the single injection case of SOI 200°CA bTDC.

Another notable feature is that the overall TKE levels in the omega tumble plane are generally higher when compared to the tumble plane, for both injection events. This

suggests that as the spray breaks up, there is greater momentum transfer taking place between the spray width and the surrounding charge, when compared to the tumble motion.

5.3.1.5 Cyclic Variations of the Flow Field Close to TDC

The maps of the standard deviation in the velocity measurements close to TDC (50°CA bTDC) for both the tested split ratios are presented in Figure 5.26. The standard deviations are consistently larger in the omega tumble plane when compared to the tumble plane for both split ratios, as was also observed with the single injection cases. This indicates large cyclic variability of the flow field in the omega tumble plane, regardless of the injection strategy. The main reason for the large variations could be the variations in the break-up of the spray width, which would generate a variation of the droplet sizes, thereby affecting the consistency of the entrainment rate and subsequently, the velocity vectors of the flow field.

The smaller split ratio on the other hand indicates low standard deviation in velocities in the tumble plane, close to the spark plug. This indicates that the high velocity vectors observed close to the spark plug are consistent per cycle, which is promising for the combustion stability. Meanwhile, large standard deviations are observed on the piston surface, which could be caused by the large second injection's interactions with the piston's surface. In this case, the spray breakup and subsequent impingement on the piston surface could affect the cyclic variability of the velocity vectors.

Contrary to this, the large split ratio indicates greater cyclic variability overall across the flow field near TDC, although the magnitudes of the uncertainties are small. This is attributed to the spray-piston interaction in the intake stroke.

Tumble plane	Omega tumble plane
a. Split 75%-25% Engine position: 50˚CA bTDC	Split 75%-25% Engine position: 50˚CA bTDC
b. Split 25%-75% Engine position: 50˚CA bTDC	Split 25%-75% Engine position: 50˚CA bTDC
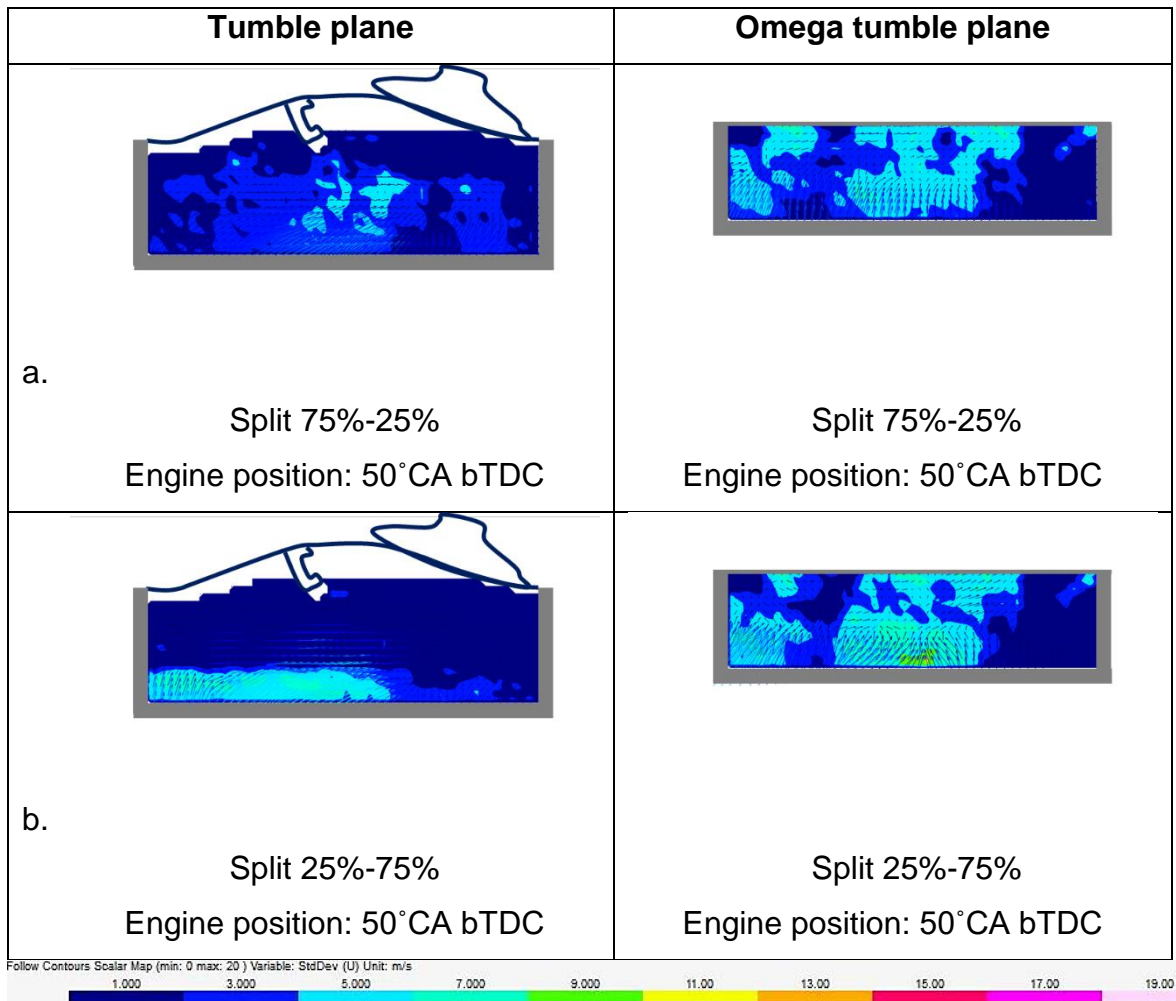
Figure 5.26: maps of standard deviation in velocities for split 75%-25% and split 25%-75% at 50˚CA bTDC (nearing TDC).

5.3.1.6 Summary

The effects of the split ratios of 75%-25% and 25%-75% on the mixture formation were investigated in this section. In this case the first injection times were kept constant and both split injections occurred at various sweeps in the intake stroke.

The large split ratio, with early first injection generated a weak charge motion in the flow field close to the spark plug, due to the injection events having sufficient time to atomise and mix uniformly in the cylinder, generating a globally homogenous mixture. As a result, the flow field in the compression stroke was relatively weak and a laminar flow field was formed closer to TDC with low cyclic variability judging by the low standard deviation in velocities. In addition, due to the high surface impingement from the early first 75% of fuel, it is suspected that this case would form pool fires.

To avoid the weak bulk motion of the flow, close to the spark plug, a split ratio of 2:1, with slightly late injection timings for both injection events, could help in the formation of a global homogeneous charge and a fuel rich charge with high bulk motion close to TDC, simultaneously.

With the smaller split ratio, a highly turbulent flow field was formed closer to TDC in both omega tumble and tumble planes, generating more favourable conditions for the turbulent propagation of the flame, and stable combustion performance. This was because of the greater amount of fuel injected in the second event, sufficiently early. These cases allowed the fuel spray to break up while preserving the high turbulence levels throughout the compression stroke and close to TDC. The second large injection was also observed to intensify the tumble charge motion in the compression stroke, which would accelerate the fuel entrainment and atomisation.

The fuel impingement is thought to have been alleviated slightly with the small split ratio, due to the shorter first PW. Fuel injection timings which would maximise interactions with piston should be avoided generally, as this can most likely generate pool fires and therefore the formation of soot particles of various sizes [142]. In order to avoid this, a later first injection in the intake stroke and a second injection event with shorter PWs, at various sweeps in the compression stroke, are investigated in the subsequent section.

5.3.2 Investigations of Early First Injection and Delayed Second Injections

A large split ratio, with the late second injection, has been shown to generate high levels of TKE which promotes fuel oxidation, induction of a faster flame propagation [47] [63], a consistent increase in IMEP caused by the reductions in surface impingements [68] and higher fuel vapourisation and heat transfer with the induced air, which further resulted in improved volumetric efficiency [68] [69].

Hadadpour et al., [145] and Li et al., [146] reported that employing a large split ratio formed a good mixture formation resulting in better efficiency when compared to single injections, as the piston bowl guided the fuel towards the spark plug. In addition, peak mass of high mixture fraction was greater for the small split ratio when compared to large spit ratio, resulting in too large an equivalence ratio. They reported that a small split ratio was not as effective at reducing the mass of the fuel-rich regions near the spark plug as injection splitting using large split ratios. A study on the large split ratio with different injection times is thus discussed in this section.

The results for the large split ratio in the previous section (Section 5.2) showed relatively low TKE levels close to TDC, which is not ideal for turbulent flame propagation. This was because the second injection occurred too early to retain high TKE levels in the compression stroke and close to TDC. As a result, the effects of the large split ratio, with second injections at various sweeps of the compression stroke are investigated in this section. Table 5.8 provides details of the injection timings. The large split ratio (75%:25%) in this case was kept constant throughout the measurements.

The larger first injection quantity in the intake stroke was intended to provide the injected fuel with sufficient time to atomise and interact with the surrounding charge prior to the start of the second injection, in order to produce a global homogeneous mixture. In addition, as observed in the previous sections, first injection in the intake stroke intensified the overall tumble charge motion as well as the local TKE levels. These characteristics would help accelerate the entrainment effects of both injections, prior to ignition. The intended function of the shorter second injection quantity was to generate a fuel rich charge with high TKE levels close to TDC, for favourable fuel-rich ignitable mixture conditions.

Table 5.8: split injections test parameters and timings of the early 1st and delayed 2nd split injection cases for split ratios of 75%-25% (3:1) and injection pressure of 35MPa.

Injection pressure (MPa)	SOI1 (˚CA bTDC)	PW1 (ms)	1st injection quantity (mg)	SOI2 (˚CA bTDC)	PW2 (ms)	2nd injection quantity (mg)
35	280	1.87	19.7	105	0.63	6.3
35	280	1.87	19.7	85	0.63	6.3
35	280	1.87	19.7	40	0.63	6.3

Additionally, due to the surface impingement observed with SOI 310˚CA bTDC, the first injection is delayed to a later second injection case, where the interaction between the fuel injected and the piston's surface is alleviated, potentially preventing the likelihood of pool fires.

From the injection mass measurements performed in section 4.2, it was confirmed that the injected masses for the single injections and split injections were similar, as long as the dwell times were maintained larger than 2ms. Table 5.9 also provides details of the dwell times corresponding to the tested injection cases, while Figure 5.27 provides a simplified schematic of the injection strategies tested.

Table 5.9: corresponding split ratios and dwell times for the specified injection parameters.

SOI2 (˚CA bTDC)	Split ratio	Dwell time (˚CA)	Dwell time (ms)
105	3:1	192.5	27
85	3:1	212.5	30
40	3:1	257.5	36
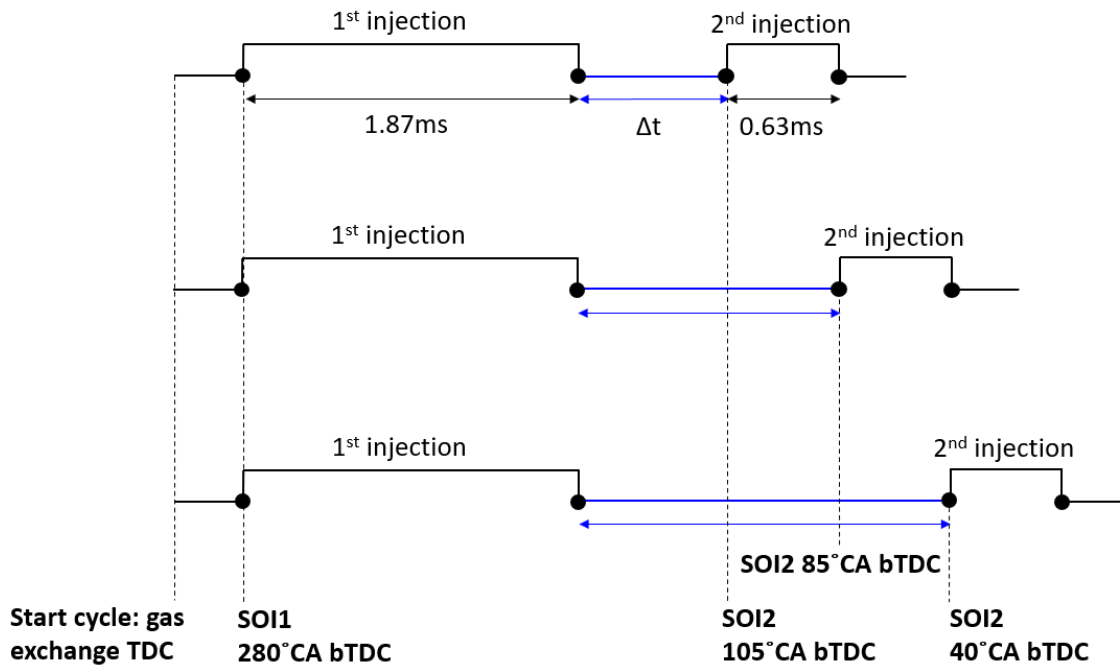
Figure 5.27: schematic representing the differences between the second injection timings for the three tested split injection cases with 75%-25% ratio and constant start of first injection timings with respect to the gas exchange TDC.

5.3.2.1 Effects of Split Injection Timings on the Gas In-cylinder Properties

Table 5.10 provides an overview of the test conditions during the measurements of the three injection strategies.

Table 5.10: recorded test conditions for the three split cases tested with the different start of second injection timings.

SOI2 (˚CA bTDC)	Average MAP (bar)	Inlet temperature (˚C)	Coolant temperature in/out (˚C)	Oil temperature in/out (˚C)	Ambient pressure (˚C)
105	0.75	30.6	50.6 / 50.4	39.9 / 40.1	1.025
85	0.74	30.8	50.8 / 50.6	40.1 / 40.6	1.025
40	0.74	30.9	50.4 / 503	39.8 / 40.3	1.025

Figure 5.28 provides in-cylinder traces for each test conditions, averaged over 300 cycles. Similar average peak pressures are observed for all three tested cases. The second injection test case of SOI2 85˚CA bTDC however, show lowest average peak

pressure in spite of the same load conditions recorded. It can be observed that for this injection case, larger coolant and oil temperatures were recorded, which could affect these traces, even though the difference is minor.
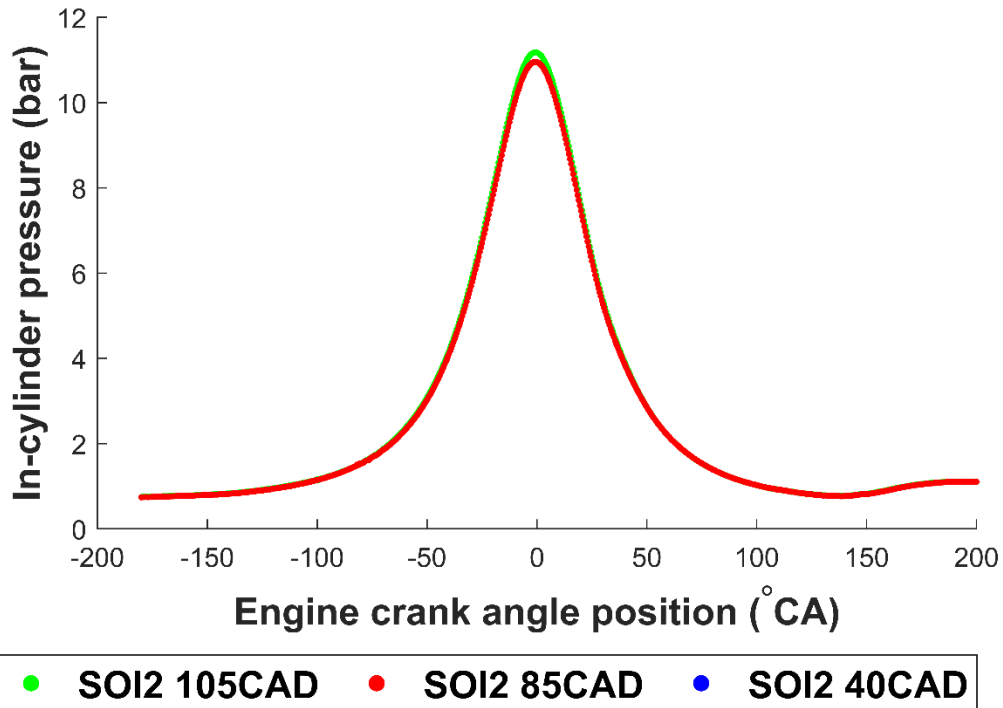
Figure 5.28: averaged in-cylinder pressure traces for the intake and compression strokes for the three tested split cases of varying start of second injection timings: 1) SOI2 105°CA bTDC, 2) SOI2 85°CA bTDC and 3) SOI2 40°CA bTDC. The in-cylinder pressure at each engine crank angle are averaged over 300 recorded cycles.

The effects of the injection strategy on the rate of pressure increase in the compression stroke and the polytropic constants are presented in Figure 5.29 and Table 5.11, respectively. The polytropic constants are almost identical to those of single injections, indicating negligible effect of the injection strategy on the rate of increase in the in-cylinder pressure in the compression stroke.
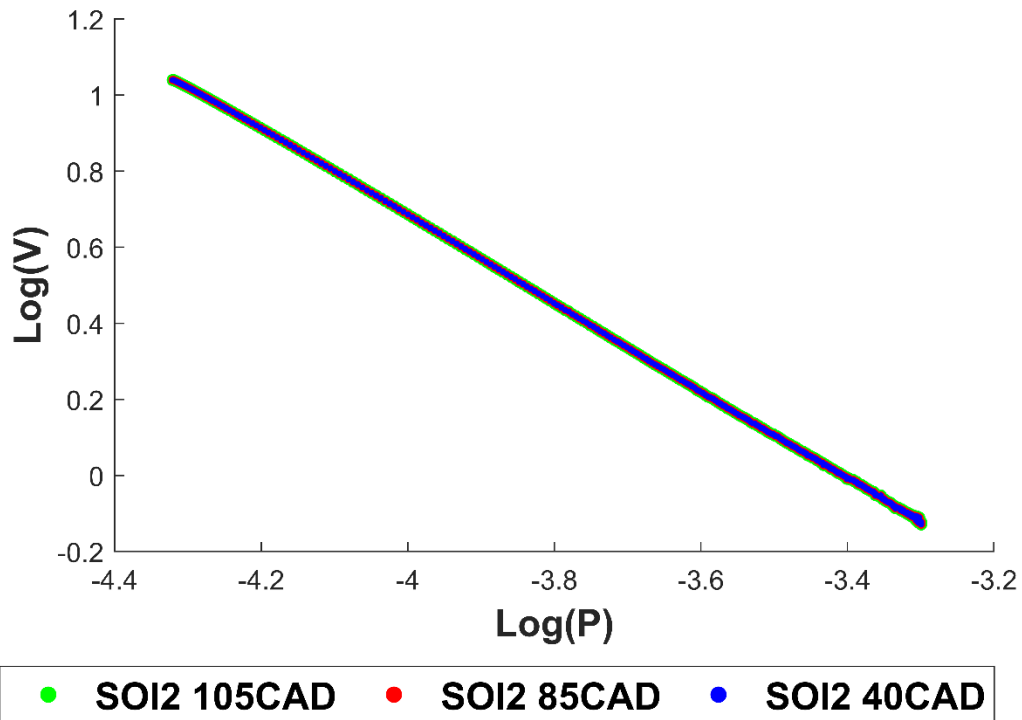
Figure 5.29: relationships between Log(P) and Log(V) recorded during the compression stroke for the three split cases tested with the varying SOI2.

Table 5.11: polytropic constants for the three tested split cases derived from the Lop(P) - Log(V) trends measured in the compression strokes.

SOI2 (˚CA bTDC)	Polytropic constant, n
105	1.15
85	1.15
40	1.15

5.3.2.2 Effects of Early First Injection on the Mixture Formation

Figure 5.30a. - c. provide ensemble averaged velocity vectors during the first injection duration measured both in the tumble plane (presented LHS column) and omega-tumble plane (presented RHS column). The first injection occurs in the intake stroke and when the piston is nearing BDC. As such, there is no immediate impingement of the first injection on the piston's surface.

Tumble plane	Omega tumble plane
a. 5˚CA ASOI1	5˚CA ASOI1
b. 7˚CA ASOI1	7˚CA ASOI1
c. EOI1	EOI1

Vector color (min: 0.0299999993294477 max: 30) Variable(X): U Variable(Y): V Unit: m/s

| 30.000E-3 | 3.0270 | 6.0240 | 9.0210 | 12.018 | 15.015 | 18.012 | 21.009 | 24.006 | 27.003 | 30.000 |

Figure 5.30: ensemble averaged velocity vectors for SOI1 280˚CA bTDC and 35MPa injection pressure representing data over the first injection period.

Observing the ensemble averaged velocity vectors in the tumble plane, large velocity vectors are seen at the head of the spray at 5˚CA ASOI-1 (Figure 5.30a). Upon injection, the large PW of 1.87ms and 35MPa injection pressure, pushes the

surrounding charge away from the spray head. At this time, the spray is just appearing in the omega-tumble plane. This can be determined by the high velocity vectors being pushed away from the centre, caused by the tip of the propagating spray.

With increasing spray duration however, where a larger injection quantity is now present at 7˚CA ASOI1 (Figure 5.30b.), the high velocity magnitude at the head of the spray is again observed to have been dissipated in the tumble flow plane. This occurs as the intake stroke develops and the eddy formed at the head of the spray grows, owing to the momentum transfer from the spray of the large PW injected at 35MPa injection pressure to the charge. As the fuel dense region appears in the image plane of the omega tumble flow plane, the surrounding charge is also observed to be displaced with high velocity magnitudes.

By EOI1 (Figure 5.30c.) the high local mean velocity observed during the spray propagation gets dissipated, as the surrounding charge forms eddies all across the spray structure in both planes. This also gives rise to large local TKE contours by EOI1 which are distributed across a large area in the tumble plane, as presented in Figure 5.31b.

A notable difference in the data between the two measurement planes by EOI1 is that the saturated areas, with the lack of PIV signal, is larger for the omega tumble plane. This occurs due to the differences in the light being scattered in both planes, as discussed earlier.

219

Tumble plane	Omega tumble plane
a. 5°CA ASOI1	5°CA ASOI1
b. EOI1	EOI1

Follow Contours Scalar Map (min: 0 max: 200) Variable: TKE Unit: (m/s)²
10.00   30.00   50.00   70.00   90.00   110.0   130.0   150.0   170.0   190.0
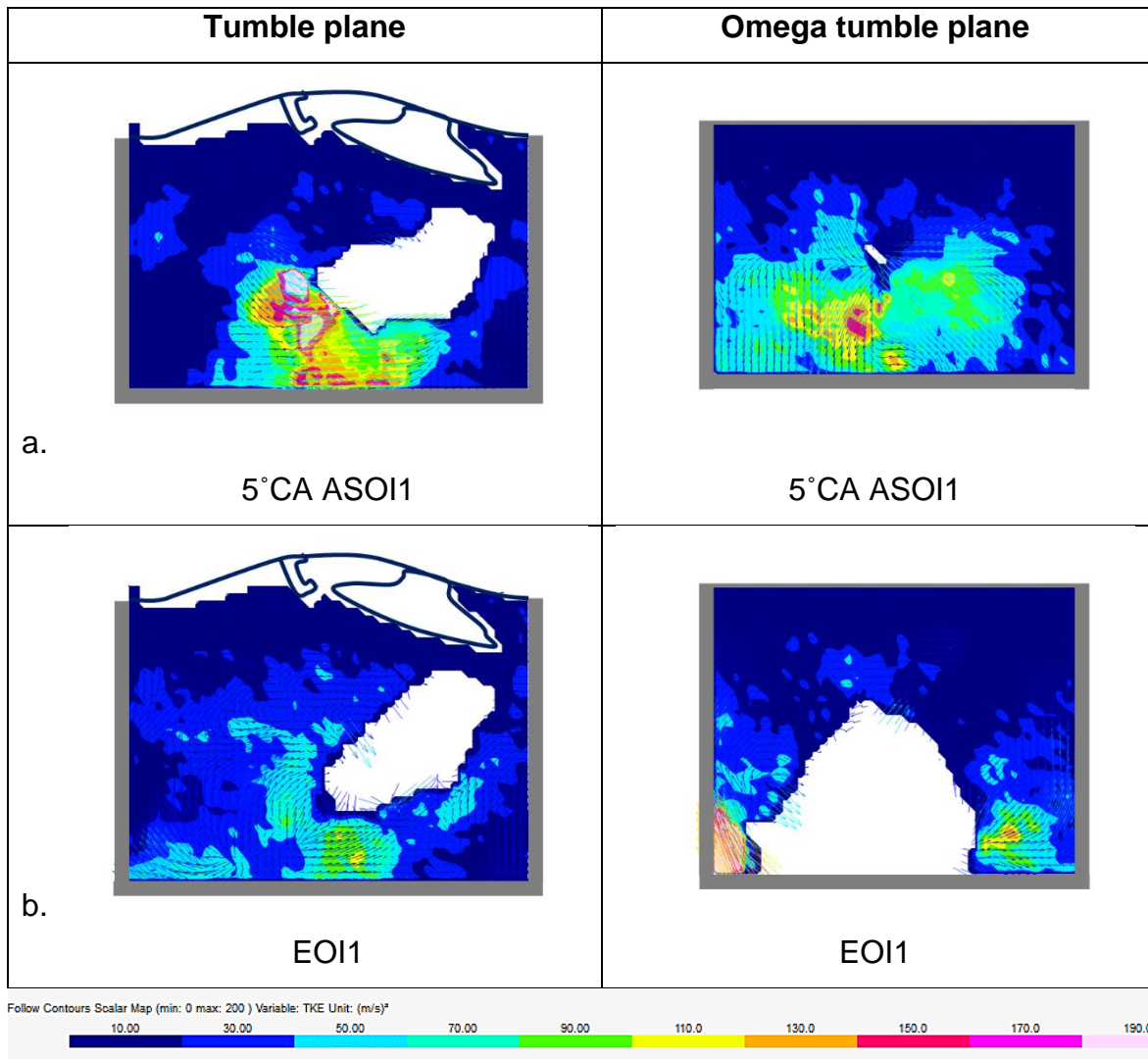
Figure 5.31: averaged TKE contours for SOI1 280°CA bTDC representing data during the first injection period.

Figure 5.32a. - c. provide ensemble averaged velocity vectors of the flow field for the remainder of the intake stroke, after EOI1. The main spray structure of the first injection collapses by at least 7°CA after end of first injection as observed in Figure 5.32a. At this point, the fuel dense spray is now replaced by a fuel-rich eddy with high local velocity magnitudes, at the centre of the flow field. It is suspected that this eddy would also entrain both the atomised fuel and the air induced via the intake valves which are fully open. A similar feature was observed in the motored case (Figure 5.22).

Tumble plane	Omega tumble plane
a. 260˚CA bTDC (7 ˚CA after end of first injection)	260˚CA bTDC (7 ˚CA after end of first injection)
b. 240˚CA bTDC	240˚CA bTDC
c. 210˚CA bTDC	210˚CA bTDC

Vector color (min: 0.0299999993294477 max: 30) Variable(X): U Variable(Y): V Unit: m/s

| 30.000E-3 | 3.0270 | 6.0240 | 9.0210 | 12.018 | 15.015 | 18.012 | 21.009 | 24.006 | 27.003 | 30.000 |

Figure 5.32: ensemble averaged velocity vectors for SOI1 280˚CA bTDC and 35MPa injection pressure representing data after the end of first injection period.

As the intake stroke develops, the strong tumble charge motion persists, moving in the counter clockwise direction with the high local velocity vectors present in the eddy at the top-half and LHS of the cylinder (Figure 5.32b.). The formation of such a distinct vorticial structure is indicative of the entrainment effects and mixture formation taking place between the fuel droplets and the induced air flow.

The corresponding omega-tumble flow plane shows a large area with the high-velocity charge formed across the plane as the fuel interacts with the surrounding charge. These features are counter rotating vortices, with high local velocities, formed across both edges of the liner. This data suggests that the injection timing and quantity provides high tumble charge motion as well as generates a dynamic flow field in the omega tumble flow plane. These phenomena would cause the fuel entrainment to accelerate, forming a well distributed homogeneous charge in the flow field.

As the tumble charge motion in the counter clock-wise direction intensifies, there are obvious eddies being formed, which travel downwards by 210°CA bTDC (Figure 5.32c.). The motion of the eddy is most likely caused by the descending piston which generates variations in the in-cylinder pressure traces. The corresponding velocity vectors in the omega-tumble plane are much lower, even though distinct eddies are still present.

Figure 5.33a. - c. provide ensemble averaged velocity vectors of the flow field for the start of the compression stroke, prior to early second injection test case of SOI2 105°CA bTDC. The tumble charge motion can be seen to persist all the way to 120°CA bTDC, albeit with the lower magnitudes of the velocity vectors. The vortices in the omega tumble plane were distinctive from the start of the compression stroke but had collapsed by 120°CA bTDC prior to the start of the second injection.

In spite of the presence of the weak vortices, the TKE maps presented in Figure 5.34a. - b. show relatively low turbulence levels in the flow field prior to the start of the second injection, with the magnitude ranging between $10m^2/s^2$ and $50 \ m^2/s^2$. This indicates the likelihood of the formation of a well entrained homogeneous flow field prior to a second post injection.

Tumble plane	Omega tumble plane
a. 190˚CA bTDC	190˚CA bTDC
b. 180˚CA bTDC	180˚CA bTDC
c. 120˚CA bTDC	120˚CA bTDC

Vector color (min: 0.0299999993294477 max: 30) Variable(X): U Variable(Y): V Unit: m/s

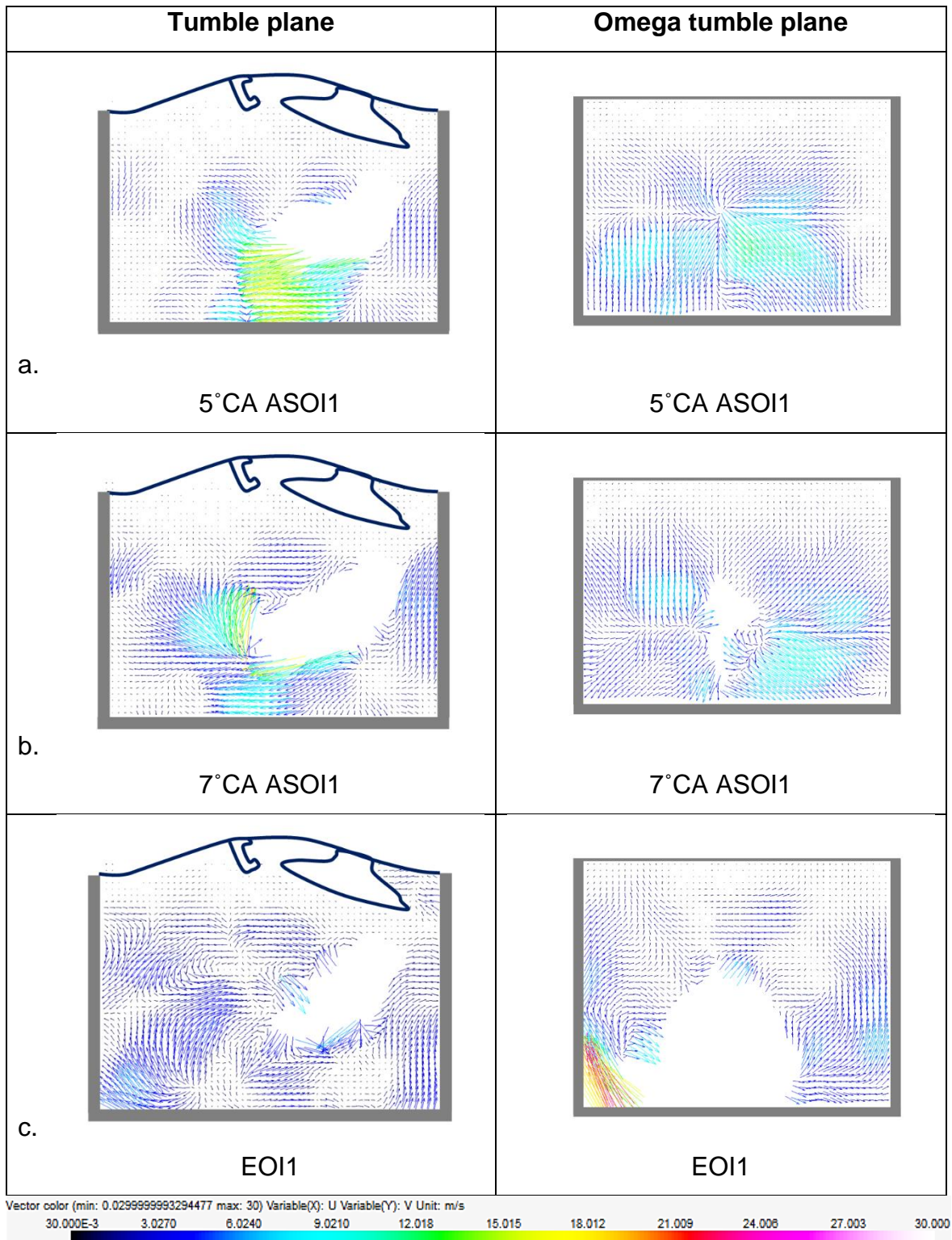| 30.000E-3 | 3.0270 | 6.0240 | 9.0210 | 12.018 | 15.015 | 18.012 | 21.009 | 24.006 | 27.003 | 30.000 |

Figure 5.33: ensemble averaged velocity vectors for SOI1 280˚CA bTDC and 35MPa injection pressure representing data of the compression stroke prior to the second injection.

Tumble plane	Omega tumble plane
a. 180˚CA bTDC	180˚CA bTDC
b. 120˚CA bTDC	120˚CA bTDC

Follow Contours Scalar Map (min: 0 max: 200) Variable: TKE Unit: (m/s)²

| 10.00 | 30.00 | 50.00 | 70.00 | 90.00 | 110.0 | 130.0 | 150.0 | 170.0 | 190.0 |
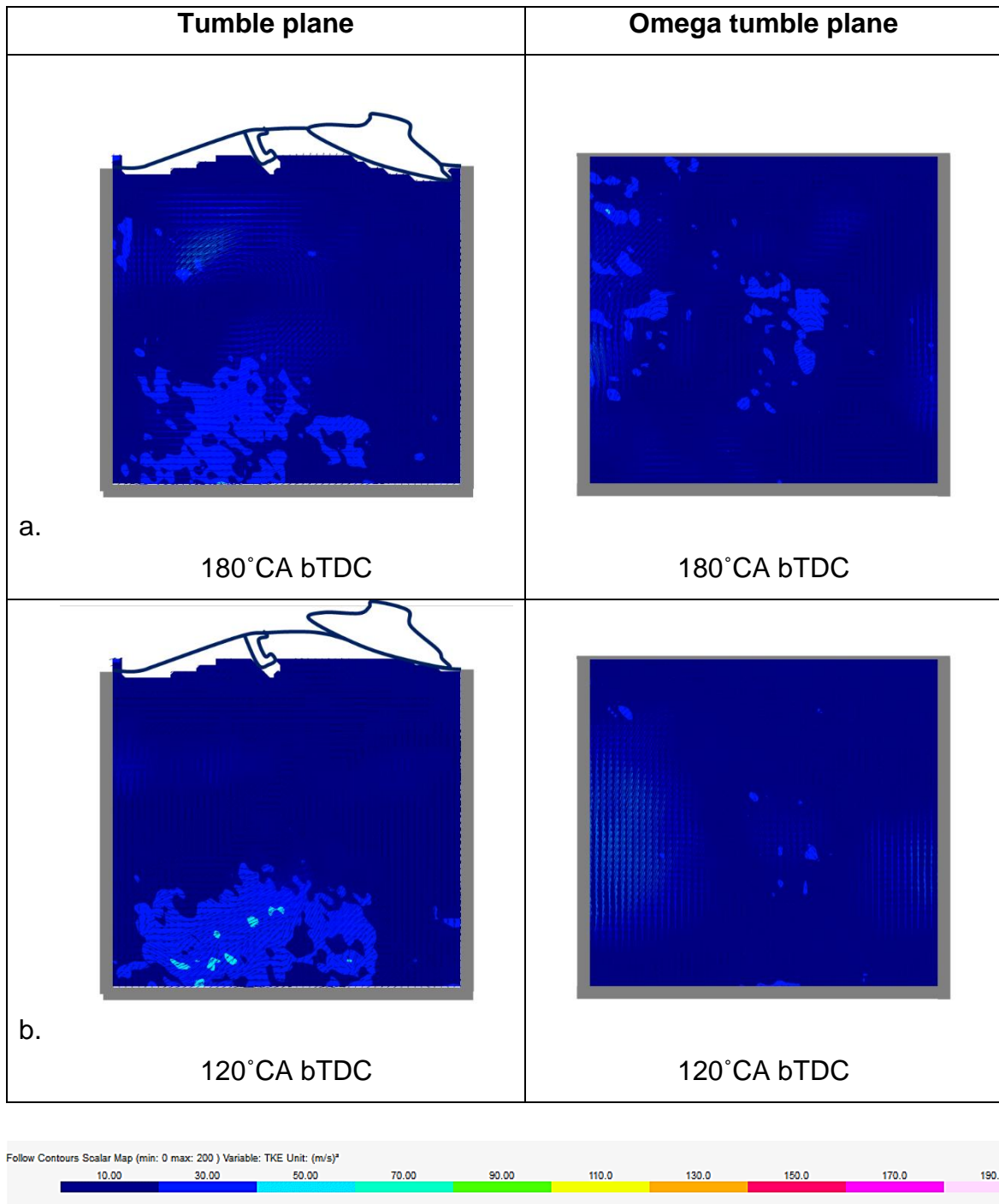
Figure 5.34: averaged TKE contours for SOI1 280˚CA bTDC representing data of the compression stroke positions prior to the second injection.

5.3.2.2.1 Effects Early Second Injection of SOI 105°CA BTDC on the Mixture
Formation

Figure 5.35a. - c. show the effects of ensemble averaged velocity vectors of the second injection duration in the tumble plane, for SOI2 105°CA bTDC. Observing the data for 3°CA after start of second injection (ASOI2), the charge after the end of the first injection possesses relatively low velocity magnitudes with weak eddies across the flow field, particularly in the tumble plane. This could be due to the low pressure difference between the increasing in-cylinder pressure and the high injection pressure.

In addition, although high local mean velocity region is present at the spray's head, the short PW means that there is a lack of sufficient momentum transfer between the injected fuel and the surrounding charge, judging by the lack of formation of eddies at the spray's head this time. The injected fuel dense spray is in the process of displacing the surrounding charge from across the spray region throughout the injection period.

It is also worth noting from the velocity vectors in the tumble plane that the main spray developed by the end of the second injection is far from both the piston's surface and the liner. In this case any potential risks of surface impingement from the second injection in the compression stroke would be inhibited.

The data in the omega tumble flow plane indicate that the head of the spray does not reach the plane of the spark plug by EOI2. The high mean velocity region observed in the centre of this plane is caused by the charge being pushed away from the spray towards the image plane. Although the main spray does not reach the image plane by EOI2, the velocity magnitudes in the flow field has increased by this point.
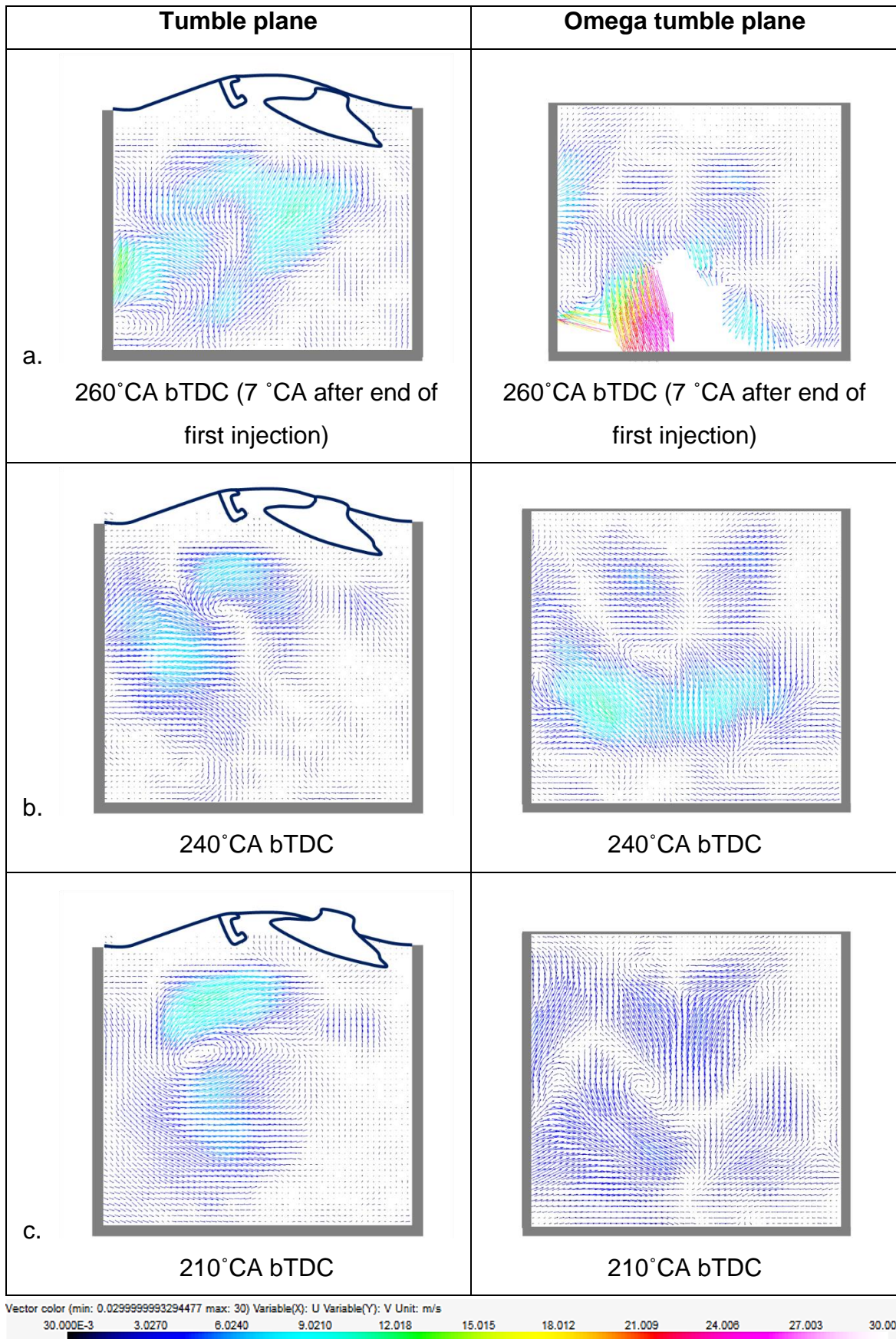
Figure 5.35: ensemble averaged velocity vectors for SOI2 105°CA bTDC and 35MPa injection pressure representing data over the second injection period.

Figure 5.36a. - c. provide ensemble averaged velocity vectors after the end of the second injection for the remainder of the cycle. Observing the tumble plane at 100˚CA bTDC (Figure 5.36a.), the magnitudes of the velocity vectors at the edges of the fuel dense spray have now increased. This is due to the injected fuel from tail of the spray, at high injection pressure, now propagating towards the stagnated head of the spray. This interaction causes large momentum transfer between the injected fuel and the surrounding charge.

Hadadpour et al., [145] had also observed an influx of ambient air vectors propagating towards the fuel rich region after the end of first injection. This high entrainment from the tail of the first injection happens twice when employing the split injection strategy, which has been stated to reduce the mass of high mixture reaction zone. This entrainment effect is reported to be one of the underlying physics in the mixing improvement in the split injection cases.

Halfway through the compression stroke (Figure 5.37b.), the fuel collapses, which is replaced by a flow field with diminished velocity magnitudes albeit with distinct eddies formed and large local TKE contours with the magnitudes of 50 m^2/s^2 (Figure 5.36b.) at the centre of the flow field. It is interesting to note here that the overall velocity magnitude and TKE contours in the flow field in the omega tumble plane is higher than that in the tumble plane.

Near TDC however, the flow weakens considerably, with collapsed vortices in both planes and low TKE levels near the spark plug (Figure 5.36c. and Figure 5.37c.).

Tumble plane	Omega tumble plane
a.	
100˚CA bTDC (3 ˚CA after the end of second injection)	100˚CA bTDC (3 ˚CA after the end of second injection)
b.	
90˚CA bTDC	90˚CA bTDC
c.	
50˚CA bTDC	50˚CA bTDC

Vector color (min: 0.0299999993294477 max: 30) Variable(X): U Variable(Y): V Unit: m/s

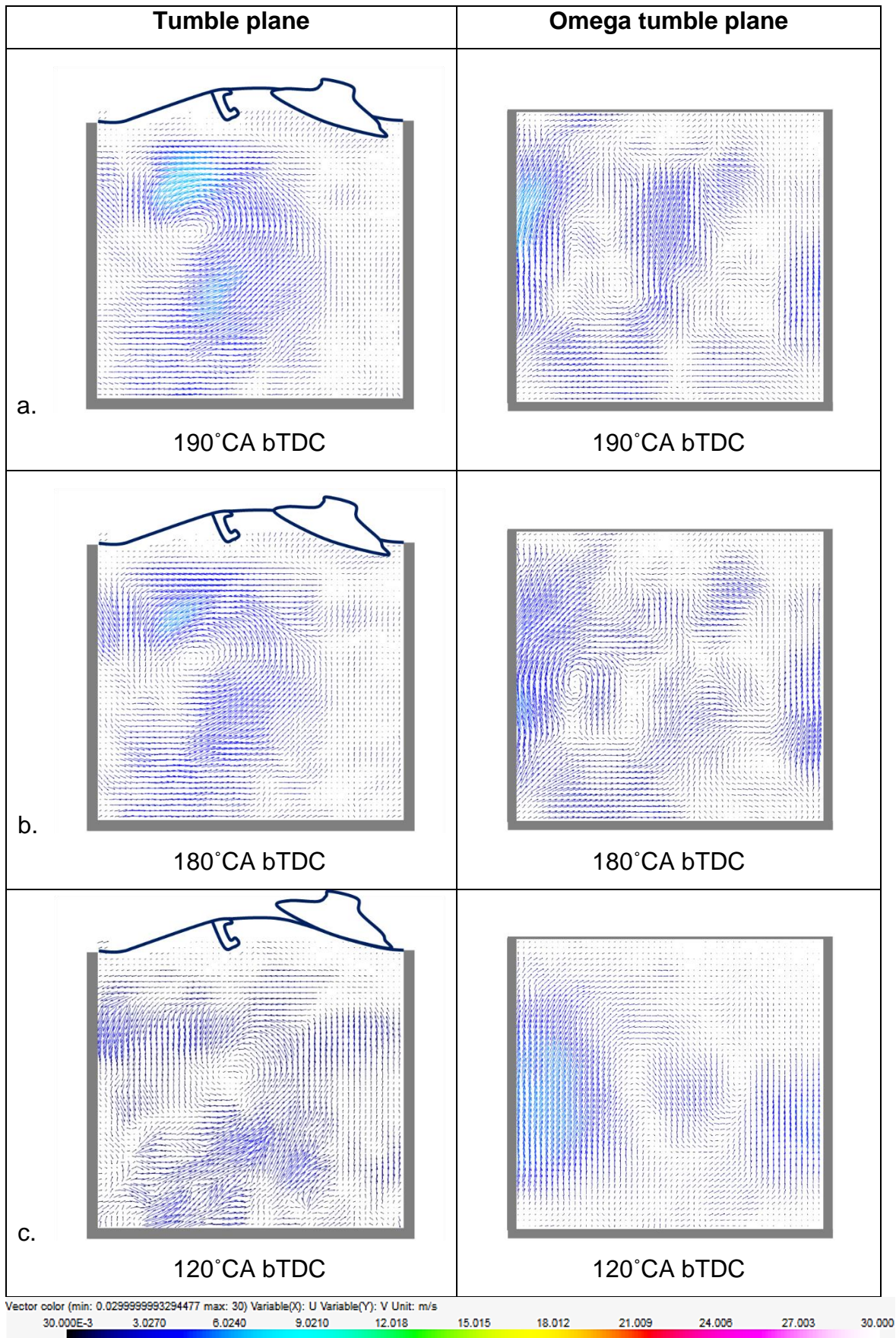| 30.000E-3 | 3.0270 | 6.0240 | 9.0210 | 12.018 | 15.015 | 18.012 | 21.009 | 24.006 | 27.003 | 30.000 |

Figure 5.36: ensemble averaged velocity vectors for SOI2 105˚CA bTDC and 35MPa injection pressure representing data after end of second injection period and the remainder of the compression stroke.

Tumble plane	Omega tumble plane
a. 90°CA bTDC	90°CA bTDC
b. 50°CA bTDC	50°CA bTDC

Follow Contours Scalar Map (min: 0 max: 200) Variable: TKE Unit: (m/s)²

10.00   30.00   50.00   70.00   90.00   110.0   130.0   150.0   170.0   190.0

Figure 5.37: averaged TKE contours for SOI2 105°CA bTDC representing data of the compression stroke positions after the end of second injection.

5.3.2.2.2 Effects Early Second Injection of SOI 85°CA BTDC on the Mixture Formation

The effects of a later second injection in the compression stroke, at SOI2 85°CA bTDC, are presented and discussed in this section. Figure 5.38a. - c. show the effects of ensemble averaged velocity vectors of the second injection duration in the tumble plane and omega tumble plane.

Tumble plane	Omega tumble plane
 a. 3˚CA ASOI2	 3˚CA ASOI2
 b. 4˚CA ASOI2	 4˚CA ASOI2
 c. EOI2	 EOI2

Vector color (min: 0.0299999993294477 max: 30) Variable(X): U Variable(Y): V Unit: m/s
30.000E-3 3.0270 6.0240 9.0210 12.018 15.015 18.012 21.009 24.006 27.003 30.000

Figure 5.38: ensemble averaged velocity vectors for SOI2 85˚CA bTDC and 35MPa injection pressure representing data over the second injection period.

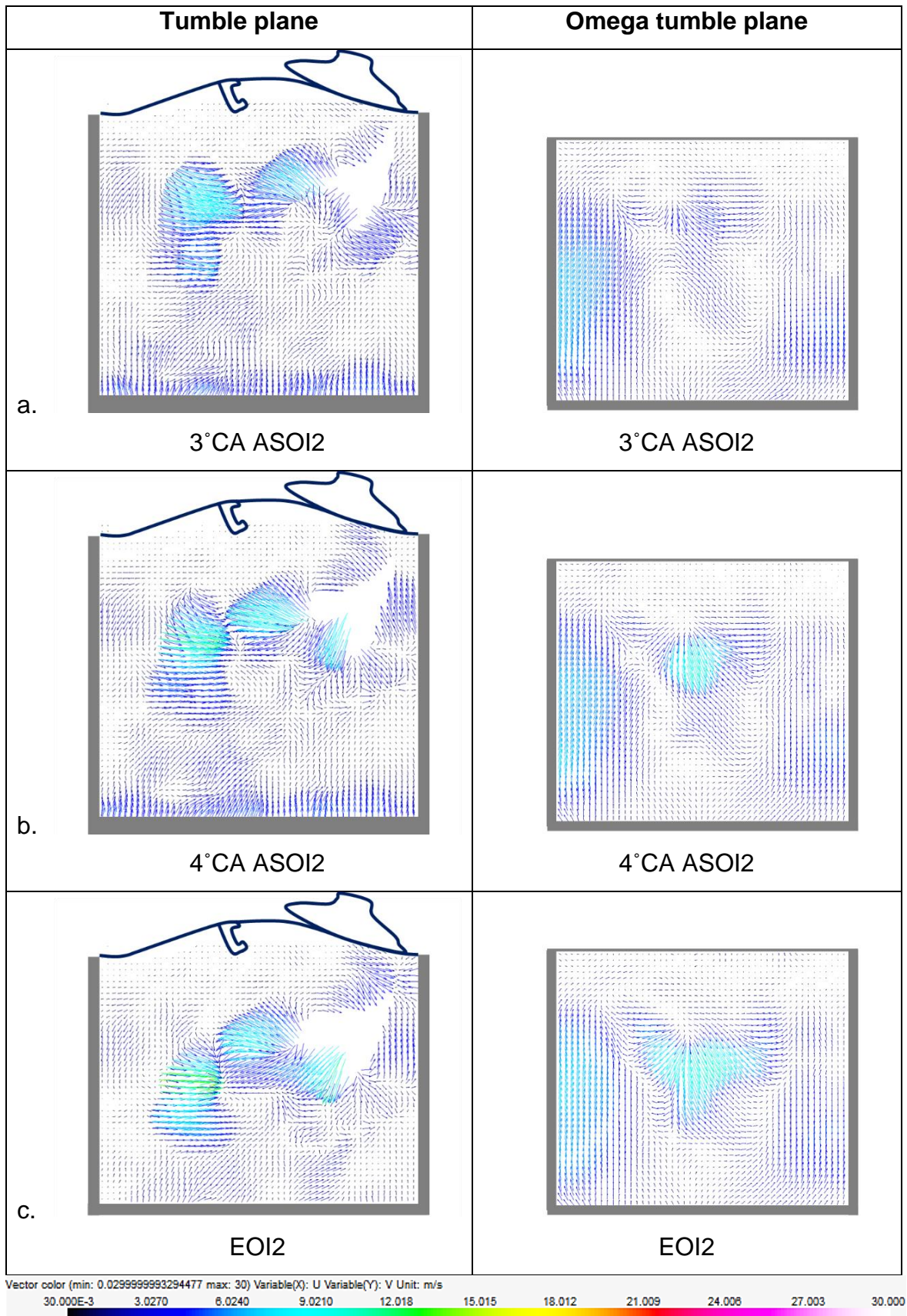The ensemble averaged velocity vectors in this case are comparable to the earlier second injection of SOI2 105˚CA BTDC. One difference however is that the main spray structure is slightly shorter in penetration length by EOI2, when compared to the earlier start of second

injection. The reason for this is that the higher in-cylinder pressure traces in the compression stroke generated resistance against the spray propagation. As a result, upon visual comparisons of both the spray structures, also presented in Figure 5.39, the penetration length of the second spray is observed to be slightly shorter when compared to the earlier second injection. In the case, the fuel rich regions most likely lie around the piston's surface, which could increase the heat transfer to the piston's surface, thereby decreasing the temperature of the mixture directed close to the spark plug, as was also reported in [144].
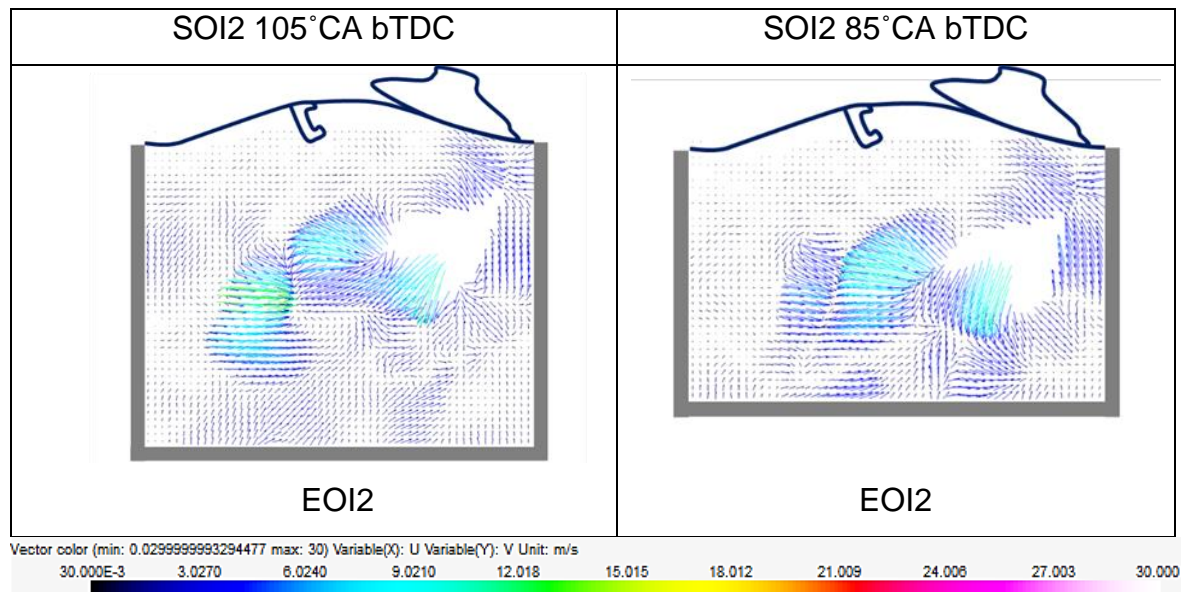
Figure 5.39: ensemble averaged velocity vectors showing the end of the second injection in the tumble plane for SOI2 105°CA bTDC and SOI2 85°CA bTDC.

Figure 5.40 a. - c. represent the ensemble averaged velocity vectors of the flow field after the end of the second injection. Again, as the spray is about to collapse, the overall velocity magnitude in both planes increase. This increase is soon dissipated, albeit with the presence of the large eddies formed on the surface of the piston as the piston reaches near TDC.

The omega-tumble plane again shows a higher mean velocity in the flow field near the spark plug. This suggests that upon ignition, high turbulence levels (as observed in Figure 5.41b.) would be present in the omega tumble flow plane to enable fast flame propagation, whose motion could be aided by the distinct eddies in the tumble plane.
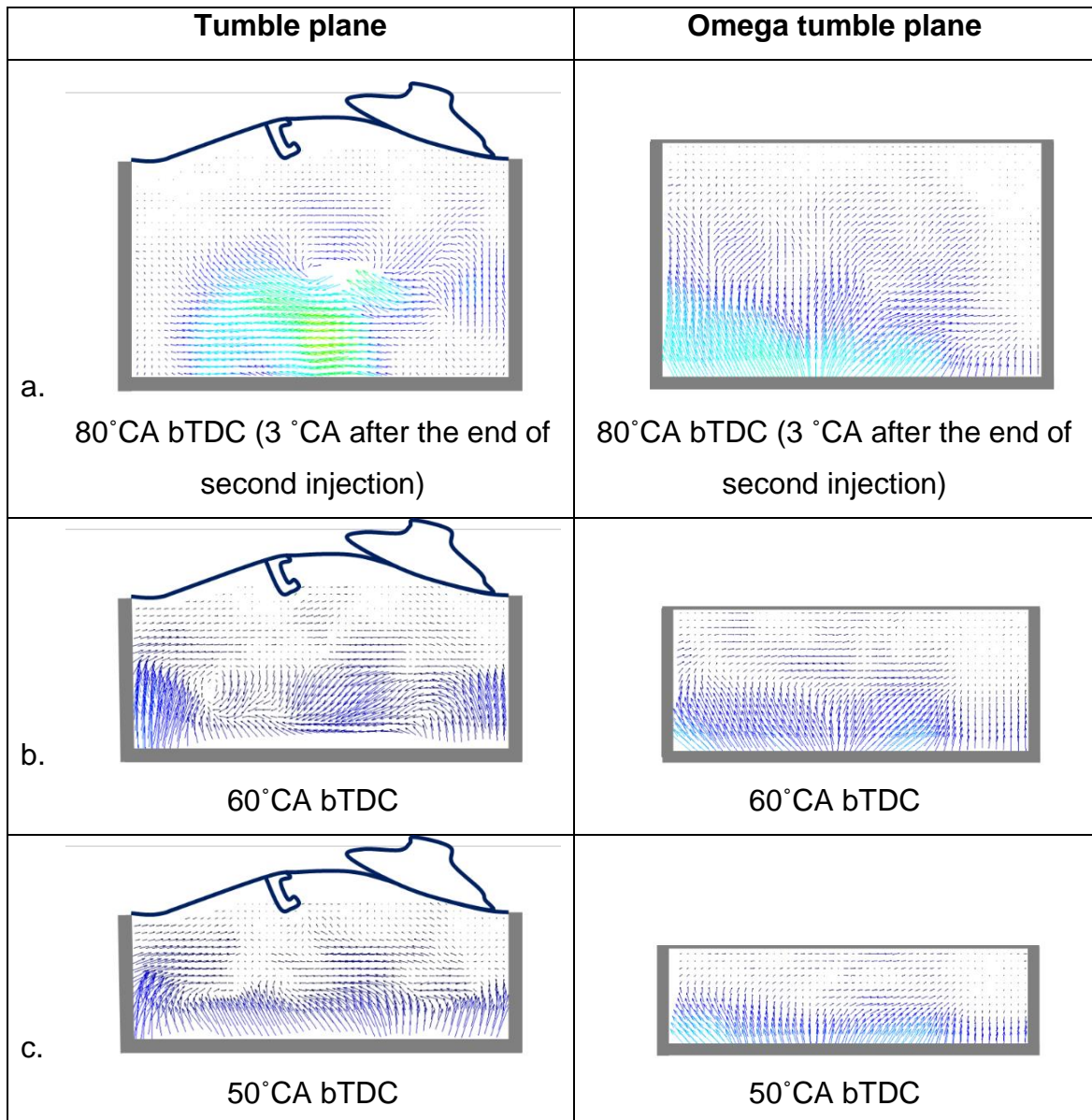
Tumble plane	Omega tumble plane
a. 80˚CA bTDC (3 ˚CA after the end of second injection)	 80˚CA bTDC (3 ˚CA after the end of second injection)
b. 60˚CA bTDC	 60˚CA bTDC
c. 50˚CA bTDC	 50˚CA bTDC

Vector color (min: 0.0299999993294477 max: 30) Variable(X): U Variable(Y): V Unit: m/s

| 30.000E-3 | 3.0270 | 6.0240 | 9.0210 | 12.018 | 15.015 | 18.012 | 21.009 | 24.006 | 27.003 | 30.000 |

Figure 5.40: ensemble averaged velocity vectors for SOI2 85˚CA bTDC and 35MPa injection pressure representing data after the end of second injection.

Overall, close to TDC, more distinct vortices are present in both planes as a result of the later second injection. The flow field at this position however still suffers from low TKE levels in the tumble plane, with magnitudes of around 10m^2/s^2.

Tumble plane	Omega tumble plane
a. 70˚CA bTDC	70˚CA bTDC
b. 50˚CA bTDC	50˚CA bTDC

Follow Contours Scalar Map (min: 0 max: 200) Variable: TKE Unit: (m/s)²
10.00 30.00 50.00 70.00 90.00 110.0 130.0 150.0 170.0 190.0
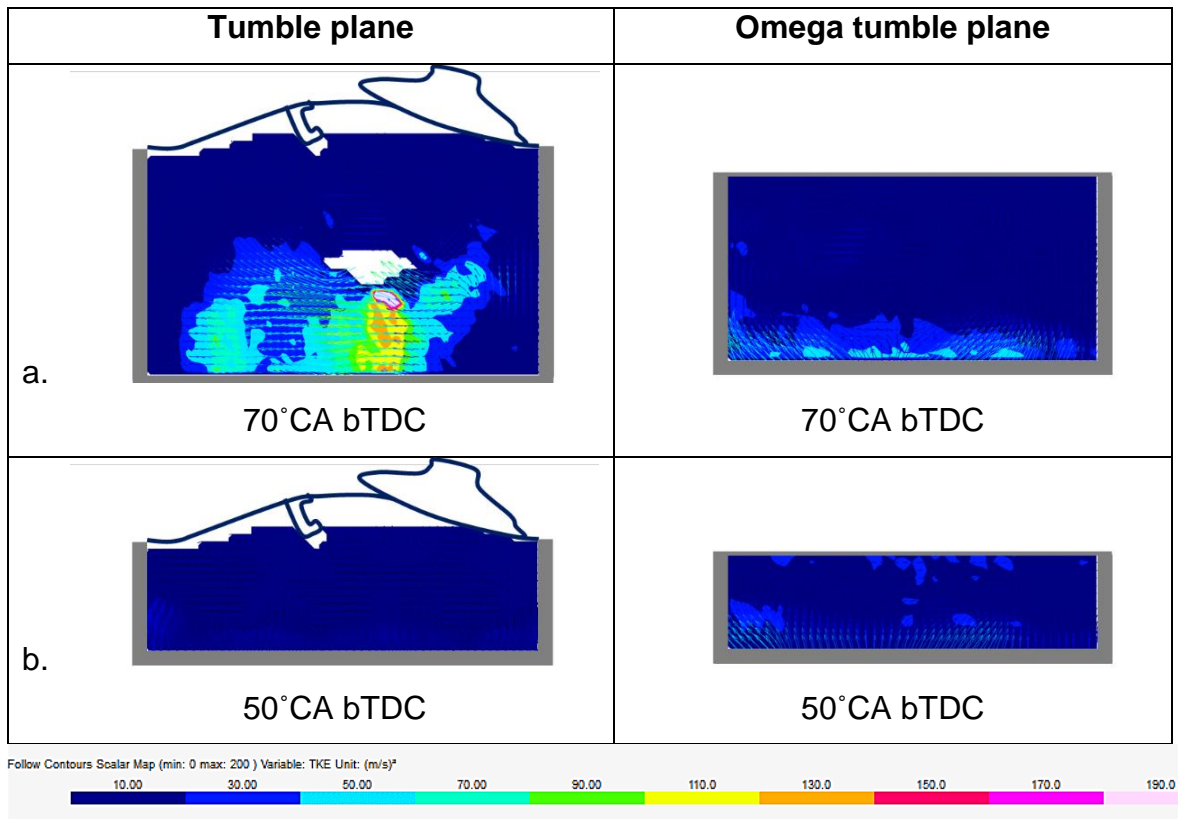
Figure 5.41: averaged TKE contours for SOI2 85˚CA bTDC representing data of the compression stroke positions after the end of second injection.

5.3.2.2.3 Effects Early Second Injection of SOI 40˚CA BTDC on the Mixture Formation

An even later injection time of SOI 40˚CA bTDC is analysed in this section. Figure 5.42a. - b. show the velocity vectors during the second injection and the flow field towards the end of the cycle.

Although the intention is to generate a fuel rich region with high local turbulence levels, close to the spark plug, such a late injection can be detrimental to the combustion performance. As observed, the piston's surface is far too close to the injector during the second injection. As a result, from SOI2 to EOI2, majority of the fuel impinges directly on the piston's surface. The spray does not even get a chance to develop globally, before interacting with the piston. It is suspected that the result here would the formation of pool fires, attached to the piston throughout the expansion stroke, as observed in [142].

Tumble plane	Omega tumble plane
a. 3˚CA ASOI2	3˚CA ASOI2
b. EOI2	EOI2

Vector color (min: 0.0299999993294477 max: 30) Variable(X): U Variable(Y): V Unit: m/s

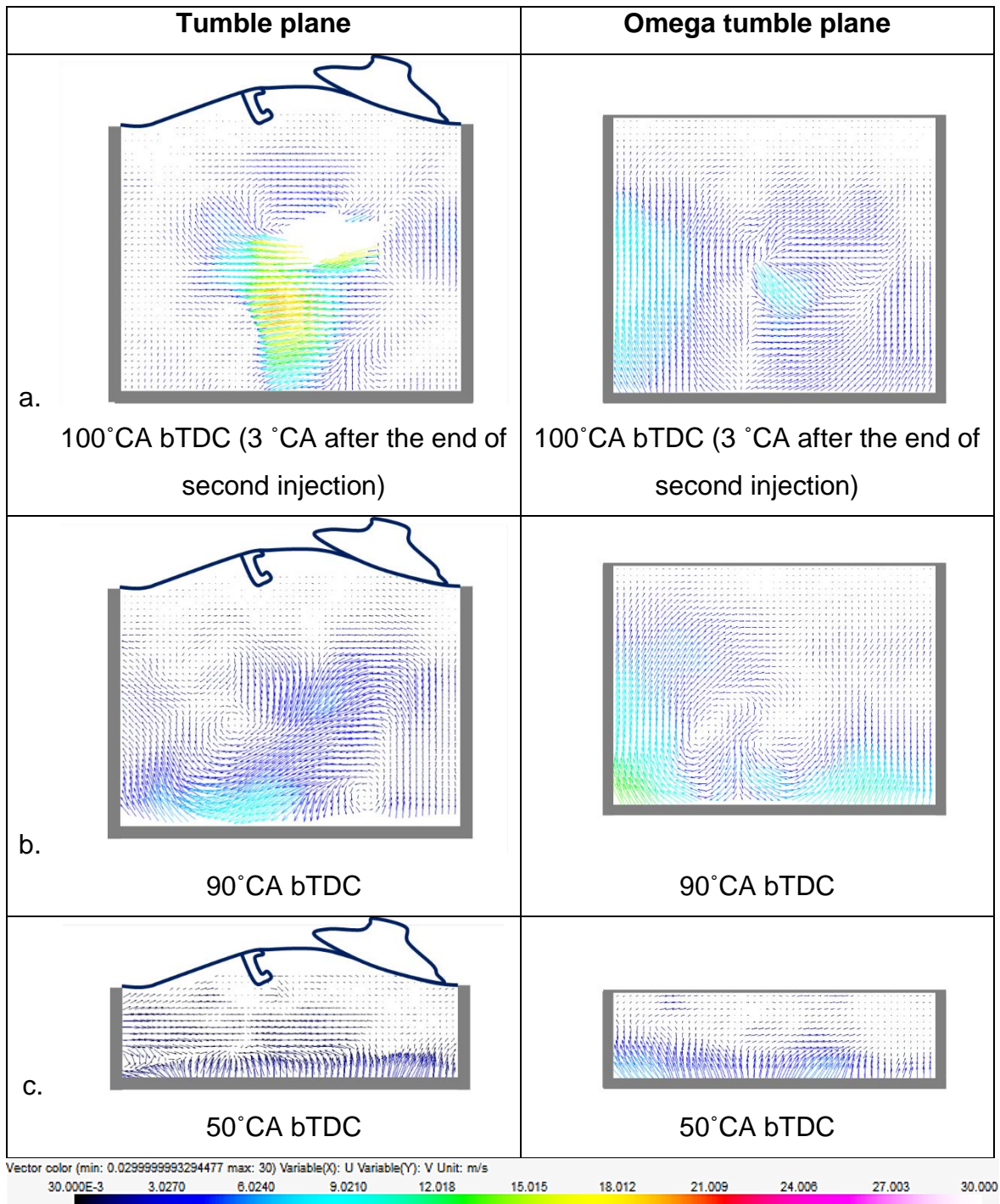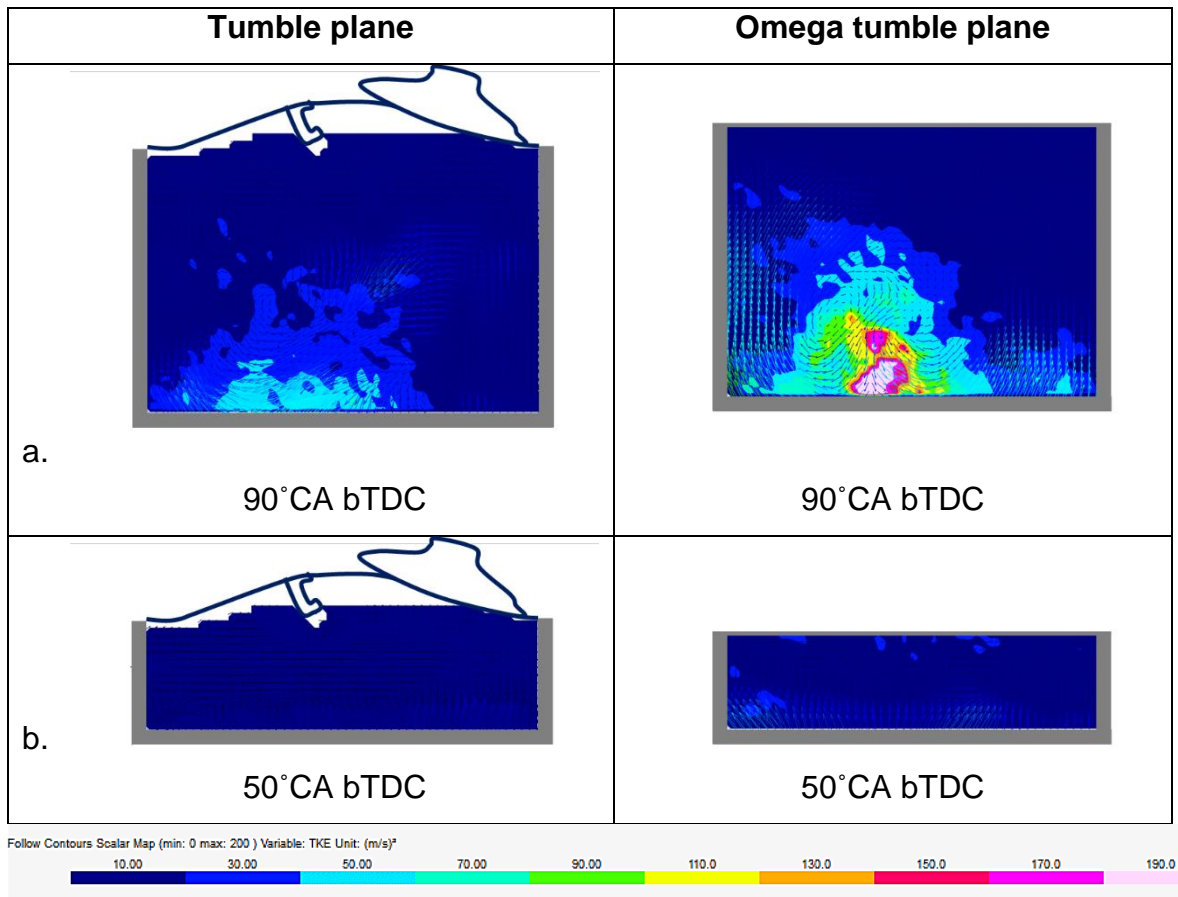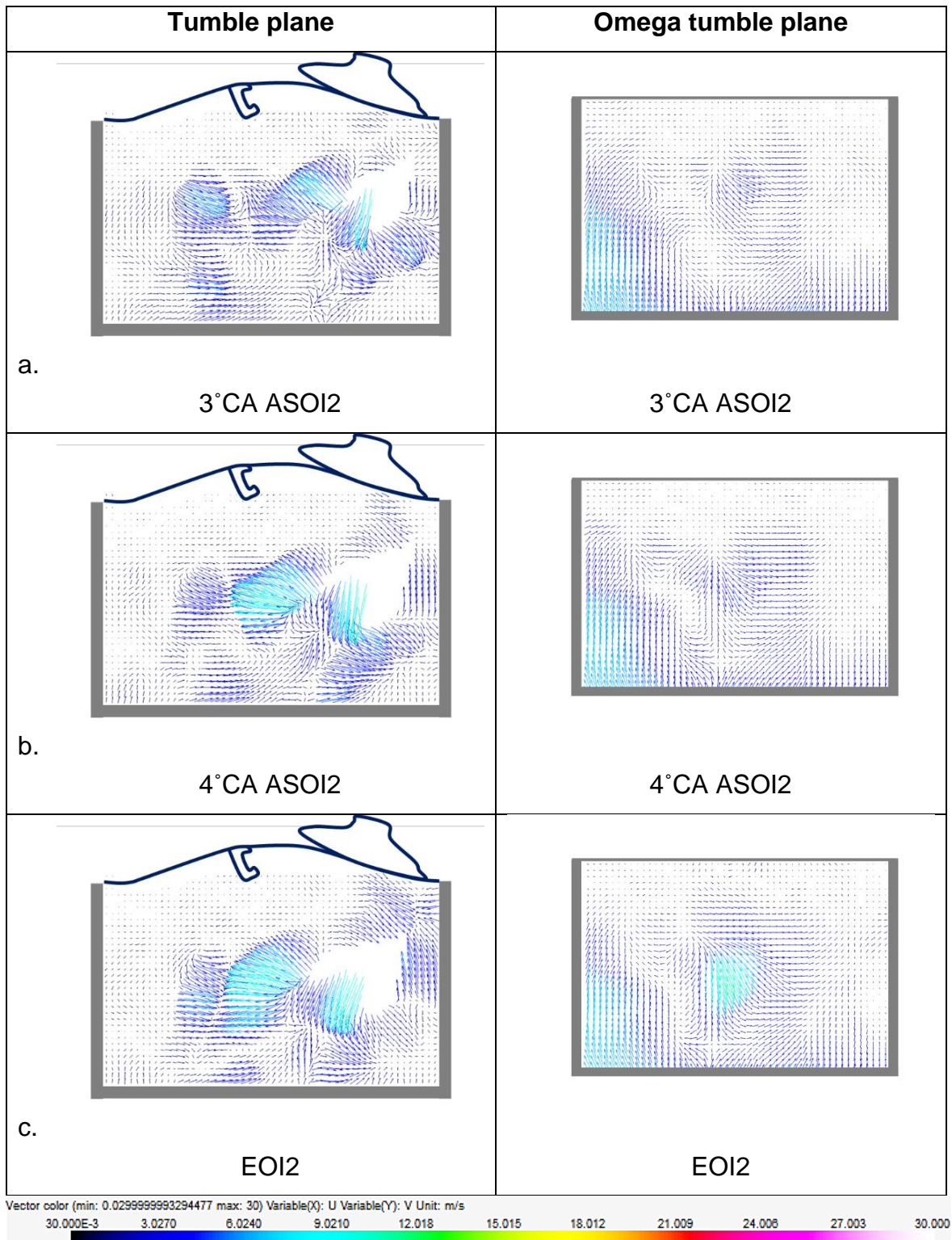| 30.000E-3 | 3.0270 | 6.0240 | 9.0210 | 12.018 | 15.015 | 18.012 | 21.009 | 24.006 | 27.003 | 30.000 |
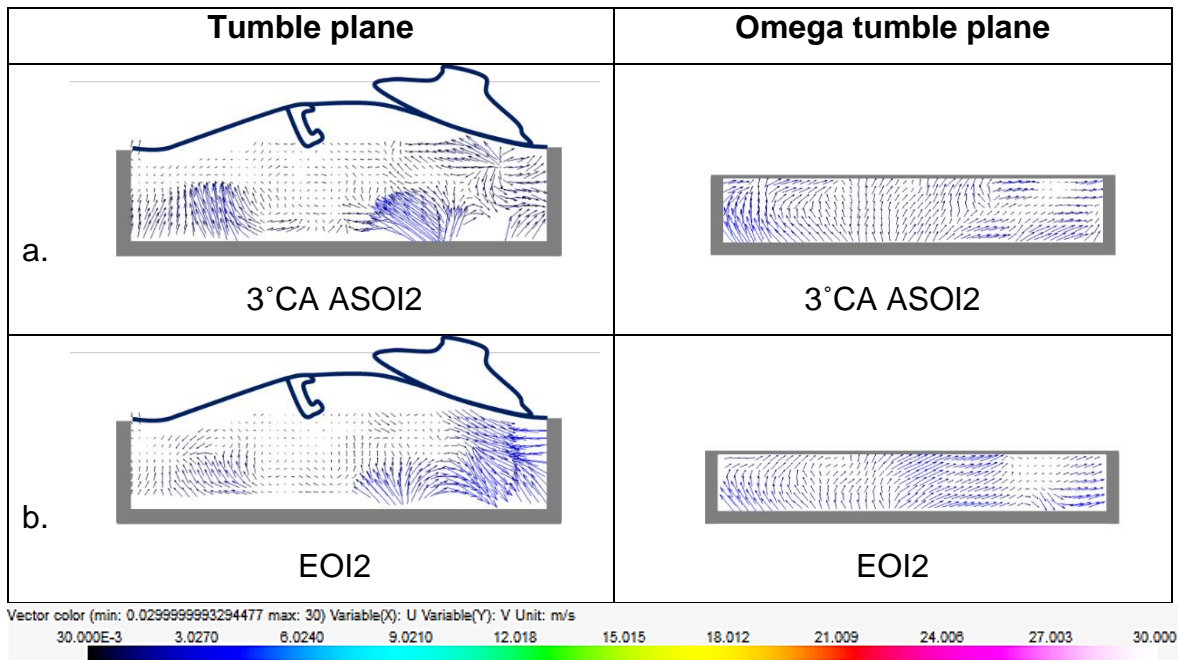
Figure 5.42: ensemble averaged velocity vectors for SOI2 40˚CA bTDC and 35MPa injection pressure representing data over the second injection period.

This effect could be alleviated with lower injection pressures. Medina et al., [33] had observed that the benefits of reduced particulate emissions with higher injection pressure had lessened for the pressure increase from 20MPa to 30MPa, when compared to the increase from 10MPa to 20MPa. Their results however showed that sufficiently high injection pressure consistently yields lower PN at all engine loads.

In addition, the fuel rich zone close to the spark plug generated by the late second injection wold reduce the temperature before ignition primarily because of evaporative cooling, as has been reported by Priyadarshini et al., [144] under 1200rpm engine speed, 1.3bar MAP and a split ratio of 4:1. When they had a second injection at 50°CA bTDC, the time available for mixing was only 30°CA bTDC, which resulted in high equivalence ratio of the mixture. If the second injection is too late, as in the current case, the fuel is injected inside a small cylinder volume. The bulk flow motion can therefore not be taken advantage of. The result is heavy piston surface impingement. In this case, it was reported that the rich zone would ignite first despite the lower temperature, which indicated that the reaction rate of the fuel and charge primarily depended on the local equivalence ratio and secondarily on the temperature.

5.3.2.3 Effects of Second Injection Timings on TKE levels near TDC

Averaged TKE maps, for the SOI2 105°CA and SOI2 85°CA close to TDC are presented in Figure 5.43a. - b. At these positions, the TKE levels close to TDC are comparable in both planes, for both second injection events. This suggests that the injections in the compression stroke has negligible impact on the TKE levels near the spark plug as the piston approaches TDC, at least for this engine configuration.

Tumble plane	Omega tumble plane
a. SOI2 105°CA bTDC (40°CA bTDC)	SOI2 105°CA bTDC (40°CA bTDC)
b. SOI2 85°CA bTDC (40°CA bTDC)	SOI2 85°CA bTDC (40°CA bTDC)

Follow Contours Scalar Map (min: 0 max: 200) Variable: TKE Unit: (m/s)²

| 10.00 | 30.00 | 50.00 | 70.00 | 90.00 | 110.0 | 130.0 | 150.0 | 170.0 | 190.0 |
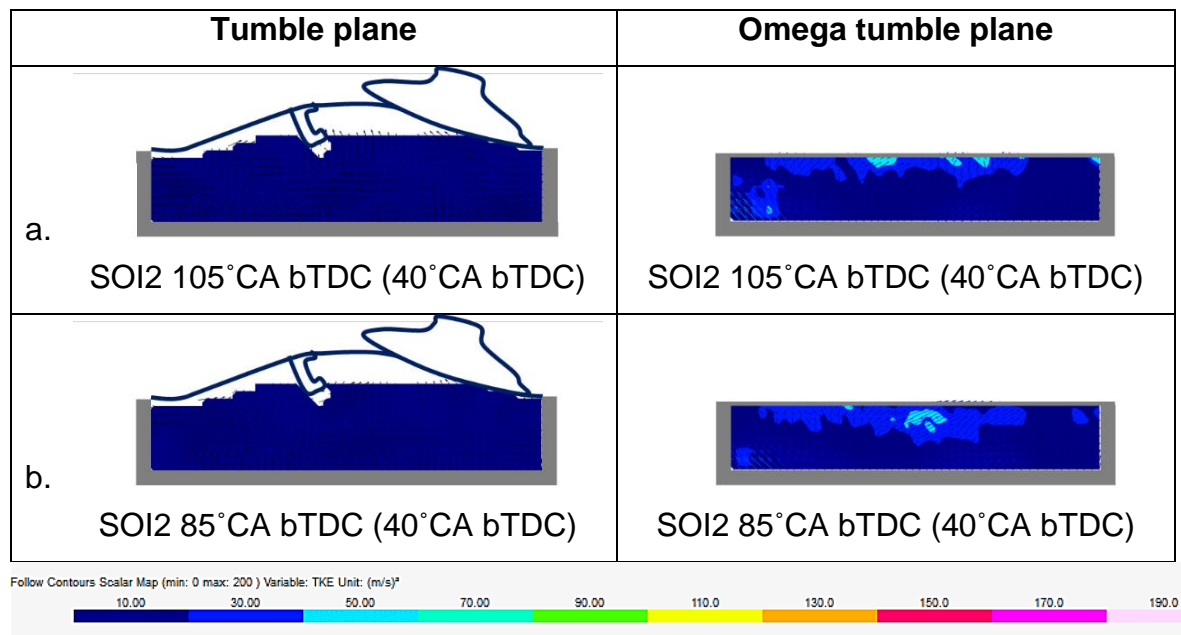
Figure 5.43: averaged TKE contours for SOI2 105°CA bTDC and SOI2 85°CA bTDC representing data for near TDC at 40°CA bTDC.

This similarity in the TKE between the two second injection cases occurs due to a short PW injected, which begins collapsing by the end of injection process and is soon entrained by the surrounding charge. This is also accelerated by the high in-cylinder pressure in the compression stroke. As a result of this, the local TKE levels diminish in the tumble plane regardless of the second injection timing in the compression stroke. The adequate mixing time of the short second injection thus contributes to low stratification.

The overall TKE levels are higher, and concentrated in the cylinder head region, away from the spark plug in the omega tumble plane. The repeated observations of higher turbulent levels and velocities measured in the omega tumble plane suggests that the flow characteristics in this plane of measurement are more dynamic when compared to the corresponding tumble plane. These high TKE levels at 40°CA bTDC

are distributed centrally in the cylinder, in close vicinity of the spark plug. This would provide suitable conditions for the flame propagation.

5.3.2.4 Cyclic Variations of the Flow Field Close to TDC

The maps of the standard deviation in the velocities close to TDC (50°CA bTDC) for both the tested split ratios are presented in Figure 5.44. This data provides an indication of the repeatability of the flow field observed close to TDC.

The standard deviations are again large in the omega tumble plane when compared to the tumble plane for both split ratios, which indicates large cyclic variability of the flow field in the omega tumble plane, regardless of the injection strategy. The main reason for the large uncertainties was earlier proposed to be the variations in the break up of the spray width, which would generate a variation of the droplet sizes, thereby affecting the consistency of the entrainment rate and the velocity vectors of the flow field.

Both split cases exhibit low standard deviation in velocities in the tumble planes, close to the spark plug. This indicates that the low velocity magnitudes observed close to the spark plug are consistent per cycle.

Tumble plane	Omega tumble plane
a. SOI2 105˚CA bTDC (40˚CA bTDC)	 SOI2 105˚CA bTDC (40˚CA bTDC)
b. SOI2 85˚CA bTDC (40˚CA bTDC)	 SOI2 85˚CA bTDC (40˚CA bTDC)

Follow Contours Scalar Map (min: 0 max: 20) Variable: StdDev (U) Unit: m/s

| 1.000 | 3.000 | 5.000 | 7.000 | 9.000 | 11.00 | 13.00 | 15.00 | 17.00 | 19.00 |
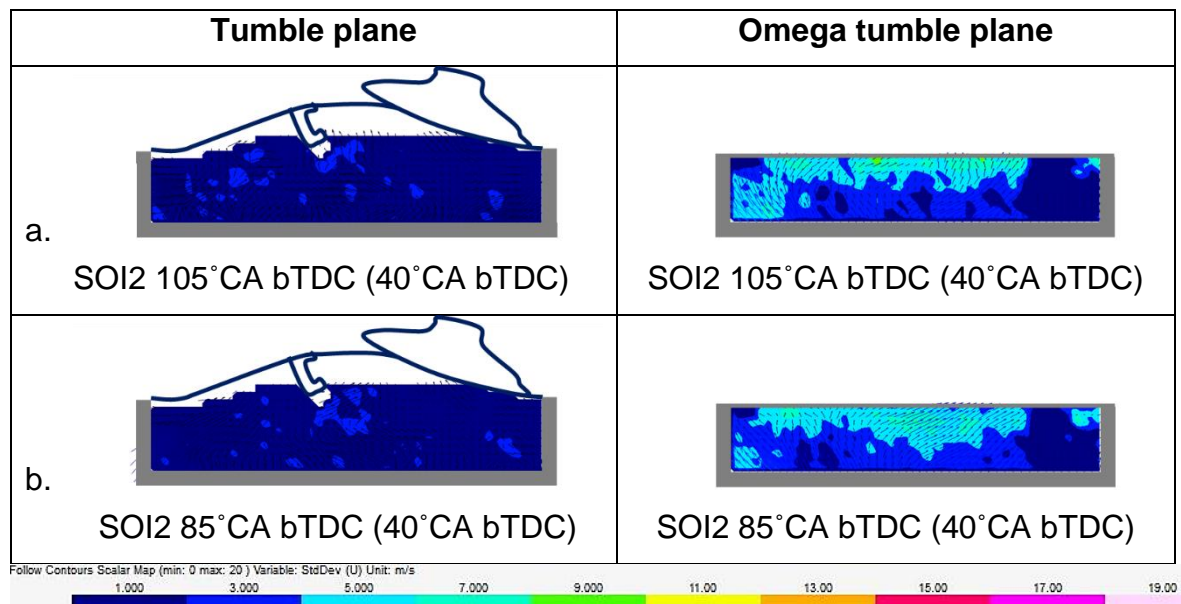
Figure 5.44: maps of standard deviation in velocities for SOI2 105˚CA bTDC and SOI2 85˚CA bTDC representing data for near TDC at 40˚CA bTDC.

5.3.2.5 Summary

The effects of a large split ratio of 75%:25%, with second injections at various sweeps of the compression stroke were investigated in this section. The first injection was in the intake stroke at 280°CA bTDC. The second injection timings tested, with the 25% fuel injection of the total quantity, were 105°CA bTDC, 85°CA bTDC and 40°CA bTDC.

The first injection provided high tumble motion which entrained the induced air within the eddy as the intake valves were fully open. The overall velocity magnitudes across both planes had increased by the end of the first injection. The formation of large eddies after the end of the first injection indicated high entrainment effects and a well distributed homogeneous charge in the flow field prior to the start of the second injection. This dynamic flow field had weakened however, by the start of the compression stroke. This was interpreted by the lower velocity magnitudes in both planes albeit with the presence of distinct vortices.

With a second injection at 105°CA bTDC, the effects of the surrounding charge and increasing in-cylinder pressure trace on the spray propagation were negligible. With an even later second injection of 85°CA bTDC, higher in-cylinder pressure traces in the compression stroke generated resistance against the spray propagation. As the piston approached near TDC, more distinct vortices were observed in both planes as a result of the later second injection.

The flow field near the spark plug however, suffered from low TKE levels in the tumble plane, for both of these tested second injection timings. It seemed difficult to preserve and control a high tumble charge motion upon spray collapse and for the rest of the cycle for injections in the compression stroke.

One way to overcome the low turbulence levels would be to maintain the two injection timings as employed in this case, and use a split ratio of 2:1, whereby slightly higher quantity would be injected in the second injection, at an injection timing of SOI2 85°CA bTDC. In order to increase the bulk flow motion close to the spark plug, the angle of inclination of the injector could also be optimised so that the plumes are directed with a larger spray angle in the tumble charge motion.

Another way of increasing the bulk flow motion is to induce triple injections, with closely coupled second and third injections in the compression stroke. This would

increase the likelihood of preserving the strong tumble charge motion that can be directed towards the spark plug prior to ignition. In this case, it is important to avoid late injections. With a second injection at 40°CA bTDC, the piston's surface was far too close to the injector during the second injection. As a result, from SOI2 to EOI2, majority of the fuel had impinged directly on the piston's surface. The spray did not even get a chance to develop globally, before interacting with the piston. This could be detrimental for the combustion performance, increasing the likelihood of diffusion combustion with pool fires. This timing could also reduce the temperature distribution of the cylinder as the mixture approaches the spark plug.

Chapter 6. Conclusions and Recommendations

6.1 Introduction

When it comes to internal combustion engines, the GDI engines have become the dominant powertrain for passenger cars, but they are still far from reaching optimum operating conditions with mitigated emission levels for a range of operating conditions. On-going optimisation in technologies thus need to be aggressively pursued.

One of the concerns related to GDI engines is the formation of high levels of PN and NOx generated from cold start and part-load conditions. It is crucial to achieve rapid activation of the exhaust catalyst by accelerating the engine warm up process. It is equally important to limit fuel impingement on the combustion chamber surfaces which result in diffusion combustion and formation of soot.

The aim of the current work therefore, was to investigate the effects of the split injection strategy on the spray characteristics and the GDI engine's in-cylinder mixture formation to achieve charge stratification under low load condition. This was done using a multi-hole Solenoid injector capable of injection pressures of up to 35MPa.

6.2 Spray Characteristics of Single and Split Injections

For the spray characterisations of both single and split injections, three key diagnostic techniques were employed. Mass measurements were performed with 1000 pulses per burst at 10Hz injection frequency using Gasoline RON95. This was followed by high-speed imaging with backlight illumination at 20KHz. This was done to obtain penetration length and spray angle data of various injection strategies. Finally, PDA measurements using n-Heptane helped obtain velocity and drop size data of a single plume within the spray, along varying axial distances downstream of the injector.

The results showed that the highest quantity of the fuel was measured with the shortest tested dwell time of 2ms. This was caused by the fuel prior to the start of the second injection interacting with the tip of the second injection. These interactions had increased the droplet sizes. With low chamber pressures, the interactions

between the droplets from different injection events, using short dwell times of 2ms or less, could affect the mixture formation and subsequently the PN levels.

The highest relative peak in the injection quantity at 2ms dwell was attributed to the short PW combination of 0.4ms-0.4ms. High speed images had revealed that the spray was attached to the injector tip for at least 100μs after EOI. This was due to the sudden closing of the valve, which interrupted the development of the peak current over time. The sudden drop in current commanded the valve to shut, but the high injection pressure had likely resisted the closing of the valve. The delayed detachment of the fuel spray using short PWs and high injection pressure with the Solenoid injector would have thus affected the injected quantity and can subsequently affect the equivalence ratio. In addition, the SMDs for the shorter PW of 0.4ms were generally larger than 0.8ms PW. Droplets in this case are affected by closely spaced opening and closing events of the solenoid valve.

Upon the valve's opening for the second time after 2ms dwell, greater number of low velocity droplets were observed, particularly in the near nozzle region (11mm downstream), when compared to the first injection. This had occurred due to a combination of recirculating droplets and droplets with plume perpendicular velocities being captured. The former is stated to have been intensified by the high injection pressure, which could cause some droplets, particularly those at the edges of the plume, to travel upwards and close to the injector tip with reduced momentum. This increases the likelihood of droplets accumulating on injector tip. This effect was alleviated with 6ms dwell and had intensified with larger PW.

6.3 Effects of Injection Strategies on In-cylinder Flow and Charge Formation

The next study was investigating the effects of split injections with short dwells (split injection in the intake stroke) and large dwells (second injections in the compression strokes) on the charge formation. Cycle resolved high-speed PIV measurements at 10KHz were performed in the tumble and omega tumble flow planes.

When studying the effects of split ratios of 75%-25% and 25%-75% on the mixture formation, the first injection times were kept constant and both split injections occurred at various sweeps in the intake stroke. The results revealed that the large

split ratio, with early first injection generated a weak charge motion in the flow field close to the spark plug, due to the injection events having sufficient time to atomise and mix uniformly in the cylinder. In addition, due to the high surface impingement from the early first 75% of fuel, it is suspected that this case would have caused fuel film to settle on the piston's surface.

With the smaller split ratio of 25%-75%, a highly turbulent flow field was formed near the spark plug close to TDC in both planes, generating more favourable conditions for the turbulent propagation of the flame. This was because of the greater amount of fuel injected in the second event, sufficiently early. The injection timing coupled with inlet valve opening had resulted in strong tumble charge motion with large scale vortices. This allowed the fuel spray to break up and accelerate the entrainment effects, while preserving the high turbulence levels throughout the compression stroke and close to TDC.

The effects of a large split ratio of 75%:25%, with second injections at various sweeps of the compression stroke were also investigated. The first injection was in the intake stroke at 280°CA bTDC. The second injection timings tested, with the 25% fuel injection of the total quantity, were 105°CA bTDC, 85°CA bTDC and 40°CA bTDC.

The first injection had intensified the tumble charge motion which entrained the induced air within the eddy, as the intake valves were fully open during the injection. This had likely generated a well distributed homogeneous charge in the flow field prior to the start of the second injection. This dynamic flow field had weakened however, by the start of the compression stroke. With a second injection at 105°CA bTDC, the effects of the surrounding charge and increasing in-cylinder pressure trace on the spray propagation were negligible. With an even later second injection of 85°CA bTDC, higher in-cylinder pressure traces in the compression stroke generated resistance against the spray propagation. As the piston approached near TDC, more distinct vortices were observed in both planes as a result of the later second injection, albeit with low turbulence levels.

The flow field near the spark plug suffered from low TKE levels in the tumble plane, for both of these tested second injection timings. It was difficult to preserve and control a high tumble charge motion upon spray collapse and for the rest of the cycle

for injections in the compression stroke, with the stated split ratio of 75%:25%. This was because the of the small-scale tumble vortices associated with the second smaller PW.

One way to overcome the low turbulence levels would be to maintain the two injection timings as employed in this case, and use a split ratio of 2:1, whereby slightly higher quantity of fuel would be injected in the second injection, at an injection timing of SOI2 85°CA bTDC. In this way, the strong tumble charge motion from the first injection coupled with induced air (injection during IVO) can be taken advantage of. The increased second injection quantity can subsequently generate intensified tumble motion with large-scale vortices that can be preserved all the way to TDC.

In order to increase the bulk flow motion close to the spark plug, the angle of inclination of the injector could also be optimised so that the plumes are directed with a larger spray angle in the tumble charge motion.

Another way of increasing the bulk flow motion is to induce triple injections, with closely coupled second and third injections in the compression stroke. This would increase the likelihood of preserving the strong tumble charge motion that can be directed towards the spark plug prior to ignition. In this case, it is important to avoid late injections, particularly when employing large PWs and injection pressures. With a second injection at 40°CA bTDC, the piston's surface was far too close to the injector during the second injection. As a result, from SOI2 to EOI2, majority of the fuel had impinged directly on the piston's surface.

Another important realisation from the study is that fuel injection timings which would maximise interactions with piston surface should be generally avoided, as this can most likely generate pool fires and therefore the formation of soot particles of various sizes. These times are effectively the first half of the intake stroke or the latter half of the compression stroke, in which cases the piston is close to the injector tip.

6.4 Recommendations for Future work

As this field of research is directly applicable for the development of GDI engines, there are various ways this study can be extended.

From the investigations of the spray characterisation, it was found that the needle behaviour had significant effects on the flow characteristics. A study focusing on the needle motion and the flow through the injector nozzle would provide useful information of the injector's behaviour, especially during the closing event. X-ray imaging inside the nozzles and high-speed imaging using a macro lens at the nozzle tips can provide useful information of the effects of both the high injection pressure and injector closing event on the purging process of the injector as well as the tip wetting phenomena, which would affect the flow characteristics and drop sizes measured further downstream.

Additionally, performing the PDA measurements with higher pressures inside the spray chamber to simulate specific engine conditions or inside the combustion chamber could provide valuable and more representative information. More specifically, better understanding of the effects of split injections on the drop size, drop velocities and mixture formation under the highly turbulent in-cylinder conditions can be achieved. These measurements were not performed in the current project due to the limitations with the project time and prioritised objectives that were also influenced by the sponsors' requirements.

High-speed PIV measurements of the flow field using various injection strategies were performed in two key planes, which provided information of the charge motion near the spark plug. The same studies conducted in the swirl plane would help obtain a complete understanding of the effects of the injection strategies in the overall bulk flow motion. Furthermore, using a bowl-shaped piston instead of a flat piston can provide more representative information of the charge motion as the combustion chamber's configuration would be similar to that of the current prototype engine configurations.

To enhance the turbulence levels in the current engine configuration, it would also be useful to perform these studies by decreasing the injector's angle of inclination seating on the cylinder head. This way the optimised plume angles could generate higher turbulence levels in the flow field.

To complete the study, investigations could be carried out to determine the fuel film distribution on the chamber surfaces with these injection strategies, by performing high-speed LIF measurements. Such measurements were planned and the relevant laser and high-speed intensified camera had been set up. Due to Covid-19 however, the measurement could not be carried out in the remaining period of the PhD study. This data would reveal potential regions of soot formation inside the chamber. Additionally, further analyses on the flame development and subsequent emissions levels would help determine the optimum injection strategies for the current tested conditions of ~0.74bar MAP and 1200rpm using a compression ratio of 11.5.

Regarding optimisation of the optical works, high-speed PIV in both planes revealed differences in the laser elastic scattering, due to the differences in the orientation of the laser with respect the to the curved cylinder. To mitigate these effects, the laser sheet could be introduced via the optical window on the piston crown for both PIV and LIF measurements in the future. This is possible with the help of the 45° mirror placed underneath the extended piston bowl, which would reflect the laser sheet through the flat optical piston in order to perform measurements in the tumble and omega tumble planes. It is expected that these orientations would significantly improve the signal to noise ratio, and alleviate the detected variations of the oversaturated regions.

List of References

[1]   G. Fraidl, W. F. Piock, and M. Wirth, "The potential of the direct injection gasoline engine," in *18th International Vienna Motor Symposium*, 1997.

[2]   D. Zimmermann, "Inflammation of Stratified Mixtures in Spray Guided DI Gasoline Engines: Optimization by Application of High Speed Imaging Techniques," in *Internationales Symposium für Verbrennungsdiagnostik*, 2004.

[3]   M. Mittal, D. L. S. Hung, G. Zhu, and H. Schock, "A Study of Fuel Impingement Analysis on In-Cylinder Surfaces in a Direct-Injection Spark-Ignition Engine with Gasoline and Ethanol-Gasoline Blended Fuels," *SAE Tech. Pap. Ser. 2010-01-2153*, 2010.

[4]   P. Sphicas, L. M. Pickett, S. A. Skeen, and J. H. Frank, "Inter-plume aerodynamics for gasoline spray collapse," *Int. J. Engine Res.*, vol. 19, no. 10, pp. 1048–1067, 2018.

[5]   K. Kawajiri, T. Yonezawa, H. Ohuchi, M. Sumida, and H. Katashiba, "Study of interaction between spray and air motion, and spray wall impingement," in *SAE Technical Papers*, 2002.

[6]   T. Landenfeld, A. Kufferath, and J. Gerhardt, "Gasoline Direct Injection - SULEV Emission Concept," *SAE Tech. Pap. Ser. 2004-01-0041*, 2004.

[7]   M. Skogsberg, P. Dahlander, R. Lindgren, and I. Denbratt, "Effects of injector parameters on mixture formation for multi-hole nozzles in a spray-guided gasoline di engine," in *SAE Technical Papers*, 2005.

[8]   N. Mitroglou, J. M. Nouri, Y. Yan, M. Gavaises, and C. Arcoumanis, "Spray structure generated by multi-hole injectors for gasoline direct-injection engines," *SAE Tech. Pap. Ser. 2007-01-1417*, 2007.

[9]   L. Allocca, M. Costa, A. Montanaro, and U. Sorge, "Study of the portability of a 3D CFD model for the dynamics of sprays issuing from multi-hole GDI injectors," in *SAE Technical Papers*, 2011.

[10]   B. Befrui, G. Corbinelli, M. D'Onofrio, and D. Varble, "GDI multi-hole injector internal flow and spray analysis," in *SAE 2011 World Congress and Exhibition*, 2011.

[11]   M. Xu, D. Porter, C. Daniels, G. Panagos, J. Winkelman, and K. Munir, "Soft spray formation of a low-pressure high-turbulence fuel injector for direct injection gasoline engines," in *SAE Technical Papers*, 2002.

[12]   X. Liu *et al.*, "Ultrafast and quantitative x-tomography and simulation of hollow-cone gasoline direct-injection sprays," in *SAE Technical Papers*, 2007.

[13]   D. Abata, "A review of the stratified charge engine concept," in *Automotive Engine Alternatives, International Symposium on Alternative and Advanced Automotive Engines*, 1986.

[14]   A. C. Alkidas and S. H. El Tahry, "Contributors to the Fuel Economy Advantage of DISI Engines Over PFI Engines," *SAE Tech. Pap. Ser.*, no. 01, 2003.

[15]   L. Schmidt *et al.*, "Multiple injection strategies for improved combustion stability under stratified part load conditions in a spray guided gasoline direct injection (SGDI) engine," *SAE Tech. Pap.*, 2011.

[16]   F. Zhao, M.-C. Lai, and D. L. Harrington, "Automotive spark-ignited direct-injection gasoline engines," *Prog. Energy Combust. Sci.*, vol. 25, no. 5, pp. 437–562, 1999.

[17]   EPA. US, "US EPA Report EPA-420-R-19-002," 2019.

[18]   W. Anderson, J. Yang, D. D. Brehob, J. K. Vallance, and R. M. Whiteaker, "Understanding the Thermodynamics of Direct Injection Spark Ignition (DISI) combustion systems: An analytical and experimental investigation," in *SAE Technical Papers*, 1996.

[19]   P. Whitaker, P. Kapus, M. Ogris, and P. Hollerer, "Measures to Reduce Particulate Emissions from Gasoline DI engines," *SAE Int. J. Engines 2011-01-1219*, pp. 1498–1512, 2011.

[20]   P. Dahlander and S. Hemdal, "High-Speed Photography of Stratified Combustion in an Optical GDI Engine for Different Triple Injection Strategies," *SAE Tech. Pap.*, vol. 2015-April, no. April, 2015.

[21]   S. S. Merola, A. Irimescu, L. Marchitto, C. Tornatore, and G. Valentino, "Effect of injection timing on combustion and soot formation in a direct injection spark

ignition engine fueled with butanol," *Int. J. Engine Res.*, vol. 18, no. 5–6, pp. 490–504, 2017.

[22]   K. Takeda, T. Yaegashi, K. Sekiquchi, K. Saito, and N. Imatake, "Mixture preparation and hc emissions of a 4-valve engine with port fuel injection during cold starting and warm-up," in *SAE Technical Papers*, 1995.

[23]   J. Hunicz and P. Kordos, "An experimental study of fuel injection strategies in CAI gasoline engine," *Exp. Therm. Fluid Sci.*, vol. 35, pp. 243–252, 2011.

[24]   K. Kimura, S. Mori, M. Kawauchi, and R. Shimizu, "An investigation for reducing combustion instability under cold-start condition of a direct injection gasoline engine," *Int. J. Engine Res.*, vol. 20, no. 4, pp. 470–479, 2019.

[25]   J. Yang and T. Kenney, "Some concepts of DISI engine for high fuel efficiency and low emissions," in *SAE Technical Papers*, 2002.

[26]   T. D. Fansler, D. L. Reuss, V. Sick, and R. N. Dahms, "Combustion instability in spray-guided stratified-charge engines: A review," *Int. J. Engine Res.*, vol. 16, no. 3, pp. 260–305, 2015.

[27]   C. Geschwindner *et al.*, "Analysis of the interaction of Spray G and in-cylinder flow in two optical engines for late gasoline direct injection," *Int. J. Engine Res.*, vol. 21, no. 1, pp. 169–184, 2019.

[28]   S. Russ, G. Lavoie, and W. Dai, "SI engine operation with retarded ignition: Part 1 - Cyclic variations," in *SAE Technical Papers*, 1999.

[29]   T. D. Fansler, M. C. Drake, and B. B, "High-speed Mie scattering diagnostics for spray-guided gasoline engine development," in *8th international symposium on combustion diagnostics, Baden*, 2008.

[30]   M. Bardi, G. Pilla, and X. Gautrot, "Experimental assessment of the sources of regulated and unregulated nanoparticles in gasoline direct-injection engines," *Int. J. Engine Res.*, vol. 20, no. 1, pp. 128–140, 2019.

[31]   J. Hélie, N. Lamarque, J. L. Fremaux, P. Serrecchia, M. Khosravi, and O. Berkemeier, "The process of tip wetting at the spray injection end," *Int. J. Engine Res.*, pp. 1–15, 2019.

[32] S. Mouvanal, "Hydro-thermal Phenomena in GDI Fuel Injector Nozzle associated with Carbon deposit formation," 2020.

[33] M. Medina, F. M. Alzahrani, M. Fatouraie, M. S. Wooldridge, and V. Sick, "Mechanisms of fuel injector tip wetting and tip drying based on experimental measurements of engine-out particulate emissions from gasoline direct-injection engines," *Int. J. Engine Res.*, 2020.

[34] P. O. Witze and R. M. Green, "Comparison of single and dual spray fuel injectors during cold start of a PFI spark ignition engine using visualization of liquid fuel films and pool fires," *SAE Tech. Pap.*, no. 724, 2005.

[35] N. J. Beavis, S. S. Ibrahim, and W. Malalasekera, "Impingement characteristics of an early injection gasoline direct injection engine: A numerical study," *Int. J. Engine Res.*, vol. 18, no. 4, pp. 378–393, 2017.

[36] J. P. Szybist *et al.*, "What Fuel Properties Enable Higher Thermal Efficiency in Spark-Ignited Engines?," *Prog. Energy Combust. Sci.*, vol. 0, no. 100876, 2020.

[37] T. Alger, M. Hall, and R. D. Matthews, "Effects of Swirl and Tumble on In-Cylinder Fuel Distribution in a Central Injected DISI Engine," *Sae Tech. Pap. Ser.*, no. 01, pp. 1–15, 2000.

[38] M. Costa, U. Sorge, S. Merola, A. Irimescu, M. La Villetta, and V. Rocco, "Split injection in a homogeneous stratified gasoline direct injection engine for high combustion efficiency and low pollutants emission," *Energy*, vol. 117, pp. 405–415, 2016.

[39] E. Stevens and R. Steeper, "Piston wetting in an optical DISI engine: Fuel films, pool fires, and soot generation," *SAE Tech. Pap.*, vol. 2001, no. 724, 2001.

[40] A. Berndorfer, S. Breuer, W. Piock, and P. Von Bacho, "Diffusion combustion phenomena in GDi engines caused by injection process," *SAE Tech. Pap.*, vol. 2, 2013.

[41] F.-Q. Zhao, M.-C. Lai, and D. L. Harrington, "A Review of Mixture Preparation and Combustion Control Strategies for Spark-Ignited Direct-Injection Gasoline

Engines," *SAE Tech. Pap. 970627*, pp. 1–44, 1997.

[42] B. A. Bruno, D. A. Santavicca, and J. V. Zello, "Fuel injection pressure effects on the cold start performance of a GDI engine," *SAE Tech. Pap. Ser. 2003-01-3163*, 2003.

[43] B. E. Milton, M. Behnia, and D. Ellerman, "Fuel deposition and re-atomisation from fuel/air flows through engine inlet valves," *Int. J. Heat Fluid Flow*, vol. 22, pp. 350–357, 2001.

[44] T. Li, M. Yamakawa, D. Takaki, K. Nishida, Y. Zhang, and H. Hiroyasu, "Characterization of mixture formation processes in D.I. gasoline sprays by the laser absorption scattering (LAS) technique - Effect of injection conditions," *SAE Tech. Pap.*, no. 724, 2003.

[45] G. K. Fraidl, W. F. Piock, and M. Wirth, "Gasoline direct injection : actual trends and future strategies for injection and combustion systems," *Sae Tech. Pap. Ser. 960465*, pp. 95–111, 1996.

[46] Z. Xu, J. Yi, S. Wooldridge, D. Reiche, E. Curtis, and G. Papaioannou, "Modeling the cold start of the ford 3.5L V6 EcoBoost engine," *SAE Tech. Pap.*, vol. 2, no. 1, pp. 1367–1387, 2009.

[47] J. Sureshkumar, G. Venkitachalam, J. M. Mallikarjuna, and R. Elayaraja, "Study on effect of engine operating parameters on flame characteristics," *SAE Tech. Pap. 2015-01-0749*, 2015.

[48] Y. Ra *et al.*, "Gasoline DICI Engine Operation in the LTC Regime Using Triple-Pulse Injection," *SAE Int. 2012-01-1131*, vol. 5, no. 3, pp. 1109–1132, 2012.

[49] B. Peterson, D. L. Reuss, and V. Sick, "On the ignition and flame development in a spray-guided direct-injection spark-ignition engine," *Combust. Flame*, 2014.

[50] AVL Deutschland GmbH, "Modeling of sprays and combustion in a spray-guided spark ignition direct injection engine," in *6th international symposium on internal combustion diagnostics, Baden-Baden*, 2004.

[51] T. D. Fansler, M. C. Drake, I. Duwel, and F. Zimmermann, "Fuel-spray and spark-plug interactions in a spray-guided direct-injection gasoline engine," in

7th international symposium on internal combustion diagnostics, Baden-Baden, 2006.

[52]   D. Martin, P. Pischke, and R. Kneer, "Investigation of the influence of multiple gasoline direct injections on macroscopic spray quantities at different boundary conditions by means of visualization techniques," *Int. J. Engine Res.*, vol. 11, no. 6, pp. 439–454, 2010.

[53]   W. Zhao *et al.*, "Flame–spray interaction and combustion features in split-injection spray flames under diesel engine-like conditions," *Combust. Flame*, vol. 210, pp. 204–221, Dec. 2019.

[54]   C. Park, S. Kim, H. Kim, S. Lee, C. Kim, and Y. Moriyoshi, "Effect of a split-injection strategy on the performance of stratified lean combustion for a gasoline direct-injection engine," in *Proceedings of the Institution of Mechanical Engineers, Part D: Journal of Automobile Engineering*, 2011, vol. 225, pp. 1415–1426.

[55]   J. Benajes, B. Tormos, A. Garcia, and J. Monsalve-Serrano, "Impact of Spark Assistance and Multiple Injections on Gasoline PPC Light Load," *SAE Int. J. Engines 2014-01-2669*, pp. 1875–1887, 2014.

[56]   M. Costa, P. Sementa, U. Sorge, F. Catapano, G. Marseglia, and B. M. Vaglieco, "Split injection in a GDI engine under knock conditions: an experimental and numerical investigation," *SAE Int. 215-24-2432*, 2015.

[57]   Y. Zhang *et al.*, "Mixing-Controlled Combustion of Conventional and Higher Reactivity Gasolines in a Multi-Cylinder Heavy-Duty Compression Ignition Engine," *SAE Int. 2017-01-0696*, 2018.

[58]   S. S. Merola, A. Irimescu, C. Tornatore, L. Marchitto, and G. Valentino, "Split Injection in a DISI Engine Fuelled with Butanol and Gasoline Analyzed through Integrated Methodologies," *SAE Int. J. Engines 2015-01-0748*, vol. 8, no. 2, pp. 474–494, 2015.

[59]   J. Serras-Pereira, P. G. Aleiferis, D. Richardson, and S. Wallace, "Mixture preparation and combustion variability in a spray-guided DISI engine," *SAE Tech. Pap. Ser. 2007-01-4033*, vol. 1, 2007.

[60] Y. Wang, H. Wei, L. Zhou, Y. Li, and J. Liang, "Effect of Injection Strategy on the Combustion and Knock in a Downsized Gasoline Engine with Large Eddy Simulation," *SAE Tech. Pap. Ser.*, vol. 1, pp. 1–15, 2020.

[61] M. C. Drake, T. D. Fansler, A. S. Solomon, and G. A. Szekely, "Piston fuel films as a source of smoke and hydrocarbon emissions from a wall-controlled spark-ignited direct-injection engine," in *SAE Technical Papers*, 2003.

[62] X. Yang, A. Solomon, and T. W. Kuo, "Ignition and combustion simulations of spray-guided SIDI engine using Arrhenius combustion with spark-energy deposition model," *SAE Tech. Pap.*, 2012.

[63] T. Kim, J. Song, and S. Park, "Effects of turbulence enhancement on combustion process using a double injection strategy in direct-injection spark-ignition (DISI) gasoline engines," *Int. J. Heat Fluid Flow*, vol. 56, pp. 124–136, 2015.

[64] R. Kumar and J. M. Mallikarjuna, "Effect of Homogenous-Stratified Mixture Combustion on Performance and Emission Characteristics of a Spray-Guided GDI Engine - A CFD Study," *SAE Tech. Pap. Ser. 2020-01-0785*, vol. 1, pp. 1–13, 2020.

[65] L. Francqueville, G. Bruneaux, and B. Thirouard, "Soot Volume Fraction Measurements in a Gasoline Direct Injection Engine by Combined Laser Induced Incandescence and Laser Extinction Method," *SAE Int.*, vol. 3, no. 1, pp. 163–182, 2010.

[66] J. Su, M. Xu, P. Yin, Y. Gao, and D. Hung, "Particle Number Emissions Reduction Using Multiple Injection Strategies in a Boosted Spark-Ignition Direct-Injection (SIDI) Gasoline Engine," *SAE Int. J. Engines 2014-01-2845*, pp. 20–29, 2014.

[67] X. Wang, J. Ma, and H. Zhao, "Analysis of mixture formation process in a two-stroke boosted uniflow scavenged direct injection gasoline engine," *Int. J. Engine Res.*, pp. 1–14, 2017.

[68] R. Daniel, C. Wang, H. Xu, and G. Tian, "Split-injection strategies under full-load using DMF, a new biofuel candidate, compared to ethanol in a GDI

engine," *SAE Int. 2012-01-0403*, 2012.

[69] T. Li, K. Nishida, Y. Zhang, and H. Hiroyasu, "Effect of split injection on stratified charge formation of direct injection spark ignition engines," *Int. J. Engine Res.*, vol. 8, no. 2, pp. 205–219, 2007.

[70] Z. Zheng, X. Tian, and X. Zhang, "Effects of split injection proportion and the second injection time on the mixture formation in a GDI engine under catalyst heating mode using stratified charge strategy," *Appl. Therm. Eng.*, vol. 84, pp. 237–245, 2015.

[71] B. Gainey, Z. Yan, S. Moser, E. Vorwerk, and B. Lawler, "Tailoring thermal stratification to enable high load low temperature combustion with wet ethanol on a gasoline engine architecture," *Int. J. Engine Res.*, 2020.

[72] J. Yang and R. W. Anderson, "Fuel injection strategies to increase full-load torque output of a direct-injection SI engine," *SAE Tech. Pap. Ser. 980495*, pp. 1–8, 1998.

[73] R. Hanson, D. Splitter, and R. D. Reitz, "Operating a Heavy-Duty Direct-Injection Compression-Ignition Engine with Gasoline for Low Emissions," *SAE Tech. Pap. Ser. 2009-01-1442*, 2009.

[74] A. A. Moiz, M. M. Ameen, S. Y. Lee, and S. Som, "Study of soot production for double injections of n-dodecane in CI engine-like conditions," *Combust. Flame*, vol. 173, pp. 123–131, Nov. 2016.

[75] L. Cao, H. Zhao, and X. Jiang, "Investigation into controlled auto-ignition combustion in a GDI engine with single and split fuel injections," *SAE Tech. Pap. Ser. 2007-01-0211*, 2007.

[76] S. Lee, Y. Oh, and S. Park, "Characterization of the spray atomization process of a multi-hole gasoline direct injector based on measurements using a phase Doppler particle analyser," *Proc. Inst. Mech. Eng. Part D J. Automob. Eng.*, vol. 227, no. 7, pp. 951–965, 2013.

[77] S. C. Li and K. Gebert, "Spray characterization of high pressure gasoline fuel injectors with swirl and non-swirl nozzles," in *SAE Technical Papers*, 1998.

[78] S. E. Parrish and P. V. Farrell, "Transient spray characteristics of a direct-

injection spark-ignited fuel injector," *SAE Tech. Pap. Ser. 970629*, 1997.

[79]   L. W. Evers, "Characterization of the transient spray from a high pressure swirl injector," *SAE Tech. Pap. Ser. 940188*, pp. 1–10, 1994.

[80]   W. F. Piock, B. Befrui, A. Berndorfer, and G. Hoffmann, "Fuel pressure and charge motion effects on GDi engine particulate emissions," *SAE Int. J. Engines 2015-01-0746*, vol. 8, no. 2, 2015.

[81]   C. Schwarz, E. Schünemann, B. Durst, J. Fischer, and A. Witt, "Potentials of the Spray-Guided BMW DI Combustion System Reprinted From : SI Combustion and Direct Injection SI Engine Technology," no. 724, 2016.

[82]   M. Wissink and R. Reitz, "The role of the diffusion-limited injection in direct dual fuel stratification," *Int. J. Engine Res.*, vol. 18, no. 4, pp. 351–365, 2017.

[83]   L. Postrioti, A. Cavicchi, G. Brizi, F. Berni, and S. Fontanesi, "Experimental and numerical analysis of spray evolution, hydraulics and atomization for a 60 MPa injection pressure GDI system," *SAE Int. 2018-01-0271*, pp. 1–17, 2018.

[84]   T. Wang, L. Zhang, S. Bei, and Z. Zhu, "Influence of injection valve opening manner and injection timing on mixing effect of direct injection compressed natural gas–fueled engine," *Int. J. Engine Res.*, pp. 1–10, 2020.

[85]   F. Liu, Z. Li, Z. Wang, X. Dai, and C. Lee, "Dynamics of the in sac cavitating flow for diesel spray with split injection strategy," *Int. J Engine Res.*, no. 5, 2020.

[86]   M. J. Borz, Y. Kim, and J. O'Connor, "The effects of injection timing and duration on jet penetration and mixing in multiple-injection schedules," *SAE Tech. Pap. Ser. 2016-01-0856*, 2016.

[87]   S. Hemdal, I. Denbratt, P. Dahlander, and J. Wärnberg, "Stratified cold start sprays of gasoline-ethanol blends," *SAE Int. J. Fuels Lubr. 2009-01-1496*, vol. 2, no. 1, pp. 683–696, 2009.

[88]   A. Wood, "Optical investigations of the sprays generated by gasoline multi-hole injectors under novel operating conditions," Loughborough University, 2014.

[89]   M. Krämer, E. Kull, M. Heldmann, and M. Wensing, "Investigations on gasoline

spray propagation behaviour characteristic for multihole injectors," *SAE Tech. Pap. 2014-01-2732*, 2014.

[90]   M. Costa, U. Sorge, and L. Allocca, "Increasing energy efficiency of a gasoline direct injection engine through optimal synchronization of single or double injection strategies," *Energy Convers. Manag.*, vol. 60, pp. 77–86, 2012.

[91]   T. Li, K. Nishida, and Y. Zhang, "An insight into effect of split injection on mixture formation and combustion of DI gasoline engines," *SAE Tech. Pap. Ser. 2004-01-1949*, 2004.

[92]   A. Marchi, J. Nouri, Y. Yan, and C. Arcoumanis, "Spray stability of outwards opening pintle injectors for stratified direct injection spark ignition engine operation," *Int. J. Engine Res.*, 2010.

[93]   M. Sjöberg, W. Zeng, and D. Reuss, "Role of Engine Speed and In-Cylinder Flow Field for Stratified and Well-Mixed DISI Engine Combustion Using E70," *SAE Int. J. Engines*, 2014.

[94]   R. Stiehl, J. Schorr, C. Krüger, A. Dreizler, and B. Böhm, "In-cylinder flow and fuel spray interactions in a stratified spray-guided gasoline engine investigated by high-speed laser imaging techniques," *Flow, Turbul. Combust.*, vol. 91, pp. 431–450, 2013.

[95]   M. Sjöberg and D. Reuss, "NOx-Reduction by Injection-Timing Retard in a Stratified-Charge DISI Engine using Gasoline and E85," *SAE Int. J. Fuels Lubr.*, 2012.

[96]   M. Sjöberg and D. L. Reuss, "High-speed imaging of spray-guided DISI engine combustion with near-TDC injection of E85 for ultra-low NO and soot," *Proc. Combust. Inst.*, 2013.

[97]   W. Zeng, M. Sjöberg, and D. Reuss, "Using PIV Measurements to Determine the Role of the In-Cylinder Flow Field for Stratified DISI Engine Combustion," *SAE Int. J. Engines*, vol. 7, no. 2, pp. 615–632, 2014.

[98]   A. Nauwerck, J. Pfeil, A. Velji, U. Spicher, and B. Richter, "A basic experimental study of gasoline direct injection at significantly high injection pressures," *SAE Tech. Pap. 2005-01-0098*, 2005.

[99]   J.-H. Yoo, S.-K. Kim, F.-Q. Zhao, M.-C. Lai, and K.-S. Lee, "Visualization of Direct-Injection Gasoline Spray and Wall-impingement Inside a Motoring Engine," *SAE Tech. Pap. No. 982702*, pp. 1–17, 1998.

[100] W. Hentschel, "Optical diagnostics for combustion process development of direct-injection gasoline engines," in *Proceedings of the Combustion Institute*, 2000, vol. 28, pp. 1119–1135.

[101] J. Lee, K. Nishida, and M. Yamakawa, "An Analysis of Ambient Air Entrainment into Split Injection D.I. Gasoline Spray by LIF-PIV Technique," *SAE Tech. Pap. Ser. 2002-01-2662*, 2002.

[102] D. L. Siebers, "Liquid-phase fuel penetration in diesel sprays," in *SAE Technical Papers*, 1998.

[103] S. E. Parrish, G. Zhang, and R. J. Zink, "Liquid and Vapor Envelopes of Sprays from a Multi-Hole Fuel Injector Operating under Closely-Spaced Double-Injection Conditions," *SAE Int. J. Engines*, 2012.

[104] P. a. Williams *et al.*, "An experimental study of the spray characteristics of pressure-swirl atomizers for DISI combustion systems," *Sae.Org 2001-01-1974*, no. 724, 2001.

[105] I. Schmitz, W. Ipp, and a Leipertz, "Flash boiling effects on the development of gasoline direct-injection engine sprays," *SAE Tech. Pap.*, vol. 2002, no. 724, 2002.

[106] Z. van Romunde, P. Aleiferis, R. Cracknell, and H. Walmsley, "Effect of Fuel Properties on Spray Development from a Multi-Hole DISI Engine Injector," *SAE Pap. 2007-01-4032*, vol. 01, pp. 776–790, 2007.

[107] D. Martin, J. Stratmann, P. Pischke, R. Kneer, and M.-C. Lai, "Experimental Investigation of the Interaction of Multiple GDI Injections using Laser Diagnostics," vol. 3, no. 1, pp. 372–388, 2010.

[108] M. Skogsberg, P. Dahlander, and I. Denbratt, "Spray Shape and Atomization Quality of an Outward-Opening Piezo Gasoline DI Injector," *SAE Tech. Pap.*, no. 2007-01–1409, 2007.

[109] S. Arndt, K. Gartung, and D. Bruggemann, "Spray structure of high pressure

gasoline injectors: analysis of transient spray propagation and spray- gas momentum transfer," in *ILASS-Europe, Zurich*, 2001.

[110] X. S. Tian, H. Zhao, H. F. Liu, W. F. Li, and J. L. Xu, "Liquid entrainment behavior at the nozzle exit in coaxial gas-liquid jets," *Chem. Eng. Sci.*, 2014.

[111] G. D. Crapper, N. Dombrowski, W. P. Jepson, and G. a. D. Pyott, "A note on the growth of Kelvin-Helmholtz waves on thin liquid sheets," *J. Fluid Mech.*, vol. 57, no. 04, p. 671, Mar. 2006.

[112] A. Aliseda, E. J. Hopfinger, J. C. Lasheras, D. M. Kremer, A. Berchielli, and E. K. Connolly, "Atomization of viscous and non-newtonian liquids by a coaxial, high-speed gas jet. Experiments and droplet size modeling," *Int. J. Multiph. Flow*, vol. 34, pp. 161–175, 2008.

[113] D. Fuster *et al.*, "Instability regimes in the primary breakup region of planar coflowing sheets," *J. Fluid Mech.*, vol. 736, pp. 150–176, Nov. 2013.

[114] H. Zhao, H.-F. Liu, J.-L. Xu, W.-F. Li, and W. Cheng, "Breakup and atomization of a round coal water slurry jet by an annular air jet," *Chem. Eng. Sci.*, vol. 78, pp. 63–74, Aug. 2012.

[115] H.-F. Liu, X. Gong, W.-F. Li, F.-C. Wang, and Z.-H. Yu, "Prediction of droplet size distribution in sprays of prefilming air-blast atomizers," *Chem. Eng. Sci.*, vol. 61, no. 6, pp. 1741–1747, Mar. 2006.

[116] E.-S. R. Negeed, S. Hidaka, M. Kohno, and Y. Takata, "Experimental and analytical investigation of liquid sheet breakup characteristics," *Int. J. Heat Fluid Flow*, vol. 32, pp. 95–106, Feb. 2011.

[117] S. H. Pham, Z. Kawara, T. Yokomine, and T. Kunugi, "Detailed observations of wavy interface behaviors of annular two-phase flow on rod bundle geometry," *Int. J. Multiph. Flow*, vol. 59, pp. 135–144, Feb. 2014.

[118] J. C. Lasheras, E. Villermaaux, and Hopfinger, E.J., "Break-up and atomization of a round water jet by a high-speed annular air jet," 1998.

[119] N. Sharma and A. K. Agarwal, "An Experimental Study of Microscopic Spray Characteristics of a GDI Injector Using Phase Doppler Interferometry," *SAE Int.*, pp. 1–10, 2016.
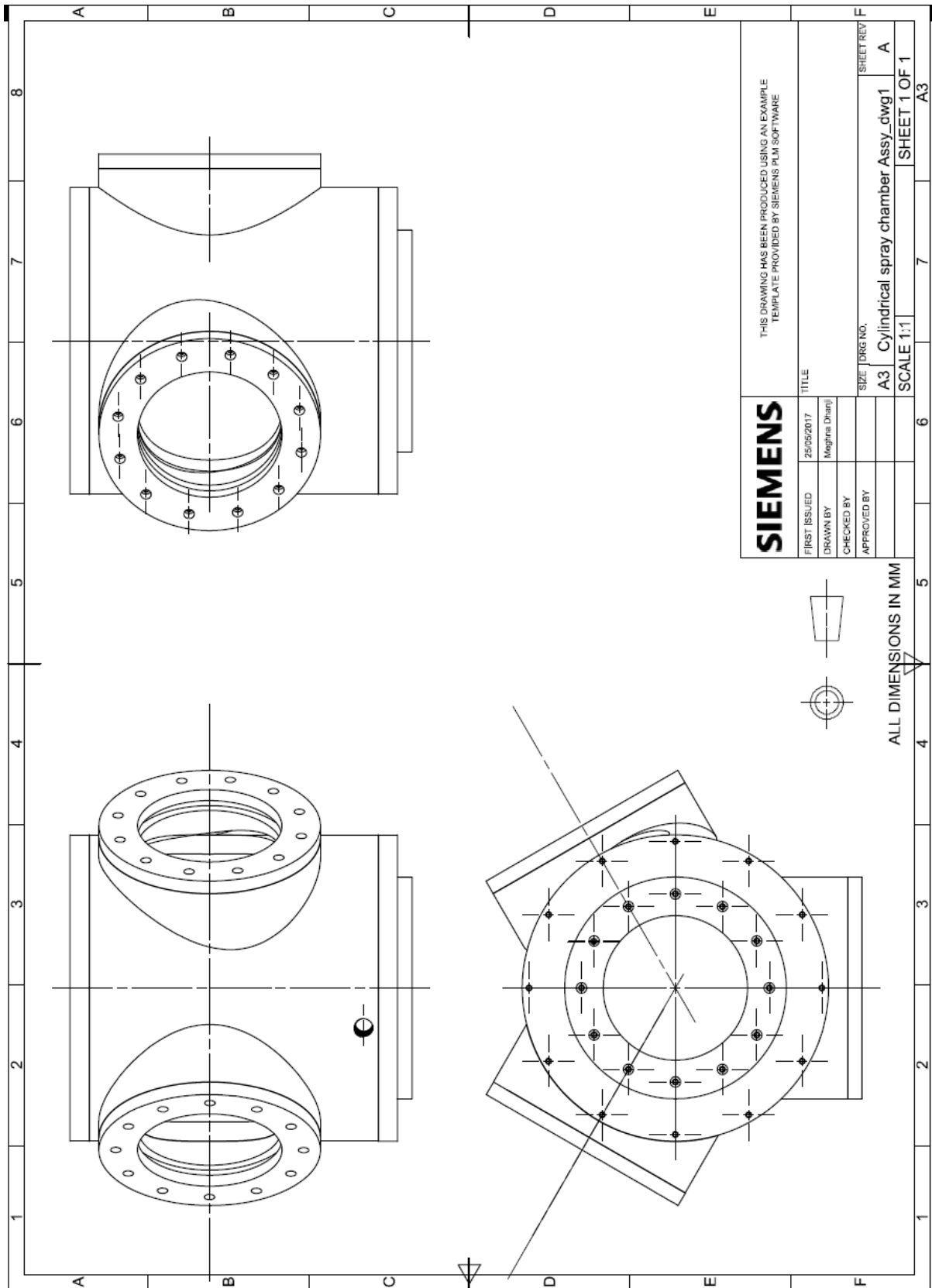
[120] W. Hentschel, a Homburg, G. Ohmstede, T. Müller, and G. Grünefeld, "Investigation of spray formation of DI gasoline hollow-cone injectors inside a pressure chamber and a glass ring engine by multiple optical techniques," *Sae Tech. Pap. Ser.*, vol. 1999-01–36, no. 724, pp. 1–11, 1999.

[121] S. Buri, S. Busch, H. Kubach, and U. Spicher, "High injection pressures at the upper load limit of stratified operation in a DISI engine," *SAE Int. J. Engines*, 2010.

[122] F. Schumann, F. Sarikoc, S. Buri, H. Kubach, and U. Spicher, "Potential of spray-guided gasoline direct injection for reduction of fuel consumption and simultaneous compliance with stricter emissions regulations," *Int. J. Engine Res.*, 2013.

[123] O. Lang *et al.*, "Potential of the spray-guided combustion system in combination with turbocharging," in *SAE Technical Papers*, 2008.

[124] A. Kneifel, S. Buri, A. Velji, U. Spicher, J. Pape, and M. Sens, "Investigations on supercharging stratified part load in a spray-guided DI SI engine," *SAE Int. J. Engines*, 2009.

[125] V. B. Richard, "Gasoline engine with direct injection: processes, systems, development, potential," in *Wiesbaden: Vieweg + Teubner*, 2009.

[126] D. L. S. Hung *et al.*, "Gasoline fuel injector spray measurement and characterization - a new SAE J2715 recommended practice," *SAE Int. J. Fuels Lubr. 2008-01-1068*, vol. 1, no. 1, pp. 534–548, 2008.

[127] G. Hassall, "A practical guide to turbulence and flow measurement by thermal anemometry (CTA), laser-Doppler anemometry (LDA) and particle-image velocitmetry (PIV)," *R. Aeronaut. Soc.*, vol. 3, no. ESDU 17008, 2018.

[128] British Standards Institution, "BS PD5500(2015) : 2015 Specification for Unfired Fusion Welded Pressure Vessels," 2015.

[129] M. Raffel, C. E. Willert, S. T. Wereley, and J. Kompenhans, "Particle Image Velocimetry: A Practical Guide."

[130] Dantec Dynamics, "DynamicStudio User Manual." Dantec Dynamics.

[131] Topas GmbH, "Di-Ethyl-Hexyl-Sebacat DEHS," p. 2.

[132] F. Zhao *et al.*, "Multi-plane time-resolved Particle Image Velocimetry (PIV) flow field measurements in an optical Spark-Ignition Direct-Injection (SIDI) engine for Large-Eddy Simulation (LES) model validations," *Oil Gas Sci. Technol. – Rev. d'IFP Energies Nouv.*, vol. 74, p. 52, 2019.

[133] G. Wigley, D. Hollis, G. Pitcher, and P. Stansfield, "A Multi-plane PIV Analysis of In-Cylinder Flow Structures in an Optical Engine under Part Load Conditions at 3500 rpm."

[134] N. Mitroglou, J. M. Nouri, Y. Yan, M. Gavaises, and C. Arcoumanis, "Spray Structure Generated by Multi-Hole Injectors for Gasoline Direct-Injection Engines Reprinted From : Diesel Injection SI Engine Technology," *City*, no. 724, pp. 776–0790, 2011.

[135] R. Payri, J. Gimeno, P. Martí-Aldaraví, and A. Viera, "Measurements of the mass allocation for multiple injection strategies using the rate of injection and momentum flux signals," *Int. J. Engine Res.*, 2020.

[136] S. Mouvanal, A. Burkhardt, S. Bakshi, and D. Chatterjee, "Numerical study of purging of a gasoline direct injection nozzle at the end of injection," *Int. J. Engine Res.*, 2020.

[137] Y. Zhou, W. Qi, Y. Zhang, and P. Zhang, "Investigation on spray cyclic variations under idle operation of engine using optical diagnostics and statistical methods," *Int. J. Engine Res.*, pp. 1–13, 2020.

[138] L. Zhou, W. Zhao, and H. Wei, "Large Eddy Simulation on the Flame Structure for Split Injections of n-dodecane at Different Temperatures and Densities," *Combust. Sci. Technol.*, vol. 190, no. 12, pp. 2224–2244, 2018.

[139] D. Martin, J. Stratmann, P. Pischke, R. Kneer, and M.-C. Lai, "Experimental investigation of the interaction of multiple GDI injections using laser diagnostics," *SAE Int. 2010-01-0596*, vol. 3, no. 1, pp. 372–388, 2010.

[140] S. Mouvanal, A. Burkhardt, S. Bakshi, and D. Chatterjee, "Numerical study of purging of a gasoline direct injection nozzle at the end of injection," *Int. J. Engine Res.*, 2020.
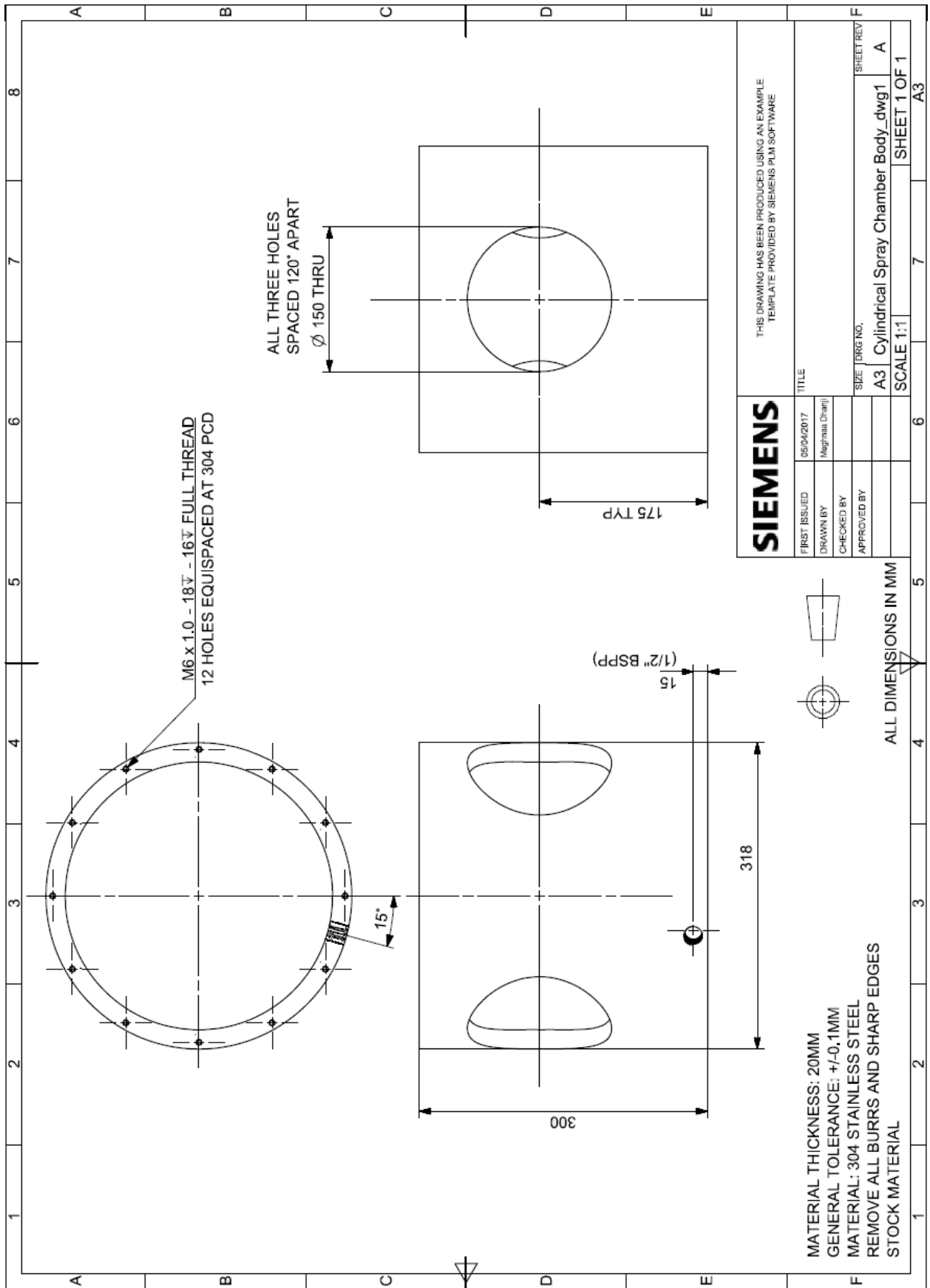
[141] C. Jiang, J. Hélie, and M. C. Parker, "Experimental Investigation of the Effect of High Pressure Nozzle Geometry on Spray Characteristics," no. September, pp. 4–7, 2016.

[142] D. Kim, Y. L. Zhang, and S. Kook, "Influence of wall-wetting conditions on in-flame and exhaust soot structures in a spark ignition direct injection petrol engine," *Int. J. Engine Res.*, 2020.

[143] M. Matsuda, T. Yokomori, M. Shimura, Y. Minamoto, M. Tanahashi, and N. Iida, "Development of cycle-to-cycle variation of the tumble flow motion in a cylinder of a spark ignition internal combustion engine with Miller cycle," *Int. J. Engine Res.*, pp. 3–14, 2020.

[144] P. Priyadarshini, A. Sofianopoulos, S. Mamalis, B. Lawler, D. Lopez-Pintor, and J. E. Dec, "Understanding partial fuel stratification for low temperature gasoline combustion using large eddy simulations," *Int. J. Engine Res.*, 2020.

[145] A. Hadadpour, M. Jangi, and X. S. Bai, "The Effect of Splitting Timing on Mixing in a Jet with Double Injections: A Large-Eddy Simulation Study," *Flow, Turbul. Combust.*, vol. 101, no. 4, pp. 1157–1171, 2018.

[146] X. Li, B. Q. He, and H. Zhao, "Numerical study of the effect of split direct injection on the lean-burn combustion characteristics in a poppet-valve two-stroke gasoline engine at high loads," *Int. J. Engine Res.*, no. 92, 2020.
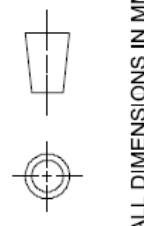
Appendix

A. 2-D Technical Drawings of the Spray Chamber Assembly

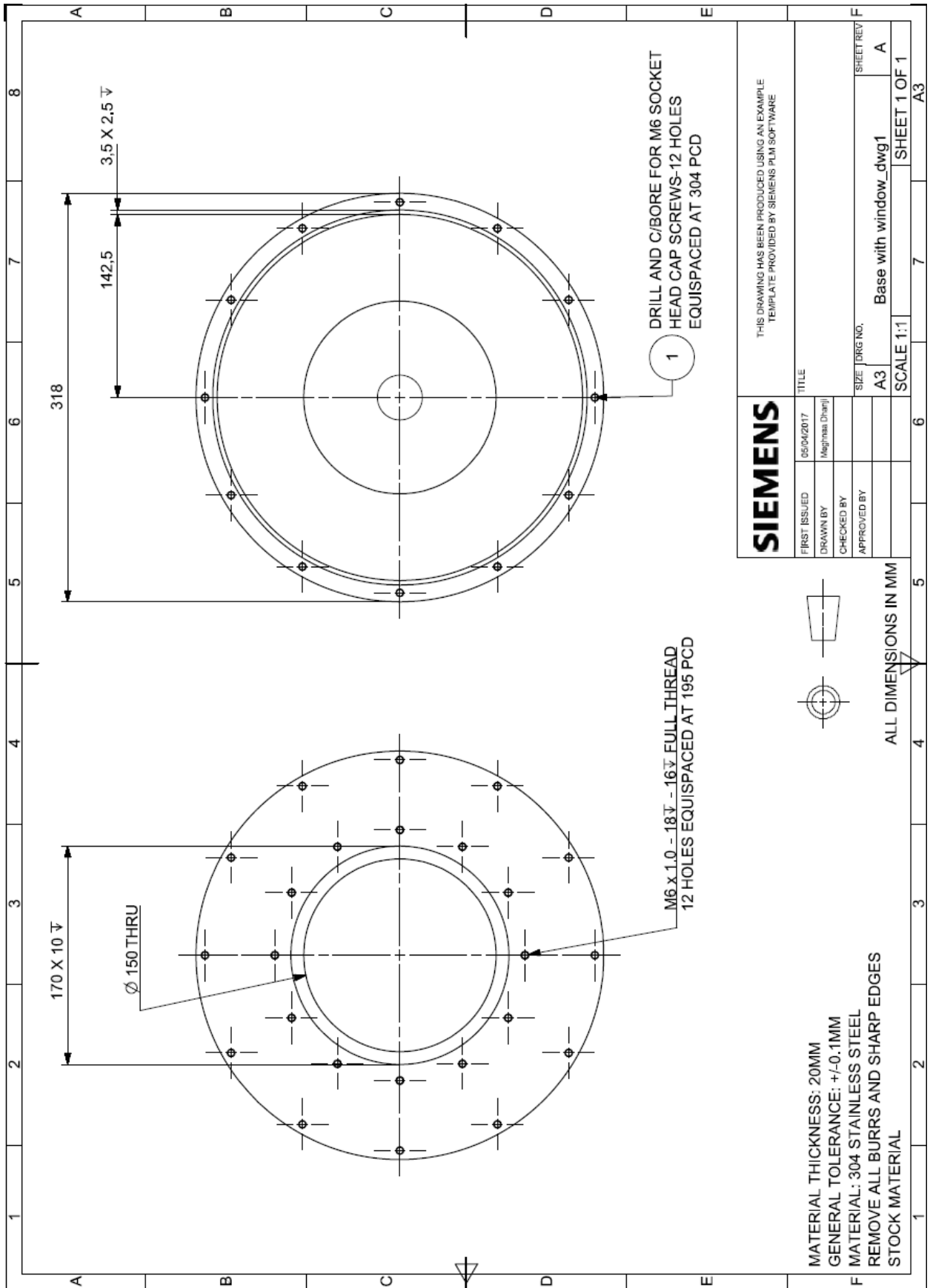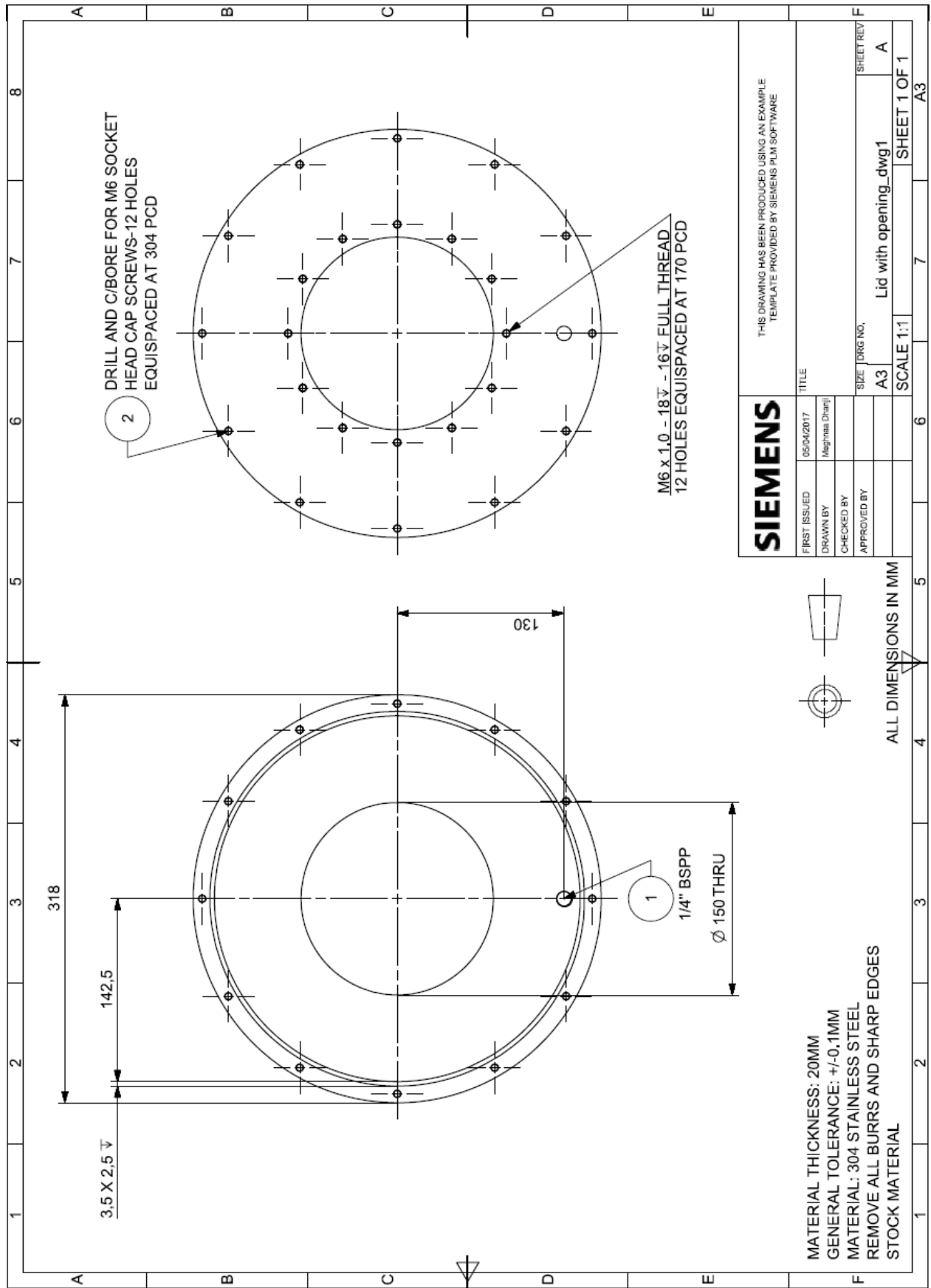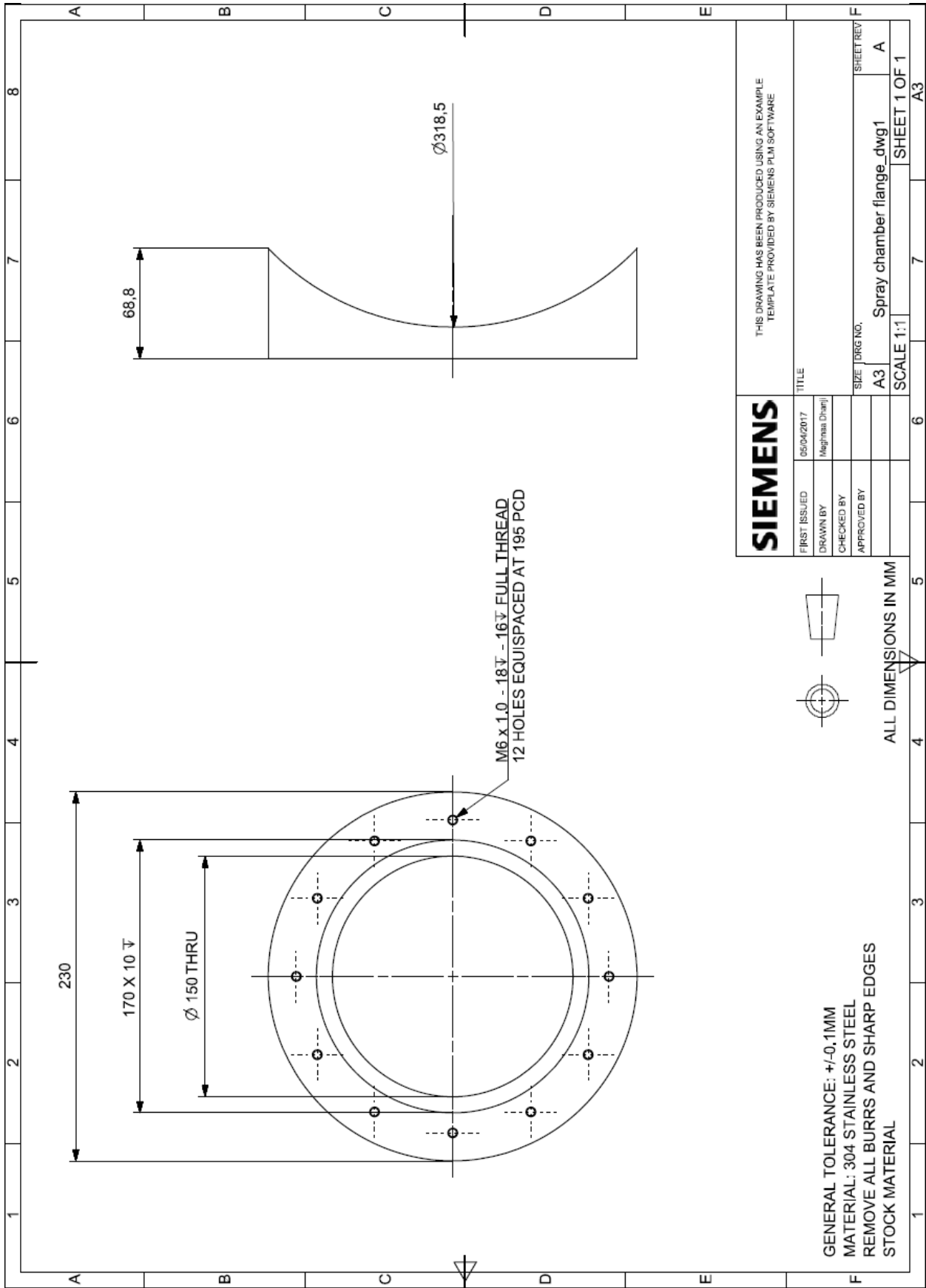# B. 2-D Technical Drawings of the Spray Chamber's Main Body

C. 2-D Technical Drawings of the Chamber Base

D. 2-D Technical Drawings of the Chamber Lid

E. 2-D Technical Drawings of the Chamber's Window Flange

F. 2-D Technical Drawings of the Chamber's Window Frame